

**CREEP FATIGUE LIFE PREDICTION
FOR ENGINE HOT SECTION MATERIALS (ISOTROPIC)
INTERIM REPORT**

by
R.S. Nelson, J.F. Schoendorf, L.S. Lin

United Technologies Corporation
Pratt & Whitney
Engineering Division

December 1986

(NASA-CR-179350) CREEP FATIGUE LIFE
PREDICTION FOR ENGINE HOT SECTION MATERIALS
(ISOTROPIC) Interim Report (Pratt and
Whitney Aircraft) 162 p CSCL 20K

N87-15491

Unclass
G3/39 40320

Prepared For
NATIONAL AERONAUTICS AND SPACE ADMINISTRATION

LEWIS RESEARCH CENTER
21000 BROOKPARK ROAD
CLEVELAND, OHIO 44135

Under Contract NAS3-23288

NASA

PREFACE

The Interim Report contained in this document details the activities performed during the first 16 months of the option portion of the NASA HOST Contract, "Creep Fatigue Life Prediction for Engine Hot Section Materials (Isotropic)", under Contract NAS3-23288. The time period covered is from June, 1984, to September, 1985. The objective of this effort is to improve the high temperature crack initiation prediction technology for gas turbine hot section components. This program is being conducted under the direction of Dr. Gary R. Halford, who serves as the NASA Program Manager. The Program Manager at United Technologies Corporation was Mr. Vito Moreno for the period from June, 1984 through March, 1985, and since that time Mr. Richard S. Nelson has acted in that capacity. Additionally, Mr. Nelson has acted as Co-Principal Investigator for the cumulative damage and TMF tasks. Mr. John F. Schoendorf also serves as Co-Principal Investigator, having oversight of the multiaxial and environmental tasks. Dr. L. S. Lin directs the metallographic examinations of the test material and specimens and provides interpretation of the results. The authors would like to express gratitude to Messrs. Francis Ashland, Napoleon Glowac, Phillip D. Retzer, and William A. Murphy for their efforts in conducting the fatigue testing, to Messrs. Gregory W. Levan and Vartkes Ajemian for their assistance with the metallographic work, and to Mr. Abamilik M. Catao and Ms. Norma C. Tutty for their efforts in preparation of the many reports

PRECEDING PAGE BLANK NOT FILMED

I, II

TABLE OF CONTENTS

Section	Page
1.0 INTRODUCTION	1
2.0 SUMMARY	2
3.0 REVIEW OF PROGRESS DURING BASE PROGRAM	7
3.1 Purpose	7
3.2 Task I - Material/Coating/Component Selection and Acquisition	7
3.3 Task II - Screening of Candidate Life Prediction Approaches	10
3.4 Task III - Evaluate Best Candidate Life Prediction Approach	12
4.0 TASK IIIC - VERIFICATION EXPERIMENTS (BASE PROGRAM)	15
4.1 Experimental Results	15
4.2 CDA Life Prediction Model Improvements	26
5.0 TASK V - THERMOMECHANICAL CYCLING MODEL	27
5.1 Experimental Results	27
5.2 TMF Life Prediction Model Development	51
6.0 TASK VI - MULTIAXIAL STRESS STATE MODEL	55
6.1 Literature Review of State-of-the-Art Multiaxial Life Prediction Models	55
6.2 Experimental Methods and Techniques	58
6.3 Initial Multiaxial Experiments	66
6.4 Future Work	90
7.0 TASK VII - CUMULATIVE LOADING MODEL	91
7.1 Experimental Methods and Test Types	91
7.2 Block Experiments	94
7.3 Sequenced Experiments	107
7.4 Interrupted Experiments	108
7.5 Modifications to CDA Life Prediction Model	117
8.0 TASK VIII - SCREENING OF POTENTIAL ENVIRONMENTAL AND PROTECTIVE COATING MODELS	127
8.1 Literature Review of Environmental Models	127
8.2 Literature Review of Coating Models	131
8.3 Specimen Evaluation	131
8.4 Candidate Model Selection	132
9.0 TASK IX - ENVIRONMENTAL ATTACK MODEL	136
9.1 Test Matrix for Environmental Experiments	136
9.2 Environmental Test Chamber Design	136
APPENDIX I	139
APPENDIX II	142
APPENDIX III	146
REFERENCES	154
DISTRIBUTION LIST	159

SECTION 1.0

INTRODUCTION

The overall operating cost of the modern gas turbine engine is greatly influenced by the durability of combustor and turbine structural components operating at high temperatures. Inadequate durability results in reduced engine efficiency and increased maintenance costs due to premature repair and replacement. To increase the durability of these components, more accurate structural analysis and life prediction methods must be developed for components operating at higher temperatures. However, improvements in the state-of-the art technology for elevated temperature durability prediction have been hampered by 1) the severe operating conditions of the engine, 2) the inability of analytical and life prediction tools used in the design of lower temperature components to predict complex material behavior and interaction of damage mechanisms of components at elevated temperatures, and 3) the high cost of engine development testing which prohibits the accumulation of adequate failure data and local operating conditions required for the systematic development and calibration of durability prediction models.

Traditionally, component durability associated with fatigue cracking has been attributed to separate crack initiation and crack propagation processes. Current cyclic crack initiation prediction methodology is based on correlative fatigue models generally developed to address a specific component or loading configuration. These prediction models are directly calibrated to macroscopically observable and predictable quantities (strain range, mean stress, etc.) and do not address the specific mechanisms associated with the initiation process. This approach has been successful at lower temperatures but its applicability at higher temperatures, where interaction of deformation mechanisms and damage accumulation is strongly temperature dependent, has not been established. This is particularly true for the higher strength isotropic alloys used in gas turbine hot section structures.

The NASA Hot Section Technology (HOST) program is aimed at developing improved life prediction technology for structures operating at elevated temperatures. As part of HOST, the present program will investigate fundamental approaches to high temperature crack initiation life prediction, identify modeling strategies and develop specific models for component relevant loading conditions. The program is a 5-year, 2-part effort (2-year base program plus a 3 year optional program) that will consider two isotropic hot section materials and protective coating systems. Under the base program, various life prediction approaches for high temperature applications have been investigated and basic models for simple cycle, isothermal loading conditions selected and developed. Models that address thermomechanical cycling, multiaxial conditions, cumulative loading, environmental effects and cyclic mean stress will be developed under the optional program. These models will be verified on an alternate material.

SECTION 2.0

SUMMARY

This report details the activities performed during the first 16 months of the option portion of NASA HOST contract NAS3-23288, "Creep Fatigue Life Prediction for Engine Hot Section Materials (Isotropic)", which covers the period from June, 1984, to September, 1985. The specific areas covered include the following tasks:

- Task IIIC - Verification Experiments (Base Program)
- Task V - Thermomechanical Cycling Model
- Task VI - Multiaxial Stress State Model
- Task VII - Cumulative Loading Model
- Task VIII - Screening of Potential Environmental and Protective Coating Models
- Task IX - Environmental Attack Model

The following information within this section highlights the important results obtained under the various tasks which were active during this reporting period. Details of the technical progress under each task is given in Sections 4-9. A brief review of the base program activities (covering the time period of June, 1982, through May, 1984) is given in Section 3.

The major results of Task IIIC, Verification Experiments (Base Program) are as follows:

1. A total of 18 additional isothermal specimen tests were completed at various conditions which complemented but generally did not duplicate conditions run during the base program. These tests examined the effects of conditions such as one-way strain holds, extended hold times, R-ratio at low strain rates and high temperature, load control, and unpolished surfaces.
2. Life predictions were completed for each of the specimen tests under this task using the Cyclic Damage Accumulation model and its associated constants developed during the base program. In most cases, very good agreement was seen between the experimental data and the analytical predictions.
3. Certain hold test conditions were somewhat overpredicted, indicating the need for a revised time dependent term in the basic CDA equation.
4. The effects of elimination of the pre-test electropolishing of the specimen gage surface were judged to have a minimal effect on specimen initiation life.

5. As expected, the load controlled tests showed initiation lives which were similar to those of strain controlled tests at the same load range. The separation lives of the load control tests were shorter, however, due to their more rapid propagation.
6. One-way strain cycling tests at 1800°F produced lives that were essentially the same as those of specimens run under fully reversed strain cycles. This was clearly due to the rapid relaxation of the mean stresses at these conditions.
7. Load controlled tests cycled one-way into compression produced the same kind of dislocation structure seen after one-way tension cycling. However, the compression tests did not cause fatigue cracks; instead, specimen failure was due to creep buckling.

The major results of Task V, Thermomechanical Cycling Model, are as follows:

1. A total of 30 thermomechanical fatigue (TMF) tests were completed during this period. The important variables explored were strain range, strain ratio, temperature range, and cycle type.
2. Strain range had the most important effect on specimen life, and the effects of other variables were shown to depend on the strain range being tested. For example, at higher strain ranges the out-of-phase cycling resulted in a higher life than in-phase cycling, but at lower strain ranges the effect was reversed.
3. Cycle type was also shown to be very important. This demonstrates the clear need for a life model which can account for the effect of cycle path implicitly in its formulation rather than merely having many sets of constants for various cycle types.
4. A "dogleg" cycle test was developed, having a rapid (6 second) strain cycle at either the high or the low temperature end of the temperature cycle and the strain being held constant for the remainder of the cycle. This represented an effort to produce conditions more like those seen during isothermal testing. However, the test results revealed that this cycle was just as complex as other TMF cycles, and the results could not be inferred from the isothermal data.
5. Maximum cycle temperature was seen to have a more important effect than minimum temperature for the conditions tested.
6. Multiple (and sometimes competing) damage modes were shown to be the cause of the unusual life data from the various test conditions. This emphasizes the need for the final life prediction code to be able to determine exactly which mode of damage will be caused by a given loading history of a component.

7. A new type of specimen was utilized after the initial series of tests. The first group of specimens had internal extensometry of the type pioneered by Pratt & Whitney many years ago. The new specimens are designed for use with external extensometers like those used for the base program isothermal tests and can therefore be made without internal ridges. This decreases specimen cost and eliminates distortion caused by the ridges.
8. Initial life predictions were completed for TMF tests using the current form of the CDA model. The out-of-phase tests were predicted reasonably well, but the trend of the in-phase test data was opposite to their predictions.
9. An incremental form of the CDA life prediction model has been formulated and is under evaluation for use in TMF life predictions.

The major results of Task VI, Multiaxial Stress State Model, are as follows:

1. A literature review was conducted to identify state-of-the-art multiaxial life prediction models. Their potential for use in predicting the multiaxial effects in hot section components of gas turbine engines was assessed.
2. Several modifications were made to improve the test facility and increase its high temperature capability to the required level.
3. Twenty-eight thin-walled tubular specimens, designed to accommodate the directly attached extensometer, were fabricated from hollow core bars cast from B1900+Hf material.
4. The specimen material was examined to characterize its microstructure with respect to gamma prime size, porosity distribution, grain size, and casting defects (if any).
5. A multiaxial fatigue test matrix utilizing twenty-six specimens was established to provide crack initiation data for life prediction model development.
6. Four multiaxial fatigue specimen tests were completed using four different strain cycles; simple tension, simple torsion, combined tension-torsion in-phase and combined tension-torsion 90° out-of-phase. Fatigue cracks were observed to initiate and grow on planes perpendicular to the maximum normal strain under all loading conditions.
7. Fracture surfaces were metallographically examined to characterize the crack initiation sites. Dross was found at the initiation site of one of the specimens which may have caused premature cracking.
8. The remaining untested specimens were inspected using X-ray, fluorescent penetrant and visual procedures and were found to be adequate.
9. Several parameters based on strain or plastic work quantities were used with limited success to correlate the specimen test data.

The major results of Task VII, Cumulative Loading Model, are as follows:

1. A total of 50 cumulative damage tests were completed during the reporting period, including 30 block tests, 9 sequenced tests, and 11 interrupted tests.
2. The block temperature tests showed very little interaction between damage accumulated at low and high temperatures. Apparently the damage was accumulated in two different places; primarily in the grains at 1000°F and in the carbides and grain boundaries at 1600°F.
3. A non-linear version of the CDA model was developed to account for the effects seen during these temperature block tests. It operates on a normalized life ratio and acts as a modifier of the damage rate calculated by the basic CDA equation.
4. The block R-ratio tests demonstrated a very strong effect from performing even a few cycles at $R=0$ followed by cycling at $R=-1$. This corroborates the data produced during the base program concerning the increased life seen during $R=0$ testing.
5. A revised method of integrating the CDA life model was developed which tracks a ductility ratio instead of the actual ductility. This allows the primary creep ductility term to change during a test, as when a block of $R=0$ cycling follows a block of $R=-1$ cycles.
6. The block hold tests showed essentially a linear relationship for damage accumulation, indicating that conventional theories fully account for this type of loading sequence.
7. The sequenced strain range tests produced no interaction with the combinations of low strain ranges, but the degree of interaction increased as the strain ranges increased. This again verified that the fundamental approach of the CDA life prediction model is correct, since this behavior would be expected based on the effect of maximum stress on primary creep ductility.
8. The sequenced strain rate tests were predominantly linear in their damage accumulation and were well predicted by the current CDA model.
9. The interrupted tests (both the pre-strain type and the alternating conditions type) showed a moderate interaction, though not as much as would be predicted by the amount of accumulated creep strain. This demonstrated the need for definition of an effective creep strain to use in such conditions instead of the actual strains.

The major results of Task VIII, Screening of Potential Environmental and Protective Coating Models, are as follows:

1. A literature survey was conducted to identify current models used for the prediction of environmental and coating effects. The models were assessed for their suitability to predict these effects in hot section components of gas turbine engines.
2. A methodology was developed for metallurgical review of environmentally influenced specimens and a trial specimen was run to check the procedures.
3. Specimen test results from previously completed tasks were evaluated to determine the extent of environmental influence in these tests.

The major results of Task IX, Environmental Attack Model, are as follows:

1. An environmental fatigue test matrix utilizing twenty-seven specimens was established to provide crack initiation data for development of an environmental attack (oxidation) model for prediction of effects on the creep-fatigue life.
2. A low pressure test chamber was designed to accommodate the environmental fatigue tests.

SECTION 3.0

REVIEW OF PROGRESS DURING BASE PROGRAM

3.1 PURPOSE

This section is intended to provide a brief review of the progress made during the first two years of this contract effort. This should be useful to persons not familiar with the early portion of this particular HOST contract and should serve as background for the work reported on in Sections 4.0 - 9.0. In particular, the data generated during the base program will not be repeated in this report. If that data or other details of the base program are desired, they may be found in the Second Annual Report (Ref. 3.1).

3.2 TASK I - MATERIAL/COATING/COMPONENT SELECTION AND ACQUISITION

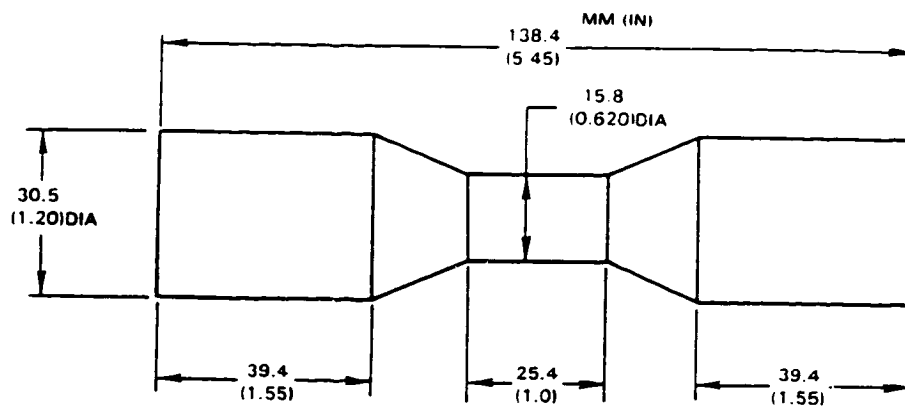
Under this task, the following materials were recommended and approved for use in both the base and option portions of the program:

Base Material	=	Cast B1900 + Hf	(PWA 1455)
Alternate Material	=	Wrought INCO 718	(AMS 5663)
Coatings	=	Diffusion Aluminide	(PWA 273)
		MCrAlY Overlay	(PWA 286)

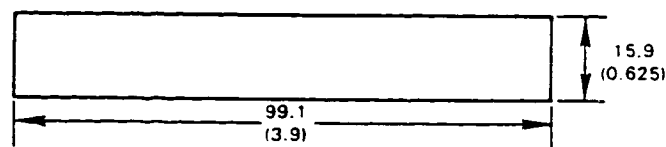
In the base program, a single heat of approximately 2500 pounds of B1900+Hf material was obtained and fully characterized regarding composition and microstructure in both the as-cast and the heat treated conditions. For the fully heat treated condition, the grain size was shown to be between ASTM 1 and 2, which represents an average grain diameter of 180-250 microns (0.007-0.010 in.). The average γ' size in this condition is approximately 0.9 microns. The configuration of the cast test bars used for the fatigue specimens is shown in Figure 3-1.

A total of 21 tensile tests were completed, covering the temperature range from room temperature to 1093°C (2000°F). Figure 3-2 shows typical stress-strain response curves for the standard strain rate of 0.005 min⁻¹. Also, a total of 19 specimens were creep tested at temperatures between 649°C (1200°F) and 982°C (1800°F). Both actual test data and post-test metallurgical examinations of these monotonic specimen tests were used to understand the deformation mechanisms active at various temperatures for this material.

All base program fatigue tests were conducted in closed loop servohydraulic test rigs with induction heating of the specimen. For the majority of these tests, the specimen used was the constant diameter, solid, ridgeless design shown in Figure 3-3. This specimen was referred to as "Type C" and was designed to work well with external extensometry. It was shown to provide data consistent with that produced by ridged specimens but without the notch failures often associated with the ridges. Specimen preparation was by centerless grinding, and a light electropolish finish was used to eliminate any residual surface stresses and stray machining marks.



(A) "Standard" Bar Configuration



(B) Constant Section Bar

Figure 3-1 Casting Geometries Used for Test Specimens

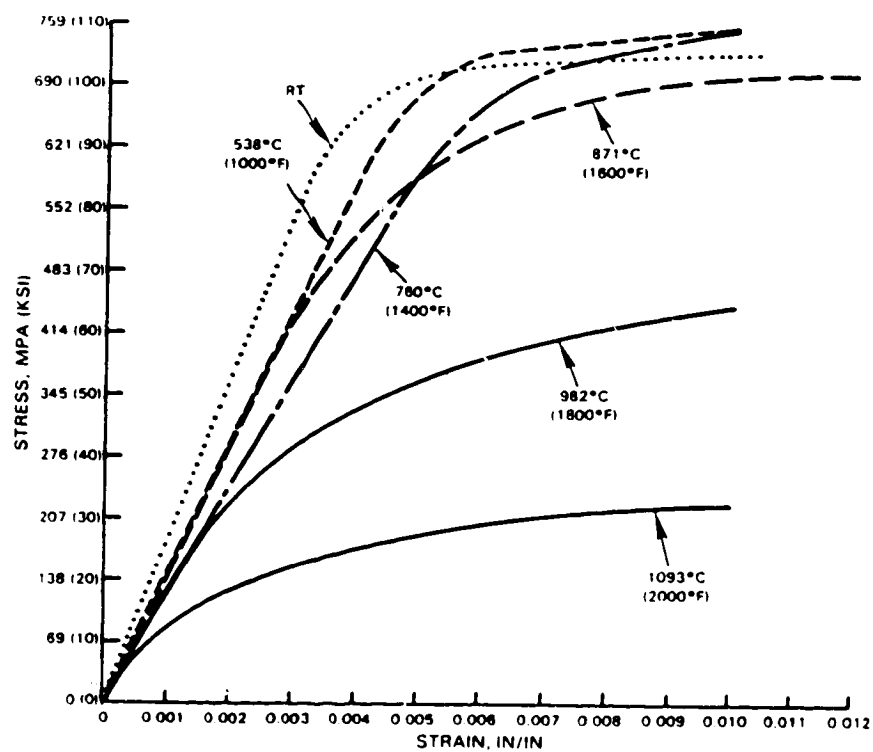


Figure 3-2 Monotonic Tensile Response, $\dot{\epsilon} = .005 \text{ min}^{-1}$

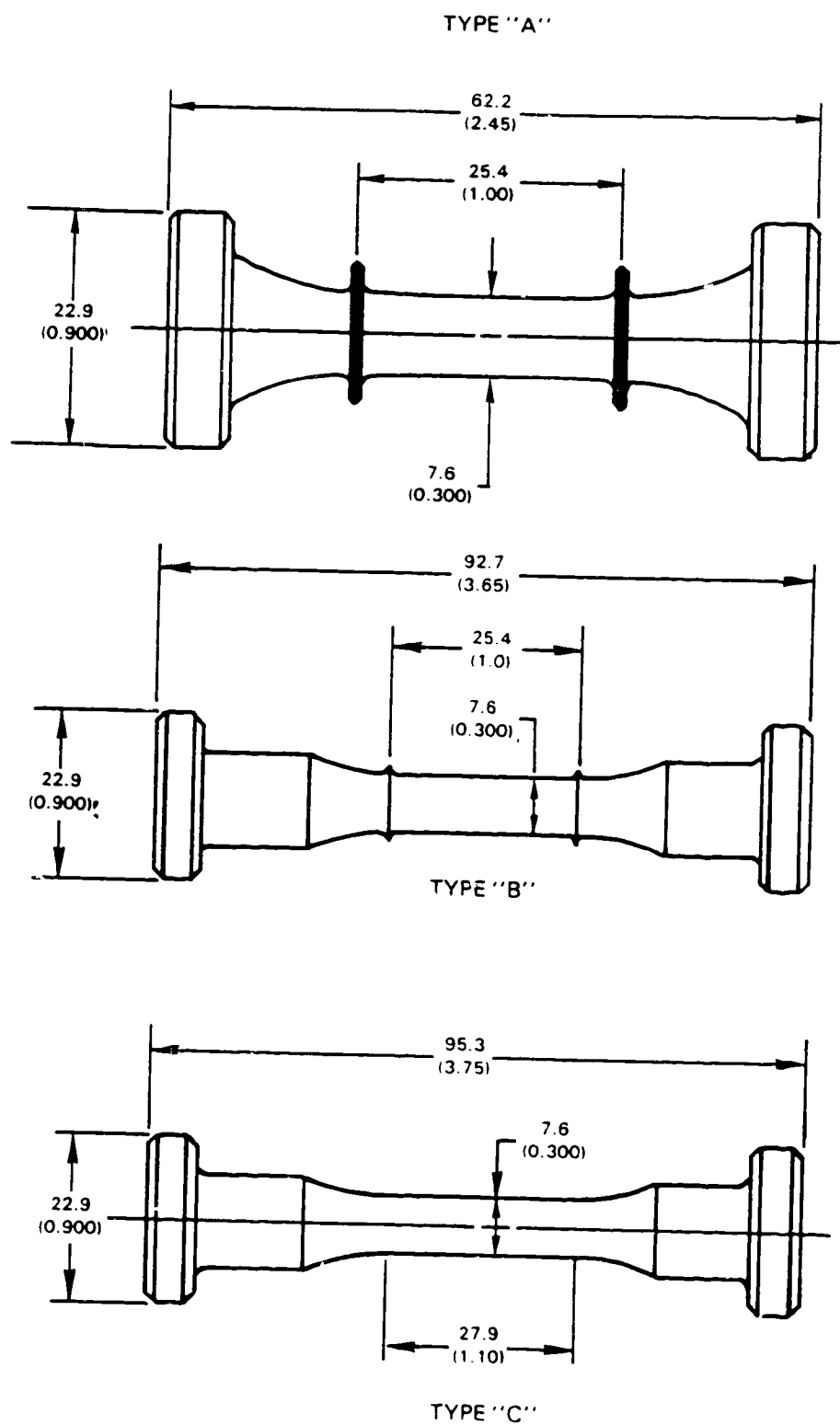


Figure 3-3 Fatigue Specimen Geometries for Initial Testing

A total of 99 isothermal fatigue tests were conducted during the base program covering the temperature range from 538°C (1000°F) to 982°C (1800°F), with the bulk of the tests being run at 871°C (1600°F). The additional variables studied included strain range, ratio, and rate, as well as hold time effects. For each specimen, a crack initiation life was determined using the results of surface replicas taken during tests conducted at similar conditions. The definition of initiation was chosen to be the generation of a 0.76 mm (0.030 in.) surface length crack. This surface length corresponds to a crack depth of about 1-2 grain diameters and hence should represent the point at which the crack may be considered to be propagating in an isotropic medium.

Many specimens were examined metallographically using optical, SEM, and TEM techniques to determine failure sites, crack paths, and dislocation networks. No statistically significant difference could be seen between failures which originated at porosity and those which originated at carbides. The initiation and propagation modes (transgranular or intergranular) were shown to be a function of both temperature and strain rate. Figure 3-4 shows that there is a greater tendency toward intergranular behavior as temperature increases and strain rate decreases. The appearance of the dislocation networks created by various loading conditions suggested that the maximum stress achieved during the initial cycling was very important to the subsequent fatigue capability of the material.

3.3 TASK II - SCREENING OF CANDIDATE LIFE PREDICTION APPROACHES

Six candidate life prediction approaches were evaluated during this task, including the following:

1. Coffin-Manson Model
2. Damage Rate Model (Majumdar)
3. Tensile Hysteresis Model (Ostergren)
4. Local Crack Tip Parameters (CTOD as $f(J \text{ integral})$; LEFM)
5. Total Strainrange Partitioning (Halford et al)
6. Ductility Exhaustion Models (Spaeth et al; Chaboche)

Each of these models was evaluated relative to the others using a ranking procedure which considered four criteria. These included the testing required to determine model constants, regression and prediction capability, fundamental basis for the model, and the amount of judgment required to apply the model to an actual component loading cycle. Ultimately, none of these candidate approaches were selected for further work. Instead, the approach and model which developed from the evaluation procedure represented a combination of the best features of the various life prediction models considered.

ORIGINAL PAGE
OF POOR QUALITY

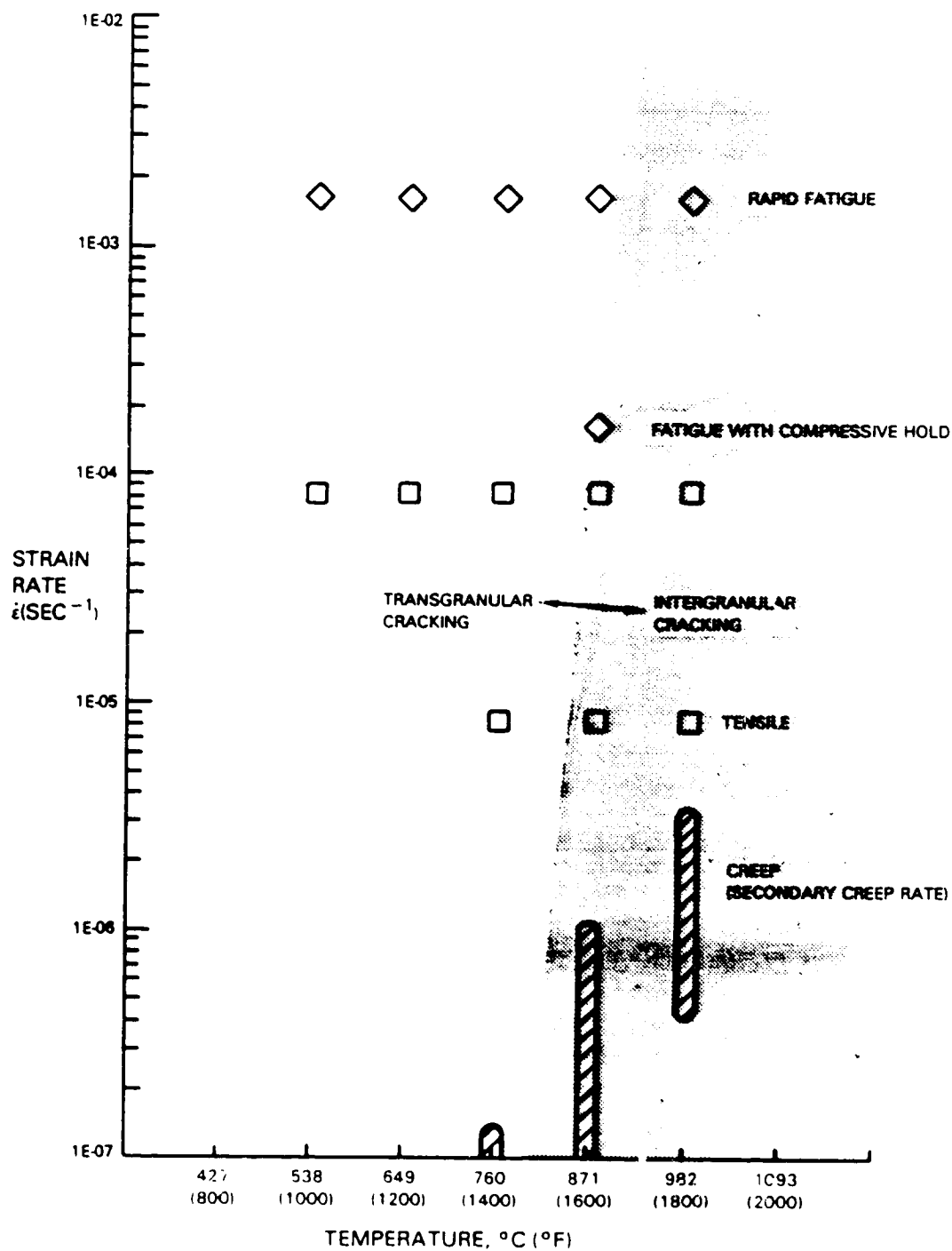


Figure 3-4 Cracking Map for B1900+Hf

3.4 TASK III - EVALUATE BEST CANDIDATE LIFE PREDICTION APPROACH

The life prediction approach which developed during the base program is called Cyclic Damage Accumulation (CDA). One of the fundamental assumptions of the CDA model is that the damage capability is related to the grain dislocation structure. Determination of the grain capability must therefore include consideration of the entire loading history of the specimen, especially the maximum stress excursions. In particular, it was assumed that the grain cyclic capability can be calculated from the maximum stress attained in the initial loading cycle and the amount of primary creep strain that could have been developed if that stress level had been held constant. Figure 3-5 shows the relationship between this maximum stress and the primary creep strain as determined from isothermal creep tests. It was further assumed that, for temperatures below 649°C (1200°F) where little or no creep occurs, the grain cyclic capability would be represented by the residual inelastic strain (percent elongation) measured after a tensile test. The result of these two assumptions is that grain cyclic capability varies as a function of temperature and stress as shown in Figure 3-6.

Another feature incorporated in the CDA life model was the use of damage ratios rather than absolute damage levels. By plotting the available data for cycles having either time-independent or time-dependent damage, it was possible to arrive at the following mathematical form of the CDA model:

$$\int_0^N \frac{dD}{dN} dN = \left[\frac{dD}{dN} \right]_{\text{Ref}} \left\{ \left(\frac{\sigma_T}{\sigma_{T_{\text{Ref}}}} \times \frac{\Delta \sigma}{\Delta \sigma_{\text{Ref}}} \right) + \left(\frac{\sigma_T}{\sigma_{T_{\text{Ref}}}} \frac{\Delta \sigma_{\text{Ref}}}{\Delta \sigma} \right)^{B'} \left[\left(\frac{t}{t_{\text{Ref}}} \right)^{C'} - 1 \right] \right\} dN \quad (3.1)$$

where a cycle by cycle integration is performed to account for evolution of the hysteresis loop.

The entire model can now be written as:

$$\bar{\epsilon}_p - \int_0^N \frac{dD}{dN} \left[\left(\frac{\sigma_T}{\sigma_{TR}} \right) \left(\frac{\Delta \sigma}{\Delta \sigma_R} \right) + \left[\left(\frac{\Delta \sigma_R}{\Delta \sigma} \right) \left(\frac{\sigma_T}{\sigma_{TR}} \right) \right]^{B'} \left[\left(\frac{t}{t_R} \right)^{C'} - 1 \right] \right] dN = 0 \quad (3.2)$$

where:

- $\bar{\epsilon}_p$ = primary creep strain ductility
- $\left. \frac{dD}{dN} \right)_{R,R}$ = reference cyclic damage rate
- σ_T = maximum tensile stress
- $\Delta \sigma$ = stress range
- t = time (total cycle period + hold times)/2
- N = cycle number
- R = reference condition
- B' = exponent on stress in primary creep power law
- C' = exponent on time in primary creep power law with shifted time origin

This equation was then calibrated using the baseline fatigue data and used to generate life predictions for various verification cycles. Sensitivity studies were also conducted to determine the effects of ratio of crack size to grain size, definition of initiation, choice of reference condition, and data requirements for life predictions. Preliminary work was also done on possible means of using this or a similar equation to predict intergranular cracking as well as transgranular.

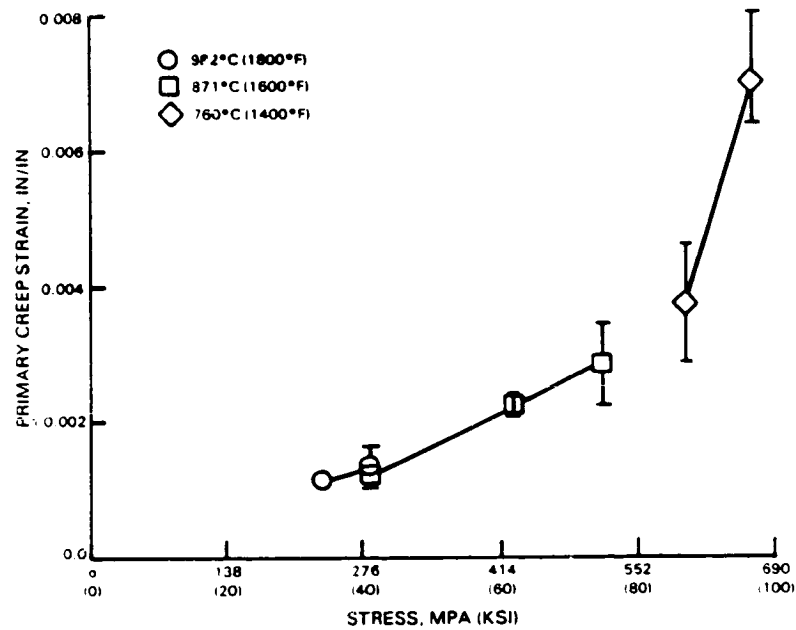


Figure 3-5 Primary Creep Strain is a Linear Function of Stress

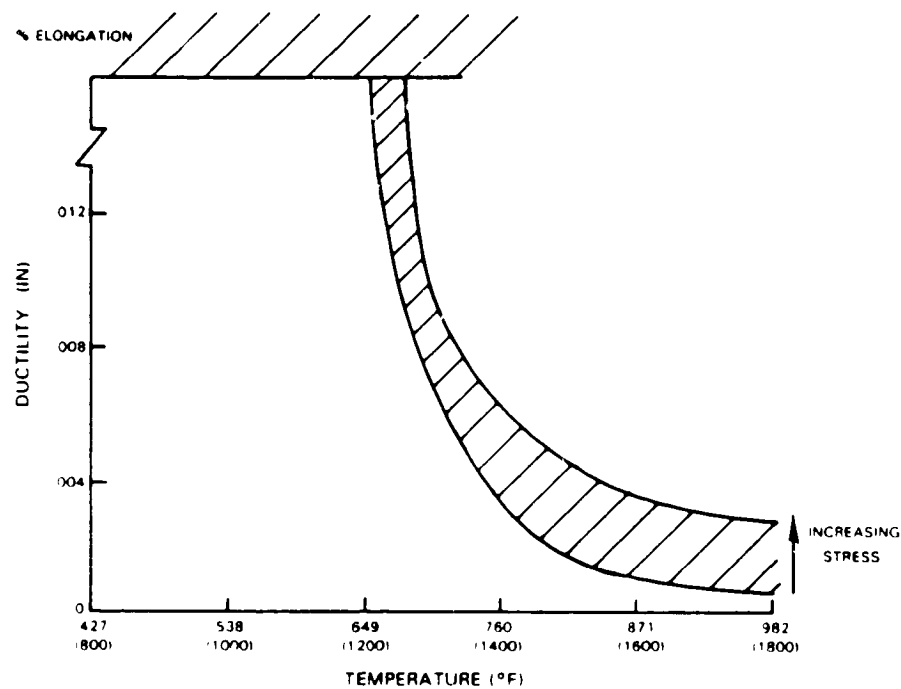


Figure 3-6 Assumed Grain Cyclic Fatigue Capability

SECTION 4.0

TASK IIIC - VERIFICATION EXPERIMENTS (BASE PROGRAM)

4.1 EXPERIMENTAL RESULTS

4.1.1 General Test Matrix

The work accomplished under this task was begun during the base program and continued for several months into the current reporting period. The purpose of these tests was to provide additional verification of the predictive capability of the Cyclic Damage Accumulation (CDA) life prediction method developed during Tasks II and III. Additionally, some of these tests were designed to answer questions regarding material behavior under various unusual conditions. A complete matrix of these tests is shown in Table 4-1, and the details of each group of tests are given in the following discussion sections. A detailed listing of the pertinent test data for each of the specimens tested may be found in Appendix I.

4.1.2 Hold Time Tests with $R=0$

A total of four specimens were run at 871°C (1600°F), 0.5% strain range, $R=0$, 10 CPM, with a one minute hold at +0.5% strain. The intent of these tests was to demonstrate the effect of a high maximum stress fatigue cycle coupled with a significant amount of simultaneous creep damage. The median observed initiation life was 225 cycles, which is about 6X lower than the median life of similar hold tests conducted at $R=-1$. Two of the specimens were replicated during the testing, and a plot of the data obtained is shown in Figure 4-1. It can be seen that the cracks grew quickly at first, then slowed considerably as the stress relaxed downward. This indicates that the higher stress experienced during the early part of these tests apparently produces a significant amount of damage, thus shortening the time to initiate a crack. However, because the relaxation causes the damage rate to slow down, the overall test length is not affected as much as the initiation life. Figure 4-2 shows TEM micrographs of the dislocation structure of one of these specimens (8D). It can be seen that the structure consists of short wavy segments in the gamma matrix, which is similar to that of creep specimens examined during the base program. This confirms that a large component of creep damage was present in these tests. Another evidence of significant creep damage is that these specimens were significantly overpredicted by the CDA model, as shown in Figure 4-3. These tests therefore suggest the need to revise the time-dependent damage term in the basic CDA equation.

For comparison with the $R=0$ tension hold results, optical and SEM examinations were completed on a $R=-1$ compression hold specimen (12D) from the base program tests. Figure 4-4 shows that the primary crack initiated at porosity and propagated mostly in an intergranular mode. This indicates that such tests also contained a measure of creep damage, and any revisions to the time-dependent damage term will have to consider these specimens.

TABLE 4-1
TEST MATRIX FOR VERIFICATION EXPERIMENTS (Base Programs)

Temp (°F)	Control Variable		Strain Rate (sec ⁻¹)	CYCLE TYPE					
				Continuously Cycled Tests			Hold Time Tests		
	Type	Value		R = 0	R = -1	R = -∞	1 Min Tens R = 0	10 Min Tens R = -1	1 Min Comp R = 0
1000	Strain	0.005	0.00167						29C
1600 ↓	Strain	0.004	0.00167		9C				
		0.005	0.00167	9A			8C, 8D, 10A, 128A		
		0.008	0.00270			101A		108C	
	Stress	75 Ksi	0.00167	11A, 47A					
	Stress	100 Ksi	0.00167	131C		131D, 121D*			
1800	Strain	0.005	0.000167	12B, 47C	131B*	128C			

*Suspended Tests

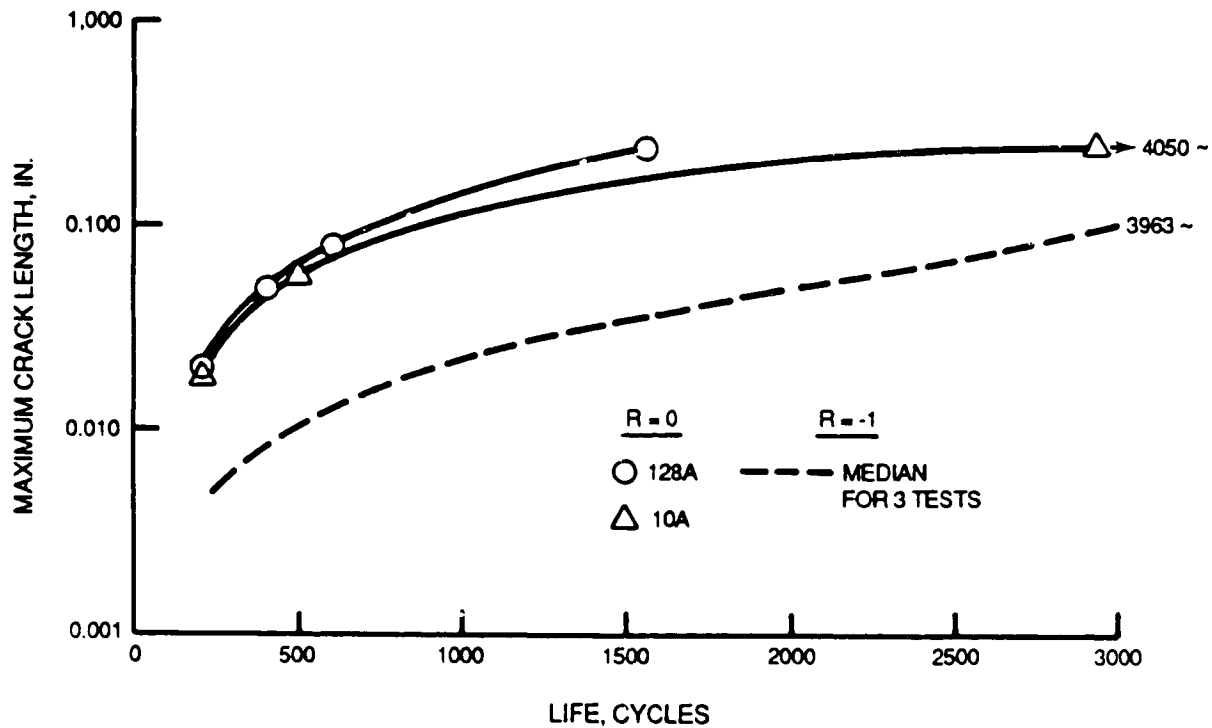


Figure 4-1 Crack Growth Data for Tensile Hold Tests Fixed Conditions: 0.5% $\Delta\epsilon$; 10CPM + 1 Min. Hold

ORIGINAL PAGE IS
OF POOR QUALITY

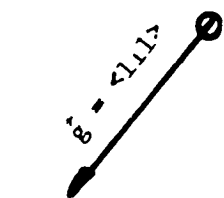


Figure 4-2 Dislocation Structure After Being LCF Tested at 1600°F, $\Delta\epsilon_t = 0$ to 0.5%, $R = 0$, 10 CPM with 1 Minute Tension Hold for 1880 Cycles (50% load drop) (Specimen 8D).

CYCLIC DAMAGE ACCUMULATION LIFE PREDICTION MODEL
PREDICTED VS ACTUAL LIVES

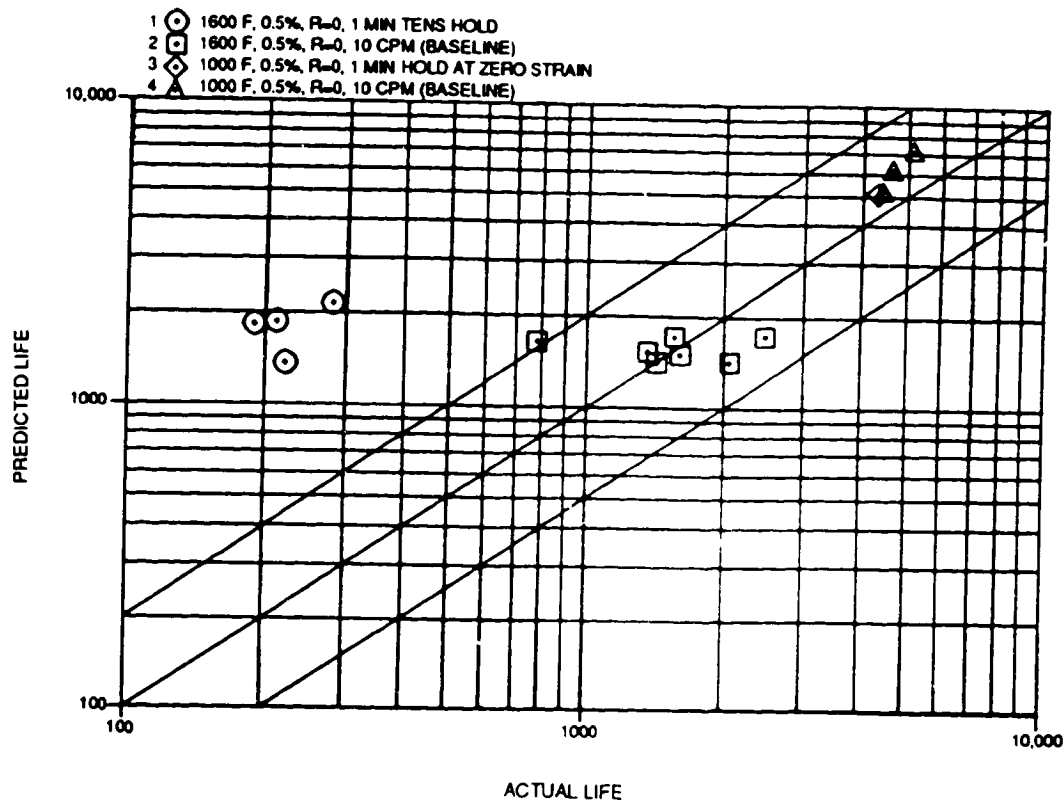


Figure 4-3 CDA Life Predictions for R=0 Hold Tests

A single specimen was run at 538°C (1000°F), 0.5% strain range, R=0, 10 CPM, with a one minute hold at zero strain. Similar conditions have been shown to cause life debits for certain alloys, even at temperatures at which there is no appreciable creep. Such conditions can cause time-dependent plasticity or reduce the equilibrium stress which would result in more damage during the tensile strain excursion. However, the resulting life was essentially the same as specimens tested at the same conditions but without the hold time imposed. The CDA life prediction for this test is also shown in Figure 4-3, and it is well predicted.

4.1.3 High Strain Range Verification Tests

The first test of this series, specimen 108C, was conducted at 871°C (1600°F), 0.8% strain range, R=-1, with a ten minute hold at +0.4% strain. This generated a much larger inelastic strain range than had been tested previously, thus providing additional data for use in determining flow equations for life models such as the Total Strain - Strain Range Partitioning life prediction model (Ref. 4.1). The life was significantly shorter than what would be predicted by the current CDA model, as shown in Figure 4-5. In fact, it should be noticed that the depression of the maximum stress caused by the long hold time actually caused the life prediction to be slightly higher than the prediction for the baseline fully reversed tests. This serves to underscore the need for a revision of the time-dependent damage term of the CDA model.

ORIGINAL PAGE IS
OF POOR QUALITY

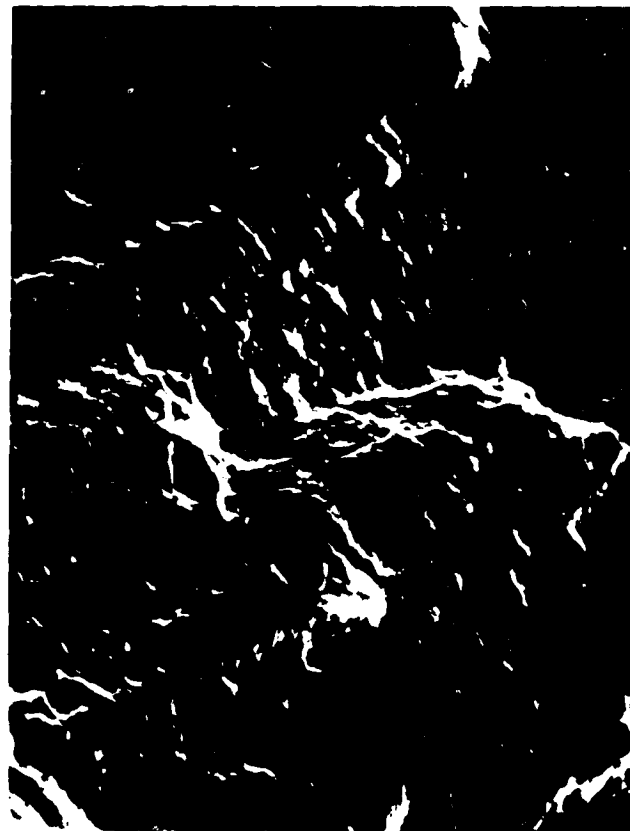


11X

(a)

origin (b)

50X



500X

(c)

Figure 4-4

Fracture surface of Specimen 12D after being LCF tested at 1600°F, $\Delta\epsilon_c = 0.5\%$, $R = -1$ with 60 sec. hold at $\epsilon = -0.25\%$ for 840 cycles (50% load drop).

(a) Optical fractography (mostly intergranular).

(b) SEM showing porosity as crack initiation site on surface.

(c) Faint fatigue striations.

CYCLIC DAMAGE ACCUMULATION LIFE PREDICTION MODEL
PREDICTED VS ACTUAL LIVES

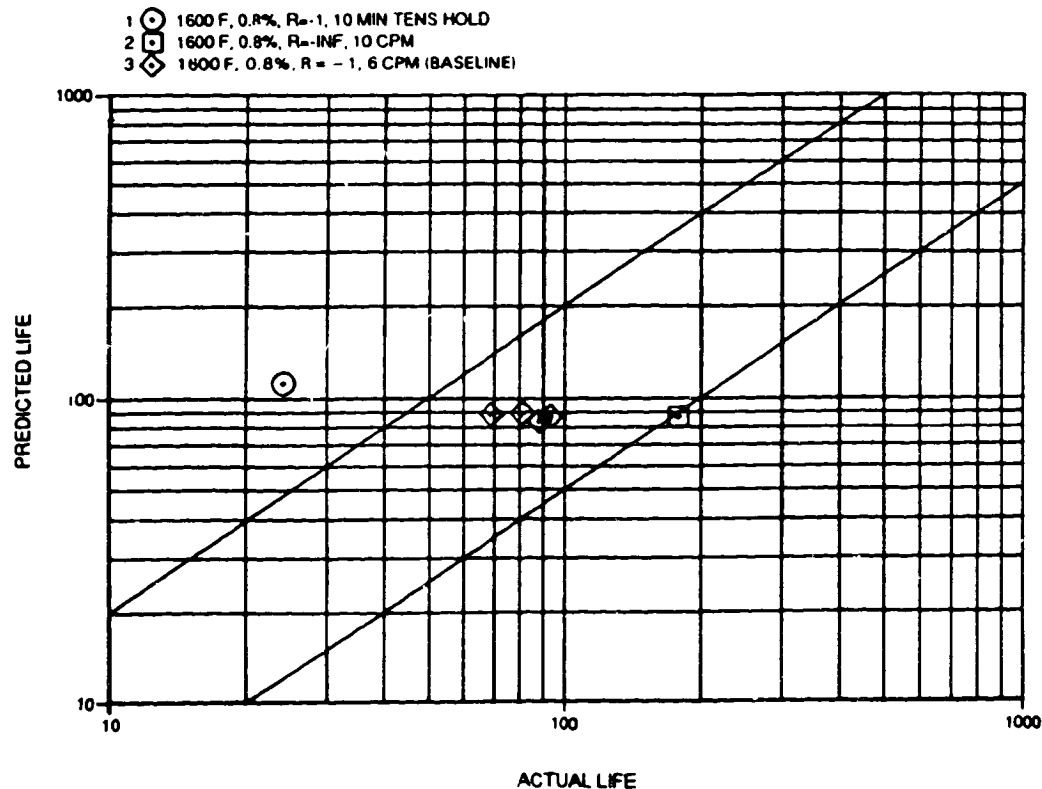


Figure 4-5 CDA Life Predictions for High Strain Range Tests

The second test was also conducted at 871°C (1600°F), 0.8% strain range, but with $R=-\infty$. As shown in Figure 4-5, the initiation life of this test was about twice that of the baseline fully reversed tests. The CDA prediction was essentially the same as that for the fully reversed conditions; revision of the model constants for this temperature is being investigated for improved accuracy.

4.1.4 R-Ratio Effects at Low Strain Rate and High Temperature

In order to explore the influence of R-ratio acting in combination with high temperature and low strain rate, a series of three specimens was tested at 982°C (1800°F), 0.5% strain range, and 1 CPM (instead of the usual 10 CPM). Two specimens were run with $R=0$, and one was tested with $R=-\infty$. The initiation lives were about 3X lower than those of similar tests conducted at $R=-1$, but the separation lives were only slightly lower. This indicates that considerable damage was done during the one-way strain excursions, even into compression. Figure 4-6 shows the fracture surface of specimen 12B, and it can be seen that the primary crack initiated at a carbide and propagated intergranularly. The SEM micrographs show a secondary crack which is likewise moving along grain boundaries. The CDA life predictions for these tests are shown in Figure 4-7, along with the baseline $R=-1$ tests at these conditions. It can be seen that the CDA predictions are in good agreement with the observed lives, since the CDA model debits the available creep ductility by the amount of unreversed inelasticity generated during the initial cycling.

ORIGINAL PAGE IS
OF POOR QUALITY



origin

(b)

100X

Figure 4-6

Fracture Surface of Specimen 12B after being LCF tested at 1800°F, $\Delta\epsilon_t = 0.5\%$, $(R = 0)$ 1 cpm for 900 cycles (50% load drop).

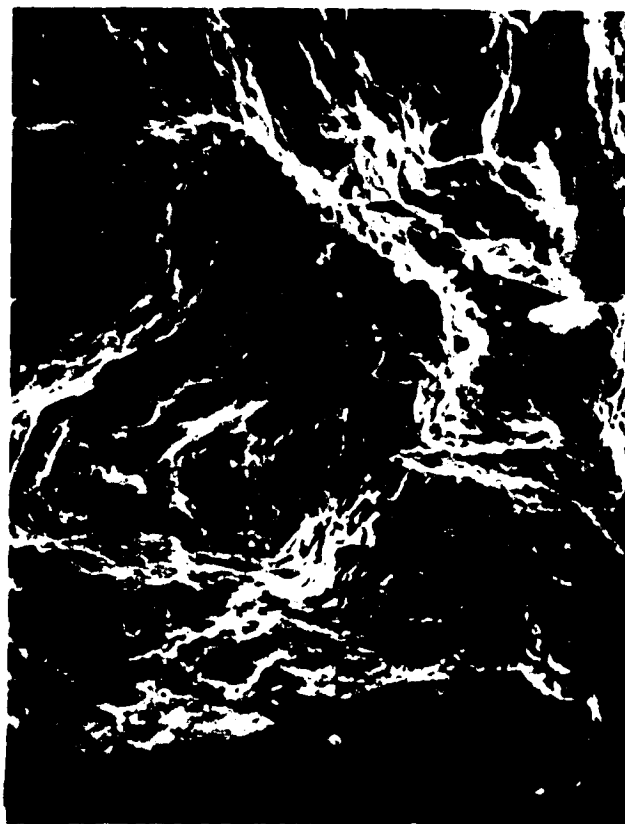
(a) Optical fractography (Intergranular).

(b) & (c) SEM showing a secondary crack moving along grain boundaries with carbide near the edge.



(a)

11X



(c)

400X

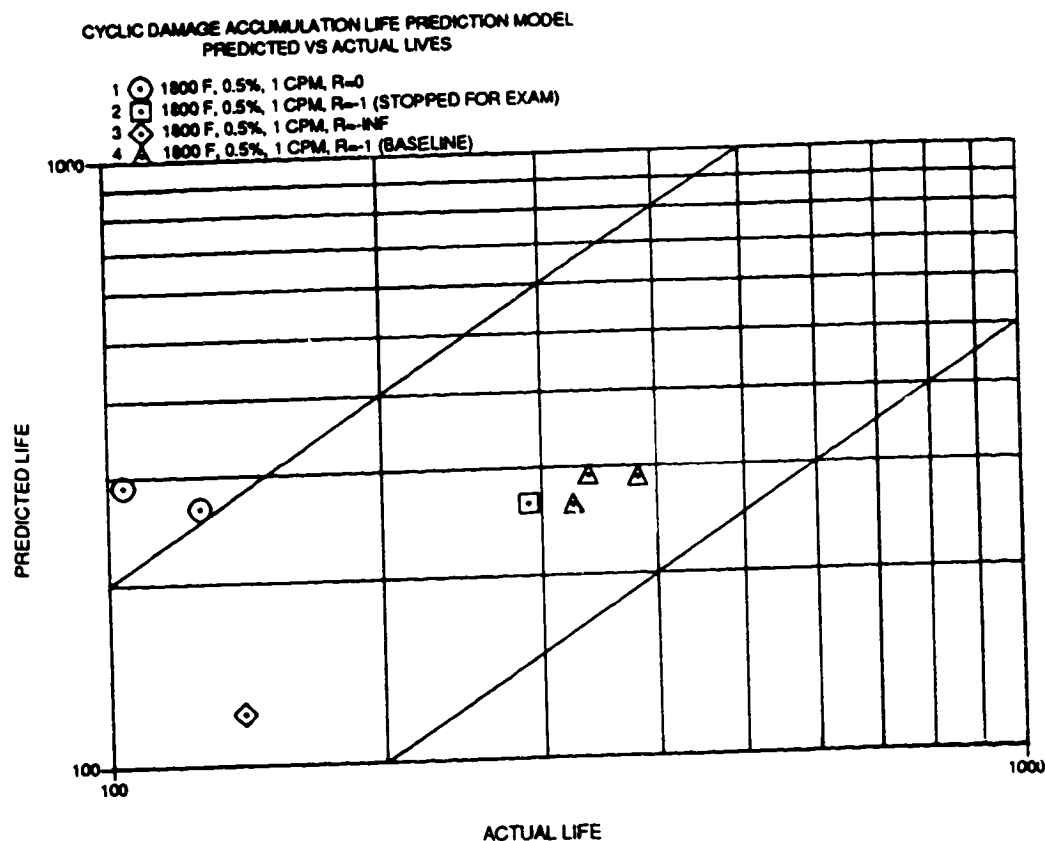


Figure 4-7 CDA Life Predictions for 982°C (1800°F) Slow Rate Tests

Another 982°C (1800°F) test was completed at the baseline conditions of 0.5% strain range, R=-1, and 10 CPM. Specimen 131B was stopped after only 350 cycles, at which time it had a 0.97 mm. (0.038 in.) surface crack. This was done to permit sectioning through the primary crack origin to determine the type of mechanisms active at this temperature. Details of the metallographic examination of this specimen are given in Section 8.

4.1.5 Load Controlled Tests

Five specimens were tested under this task using load control to simulate hot section components subjected to a constant load instead of a fixed displacement. These were also intended to provide direct information concerning the effect of maximum stress on fatigue life. All five were run at 871°C (1600°F) and 10 CPM to facilitate comparison with base program test results.

The first two specimens of this series were run at 0 to +75 Ksi, which is approximately the same as the stabilized maximum stress of 0.5%, R=0 strain controlled tests. The initiation lives were, however, more than three times longer than the median initiation life of R=0 strain controlled tests. As expected, the propagation lives were much shorter, confirming that maximum stress alone is not sufficient for prediction of initiation life since these tests all had approximately the same maximum stress but different strain ranges.

Another specimen, 131C, was tested at 0 to +100 Ksi to provide data from a test which combined a high maximum stress with a moderate strain range (approximately 0.4%). This test had initiation and separation lives which were more than an order of magnitude lower than the median lives of strain controlled tests conducted at the same strain range but with a much lower maximum stress. This test showed that maximum tensile stress is very important for the prediction of fatigue life. A preliminary TEM examination of this specimen revealed multiple planar slip with heavy dislocation activity in the gamma region and dislocations piling up against gamma prime particles.

The last two specimens of this series were tested at 0 to -100 Ksi to evaluate the effect of a moderate (about 0.4%) strain range with zero maximum stress. The first such test was specimen 131D which ran for 4000 cycles with no visible cracks but was stopped at that point due to the onset of creep buckling. The specimen was already S-shaped and posed a threat to the rig alignment if the test was continued. TEM analysis of this specimen revealed fairly diffuse slip activity with dislocations tangled around cooling gamma prime particles in the gamma matrix and cutting through some of them. The second specimen, 121D, was stopped after only 400 cycles to avoid specimen distortion associated with buckling of the first test. Figure 4-8 shows the dislocation structure from this specimen, which is radically different from that of the first test; in fact, this structure is very similar to the slip bands observed in the tension-only specimen (131C). Apparently the dislocation structure of the first compression specimen was strongly affected by the buckling, and the inelasticity associated with that overshadowed the effects of the compression cycling.

Figure 4-9 shows CDA life predictions for the three tension tests from this series, along with relevant baseline data from strain controlled tests. These were produced using the current form of the model, with no adjustments for load control effects other than incorporation of the measured stress-strain histories. The predictions are seen to be somewhat higher than the test results, indicating that more work could be done to improve the ability of the model to work with load controlled situations.

4.1.6 Tests Using Unpolished Specimens

To determine the effect of the light electropolish on specimens in this program, two specimens were tested with an as-machined surface finish. The test conditions were considered to be sensitive to surface finish effects: one was tested at 0.5% strain range with $R=0$, and the other was at 0.4% strain range and $R=-1$. The resulting unpolished specimen lives were equal to or only slightly higher than the median lives of electropolished baseline specimens at the same conditions. This may reflect some slight beneficial effect of the compressive surface stress which is removed by the electropolish. However, the observed lives were well within the data scatter observed in the baseline tests, so no corrections were considered necessary for the life prediction modeling. Figure 4-10 shows CDA life predictions for these two specimens, and it is clear that they are in good agreement with the unpolished data.

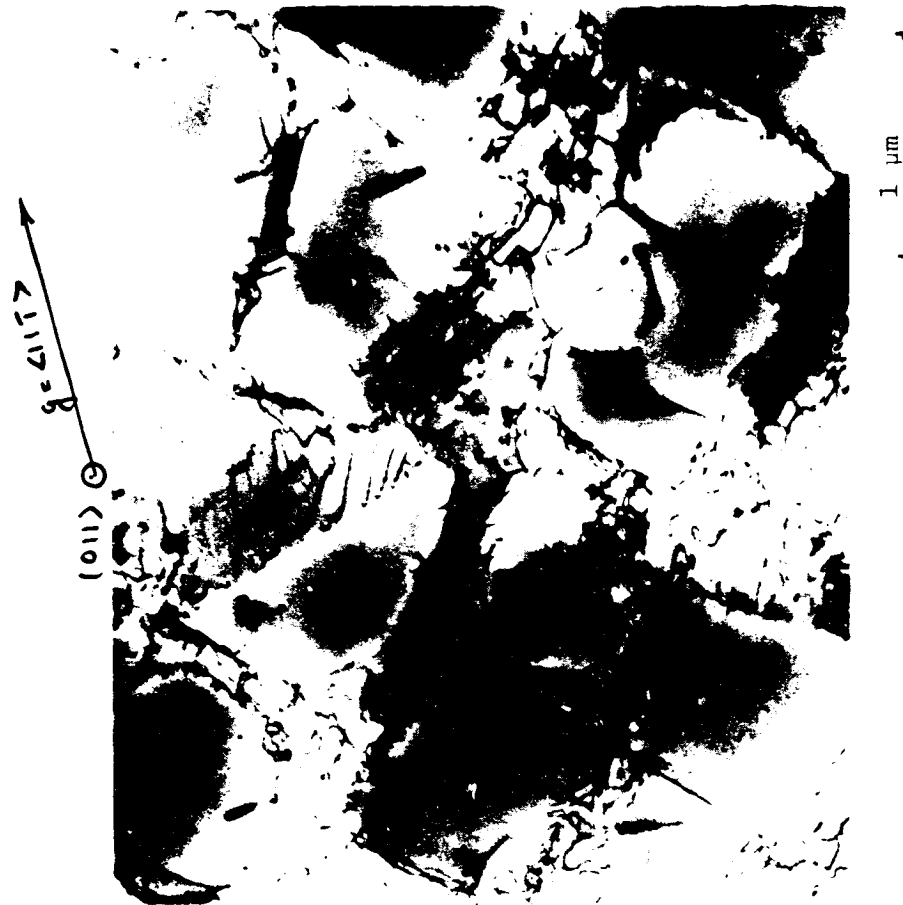


Figure 4-8 Dislocation structure of Specimen 121D after load controlled (σ to -100 Ksi) LCF testing at 1600°F , 10 cpm, for 400 cycles, interrupted before specimen failure.

ORIGINAL PAGE IS
OF POOR QUALITY

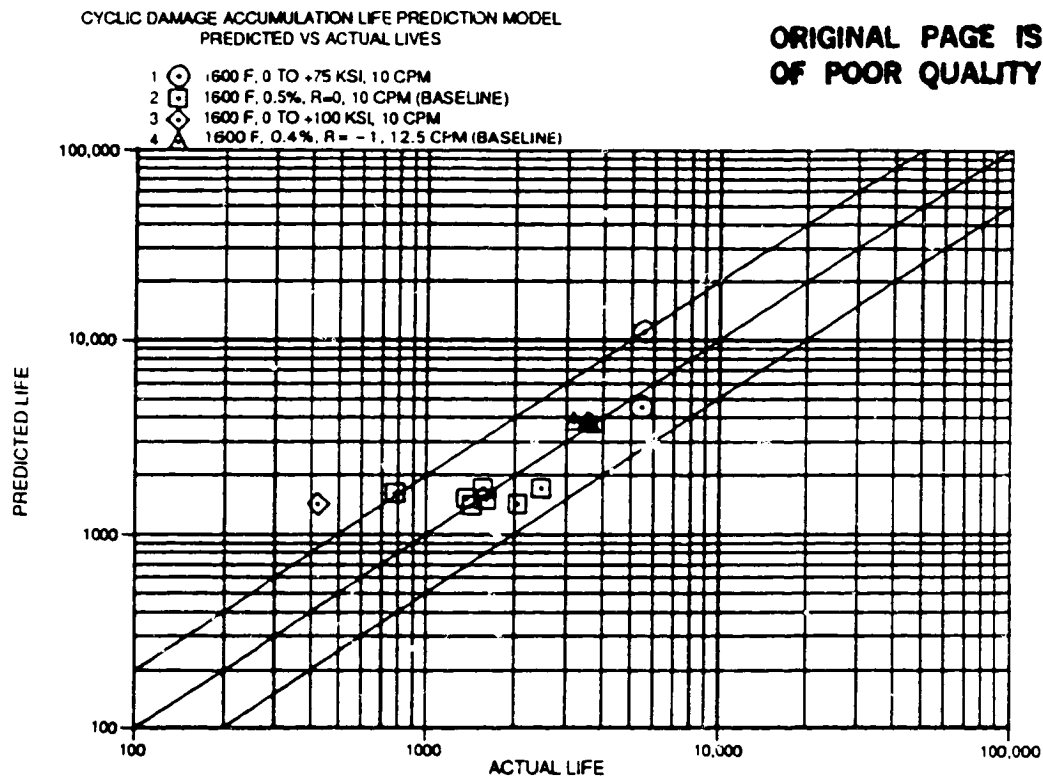


Figure 4-9 CDA Life Predictions for Load Controlled Tests

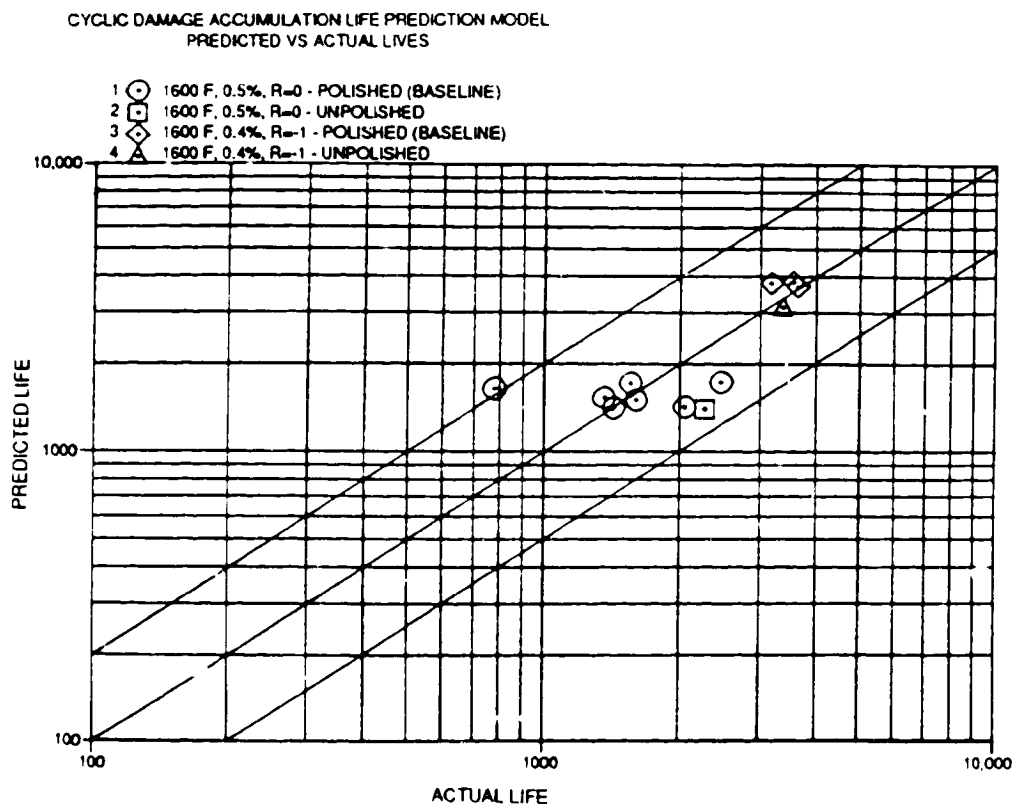


Figure 4-10 CDA Life Predictions for Polished and Unpolished Specimens

4.2 CDA LIFE PREDICTION MODEL IMPROVEMENTS

As noted in the previous section, there is a need to continue the development of the CDA life prediction model as more experience is gained. Comparison with existing creep fatigue life prediction models has been continuing to determine the areas where improvements could be made (Refs. 4.2-4.5). These areas are: (1) How the ductility of the material in question clearly influences the manner in which damage accumulates (Ref. 4.6); (2) The type of damage which is occurring, especially when the temperature and strain rate are such that intergranular failures become important (Refs. 4.7-4.8); (3) The effect of environment since it has been shown that environmentally assisted fatigue can be the main failure mode under certain conditions; this will be more fully addressed under Task IX (Refs. 4.9-4.10). Other investigators have found that, even in the absence of environmental effects, there is good reason to formulate the model with separate time-independent and time-dependent damage terms (Ref. 4.11); and (4) Statistical considerations that must be addressed for a practical life prediction model for engineering use, perhaps based on the distribution of grain size or other microstructural parameters (Refs. 4.12-4.13). These effects as well as those being investigated in the various option tasks should be considered for incorporation into the final form of the CDA model.

SECTION 5.0

TASK V - THERMOMECHANICAL CYCLING MODEL

5.1 EXPERIMENTAL RESULTS

5.1.1 Overview of TMF Test Matrix

The purpose of this task is to simulate engine operating conditions by varying both strain and temperature simultaneously. Although the tests under this task are more costly and complex than isothermal tests, they provide results which can lead to an increased understanding of the damage mechanisms of actual components. These tests characterized the influence of cycle type, strain range, R-ratio, and temperature range. Table 5-1 shows a matrix of 30 TMF tests performed during this reporting period. The detailed test results for each specimen are listed in Appendix II.

TABLE 5-1
UNCOATED PWA 1455 TMF SPECIMEN TEST MATRIX

Temp. Range (°F)	Strain Range	R	CYCLE TYPE									
			I	II	CW	CCW	I+Hold	II+Hold	LT	LC	HT	HC
1000-1600	0.004	0	126A									
		-1	122A	128B	122B	1260	123D	124A				
		-∞	107C									
	0.0005	0	46C	42D								
			42C	104A								
		-1	45A	42B	127D	1090			42A	45D	108A	46A
			105D	102C	129B	1250			101B			105C
		-∞	46D									
1000-1700	0.0004	-		103B								
1000-1800	0.0005	-	106C									
800-1700	0.0005	-	45C									

Due to the wide variation in strain-temperature history encountered during analysis of actual components, several different cycle types were investigated, some of which were developed for this program, to understand the effect of strain-temperature on fatigue life. In these tests, the temperature-time waveform was sinusoidal with a period of 60 seconds. The strain-time waveform was chosen to produce the desired relationship between strain and temperature. Figure 5-1 shows some of the types of strain-temperature cycles used in these tests. The traditional TMF cycles are the out-of-phase and in-phase, which were produced using sinusoidal strain cycles with the appropriate phase relationships (0 degrees or 180 degrees). Figure 5-1 also shows the elliptical cycle, which is a new type of "faithful" cycle (more like an actual hot section component). The cycles can use a phase angle of +135 degrees to produce counterclockwise movement around the ellipse or -135 degrees to produce clockwise movement. Figure 5-2 shows the dogleg cycle, another new type of cycle investigated during this tests eries. In this type of test, the strain excursion occurs during only 6 seconds at either the the maximum or minimum temperature. The strain is then held in either tension or compression for the remaining 54 seconds while the temperature is varied. Four possible cycle combinations are produced, identified by the temperature at which the strain excursion occurs (L=low, H=high) and the type of strain hold (T=tension, C=compression). These cycles were intended to provide a stepping stone between isothermal hold tests and the standard TMF cycle types; however, as will be shown later, they proved to be just as complex as other TMF cycles.

5.1.2 Experimental Procedure

All tests were conducted under strain control in an MTS closed loop servo-hydraulic testing machine similar to that used for the base program tests. The gage section temperature was monitored continuously by an infrared pyrometer which provided feedback for closed loop control of an induction heating arrangement. Cooling was provided by jets of air impinging on the specimen OD. All control signal generation and data acquisition duties were handled by a PDP-11/23 computer interfaced to the MTS control system. This test setup has been used at Pratt & Whitney for many years and is described in Reference 5.1.

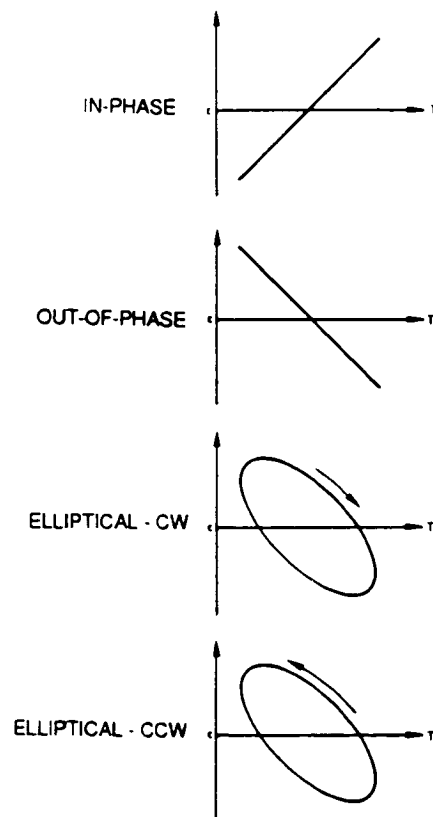
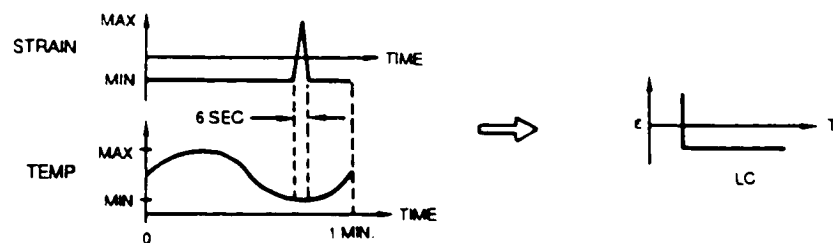
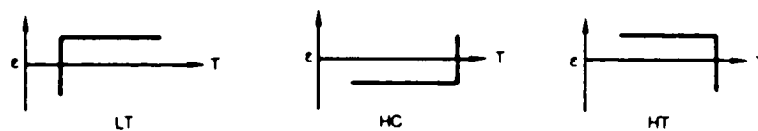


Figure 5-1 Comparison of TMF Cycle Types



A. STRAIN AND TEMPERATURE HISTORIES LC DOGLEG CYCLE



B. OTHER DOGLEG CYCLES USED FOR TESTING

Figure 5-2 Dogleg TMF Cycles

The initial testing utilized tubular specimens with internal ridges as shown in Figure 5-3. This permitted the use of an internal extensometer arrangement, thus freeing the specimen OD for replication and cooling. However, the local stiffening of the gage section caused by the ridges was found to induce a slight discrepancy between the apparent strain (as measured from the ridge deflection) and the true gage section strain (3-6% difference). To eliminate this problem and to reduce specimen machining costs, a new ridgeless specimen design was developed, as shown in Figure 5-4. The gage section diameter and wall thickness are the same as those used previously, except that the length of the constant diameter section was increased by 2.54 mm. (0.100 in.) to allow placement of an external extensometer. Both strain gage testing and finite element models were used to qualify the new specimen as a reliable replacement for the internally ridged specimen. The specimens were prepared by grinding, followed by light polishing of the OD and liquid honing of the ID.

5.1.3 Out-of-Phase and In-Phase Testing

As noted in Table 5-1, six fully reversed TMF specimen tests were completed at two nominal strain ranges, using both in-phase and out-of-phase cycling. The temperature range was 538-871°C (1000-1600°F), and the rate was 1 CPM. A plot of initiation life vs. total mechanical strain range is shown in Figure 5-5, along with median life data from isothermal baseline tests at the same cyclic rate. As expected, the TMF results are lower in life than isothermal data from even the maximum cycle temperature. Note also that the difference in life between in-phase and out-of-phase cycling is a function of strain range; at lower strain ranges, the in-phase cycling produces higher life, while at the higher levels, the out-of-phase life is higher. Obviously, the number of data points in this set is limited, but this behavior has also been noted during other TMF testing. This serves to emphasize the need to understand and model the actual damage mechanisms active under these conditions; simple data correlations based on one or the other cycle type may not always give conservative predictions.

Various metallographic examinations of the fracture surfaces of two of these specimens were also completed. Figure 5-6 shows optical and SEM micrographs of one of the higher strain range in-phase specimens (42B). The fracture was clearly intergranular, and the origin was from porosity. Figure 5-7 shows TEM micrographs of typical dislocation structures generated by in-phase cycling; it is seen to be a mixture of short segments (indicated by "X") and network surrounding the gamma prime ("Y"). However, it should be noted that these are not representative of any one isothermal LCF dislocation structure; instead, they appear to be a combination of features resulting from various isothermal tests. These observations indicate that the observed TMF specimen lives are the result of several LCF mechanisms which are active at different temperatures.

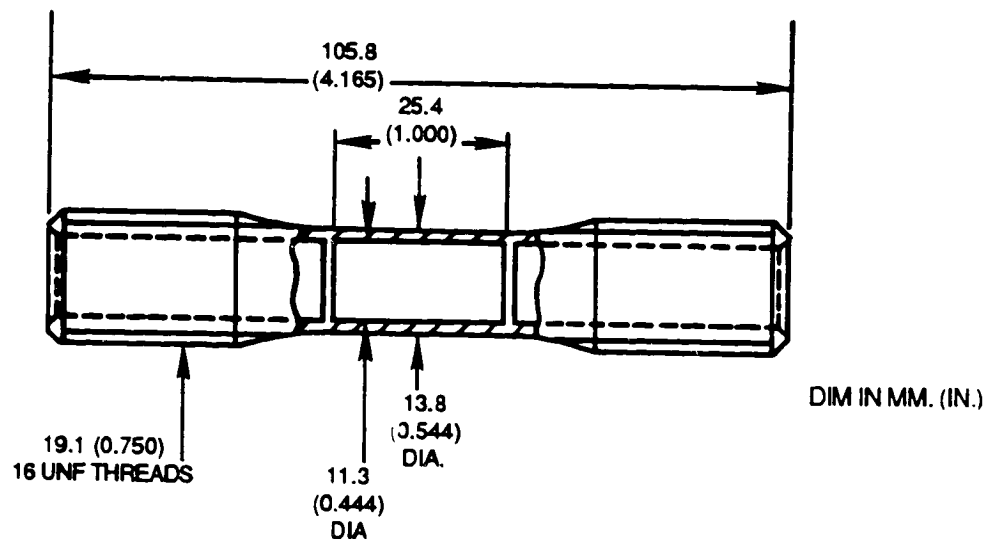


Figure 5-3 Internally Ridged TMF Specimen

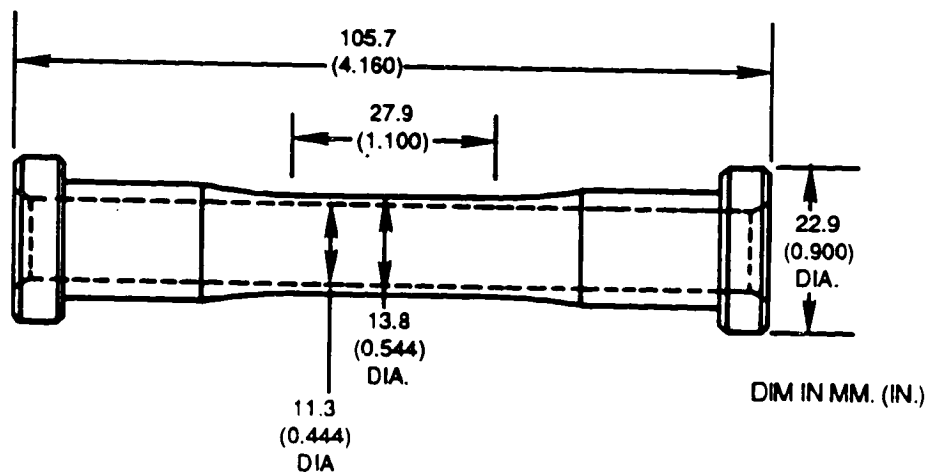


Figure 5-4 TMF Specimen for External Extensometer

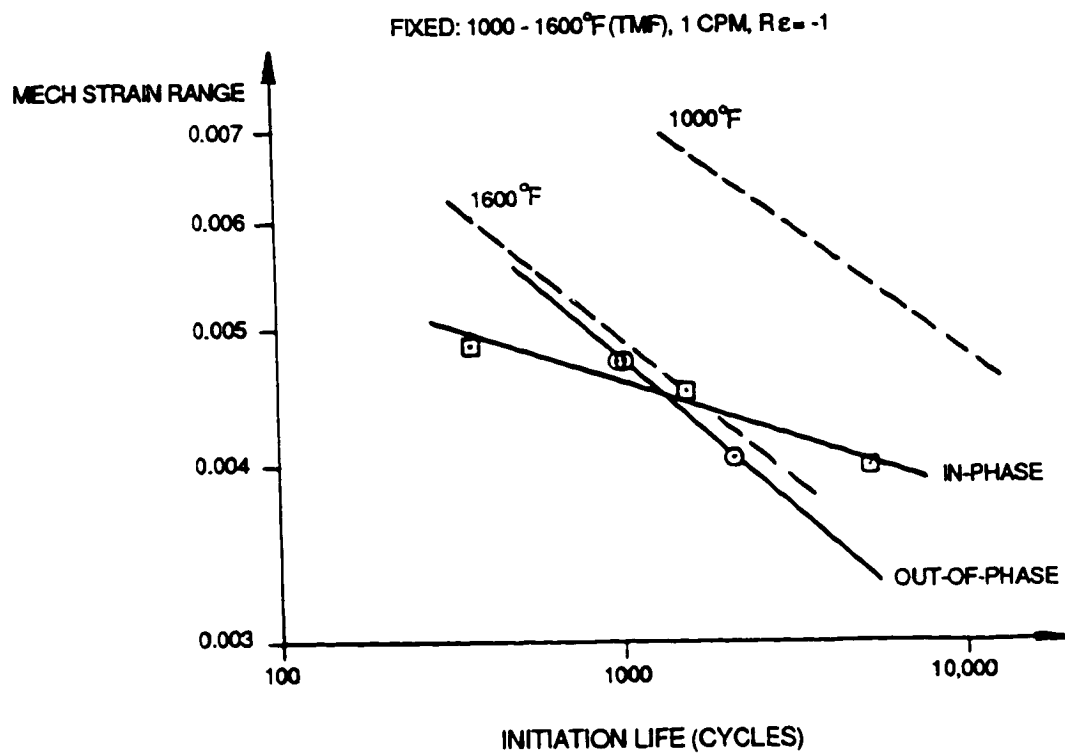
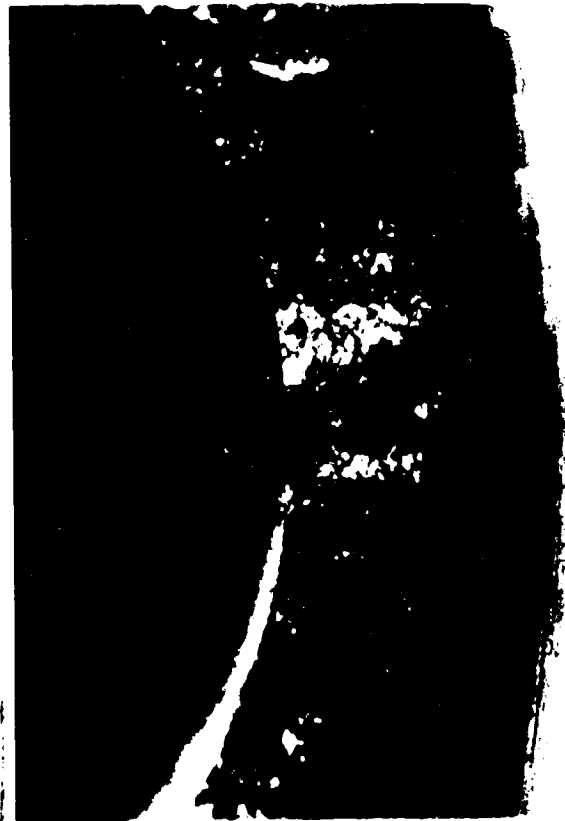


Figure 5-5 TMF Results for In-Phase and Out-of-Phase Cycles

ORIGINAL PAGE IS
OF POOR QUALITY



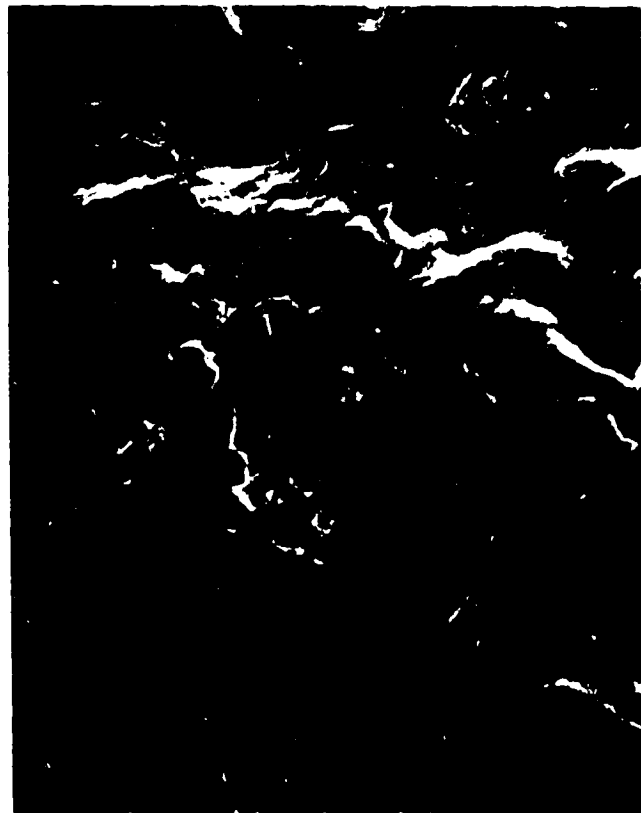
20X

(a)



(b)

70X



200X

(c)

Figure 5-6

Fracture surface of specimen 42B after being
TMF tested between 1000-1600°F, $\Delta\epsilon_t = 0.5$,
 $R = 1$, with in-phase cycling for 2041 cycles
(50% load drop).

(a) Optical fractography showing ID initiation
(Intergranular).

(b) & (c) SEM showing porosity as crack
initiation site.

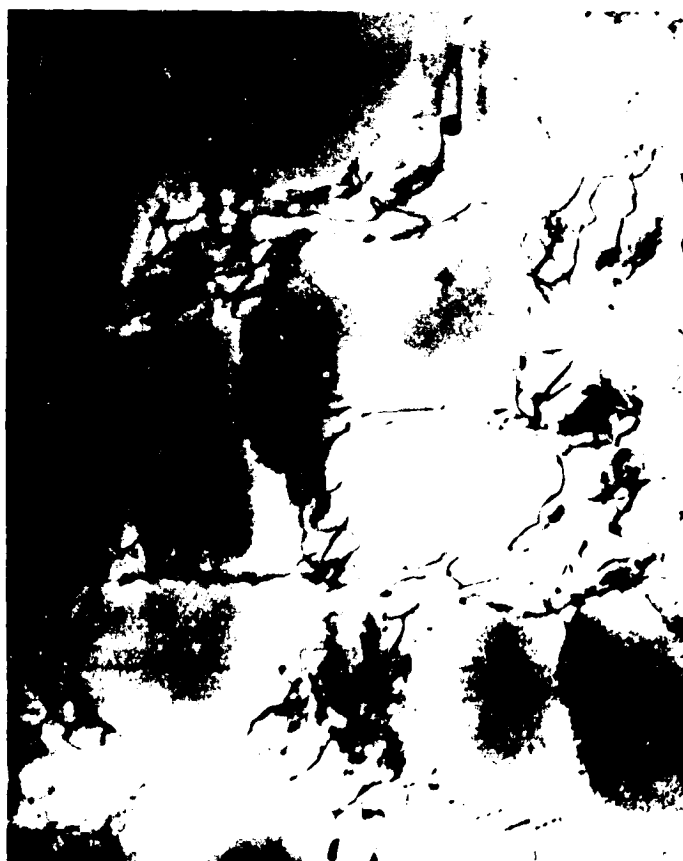
(111)



1 μm

ORIGINAL PAGE IS
OF POOR QUALITY

(111)



1 μm

Figure 5-7 Dislocation structure for Specimen 42B TMF tested at temperature range 1000-1600°F, strain range -0.25 to +0.25%, in-phase cycling, frequency 1cpm for 2041 cycles (50% load drop) (foil was prepared longitudinally).

5.1.4 R-Ratio Effects on TMF Life

To gain insight into the relationship between mean strain and TMF life, a series of 7 tests was completed using one-way strain cycling. As noted in Table 5-1, five specimens were run at $R=0$ conditions and two were run using $R=-\infty$. For all these tests, the temperature range was 538-871°C (1000-1600°F), and the cyclic rate was 1 CPM. Figure 5-8 shows a comparison between the results of the one-way tests and the fully reversed TMF data for out-of-phase cycling. The ordering of the life curves follows the expected trend, with the $R=0$ tests producing the lowest lives and the $R=-\infty$ being the highest. However, Figure 5-9 shows the results for the $R=0$, in-phase tests, and at these conditions no significant difference is seen relative to the fully reversed tests. In fact, the $R=0$ tests appear to be slightly higher in life, similar to what was seen in the isothermal base program tests at 871°C (1600°F). This may be due to inherent scatter in the limited data set, or it may be caused by competing damage mechanisms under these in-phase conditions which effectively cancel each other's effects when the R-ratio is varied.

Of special interest is the variation in crack growth rate during these R-ratio tests. Figure 5-10 is a plot of replica data taken during four tests conducted at the lower strain level (0.4%) and with various R-ratios and phase relationships. The cracks obviously grew at different rates for each of the tests observed, with the $R=-1$ in-phase test producing the slowest growth. The effect of the definition of "initiation" is also highlighted in this figure, since a crack size of less than 0.030 in. for initiation could produce a reordering of the data. It is likely the most powerful driver of the crack growth is the maximum tensile stress in each cycle. Figure 5-11 shows the tensile stress history for each test. Note that the in-phase test had the lowest tensile stress for most of its life, which agrees with the observed crack growth rates.

Three of the specimens in this series were examined metallographically to determine fracture morphology, initiation sites, and dislocation structures. Figure 5-12 shows the fracture surface of specimen 42D, which was tested using in-phase cycling at $R=0$. The crack grew intergranularly, and the initiation site was a carbide on the specimen OD. The dislocation structure of this specimen is shown in Figure 5-13; it is seen to consist of a mixture of networks clustering both the gamma and gamma prime (indicated by "Y") and dislocations encasing the gamma prime ("Z"). Figure 5-14 shows the dislocation structure of specimen 46C, which was tested at the same conditions except with out-of-phase cycling. Here the structure consists of a mixture of short segments ("X") and network surrounding the gamma prime ("Y"). Observation of the fracture surface of this specimen revealed that it failed transgranularly from a carbide on the OD. Finally, specimen 46D was examined after being tested with out-of-phase cycling and $R=0$. Figure 5-15 shows that it also fractured transgranularly from a carbide similar to the out-of-phase test (specimen 46C). The dislocation structure consists mainly of short segments, as seen in Figure 5-16. Once again, no direct correlation can be made between these examinations and similar work performed on isothermal tests; the TMF failures appear to result from the simultaneous action of several damage mechanisms. Also, the mode switch from transgranular to intergranular fracture indicates that a practical but general life prediction model must be able to account for such changes.

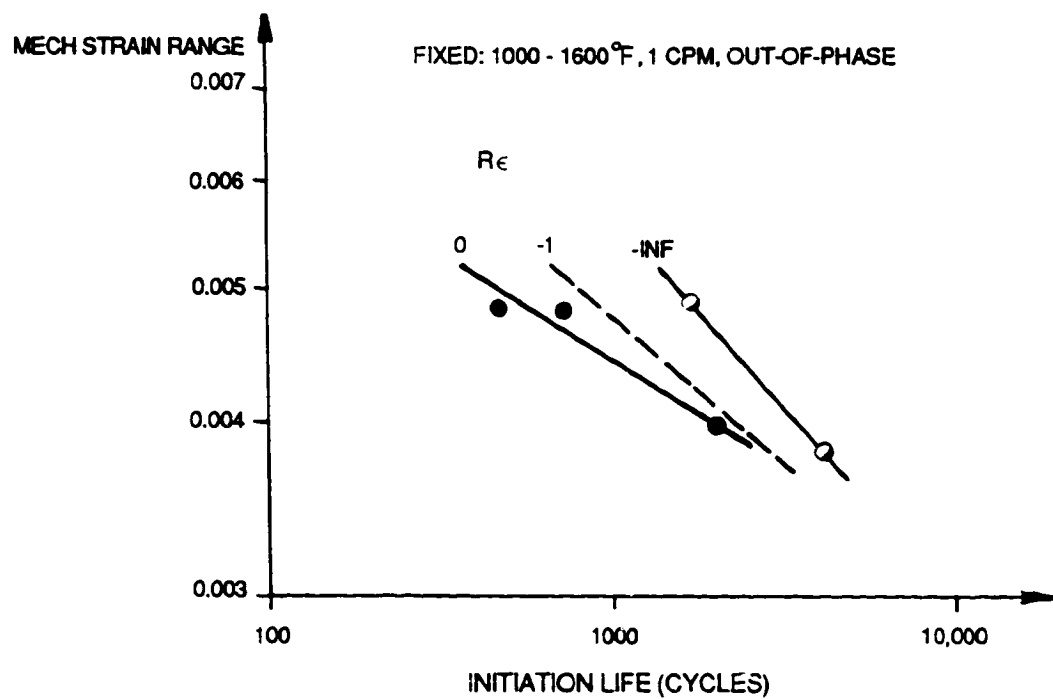


Figure 5-8 Strain Ratio Effect on Out-of-Phase TMF Life

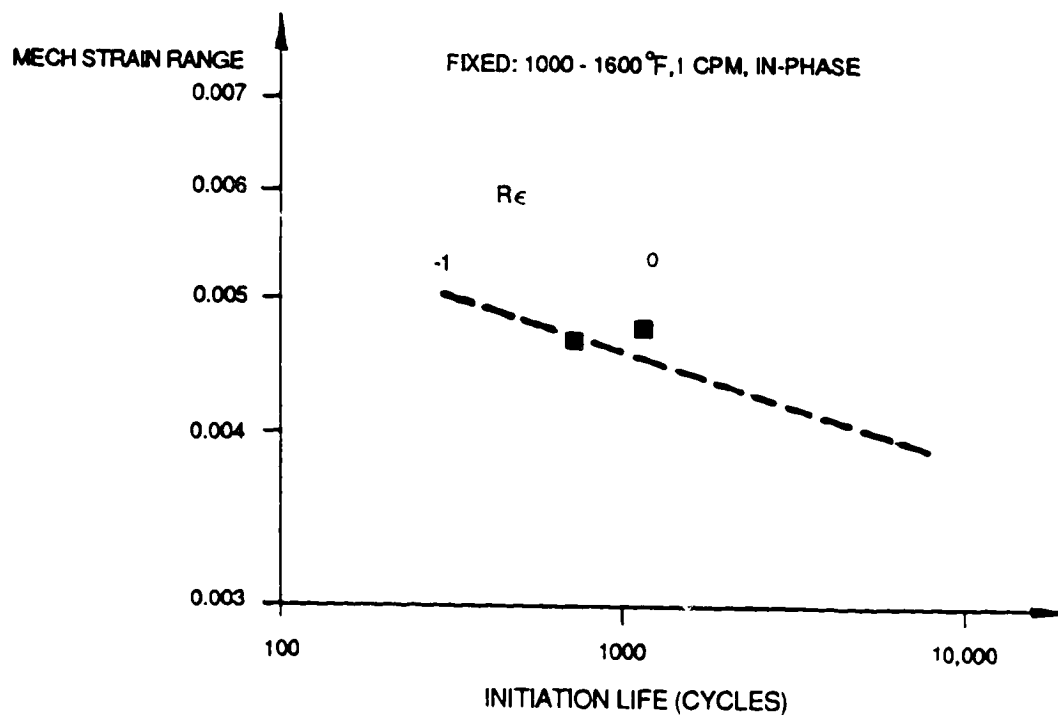


Figure 5-9 Strain Ratio Effect on In-Phase TMF Life

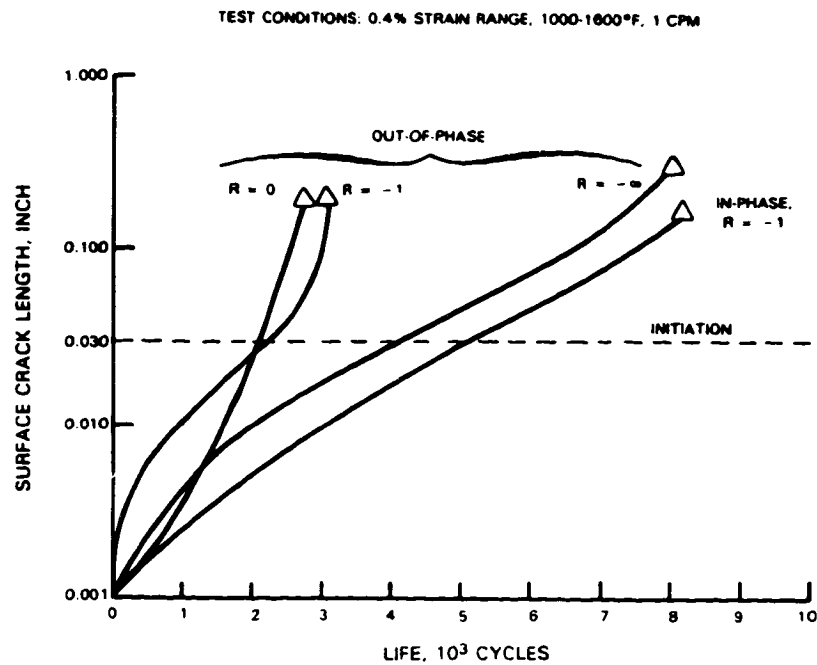


Figure 5-10 Crack Growth Data for Low Strain Range TMF Tests

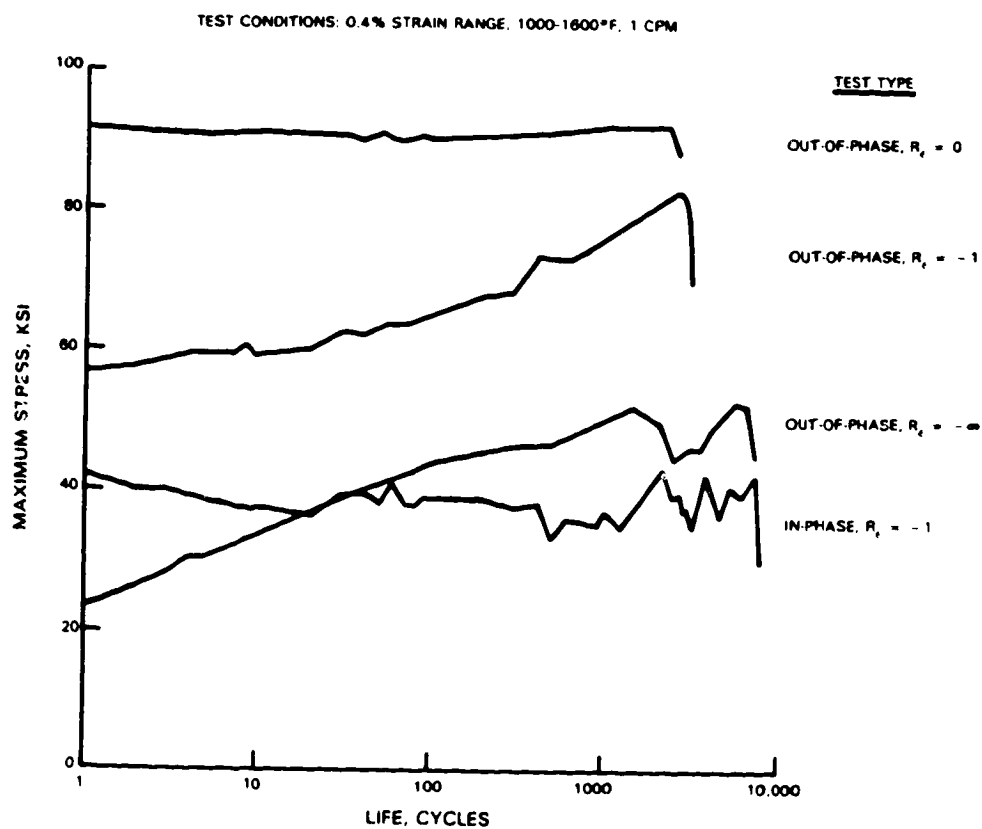


Figure 5-11 Maximum Stress Evolution for Low Strain Range Tests

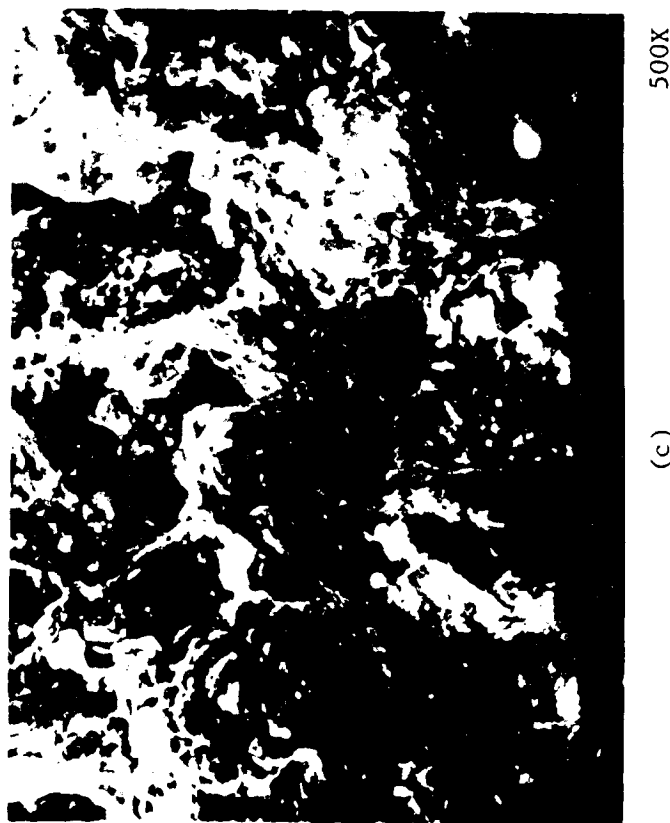
ORIGINAL PAGE IS
OF POOR QUALITY



Figure 5-12 Fracture surface of Specimen 42D after being
TMF tested between 1000-1600°F, $\Delta\epsilon_t = 0.5$,
R = 0, in-phase, for 2951 cycles (50% load drop).

(a) Optical fractography showing OD
initiation (Intergranular).

(b) & (c) SEM showing carbide as crack
initiation site.



ORIGINAL PAGE IS
OF POOR QUALITY

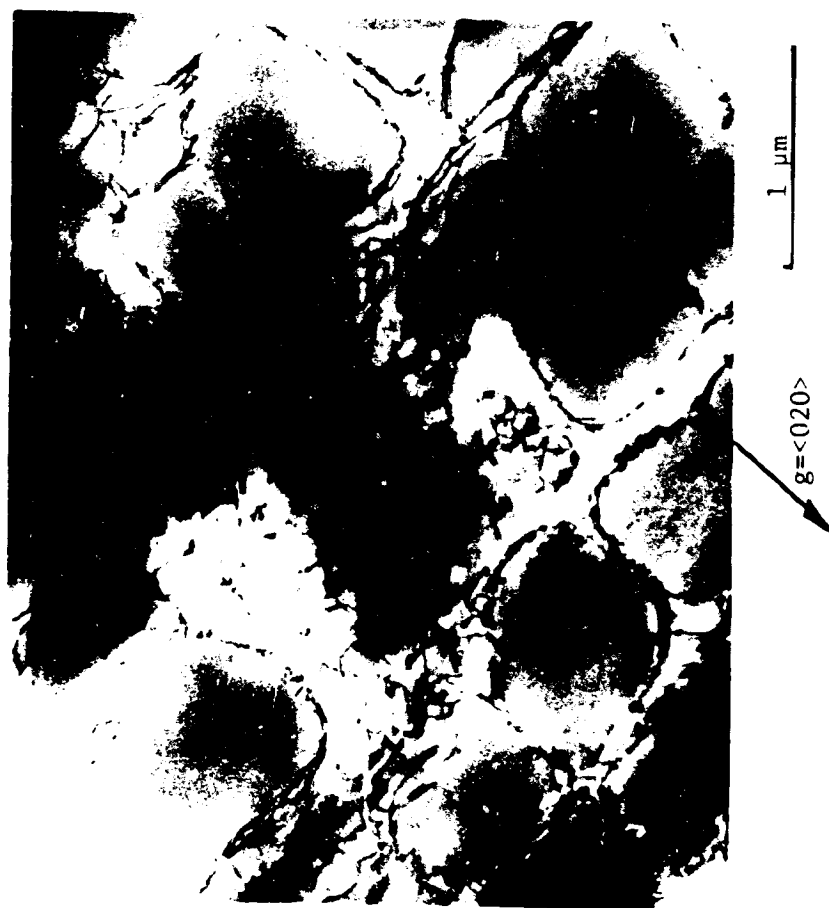
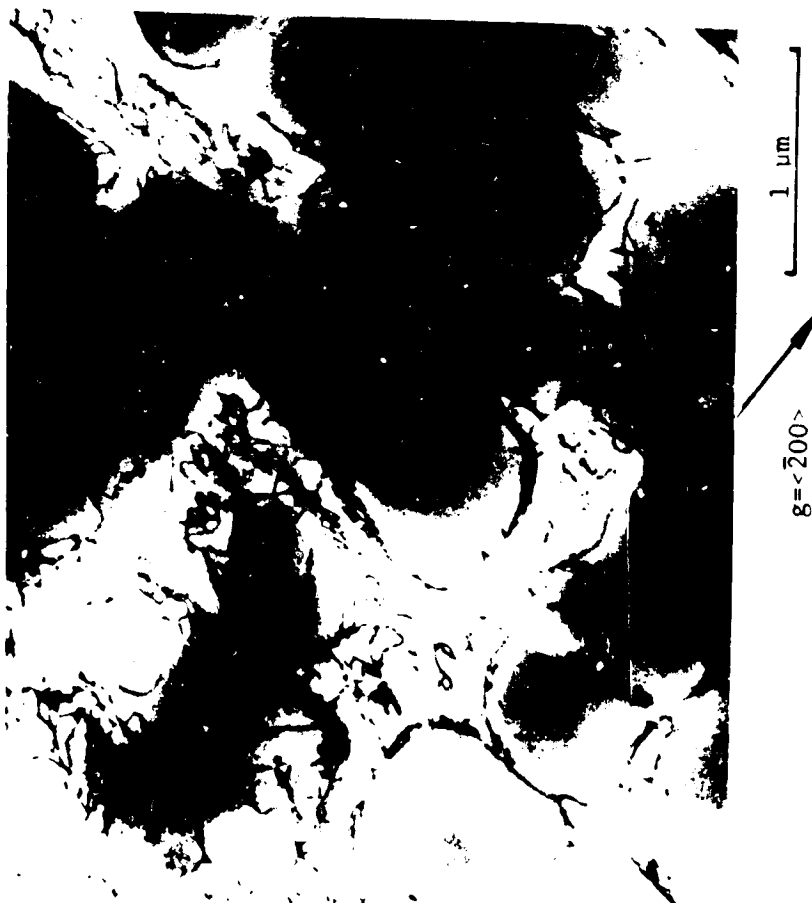


Figure 5-13 Dislocation structure for Specimen 420 after being TMF tested at temperature range 1000-1600°F, strain range 0 to 0.5%, in-phase, frequency 1 cpm for 2951 cycles (50% load drop).

ORIGINAL PAGE IS
OF POOR QUALITY

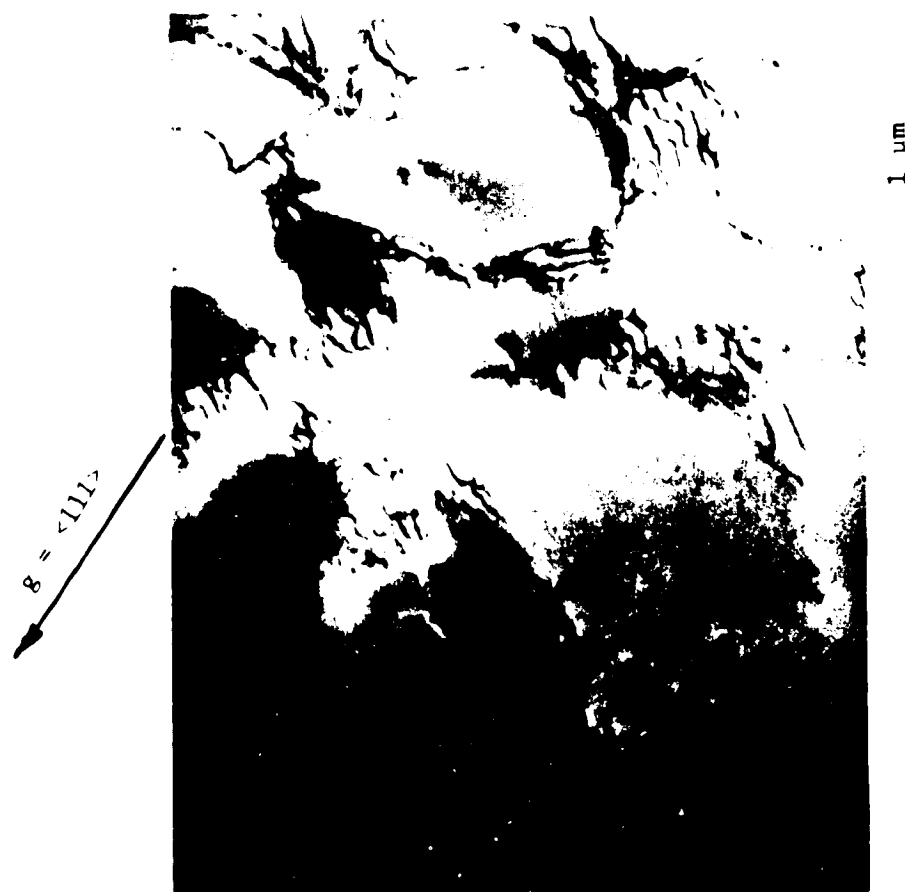
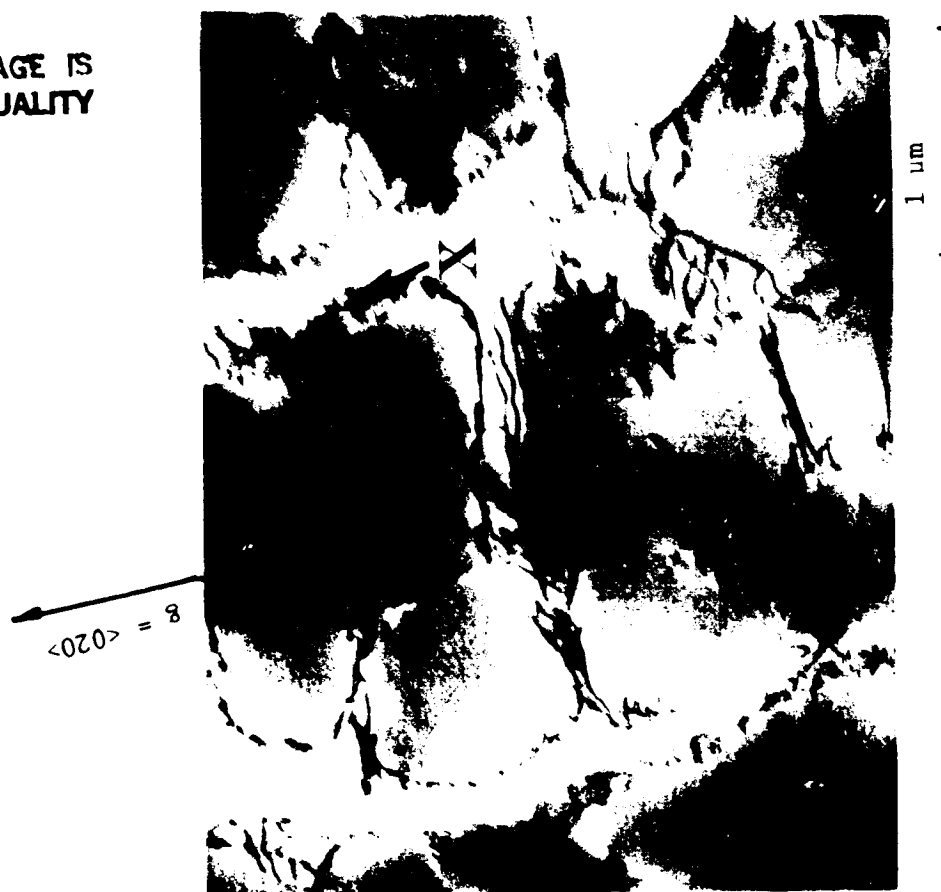
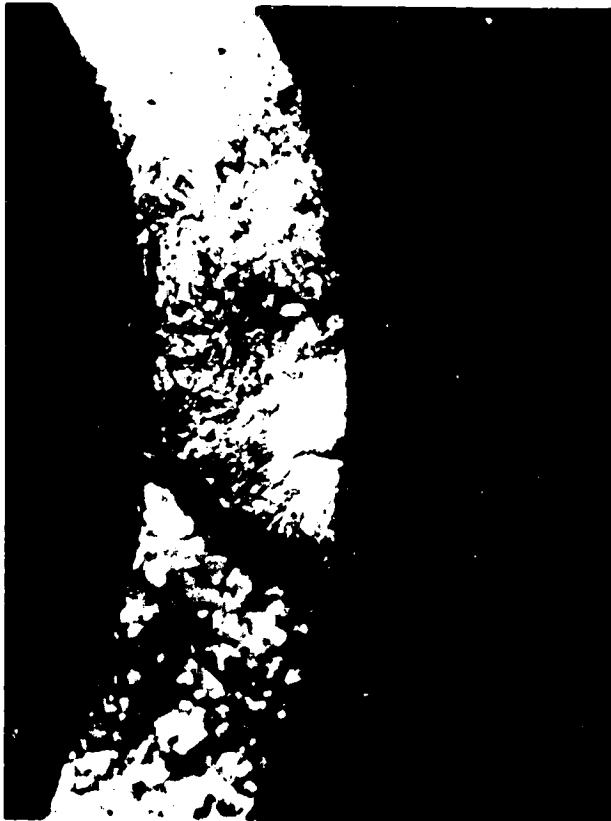


Figure 5-14 Dislocation structure for Specimen 46C after being TMF tested at temperature range 1000-1600°F, strain range 0 to 0.5%, out-of-phase, frequency 1 cpm for 1456 cycles (50% load drop) (foil was prepared longitudinally).

ORIGINAL PAGE IS
OF POOR QUALITY



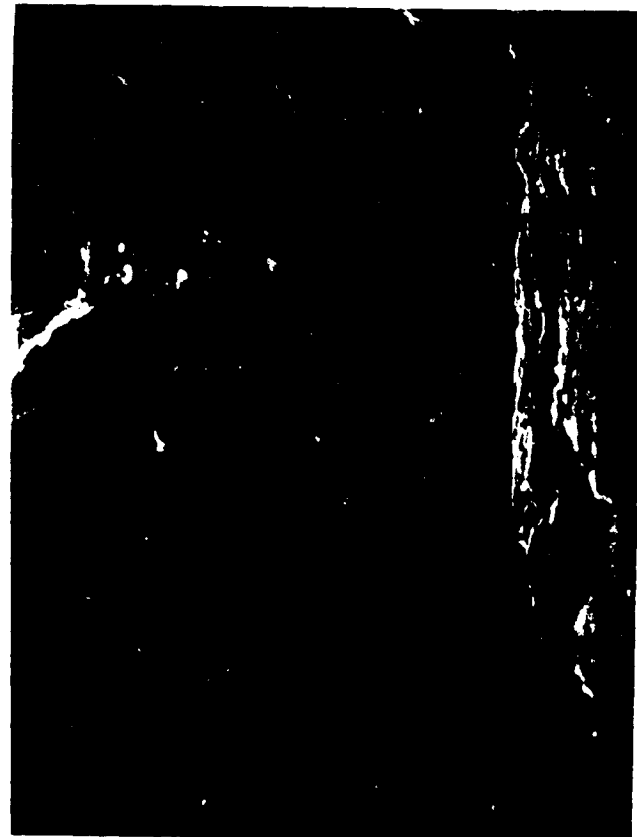
(a)

20X



(b)

160X



(c)

400X

Fracture surface of Specimen 46D after being TMF tested between 1000-1600°F, $\Delta\epsilon_t = 0.5\%$, $R = -\infty$, out-of-phase, for 2769 cycles (50% load drop).

(a) Optical fractography showing an initiation (Transgranular).

(b) & (c) SEM showing carbide as crack initiation site.

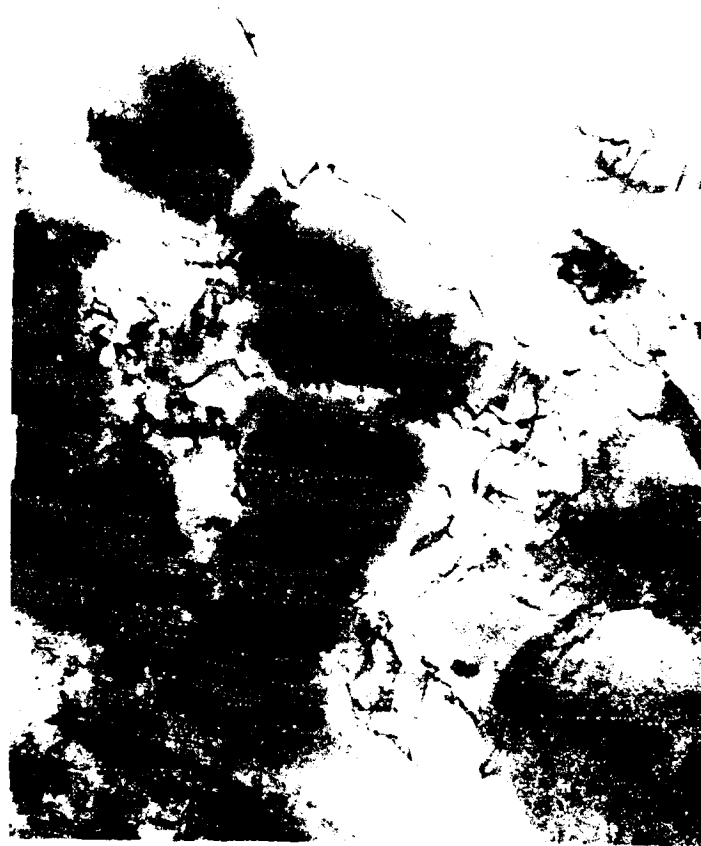
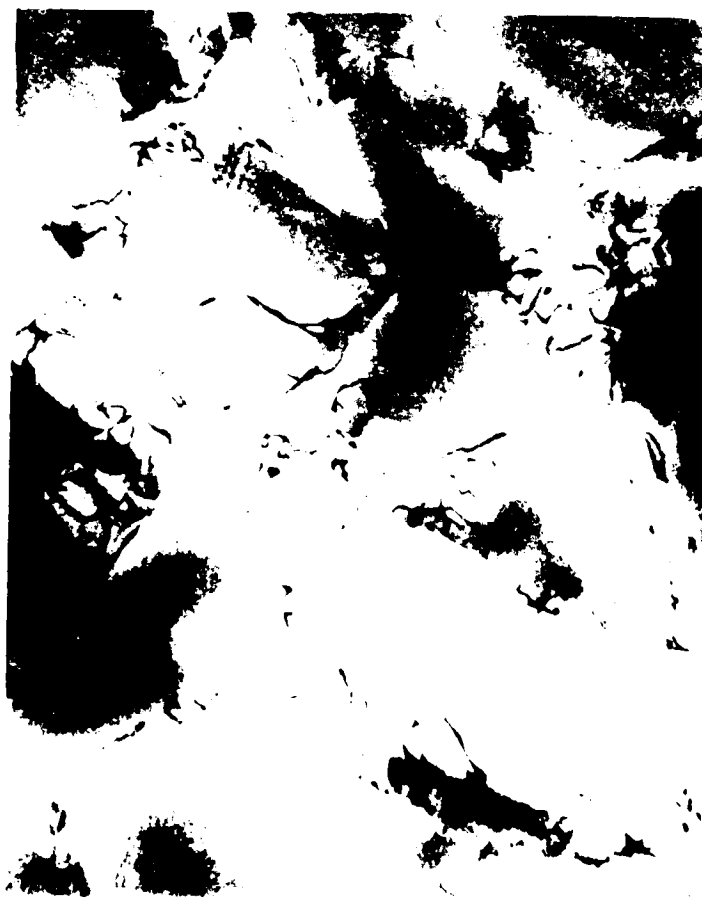


Figure 5-16 Dislocation structure for Specimen 46D after being IMF tested at temperature range 1000-1600°F, strain range -0.5 to 0%, out-of-phase, frequency 1 cpm for 2769 cycles (50% load drop).

5.1.5 Dogleg Tests

As noted earlier, this type of test was conceived as an intermediate step between an isothermal hold test and a traditional TMF test (in-phase or out-of-phase). Six specimens were tested using dogleg cycles at a temperature range of 538-871°C (1000-1600°F) and a rate of 1 CPM. The strain range for all tests was 0.5%, with $R=-1$. Their initiation lives are shown plotted in Figure 5-17 along with comparable isothermal and TMF (in-phase and out-of-phase) median test results. It should be noted that the initiation lives of the dogleg tests have been adjusted to reflect a uniform strain range of 0.5%. The dogleg tests with the hold in compression ("LC" & "HC") are about 2X higher in initiation life than the isothermal compression hold tests. However, the lives from the tension hold dogleg tests ("LT" & "HT") are nearly four times lower than those of similar isothermal tests. By using the median lives from the in-phase and out-of-phase TMF tests, the solid trend line shown in Figure 5-17 can be drawn, and it is obviously opposite to what was found during the isothermal testing. It is therefore clear that the non-isothermal hold has a significant influence on specimen life, no doubt by activating different damage mechanisms as the temperature varies.

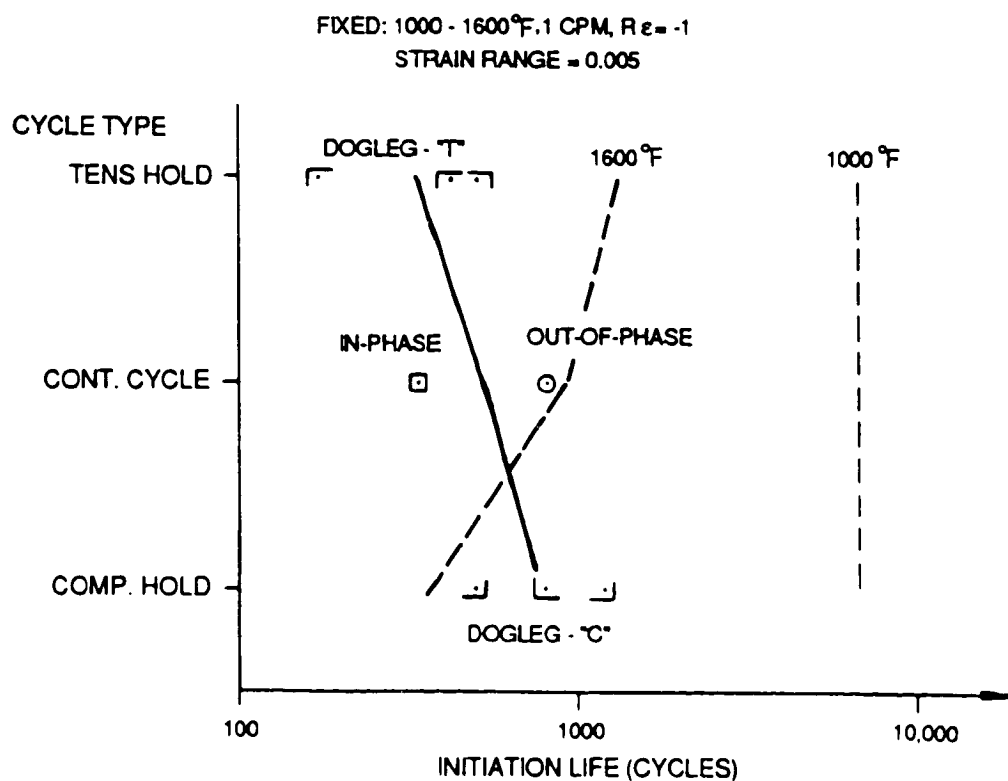


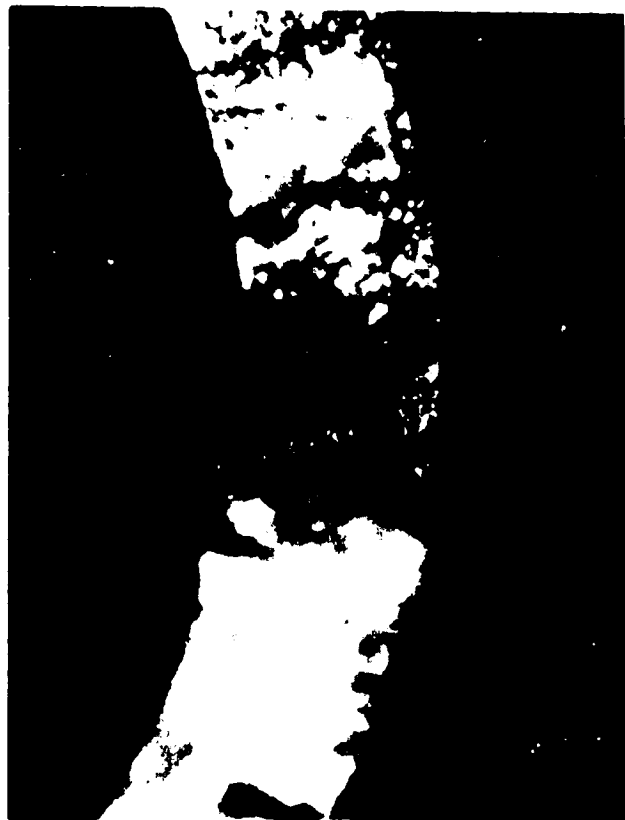
Figure 5-17 Dogleg TMF Test Results

Metallographic examinations of three of the dogleg test specimens were completed, and the results confirm that these tests are as complex as other TMF tests. Specimen 42A was tested with a tension hold "LT" cycle, and Figure 5-18 shows that its failure mode was intergranular and that the primary crack originated from a carbide on the OD. As shown in Figure 5-19, the dislocation structure of this specimen consists of a mixture of short segments (indicated by "X"), a network surrounding the gamma prime ("Y"), and dislocations encasing the gamma prime ("Z"). Similar examinations were also made for specimen 45D which was tested using a compression hold "LC" cycle. Figure 5-20 shows that the fracture mode of this specimen was transgranular, with the primary initiation site again being a carbide on the OD; multiple cracking was observed on both OD and ID. The dislocation structure of this specimen is shown in Figure 5-21, and it has the same features noted for the "LT" cycle tests, specimen 46A (Figure 5-22), indicates the fracture mode was mixed transgranular/intergranular and that the initiation site was also mixed with both carbide and porosity present. Life prediction methodology for these tests should account properly for these differences in propagation mode as well as the effect of both carbides and porosity.

5.1.6 Elliptical Cycle Tests

Perhaps the most interesting results obtained so far under this task are those from the elliptical cycle tests. Eight specimen tests were completed under this series, including both clockwise (CW) and counterclockwise (CCW) cycles. One of these specimens (125D) failed prematurely from a large region of porosity and was therefore not included in the life correlations. The CCW cycle is a good simulation of the strain-temperature history experienced by many actual hot section components. Although there are some components which have a CW movement around their strain-temperature history, the CW cycle results are most valuable when compared to the CCW results; the only apparent difference is the direction of motion around the loop. Figure 5-23 shows a plot of the elliptical test results, and it is clear that there is a large difference in life between the two types of cycles. Note that life prediction methods based solely on the extremes of the cycle were not able to predict this behavior since they cannot distinguish between these two cycles. This therefore shows the need for advanced life prediction techniques, perhaps based on an integration of damage around the cycle in question to account for such effects.

The elliptical cycle testing also emphasizes the influence of the variation of elastic modulus with temperature. During a traditional TMF test, the stress-strain hysteresis curve will have a distinct curvature, with a higher slope at the low temperature portion of the cycle. However, the elliptical cycle tests have two different moduli at any given strain: one while temperature is increasing, and the other while temperature is decreasing. This results in a "figure-8" hysteresis loop, as shown for cycle 1 in Figure 5-24. Near the end of the test, cracks develop to the extent that they influence the specimen stress, and the loops open up somewhat, as shown for cycle 2551. Obviously, the only way to determine inelastic strain is analytically, since it no longer corresponds directly to the width of the loop.



(a) 20X



(b) 50X

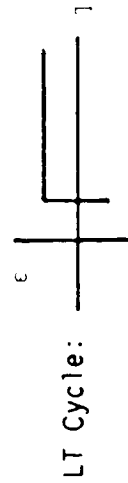


(c) 200X

Figure 5-18 Fracture surface of Specimen 42A after being TMF tested between 1000-1600°F, $\Delta\epsilon_t = 0.5\%$, $R = -1$, for 3292 cycles (50% load drop).

(a) Optical fractography showing an OD initiation (Intergranular).

(b) & (c) SEM showing carbide as initiation sites.



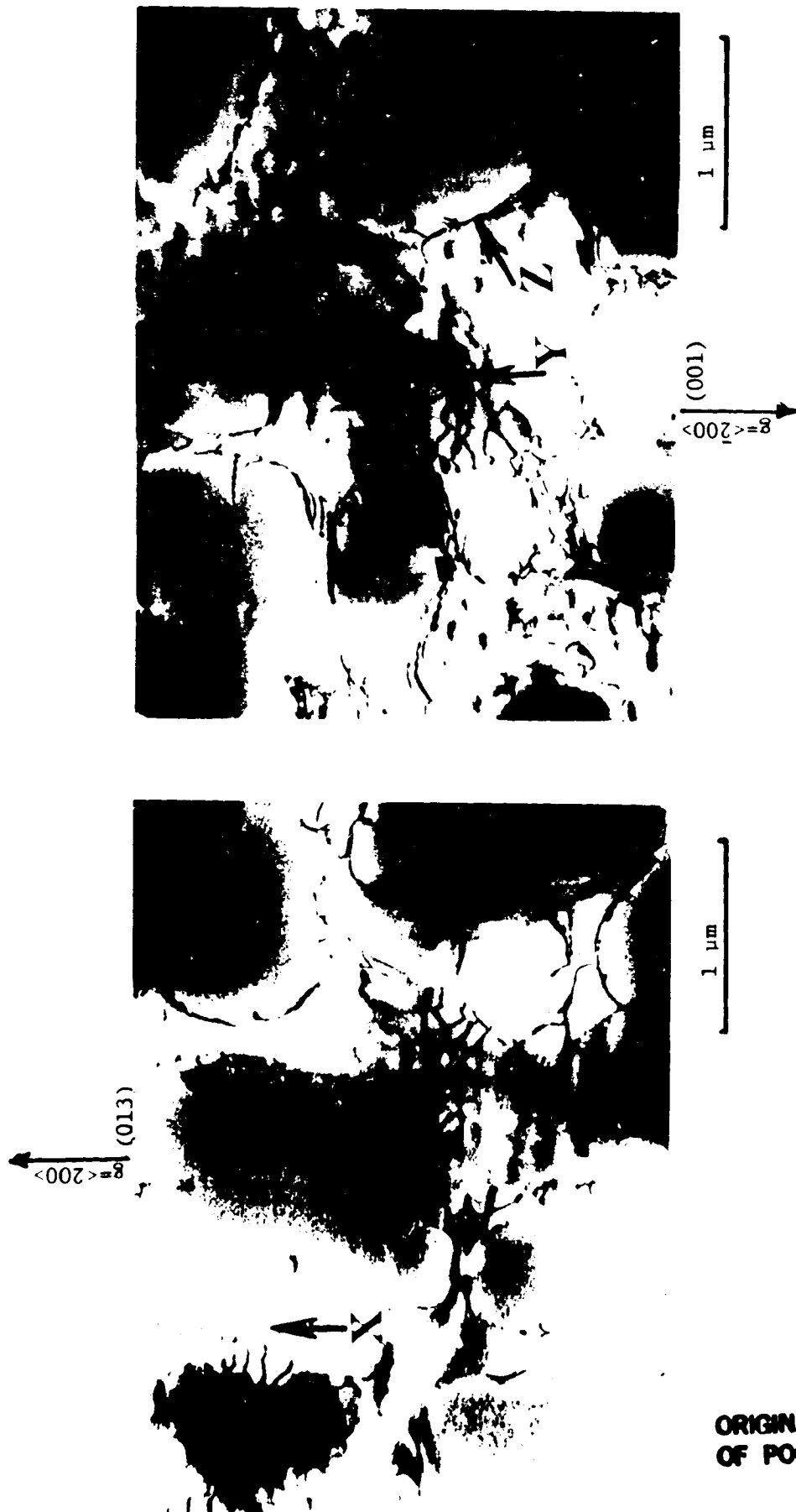


Figure 5-19 Dislocation structure for Specimen 42A. TMF test with temperature range 1000-1600°F, strain range -0.25 to +0.25, LT cycle type $\epsilon \begin{array}{c} \text{---} \\ \text{---} \\ \text{---} \end{array} \frac{1}{T}$, frequency = 1 cpm for 3292 cycles (50% load drop) (foil was prepared longitudinally).

ORIGINAL PAGE IS
OF POOR QUALITY



(a)

20X



(c)

400X



(b)

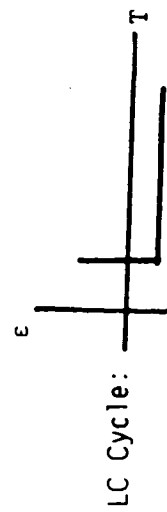
200X

Figure 5-20

Fracture surface of Specimen 45D after being TMF tested between 1000-1600°F, $\Delta\epsilon_t = 0.5\%$, $R = -1$, for 2096 cycles (50% load drop).

(a) Optical fractography showing an OD initiation (Transgranular).

(b) & (c) SEM showing carbide as initiation sites.



ORIGINAL PAGE IS
OF POOR QUALITY

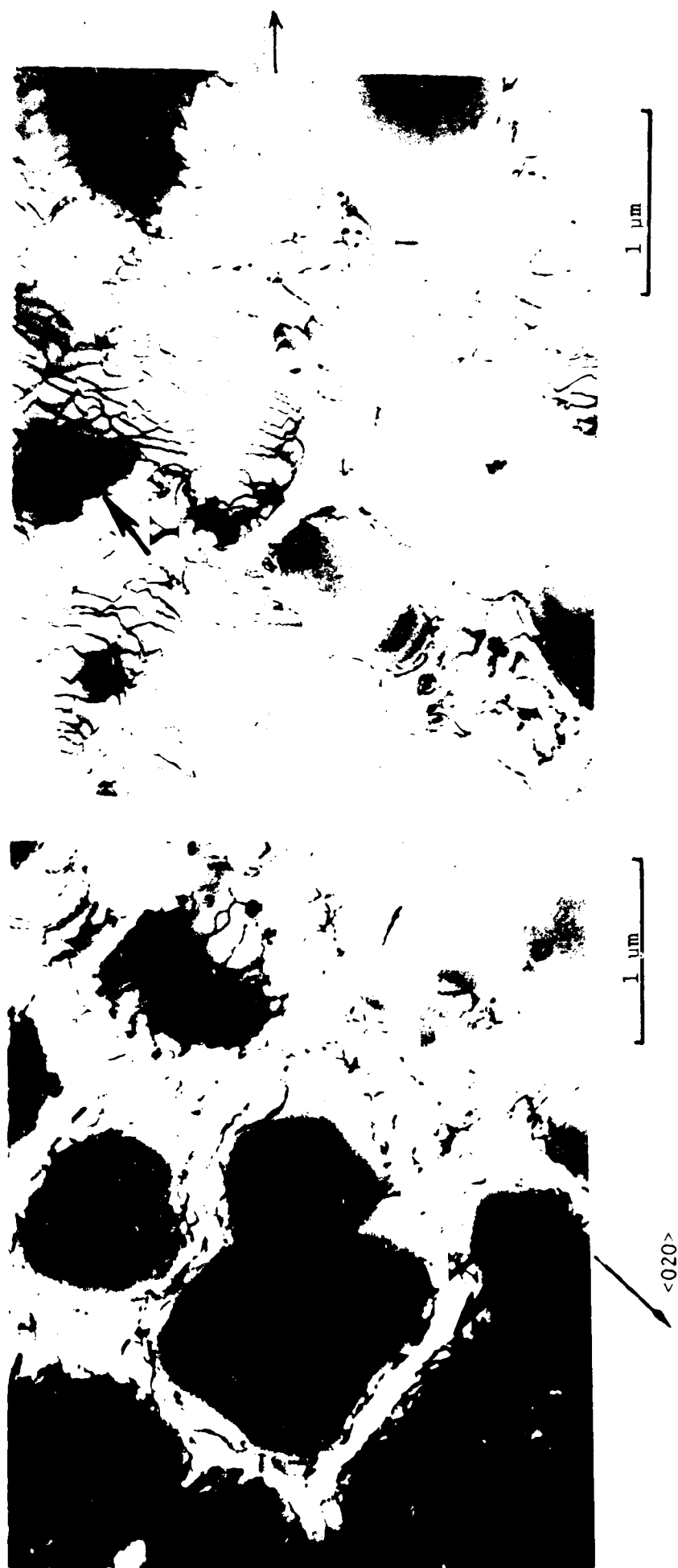
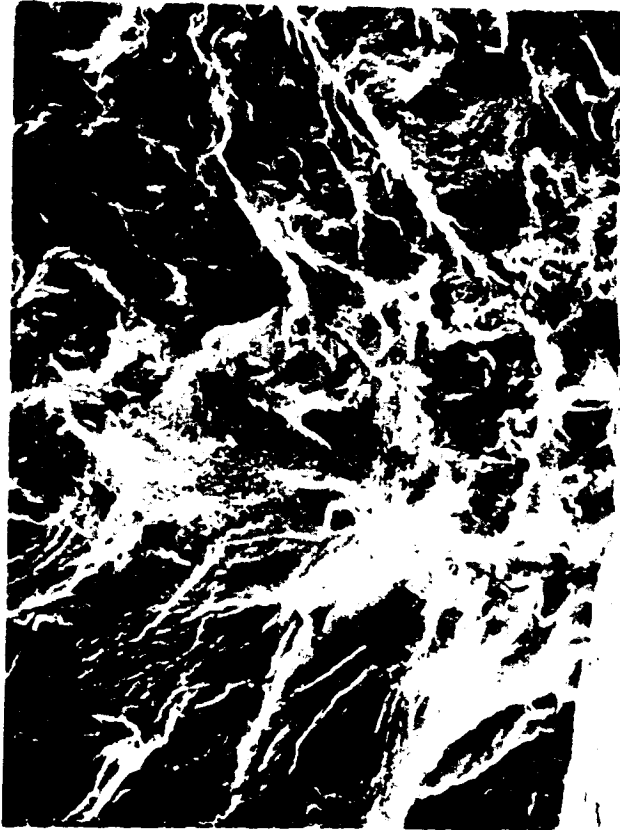


Figure 5-21 Dislocation structure for Specimen 45D after being TMF tested with temperature range 1000-1600°F, strain range -0.25 to 0.25, LC cycle type $\frac{\epsilon}{\tau}$, frequency = 1 cpm for 2096 cycles (50% load drop).



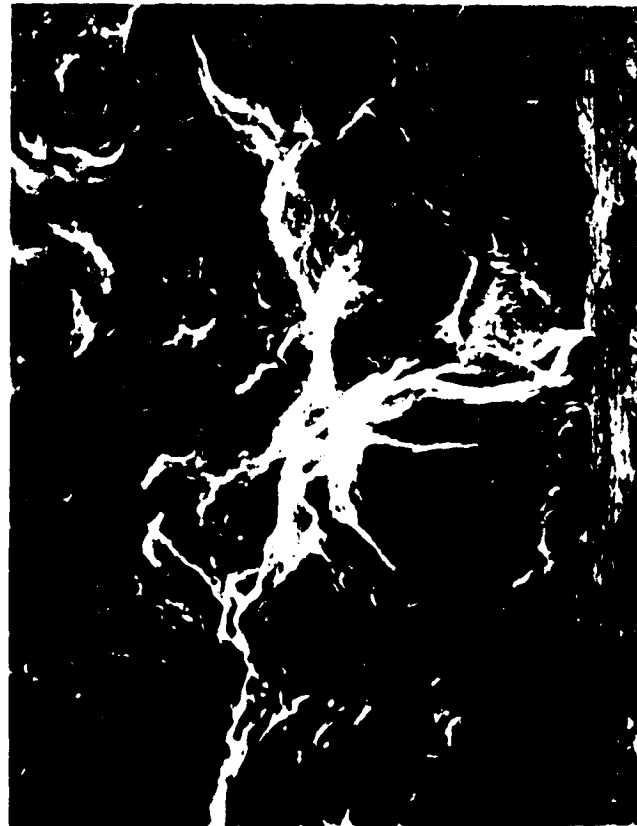
20X

(a)



85X

(b)



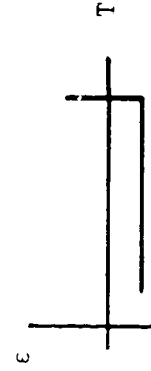
350X

(c)

Figure 5-22 Fracture surface of Specimen 46A after being TMF tested between 1000-1600°F, $\Delta \epsilon_t = 0.5\%$, $R = -1$, for 2415 cycles (50% load drop).

(a) Optical fractography showing OD initiation (mixed).

(b) & (c) SEM showing carbide/porosity as initiation site.



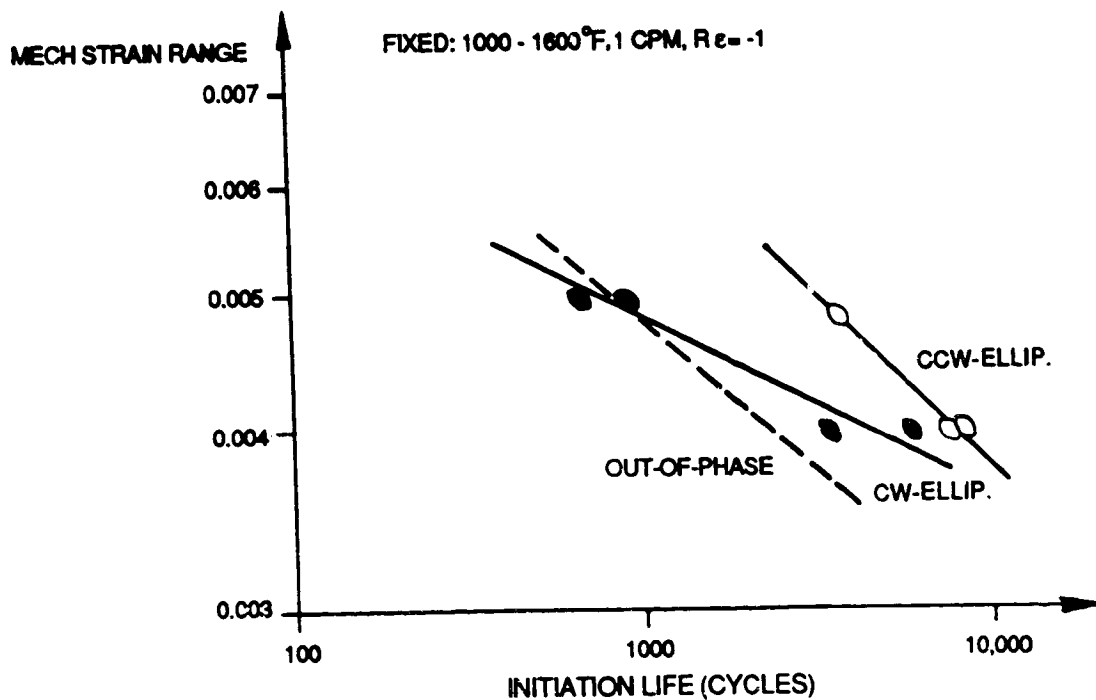


Figure 5-23 Elliptical Cycle TMF Test Results

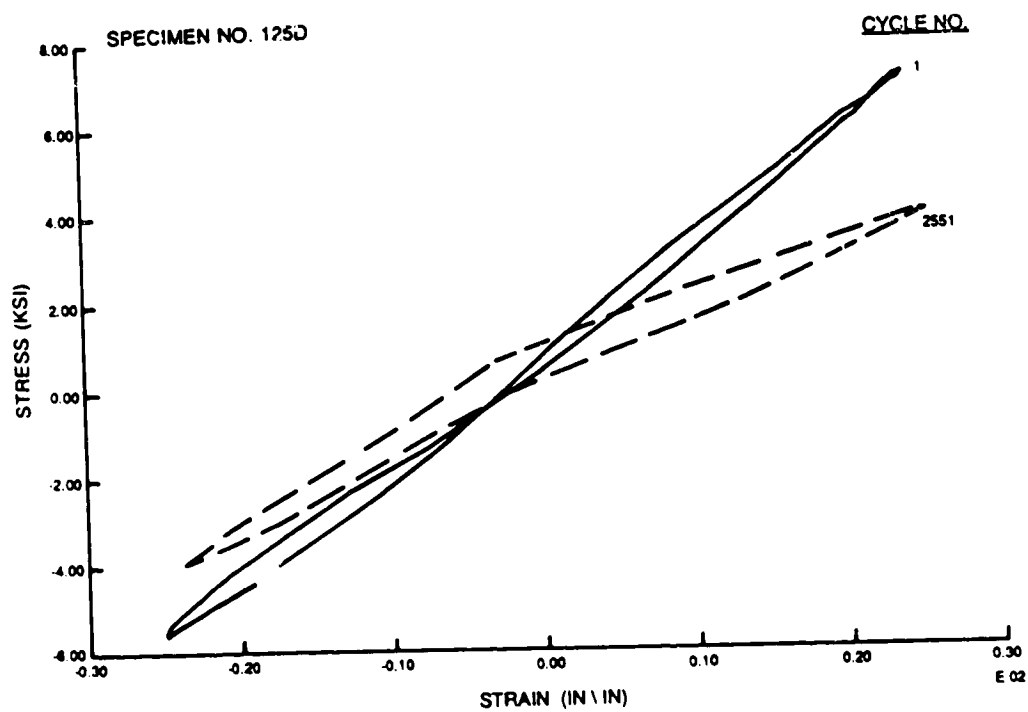


Figure 5-24 Hysteresis Loops for Counter-Clockwise Elliptical Test

5.1.7 Temperature Range Effects

In order to investigate the influence of temperature range on TMF life, three specimens were tested at ranges other than the baseline 538-871°C (1000-1600°F). The other test conditions duplicated those used for previous fully reversed TMF tests (Section 5.1.3) to facilitate direct comparison with those results. Figure 5-25 presents the initiation lives of these specimens relative to the baseline out-of-phase and in-phase test results. The higher temperature range tests are slightly lower in life than the baseline tests, and the amount of debit seems to be associated mostly with the maximum temperature. This may be a result of the fact that the baseline temperature range already exercises most of the damage mechanisms which are important to TMF life.

As with the R-ratio testing, this series of tests showed that the effect of temperature range is a function of the definition of initiation. Figure 5-26 shows a comparison plot of crack growth data for a 538-927°C (1000-1700°F) test relative to a baseline 538-871°C (1000-1600°F) test at the same conditions. At the higher range, the crack grew more quickly at first but slowed down significantly due to the relaxation of the mean stress during the test. This large difference in crack growth resulted in a lower initiation life of about 2X relative to the baseline test even though the separation life was 2.5X higher.

5.2 TMF LIFE PREDICTION MODEL DEVELOPMENT

One method of predicting TMF life is to simply use a model developed for isothermal conditions, taking the maximum cycle temperature as constant for the whole test. Early in this reporting period, this technique was used with the isothermal CDA model to obtain life predictions for TMF tests. Figure 5-27 shows these CDA predictions for the five out-of-phase tests available at that time. Note that the trend of the data was predicted fairly well, although the predicted lives were consistently lower than the actual lives. On the other hand, Figure 5-28 shows that the in-phase and dogleg tests were not correctly predicted. This is likely caused by new damage mechanisms active during these tests, as suggested by the intergranular fracture surfaces common to these conditions. In light of this work, an advanced TMF model is under development, using an incremental form of the CDA equation which can be integrated around any arbitrary strain-temperature history to obtain an accurate assessment of the damage done per cycle. Other TMF testing and model development work, both past and present, has been reviewed and will also be used to guide the CDA work (Refs. 5.2 - 5.4).

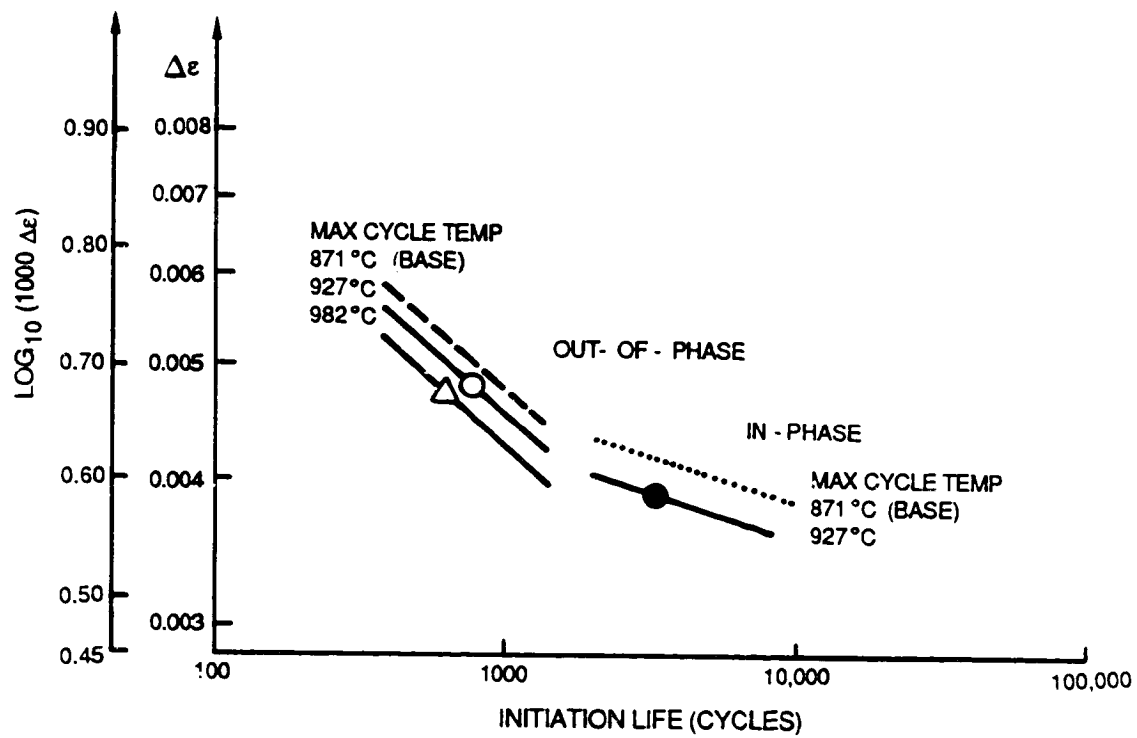


Figure 5-25 Variable Temperature Range TMF Tests

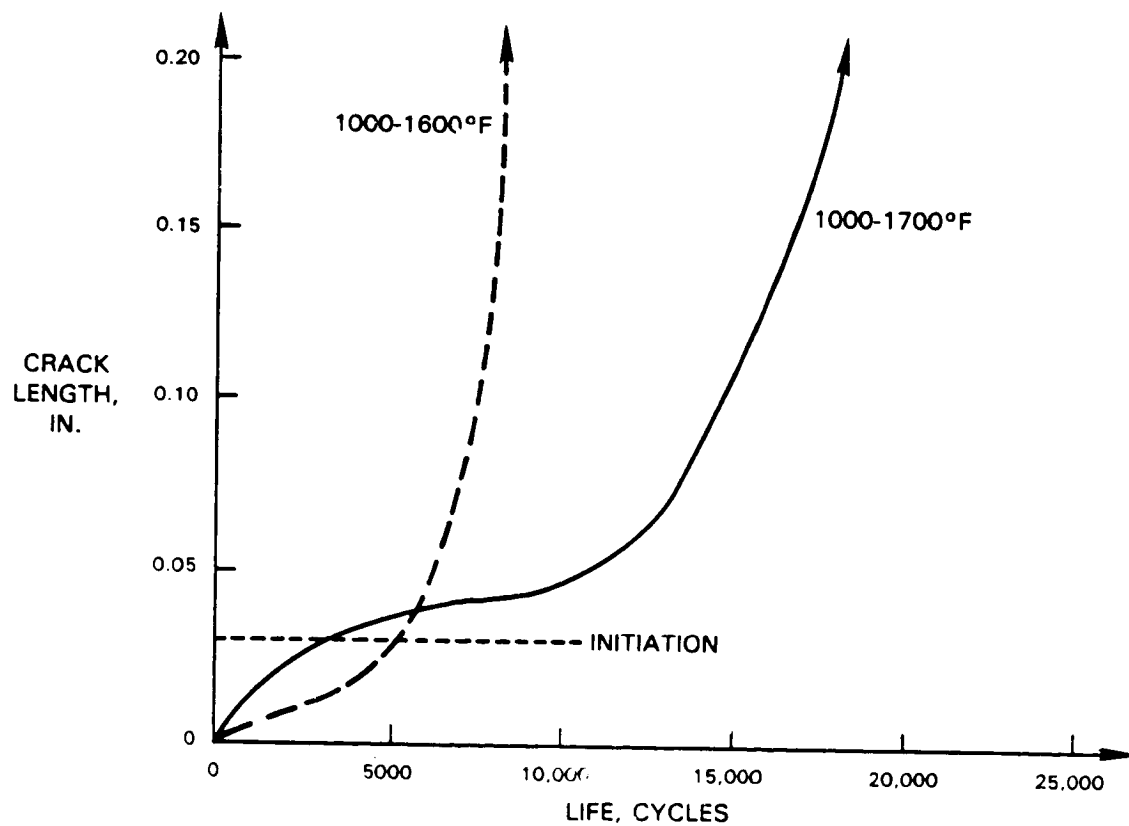


Figure 5-26 Crack Growth Data for In-Phase TMF Testing, ± 0.20 Percent Strain Range

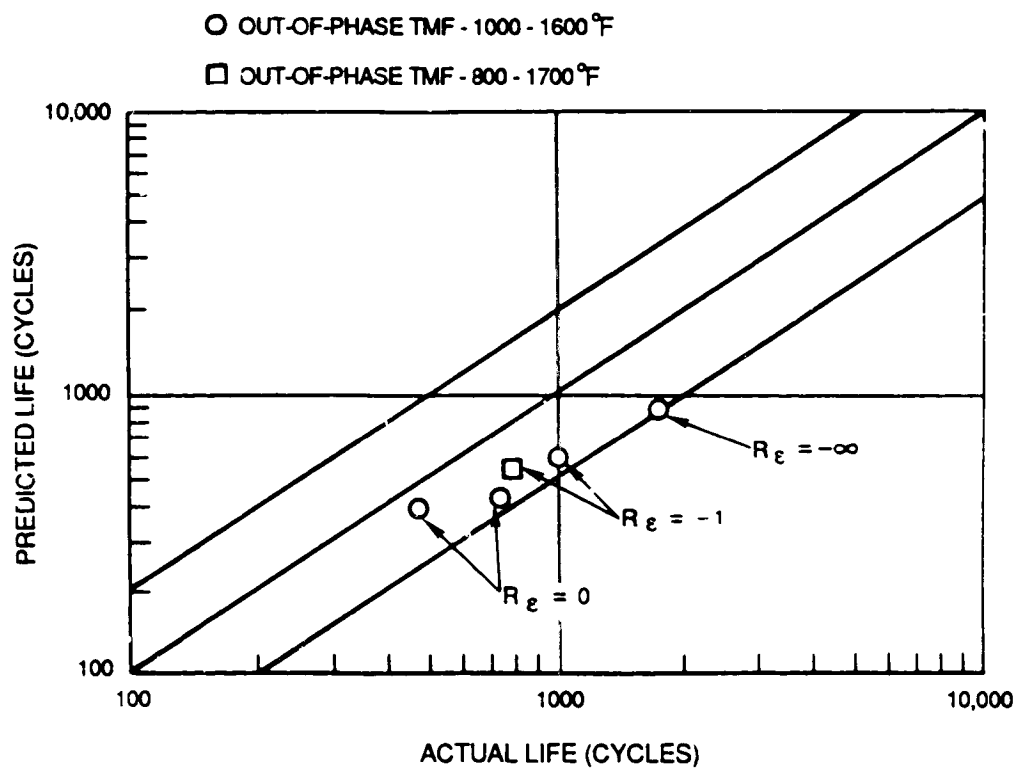


Figure 5-27 Prediction of Out-of-Phase TMF by CDA Model

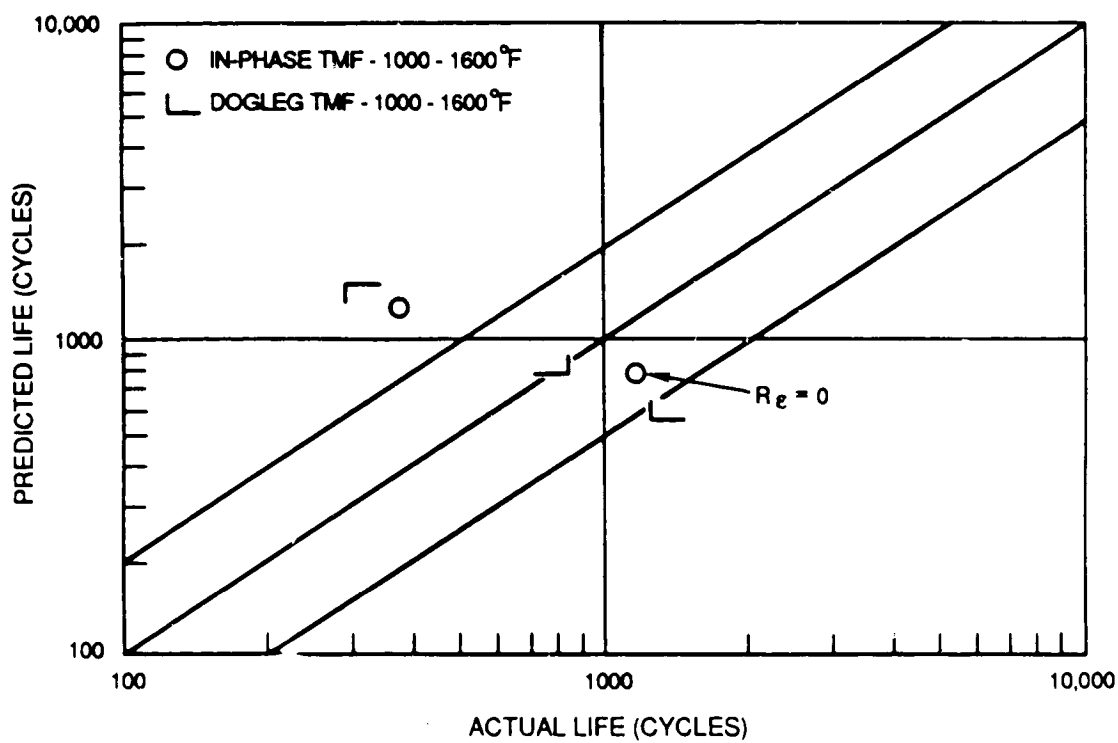


Figure 5-28 Prediction of In-Phase and Dogleg TMF by CDA Model

SECTION 6.0

TASK VI - MULTIAXIAL STRESS STATE MODEL

6.1 LITERATURE REVIEW OF STATE-OF-THE-ART MULTIAXIAL LIFE PREDICTION MODELS

A survey of current multiaxial life prediction approaches was conducted and the potential for these approaches to predict the multiaxial effects in hot section components of gas turbine engines was assessed.

Evaluation of the life prediction approaches was based on the following criteria:

1. Since multiaxial straining in hot section components is often non-proportional, the approach should demonstrate the capability to predict non-proportional loading effects.
2. Multi-parameter models show considerably more accuracy in predicting fatigue lives; therefore, the approach should use two or more independent parameters to characterize multiaxial fatigue behavior.
3. Since multiaxial testing is expensive and difficult to accomplish and the vast majority of available material fatigue data are uniaxial, the approach should require only a minimal amount of multiaxial data to determine all constants in the model.
4. The final consideration is that the approach should be compatible with the Cyclic Damage Accumulation model.

The issue of non-proportional loading is important because it can be more damaging than proportional loading. Non-proportionality occurs in areas where two strain states arising from different loading mechanisms are superimposed. Two general categories of different loading mechanisms can be identified for hot section components: mechanical and thermal loads that are not in-phase and thermal loading by local and global gradients that develop at different rates.

There are two aspects of the stress/strain history which are non-proportional:

- 1) The ratio of magnitude of the principal stresses/strains varies with time.
- 2) The principal stress/strain axis rotates with time. This difficulty is more exaggerated in low cycle fatigue where the stress and strain axes are not coincident.

The latter aspect may be the more potent. It is thought that the rotation of the maximum shear vector may cause slip to occur in a larger number of planes thus more fully exploiting the hardening potential of the material. Therefore, non-proportional cycling can cause damage on many planes with different orientation in possibly different directions, whereas, proportional cycling causes damage which apparently can be characterized by a single invariant of the stress and strain tensors.

Three stress parameters and their strain versions, which are based on static yield theories (maximum normal stress, maximum shear stress and octahedral shear stress), have been used successfully to correlate multiaxial fatigue results for a wide variety of materials and stress states. However, there is considerable evidence indicating the inadequacies of such approaches (Refs. 6.1, 6.2). Many modifications have been made that are either empirical or account for various observed effects. These more complicated, multi-parameter models are considerably more accurate in predicting fatigue lives. A fundamental reason for this success is the inclusion of terms that account for the effects of hydrostatic pressure in some manner.

Manson and Halford (Refs. 6.3, 6.4) used the triaxiality factor to compute an effective ductility which accounts for the multiaxial effect on ductility due to hydrostatic pressure. The factor has been adjusted to account for torsional and axial fatigue behavior.

$$TF = \frac{\sqrt{2} (\sigma_1 + \sigma_2 + \sigma_3)}{\left((\sigma_1 - \sigma_2)^2 + (\sigma_2 - \sigma_3)^2 + (\sigma_3 - \sigma_1)^2 \right)^{1/2}}$$

where: $\sigma_1 > \sigma_2 > \sigma_3$ are the principal stresses.

The strain-range partitioning method was further modified by use of equivalent inelastic strain-ranges. These concepts could easily be introduced into the Cyclic Damage Accumulation model.

The use of the above approaches is limited to proportional loading or to materials in which non-proportional loading has only a small effect on fatigue life.

A number of different approaches to the problem of picking representative stress or strain values for non-proportional loading have been developed. The approaches can be divided into two categories. The first category considers stress, strain or energy variation without regard to how these quantities are distributed with respect to material planes. The second category considers the variation of some quantity on a critical material plane. The two most promising methods representative of these categories are discussed below.

Garud (Ref. 6.5) has related fatigue life (to crack initiation) to the plastic work per cycle independent of material planes. The approach includes explicit consideration of the stress-strain response which is considered crucial because of the path dependence of the fatigue process. The plastic work essentially represents an integrated effect of the two most important quantities generally believed to govern the fatigue process, namely the shear stresses and the plastic strains.

$$W_c = \int T \cdot d \epsilon_p$$

where: W_c = plastic work per cycle
 T = Cauchy stress tensor
 $d \epsilon_p$ = differential of plastic small strain tensor

The theory in its improved modified form assumes plastic work done by applied shear stress only counts half as much as other plastic work. This approach has demonstrated a capability to predict non-proportional loading effects. There are several drawbacks to the plastic work theory: as in any energy based theory it cannot predict the crack growth direction; life assessment is difficult when cyclic plastic work is small, that is, when fatigue lives exceed several thousand cycles; and plastic work is a very difficult and tenuous quantity to calculate in component analysis.

The critical plane method of Brown and Miller has been used to successfully correlate non-proportional loading data (Ref. 6.6). The method is based on a study of the physical processes of deformation and fatigue crack growth. It was found that Stage I fatigue cracks initiate on that plane of maximum shear strain range which experiences the greatest amplitude of normal strain. The theory is represented graphically by contours of constant life which are expressed mathematically by:

$$(\epsilon_1 - \epsilon_3)/2 = f [(\epsilon_1 + \epsilon_3)/2]$$

where: $\epsilon_1 > \epsilon_2 > \epsilon_3$ are the principal strain.

Unfortunately a large amount of multiaxial fatigue data is required to define these contours unless a mathematical form is available.

Recent testing of Hastelloy-X material (Ref. 6.7) resulted in cracks on the maximum shear stress planes for the room temperature tests, which is consistent with this critical plane theory, but at elevated temperature all cracking was on the maximum normal strain plane. This indicates a change in the fatigue initiation mechanism and suggests that the theory of Brown and Miller may not be universally applicable.

Socie and Shield (Ref. 6.8) observed that the mean stress affected the rate of crack growth and distribution of cracks. An additional parameter, mean stress normal to the plane of maximum shear strain amplitude, was included with the maximum plastic shear strain amplitude and normal strain amplitude.

The plastic work and critical plane theories described above obtained the same degree of scatter when applied to the same non-proportional loading data set. Other methods based on a single equivalent stress or strain quantity were non-conservative and considered not suitable for design purposes. It appears that of the existing methods the critical plane and plastic work theories hold the most potential for predicting the multiaxial effects in hot section components.

6.2 EXPERIMENTAL METHODS AND TECHNIQUES

Multiaxial strain controlled fatigue tests are being conducted at elevated temperature utilizing thin-walled, tubular specimens subjected to simple tension and torsion, as well as combined tension-torsion in proportional and non-proportional loading. The physical damage processes are being studied closely by monitoring fatigue crack initiation and growth during test through the use of cellulose acetate surface replicas and by post-test fractographic analysis. Material deformation behavior is also being monitored and recorded on computer files.

6.2.1 Test Facility

Unique apparatus, including extensometry to measure axial and torsional displacements, are required to perform these tests. Therefore, an existing experimental test facility at the University of Connecticut (Dr. E. H. Jordan), which has the necessary capabilities, has been retained to conduct the multiaxial fatigue tests. A complete description of this test facility including details concerning the servohydraulic testing machine and extensometer, which uses capacitance probes to measure axial displacement and angle of twist, are contained elsewhere (Ref. 6.7). Prior to initiation of testing, several modifications were made to improve the facility and increase its high temperature capability to the required level. Also, computer software codes were written for running the fatigue tests and recording data.

The design of the specimen fixturing system was simplified by the incorporation of collet grips purchased from Super-Flex Corporation. These eliminated the need for adaptors and flanges brazed or welded to the specimen and associated tight machining tolerances used in the previous design. Although the collets demonstrated adequate gripping capability, it was found that this capability depends upon the depth to which the specimens are inserted. Therefore, the manufacturer supplied modified collets which work properly with only one inch insertion and maintain the space required for extensometry, heating and cooling apparatus. In order to reduce the possibility of slippage, the outer diametral surface at the grip ends of the specimens have been roughened by shot peening. Alignment was checked using a strain gaged specimen. An acceptably low level of bending was obtained by inserting shims under the collet grip base. Although the shims are not disturbed during mounting and removing the specimens, alignment is being checked periodically during the test program.

The high temperature modifications include an effective specimen heating system that incorporates an induction heating coil. The coil provides uniform temperature distribution in the specimen gage section at the required temperature levels and also provides sufficient access to allow specimens to be replicated without requiring partial teardown of the test setup. The potential problem of local crack tip heating due to the crack concentrating the induction field is relevant in multiaxial fatigue because of the multi-directionality of the cracking. However, Jordan (Ref. 6.7) has demonstrated consistent fatigue results using an induction heating coil operating at a low (10 KHz) audio frequency. Another modification was the inclusion of two copper water cooling collars which clamp to the specimen

between the heater and the grips and prevent heat transfer to the collet grips. Finally, the tungsten carbide points, which are used to attach the extensometer to the specimen, have been changed to a more durable design capable of higher temperatures.

6.2.2 Specimen Design and Fabrication

Eight inch long, hollow core bars of B1900+Hf material were cast by Hitchiner Manufacturing, Milford, New Hampshire for use as the multiaxial fatigue test specimens. The B1900+Hf material was from Certified Alloy Products, Inc. heat W-0098 that is being used in the base and optional programs of this contract and in the NASA Isotropic Constitutive Modeling Contract. The chemical composition of this heat is given elsewhere (Ref. 6.9). The bar geometry and casting parameters, pour and mold temperatures were the same as those that had been established previously for fabrication of the constitutive modeling biaxial test specimens. These specimens had been subjected to considerable development with a number of geometry design changes and casting trials evaluated prior to meeting material grain size and integrity goals.

All of the test bars were fully heat treated prior to machining according to the following schedule:

Solution Heat Treat: $1079 \pm 14^{\circ}\text{C}$ ($1975 \pm 25^{\circ}\text{F}$) for 4 hours; air cool
Precipitation heat treat: $899 \pm 14^{\circ}\text{C}$ ($1650 \pm 25^{\circ}\text{F}$) for 10 hours; air cool

The structure of the material in a fully heat treated multiaxial specimen was examined optically for grain size and porosity and by TEM replica for gamma prime (γ') size. An acceptable level of microporosity was found uniformly distributed throughout the specimen. No higher density areas of porosity were found. Figure 6-1 shows a typical example of the porosity distribution. The gamma prime (γ') size, shown in Figure 6-2, and distribution within the grains are similar to those observed in base program specimens. The grain size was examined in three (3) mutually perpendicular directions as shown in the schematic diagram of Figure 6-3 (radial (A), transverse (B), longitudinal (C)). The optical micrographs of Figure 6-4B and 6-4C show that the grains have a roughly ellipsoidal shape running in the radial direction with the grains at the inner diameter smaller than those at the outer diameter. The grain size in the radial view, Figure 6-4A, is \geq ASTM No. 1. The specimen wall thickness contains approximately two grains; therefore, elastic anisotropy may require more careful consideration in the case of the multiaxial specimens than the base program specimens.

The specimen design, shown in Figure 6-5, has a double-stepped outer diameter that results in low strain concentrations at the ends of the gage section and allows attachment of the extensometer in a slightly thicker section to help preclude failures from the extensometer points. The susceptibility of this design to inner diameter initiated fatigue cracking was investigated with a two-dimensional elastic finite element analysis of the specimen (Figure 6-6) subjected to an axial load. The resulting strain distribution in the gage section, shown in Figure 6-7, is fairly uniform which indicates that use of the 'average' extensometer strain introduces little error. The transition to a thicker section imposes local bending strains which does cause higher

ORIGINAL PAGE IS
OF POOR QUALITY

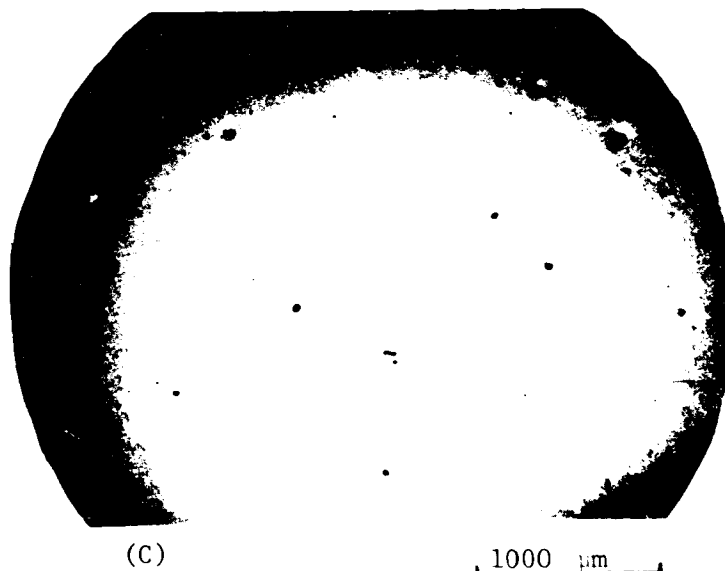


Figure 6-1 Typical Porosity Distribution in Gage Length of Multi-axial Specimen

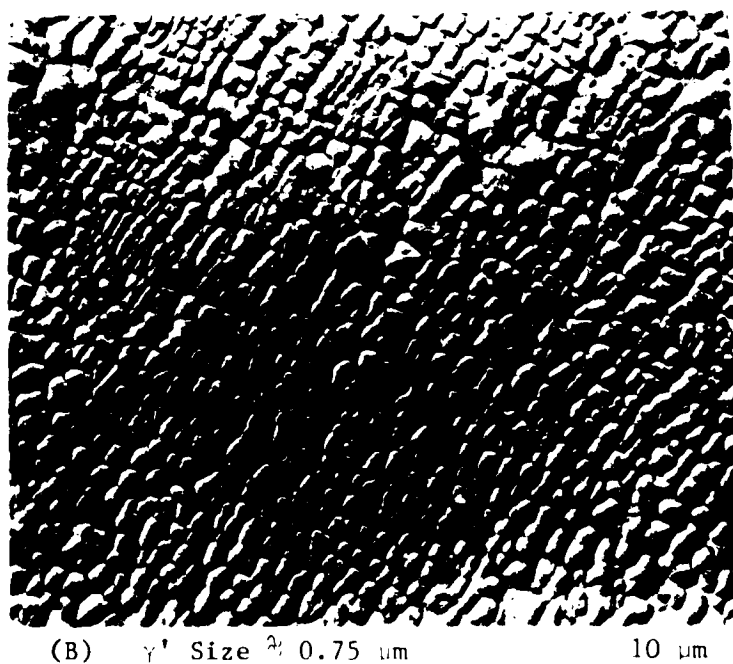


Figure 6-2 Gamma Prime (γ') Size in Gage Length of Multi-axial Specimen

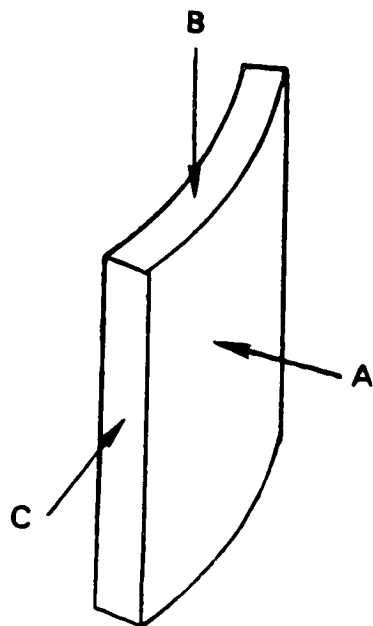
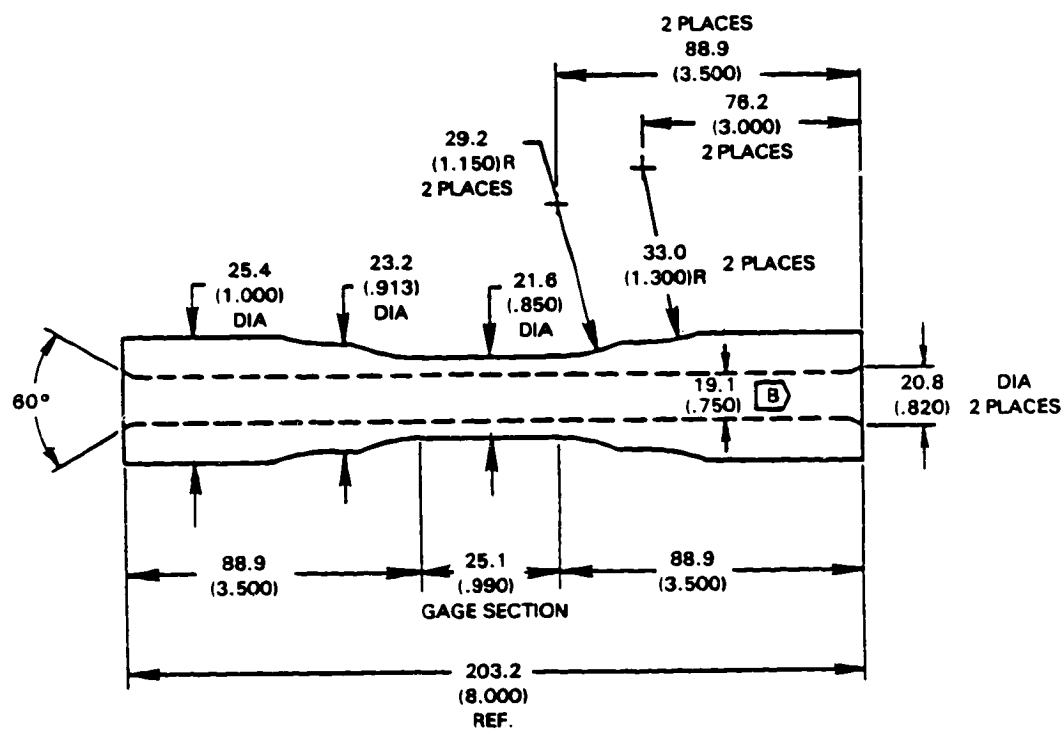


Figure 6-3 Schematic diagram of multi-axial gage section showing orientations used for grain size characterization. A - Radial; B - Transverse; C - Longitudinal

ORIGINAL PAGE IS
OF POOR QUALITY



Figure 6-4 Optical micrographs of gage section of multi-axial specimen using orientations as shown in Figure 6-3. (A) Radial, (B) Transverse, (C) Longitudinal



DIMENSION IN MM (in)

Figure 6-5 Biaxial Tension Torsion Specimen



Figure 6-6 2-D Finite Element Analysis of Biaxial Fatigue Specimen

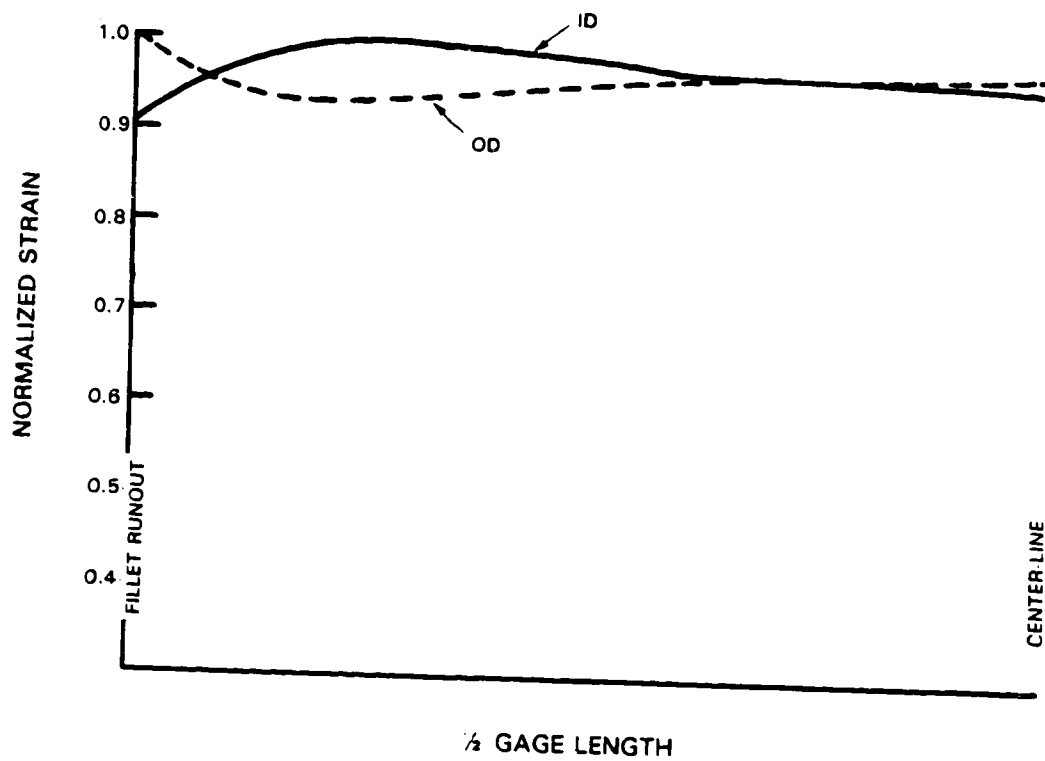


Figure 6-7 Strain Distribution in Biaxial Fatigue Specimen due to Axial Load (Finite Element Analysis Results)

strains on the specimen inner diameter near the ends of the gage section. However, a subsequent tensile fatigue test resulted in outer diameter crack initiation near the center of the gage section. The criticality of this location is probably increased by thermal gradient and plasticity effects not included in the finite element analysis.

A total of twenty-eight multiaxial specimens were fabricated. All specimens were then electropolished on the outer diameter except for the grip ends which were left as-machined.

6.2.3 Test Program and Procedures

The multiaxial fatigue test program, which consists of 26 tests utilizing the B1900+Hf thin-walled, tubular specimens described in Section 6.2.2, is summarized in Table 6-1. These isothermal, strain controlled tests are being conducted to provide crack initiation data to use in the development and verification of a multiaxial stress state creep-fatigue life prediction model.

Four types of strain cycles are employed in the tests: simple tension or torsion, combined tension-torsion in-phase and combined tension-torsion 90 degrees out-of-phase. All applied axial and torsional strain ranges are fully reversed ($R=-1$) with triangular waveforms. Two temperature levels (871°C (1600°F), 538°C (1000°F)) and two frequency levels (10 CPM; 1 CPM) are being investigated to determine their effect on the cracking behavior and possible changes in stress state dependence. The variation in fatigue life with strain range is also being investigated by conducting similar tests at two strain range levels.

TABLE 6-1
MULTIAXIAL TEST PROGRAM MATRIX

Specimen	Type	Equivalent Strain Range $\Delta\epsilon_{e1}$ $\Delta\epsilon_{e2}$	Strain Ratio (Torsional/Axial)			Phase Angle		Temp. (°F)		Freq. (CPM)		
			0	1.5	∞	0°	90°	1000	1630	0	1.0	10
1	BASE	N/A (Creep Load)	X						X	X		
2		X	X					X				X
3		X	X						X			X
4		X			X			X				X
5		X			X				X			X
6			X					X				X
7			X					X				X
8					X				X			X
9					X			X				X
10	IN PHASE	X		X		X		X				X
11		X		X		X			X			X
12			X			X		X				X
13			X			X			X			X
14	OUT OF PHASE	X		X		X	X			X		
15		X		X		X	X					X
16		X		X		X			X	X		
17		X		X		X			X			X
18			X			X	X				X	
19			X			X	X				X	
20			X			X		X				X
21			X			X			X		X	

22-26 TO BE DEFINED (OR DUPLICATE) TESTS

As in the base program, approximately one-half of the specimens are being inspected during testing by the cellulose acetate replication method to determine the evolution of the fatigue cracks. The size, number and angle of the surface cracks are determined by micrographic examination of the replicas. Crack initiation is defined as the generation of a 0.76 mm (0.030 in.) long surface crack. The test is terminated subsequent to a 50% drop in cyclic load range (tensile load drop for a tension-torsion test) or at complete separation of the specimen.

Strain control during the multiaxial tests refers to control of the longitudinal and torsional strains. However, complete knowledge of the full strain tensor is required to determine principal strains, equivalent strain and other parameters used to correlate fatigue data. The usual procedure is to calculate the circumferential and through-thickness strains using an effective Poisson's ratio. In the elastic-plastic regime encountered in low cycle fatigue testing, Poisson's ratio lies between the elastic value and 0.5 for constant volume plastic deformation. An effective value of 0.4 is assumed for Poisson's ratio in this report.

6.3 INITIAL MULTIAXIAL EXPERIMENTS

Four multiaxial fatigue tests have been completed to date using the four different types of strain cycles specified in the test program. The idealized strain paths in $\epsilon - \gamma$ space for these tests are shown in Figure 6-8. All of the tests were conducted at 871°C (1600°F) and 10 CPM with an equivalent strain range of approximately $\pm 0.25\%$.

6.3.1 Test Results

Test data and results are listed in Table 6-2. The applied strains and stresses given in the table are based on measurements taken from hysteresis loops at approximately half-life. These hysteresis loops, along with plots of applied strain versus time, are shown in Figures 6-9 to 6-12. After the initial test (Specimen 204), the number of strain control input signals was increased by a factor of five which resulted in much smoother loops. The upward drift of the tensile hysteresis loops observed during testing revealed a possible problem with the test rig. After a brief investigation, the cause of the problem was found to be a malfunctioning axial capacitance displacement probe in the extensometer which has since been repaired. Uniaxial test experience in the base program indicates that the tensile mean stress levels developed in the multiaxial tests did not have a large effect on the resultant cyclic lives.

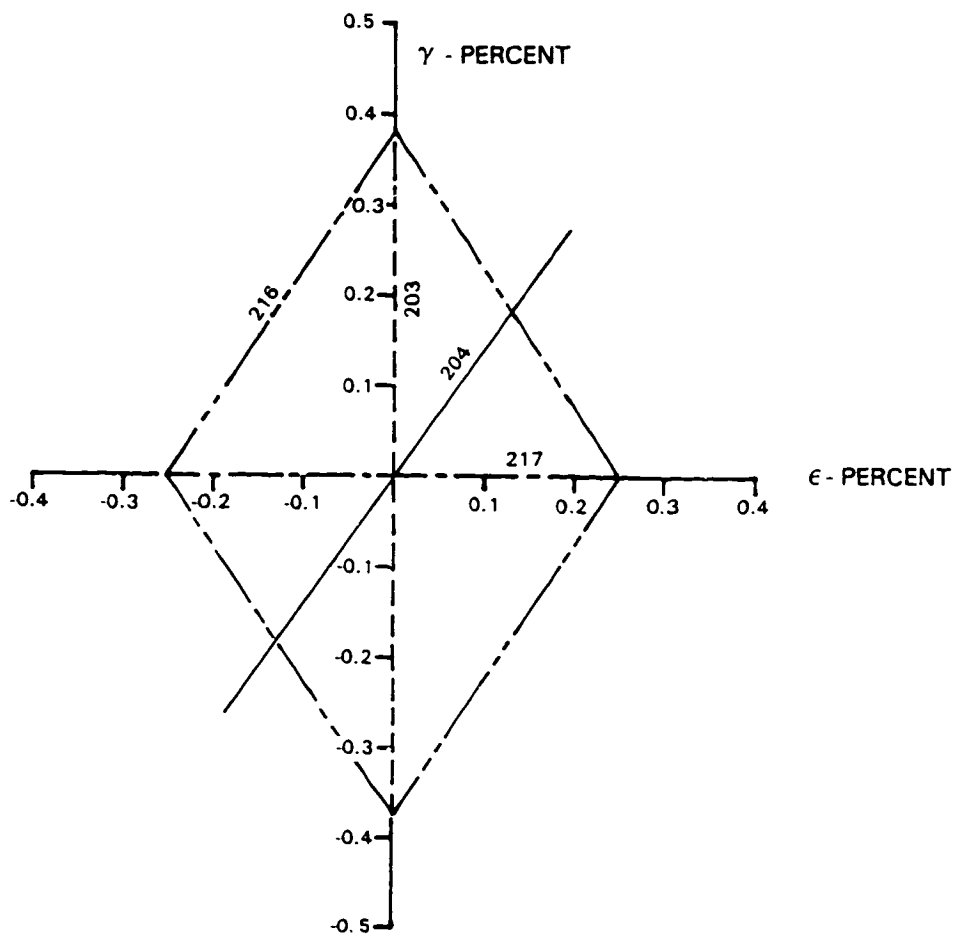


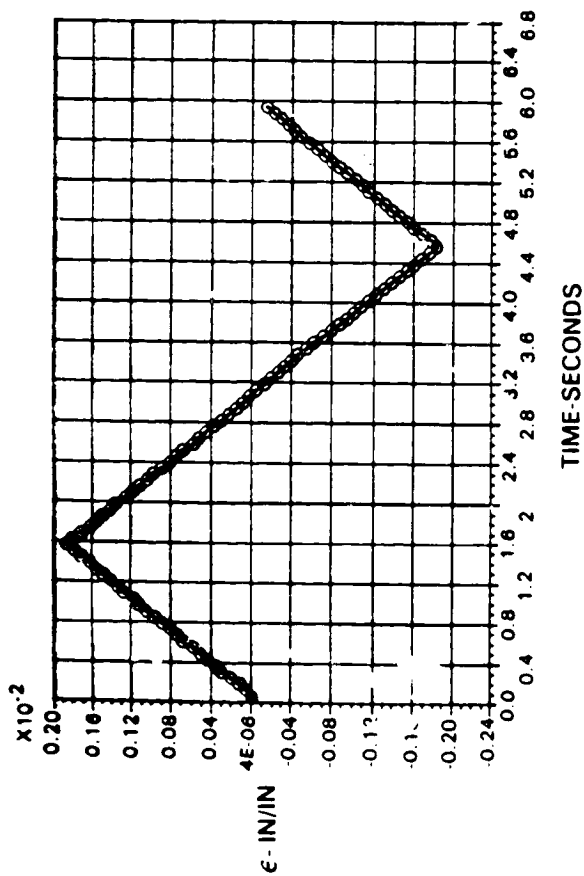
Figure 6-8 Multiaxial Test Specimen Strain Paths

TABLE 6-2
TEST RESULTS

Specimen Number	Temp (°F)	Freq. (cpm)	$\Delta\epsilon$ (%)	$\Delta\gamma$ (%)	Phase Angle (deg.)	σ_m/T_m (ksi)	$\Delta\sigma/\Delta T$ (ksi)	Crack Angle (deg.)	Initiation Life (cycles)	50% Load Drop Life (cycles)
204	1600	10	± 0.185	± 0.260	0	7.7/-0.7	63.5/35.2	65	350	1085
203	1600	10	0.0	± 0.404	—	—/-0.6	—/62.3	-45	8100	11224
217	1600	10	± 0.250	0.0	—	10.9/—	100.3/—	90	1150	2317
216	1600	10	± 0.250	± 0.375	90	15.3/-1.0	106.1/63.6	90	1250	1880

- (1) Applied strains and stresses are based on measurements taken at approximately half-life.
 (2) Crack angle is measured relative to the specimen longitudinal axis with clockwise being positive.

88 (a) APPLIED STRAINS VERSUS TIME



(b) HYSTERESIS LOOPS

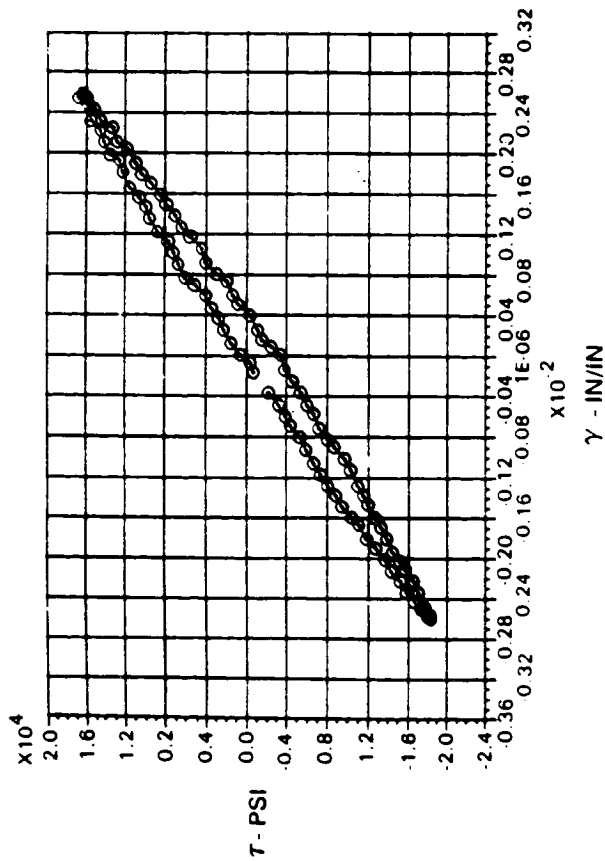
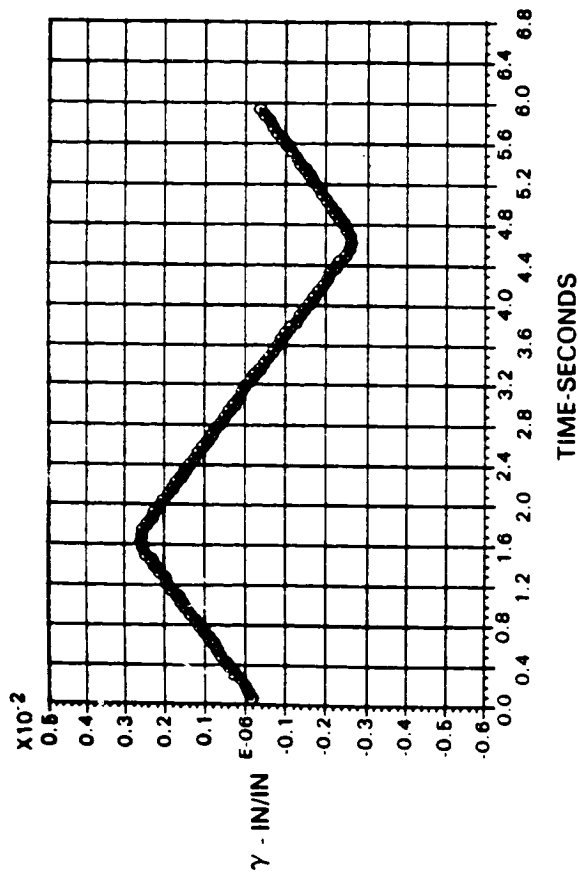
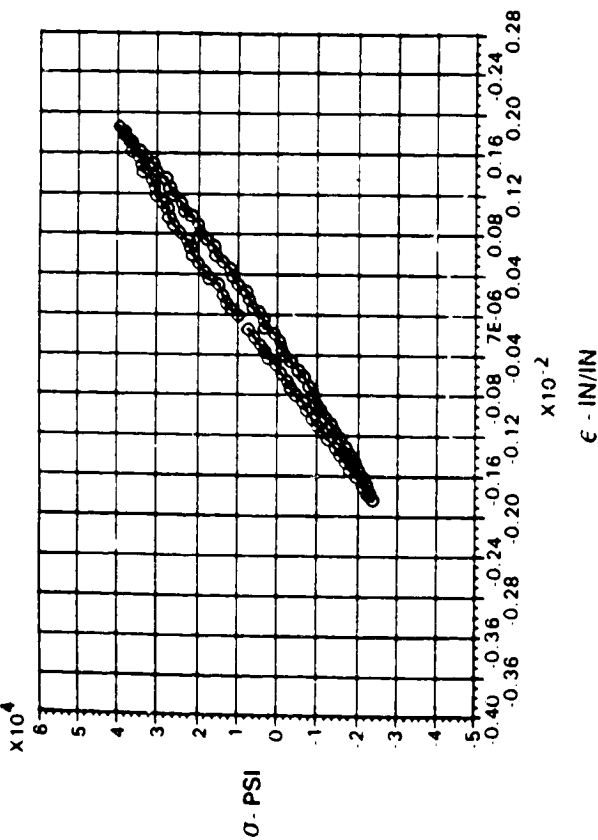


Figure 6-9 Specimen 204 Tension - Torsion In-Phase

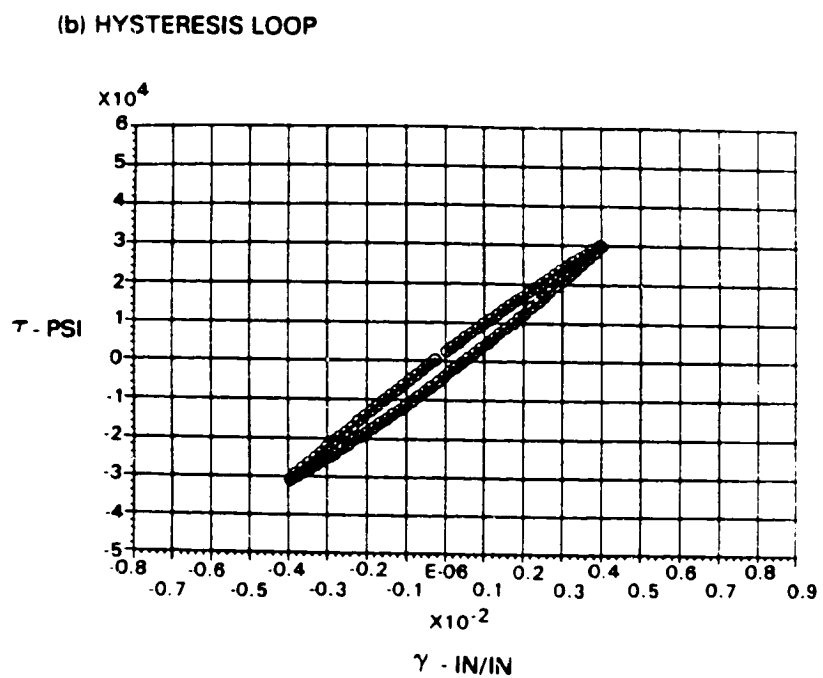
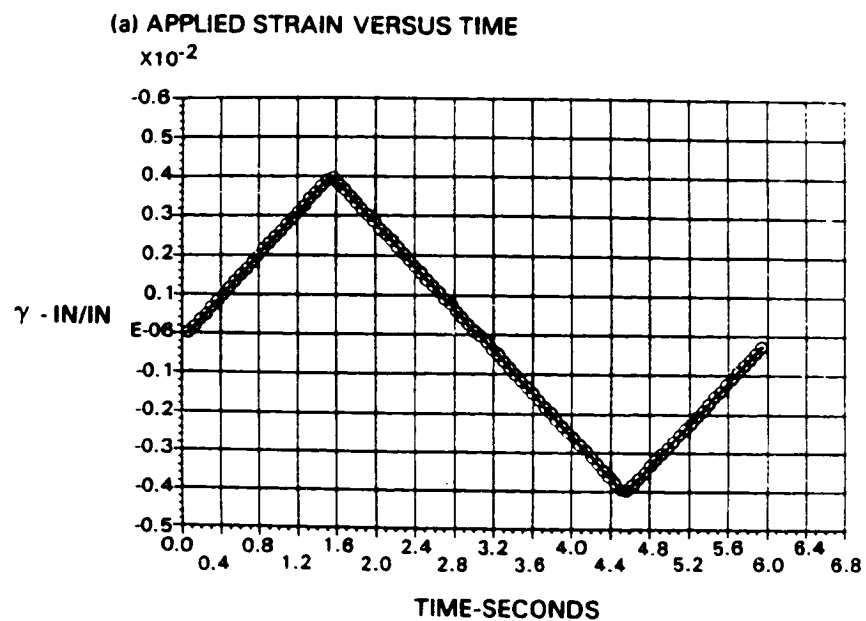


Figure 6-10 Specimen 203 Torsion Only

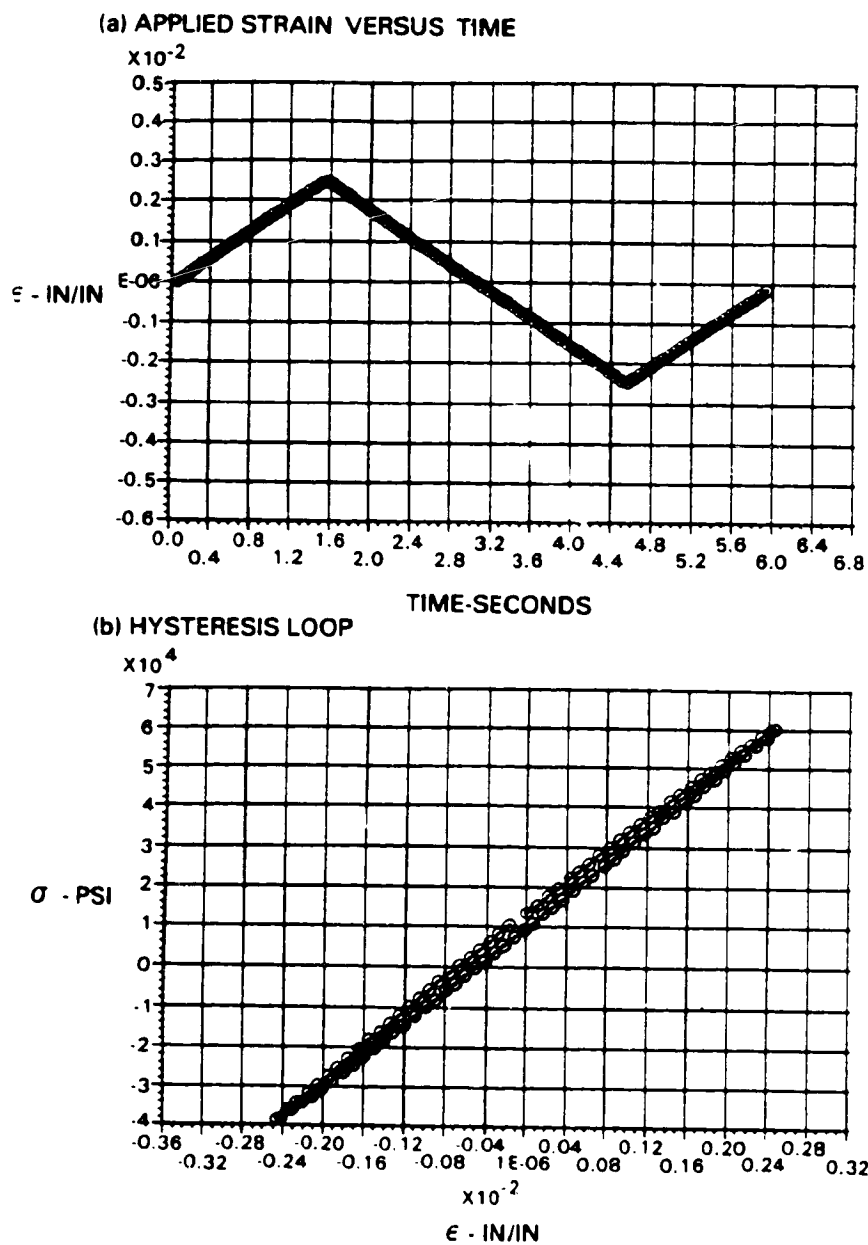


Figure 6-11 Specimen 217 Tension Only

SPECIMEN 216
TENSION-TORSION 90° OUT-OF-PHASE

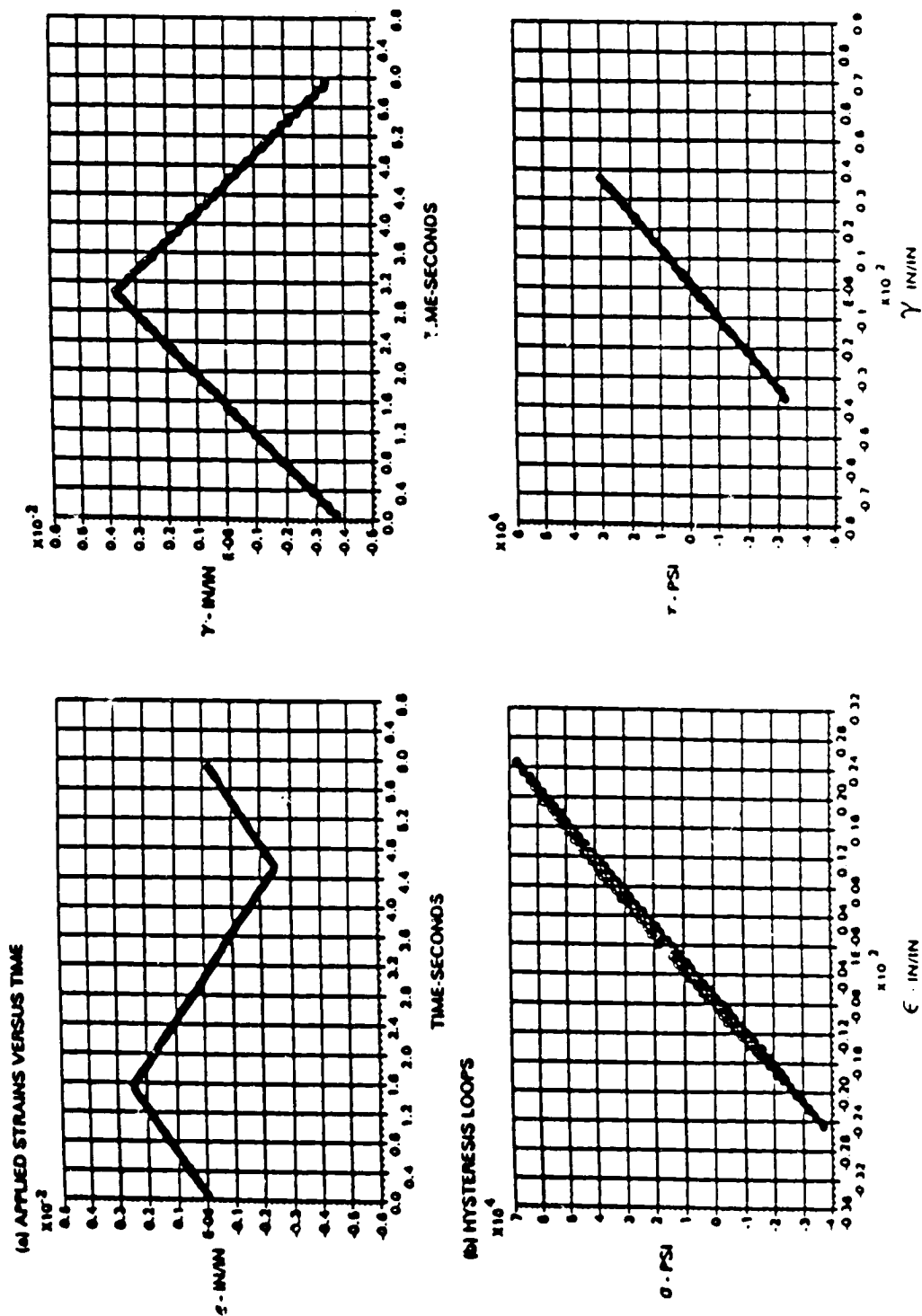


Figure 6-12 Specimen 216 Tension - Torsion 90° Out-of-Phase

6.3.2 Fractographic Observations

The in-phase tensile-torsion test of specimen 204 resulted in a long crack oriented at approximately 65° to the specimen longitudinal axis, as shown in Figure 6-13a, with no secondary surface cracking. A surface replica taken during the test revealed two separate cracks that eventually coalesced. Two initiation sites were found 8.89 mm (350 mils) apart at the outer diameter. Figure 6-13b is an optical picture of the most obvious initiation site. Figure 6-14a is an SEM micrograph of the initiation site showing it in greater detail. A tantalum (Ta) x-ray map of the initiation site, Figure 6-14b, shows the area to be rich in Ta. In the base program, initiation sites with a high Ta content or other constituents found in the grain boundary carbides were identified as MC carbide related failures; however, the size of the Ta rich areas in specimen 204 is much too large for an MC carbide. The specimen was sectioned longitudinally through the Ta rich area as indicated by the dashed line in Figure 6-14a and the schematic diagram of Figure 6-15a. A SEM micrograph of the longitudinal section at the area of the initiation site is shown in Figure 6-15b. An oxide layer ranging in thickness from 2×10^{-3} mm to 3×10^{-2} mm is present at the fracture surface as well as at the secondary crack beneath the fracture. X-ray energy spectroscopy results show this oxide to be Ta rich. This type of oxide buildup suggests that the crack initiated from a dross at location A, Figure 6-15b.

ORIGINAL PAGE IS
OF POOR QUALITY

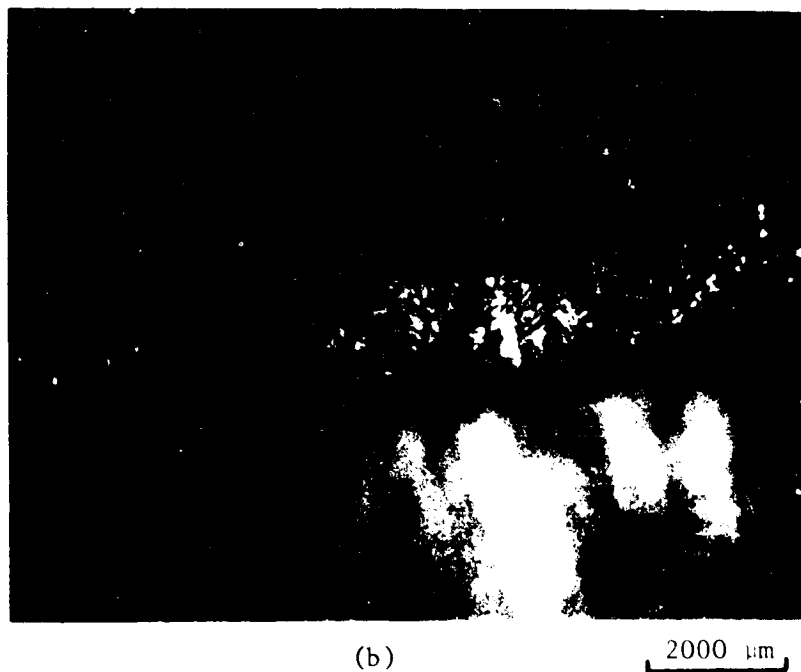
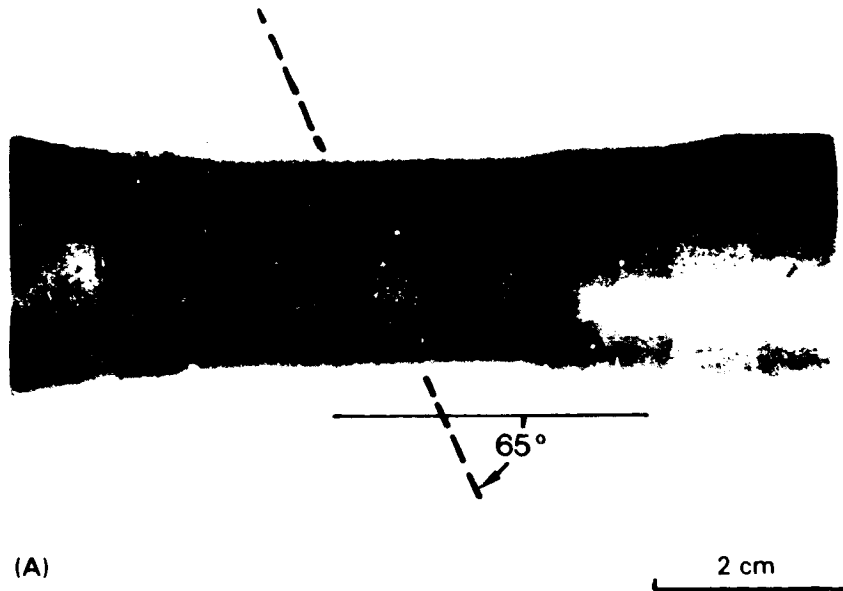


Figure 6-13 Multiaxial test specimen 204 using a tension strain range of $\pm 0.185\%$ and a torsion strain range of $\pm 0.26\%$, in phase, (effective strain range $\pm 0.245\%$) at 1600°F for 1085 cycles (50% load drop).

(a) Crack slanted at an angle of 65° with specimen axis,
(b) Major initiation site by optical.

ORIGINAL PAGE IS
OF POOR QUALITY

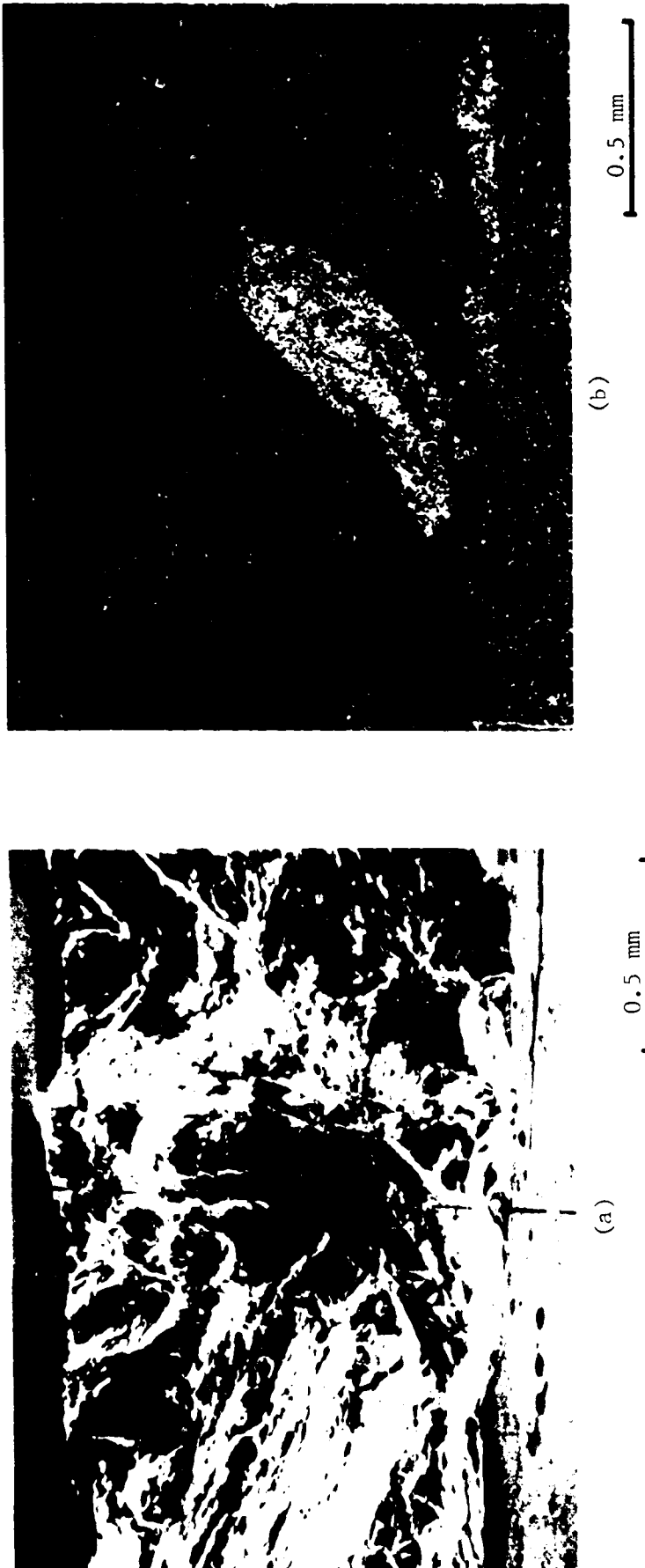


Figure 6-14 Initiation site of multiaxial specimen 204.

- (a) SEM micrograph showing location where specimen was sectioned longitudinally.
- (b) Ta x-ray map of initiation site.

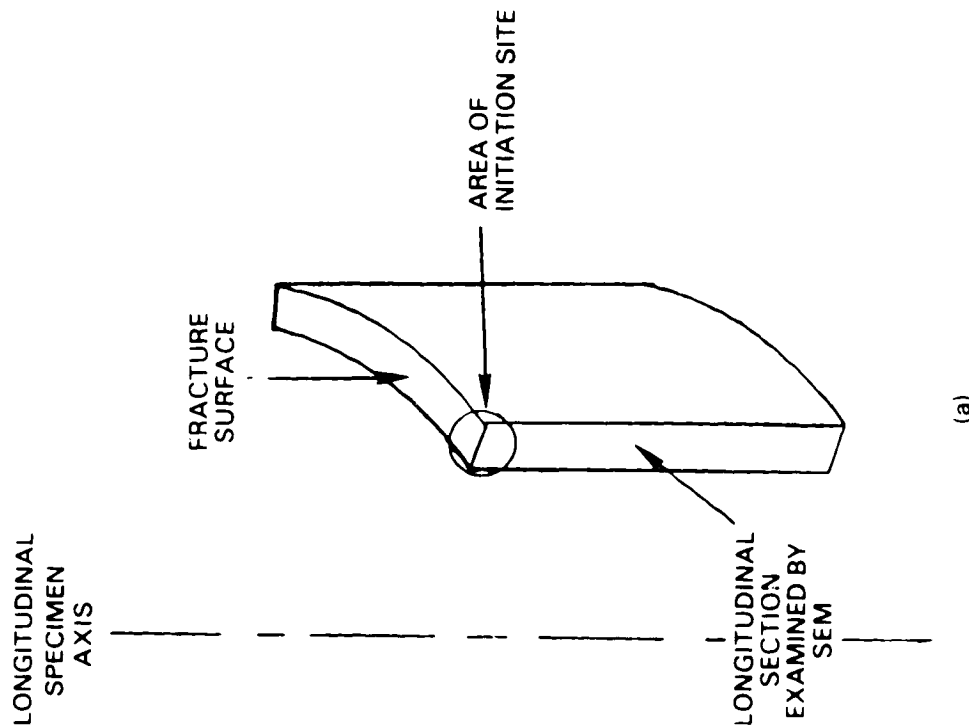


(b)

0.1 mm

Figure 6-15 Characterization of longitudinal section through initiation site of specimen 204.

- (a) Schematic diagram showing orientation of section examined by SEM.
- (b) SEM micrograph of longitudinal section at initiation site showing oxide buildup on fracture surface as well as in secondary crack.



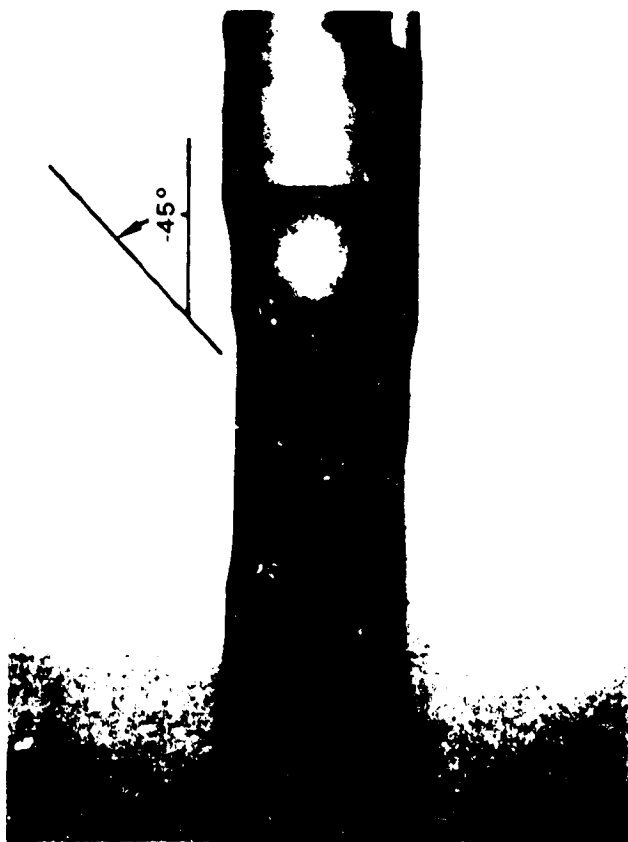
(a)

The torsional test of Specimen 203 resulted in a crack angled at -45° with respect to the longitudinal axis of the specimen as shown in Figure 6-16a. Again, a dominant crack developed early with few secondary cracks. The suspected initiation site is shown in Figure 6-16b. Note the secondary cracks propagating at right angle to the primary crack. Figures 6-17a and 6-17b show the optical and SEM micrographs of the initiation site with no anomalous features evident other than the secondary crack.

The tensile test of Specimen 217 resulted in a crack oriented at 90° to the specimen longitudinal axis as shown in Figure 6-18. Figure 6-19 shows the optical and SEM micrographs of an initiation site exhibiting porosity which is considered typical for the test material. Two separate cracks, that eventually coalesced, and their initiation sites were found on specimen surface replicas taken during test. Figure 6-20 presents replica micrographs that show a crack evolving at one of the initiation sites with an atypical surface appearance. As shown in Figure 6-20c, a 0.25 mm (10-mil) long crack evolved after 800 cycles. Figure 6-21 shows crack growth data based on crack surface length measurements from replicas versus cyclic life.

The 90° out-of-phase tension-torsion test of specimen 216 resulted in a crack composed of straight line segments with its major portions roughly perpendicular to the longitudinal specimen axis as shown in Figure 6-22. Replicas show that three separate cracks grew simultaneously perpendicular to the longitudinal specimen axis, then joined together through crack segments that grew roughly parallel to the specimen axis. Optical micrographs of two adjacent crack segments are shown in Figure 6-23. The out-of-phase loading caused extensive rubbing of the opposing fracture surfaces which obscured most fracture surface details, making examination by SEM ineffective.

In order to examine the dislocation structures of specimen 204 (in-phase tension-torsion) and specimen 203 (pure torsion), TEM thin foils were prepared from material taken below the initiation sites. The multiaxial dislocation structure of specimen 204 shown in Figure 6-24 consists of short segments of wavy dislocations enveloping the γ' at the γ/γ' interface. The matrix itself as well as the γ' particles are virtually free of dislocations. This is in contrast to the appearance of dislocations resulting from a uniaxial $R = -1$ LCF test which generally form directional bands of short segments throughout the γ matrix between γ' particles. The multiaxial structure also differs considerably from the dislocation structure that results from a creep test which form distribution networks around γ' particles. The pure torsion baseline dislocation structure of specimen 203 is shown in Figure 6-25. The structure consists of wavy dislocation segments that are roughly parallel to one another surrounding γ' particles. This type of structure is similar to that observed in specimen 204. This observation may indicate that life modeling for multiaxial testing will require more reliance on pure torsion baseline test data.



(a)



(b)

ORIGINAL PAGE IS
OF POOR QUALITY

Figure 6-16 Multiaxial specimen 203. (+0.404% torsion; 11,224 cycles to 50% load drop).

(a) Overall view.

(b) Higher magnification view of suspected initiation site.

ORIGINAL PAGE IS
OF POOR QUALITY

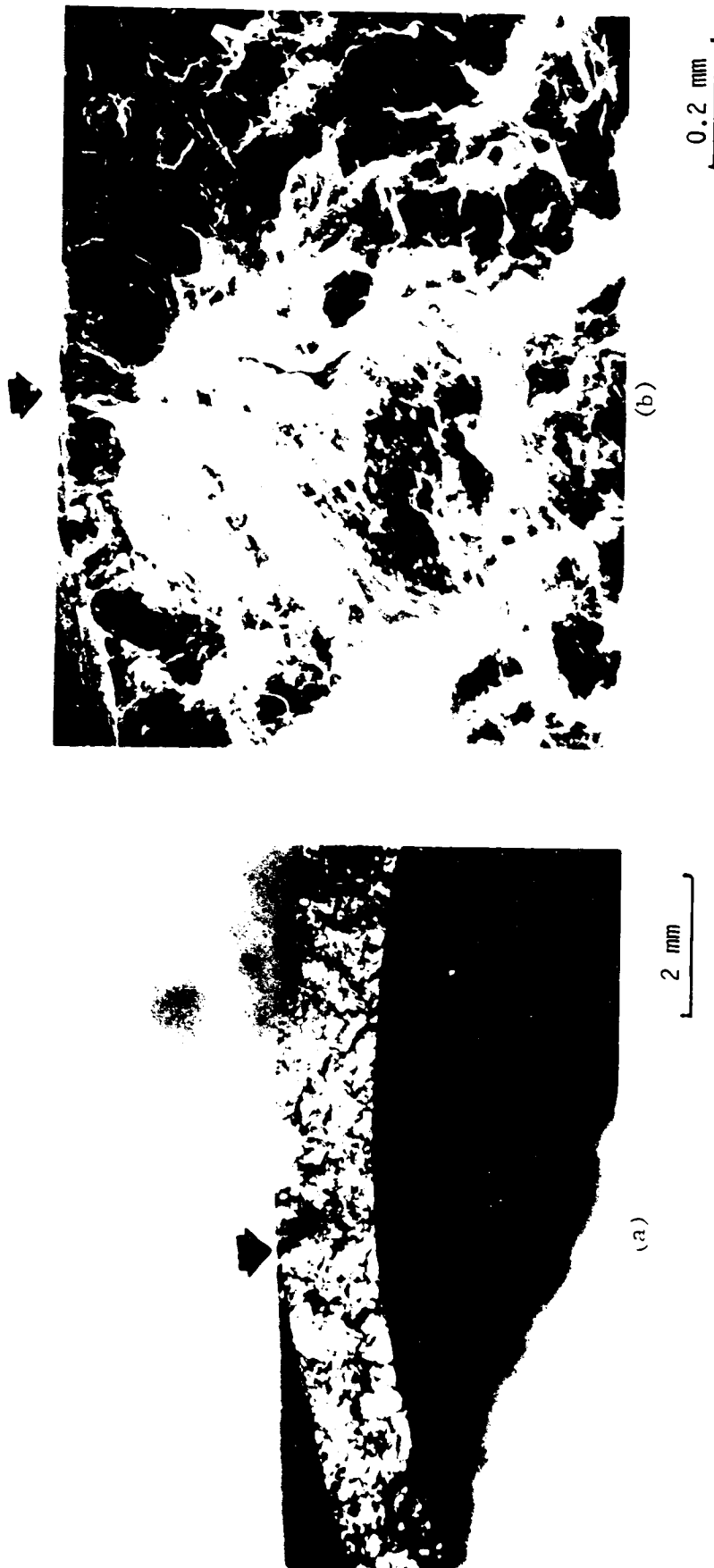


Figure 6-17 Multiaxial specimen 203 (torsion only). (a) Optical and (b) SEM micrographs of initiation site showing secondary crack perpendicular to primary crack.

ORIGINAL PAGE IS
OF POOR QUALITY

LONGITUDINAL
SPECIMEN AXIS



5 mm



1 mm

Figure 6-18 Multiaxial specimen 217 (+ 0.25% tension, 0% torsion, 2442 cycles to 50% load drop), suspected initiation site.



(a)

2 mm



(b)

100 μm

Figure 6-19 Multiaxial specimen 217 (Tension only + 0.25%, 2442 cycles 50% load drop).

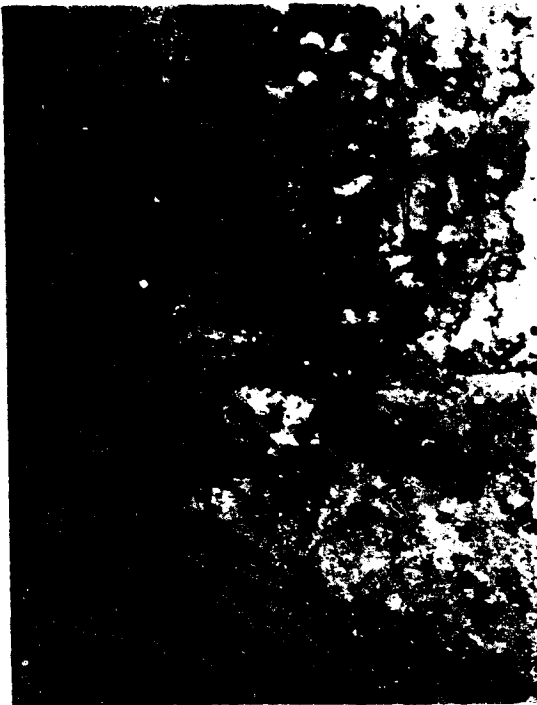
(a) Optical micrograph of area of initiation site.

(b) and (c) SEM micrographs showing porosity at initiation site as well as secondary cracking.



(a)

0.2 mm



(b)

0.2 mm



(c)

0.2 mm

Figure 6-20 Surface replicas of multi-axial specimen 217 (tension only).
Micrographs at initiation site:

- (a) At 0 cycles showing atypical surface appearance.
- (b) At 400 cycles showing small cracks had developed.
- (c) At 800 cycles showing 10 mil long surface crack.

ORIGINAL PAGE IS
OF POOR QUALITY

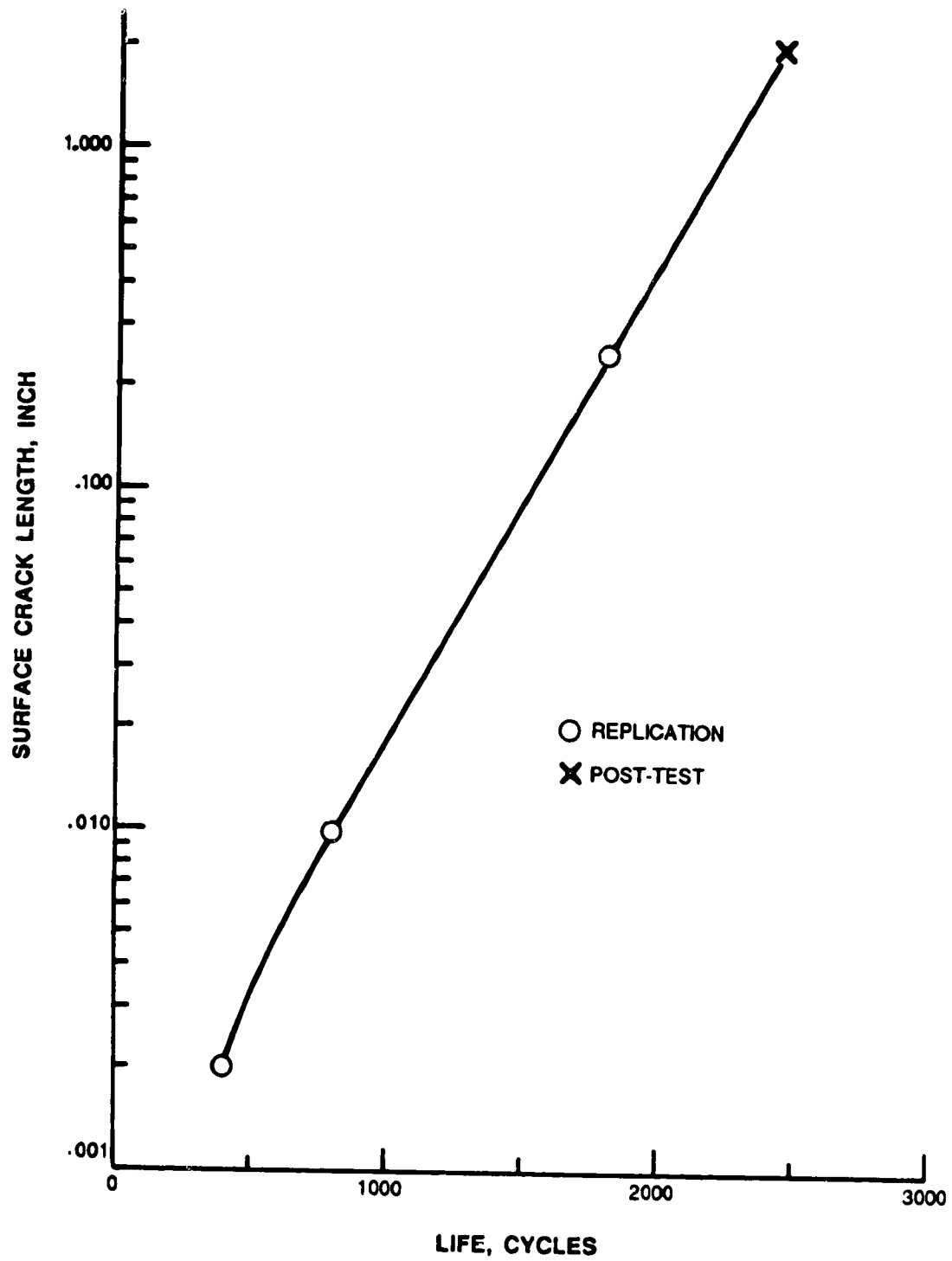


Figure 6-21 Crack Growth Data for Multiaxial Specimen 217 (tension only)

ORIGINAL PAGE IS
OF POOR QUALITY

LONGITUDINAL
SPECIMEN AXIS



5 mm



1 mm

Figure 6-22 Multiaxial specimen 216 (+0.25% tension, +0.375% torsion, 90° out of phase, 1973 cycles to 50% load drop), suspected initiation site.

ORIGINAL PAGE IS
OF POOR QUALITY



2 mm



2 mm

Figure 6-23 Multiaxial specimen 216 (tension + 0.25%, torsion + 0.375%, 90° out of phase, 1973 cycles to 50% load drop). Optical micrographs showing extensive rubbing of fracture surface features.

$g = \langle 200 \rangle$
(011)



1 μm

ORIGINAL PAGE IS
OF POOR QUALITY

$g = \langle 111 \rangle$
(011)



1 μm

Figure 6-24 Dislocation structure of multi-axial test specimen 204 using a tension strain range + 0.185% and a torsion strain range of + 0.26% in phase, (effective strain range + 0.245% at 1600°F for 1085 cycles (50% load drop).

ORIGINAL PAGE IS
OF POOR QUALITY

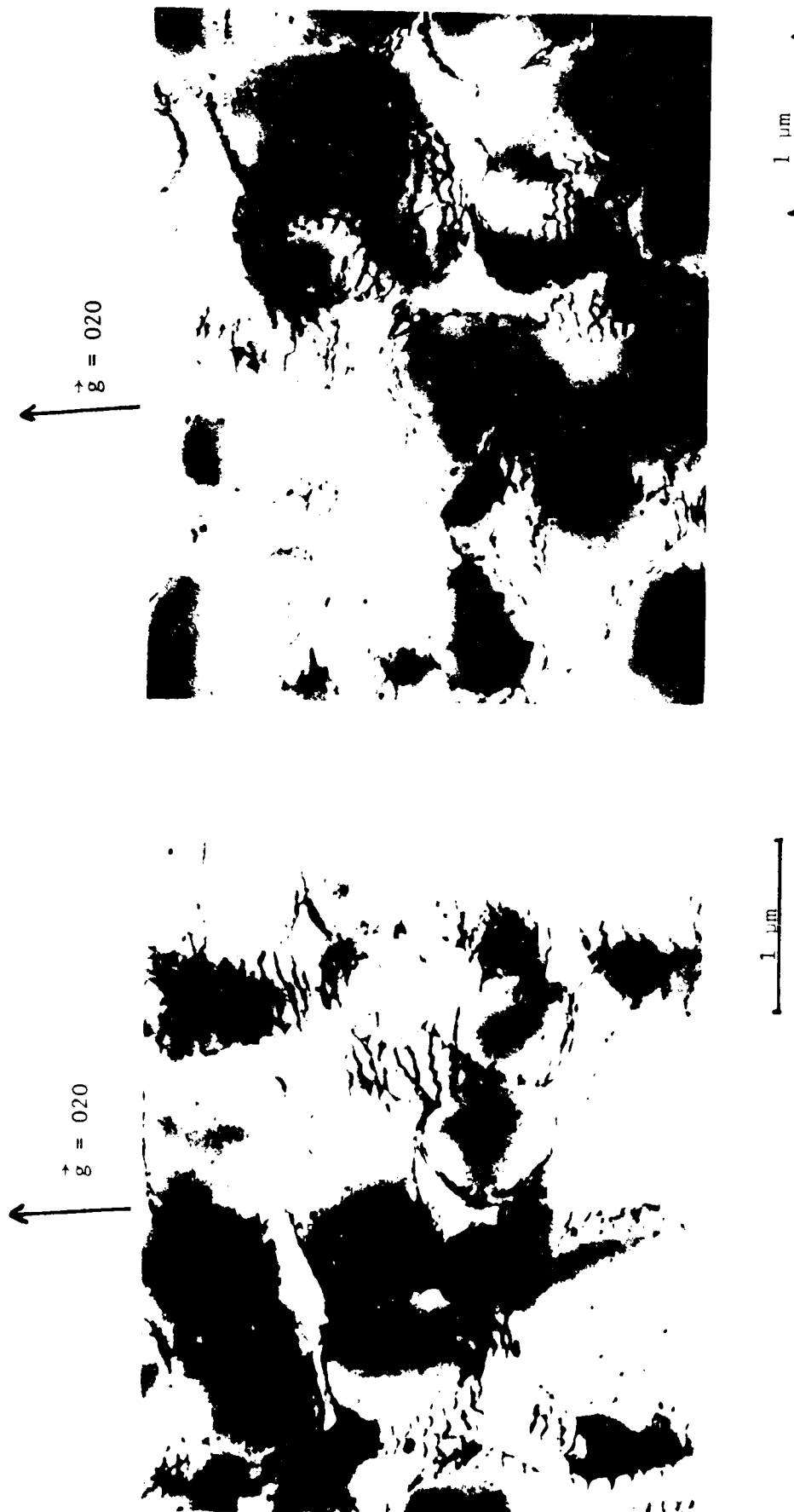


Figure 6-25 Multiaxial specimen 203 dislocation structure after pure torsion testing (torsional strain range of $\pm 0.404\%$ for 11,224 cycles 50% load drop).

6.3.3 Discussion of Results

The crack initiation lives for the four multiaxial tests presented in Table 6.2 range from 350 cycles for the in-phase tension-torsion test of specimen 204 to 8100 cycles for the pure torsion test of specimen 203. The tensile test of specimen 217 allows direct comparison with previous data obtained on solid cast uniaxial specimens tested in the base program. The crack initiation life of 1150 cycles for specimen 217 compares very closely with the 1234 cycle average life for the twelve base program specimens tested at the same conditions. This result demonstrates the capability of producing consistent fatigue data with the multiaxial test rig and specimen.

The non-proportional loading path of specimen 216 apparently caused no detrimental effect since its initiation life of 1250 cycles is consistent with the tensile test data. Damage from non-proportional loading may depend on a number of variables such as material, temperature level and strain amplitude and, therefore, be difficult to characterize. By contrast, the life of specimen 204 may have been adversely affected by the dross found at the initiation site. Subsequent to the discovery of dross in specimen 204, an inspection program was undertaken to screen the remaining twenty-two untested specimens using X-ray, fluorescent penetrant and visual inspection procedures. Although indications of minor subsurface shrinkage were found in most of the specimens, no surface or subsurface discontinuities were discovered that would compromise the integrity of future test results.

The initiation life in pure torsion was approximately 7X greater than that for pure tension despite being subjected to the same equivalent strain range. Obviously, this parameter is ineffective for correlating the multiaxial test results. It has been suggested (Ref. 6.6) that parameters based on the observed physical damage would be most suitable for correlating multiaxial fatigue behavior. Observations of cracking in these tests indicate that the fatigue cracks initiate and grow on planes perpendicular to the maximum normal strain under all loading conditions. Therefore, a single parameter that is consistent with the cracking mode, the maximum normal strain, was used to correlate the test results. Figure 6-26 shows a plot of the maximum normal strain range versus crack initiation life with the data fairly well ordered except for the dross initiated cracking of specimen 204.

Other parameters have been used to correlate the test results with little success. Figure 6-27 shows a plot of the maximum shear strain range versus crack initiation life. No correlation was obtained. Figure 6-28 shows a plot of the plastic work per cycle versus crack initiation life. Estimates for plastic work $(\Delta\sigma \times \Delta\epsilon_{in}) + (\Delta\tau \times \Delta\gamma_{in})$ were determined from cycles at approximately half-life. The torsional data point does not correlate even with the weighing factor of 1/2 applied to plastic work done by the applied shear strain as suggested by Garud (Ref. 6.5). A plot of this modified plastic work parameter versus crack initiation life is shown in Figure 6-29. The weighing factor was also applied to the tension-going plastic work per cycle estimated by $(\sigma_{max} \times \Delta\epsilon_{in}) + (\tau_{max} \times \Delta\gamma_{in})$. As shown in Figure 6-30, this parameter results in improving the correlation.

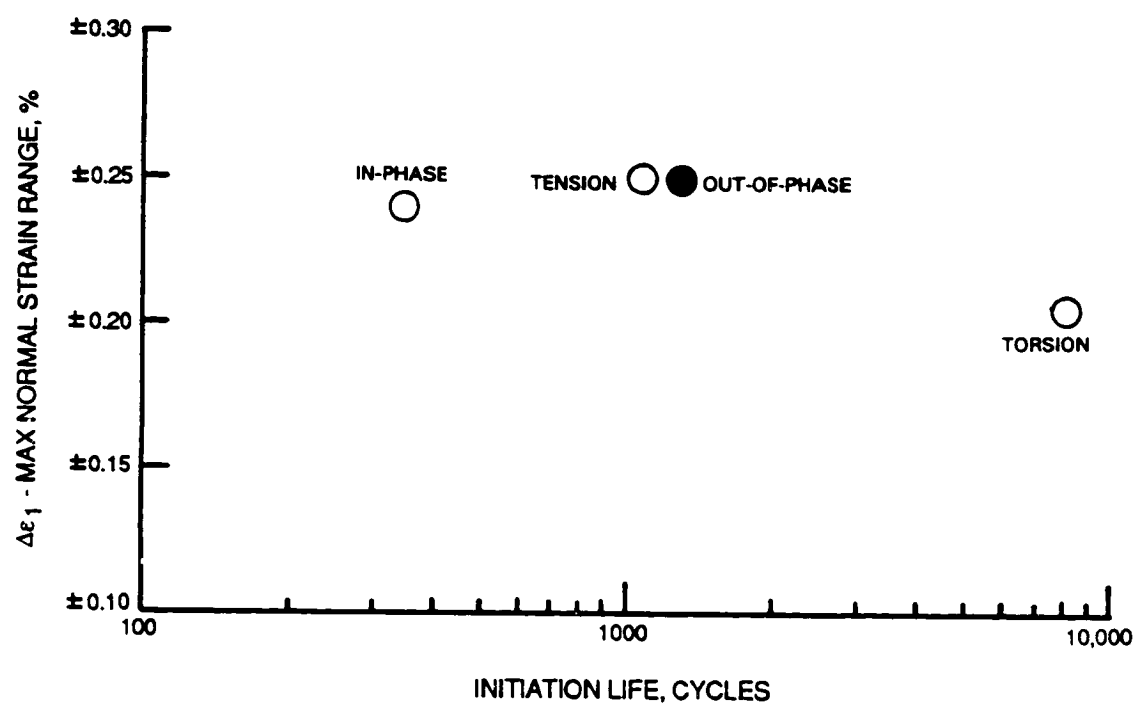


Figure 6-26 Maximum Normal Strain Range Versus Crack Initiation Life

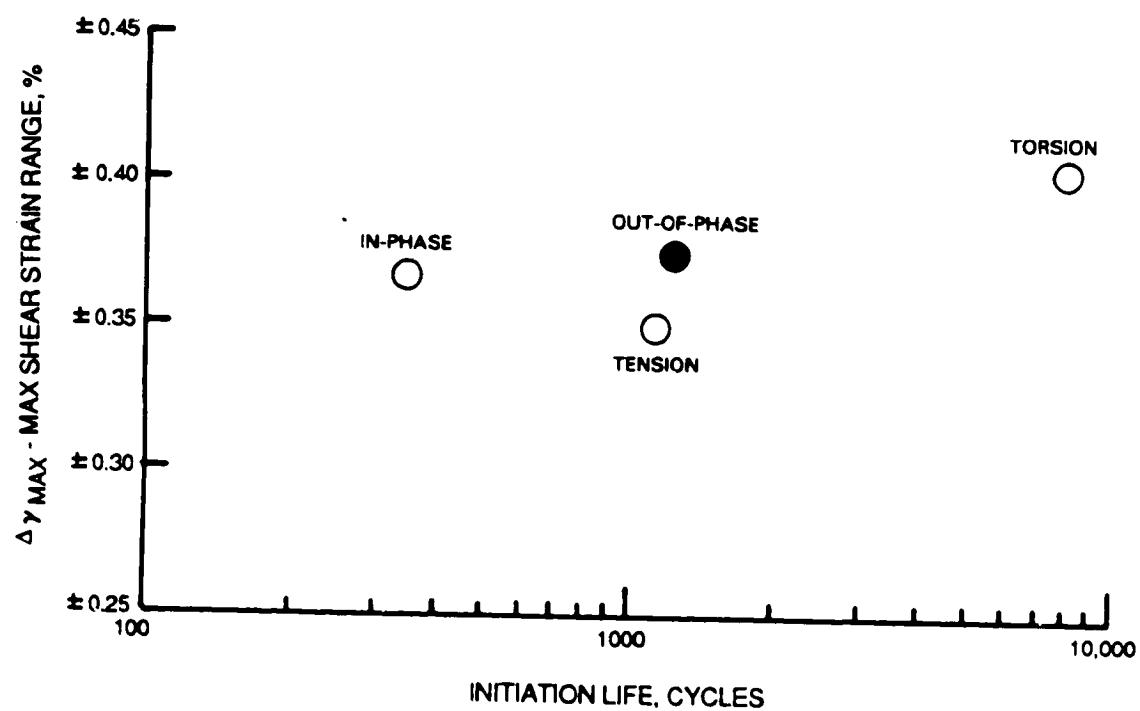


Figure 6-27 Maximum Shear Strain Range Versus Crack Initiation Life

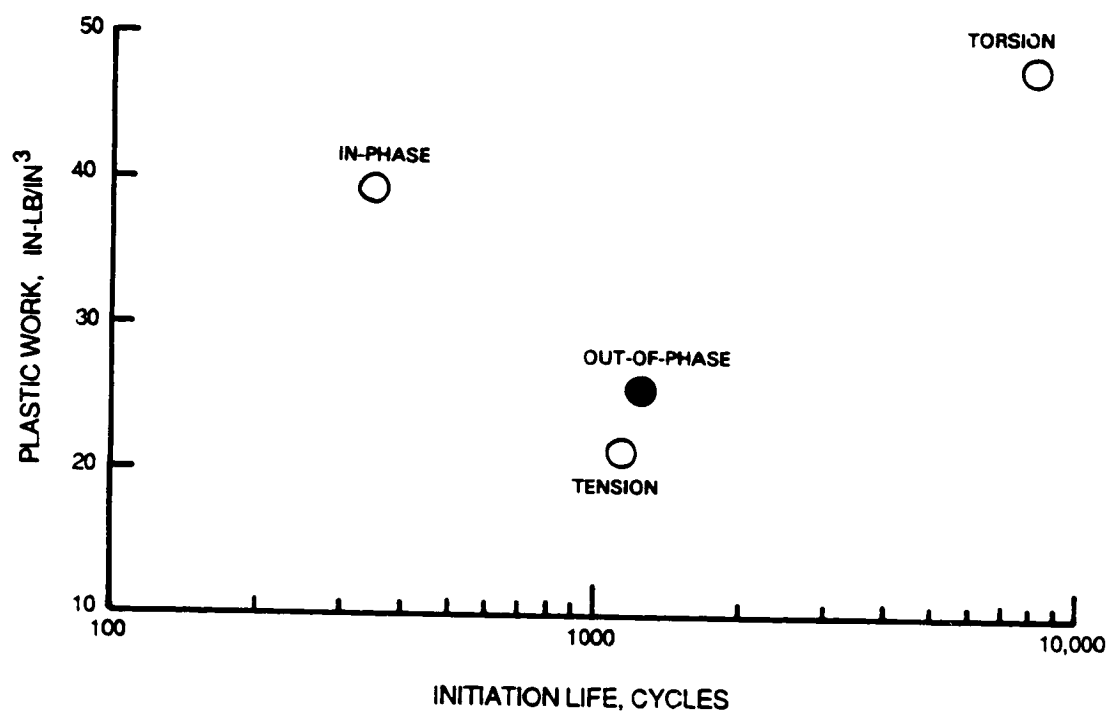


Figure 6-28 Plastic Work Versus Crack Initiation Life

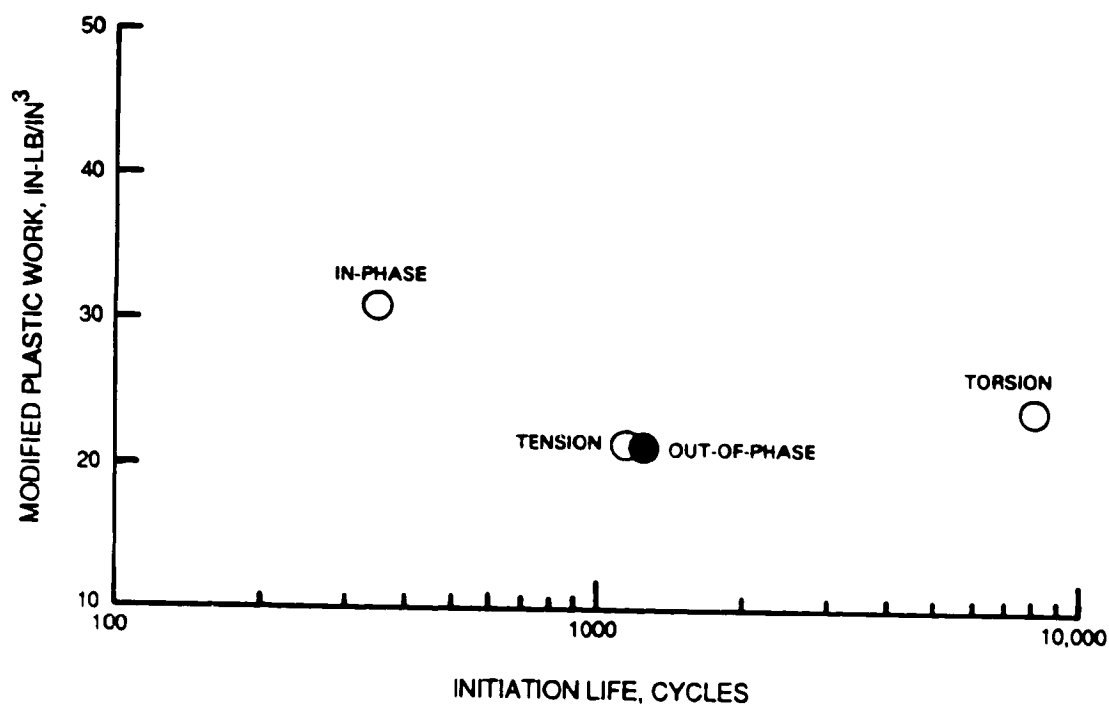


Figure 6-29 Modified Plastic Work Versus Crack Initiation Life

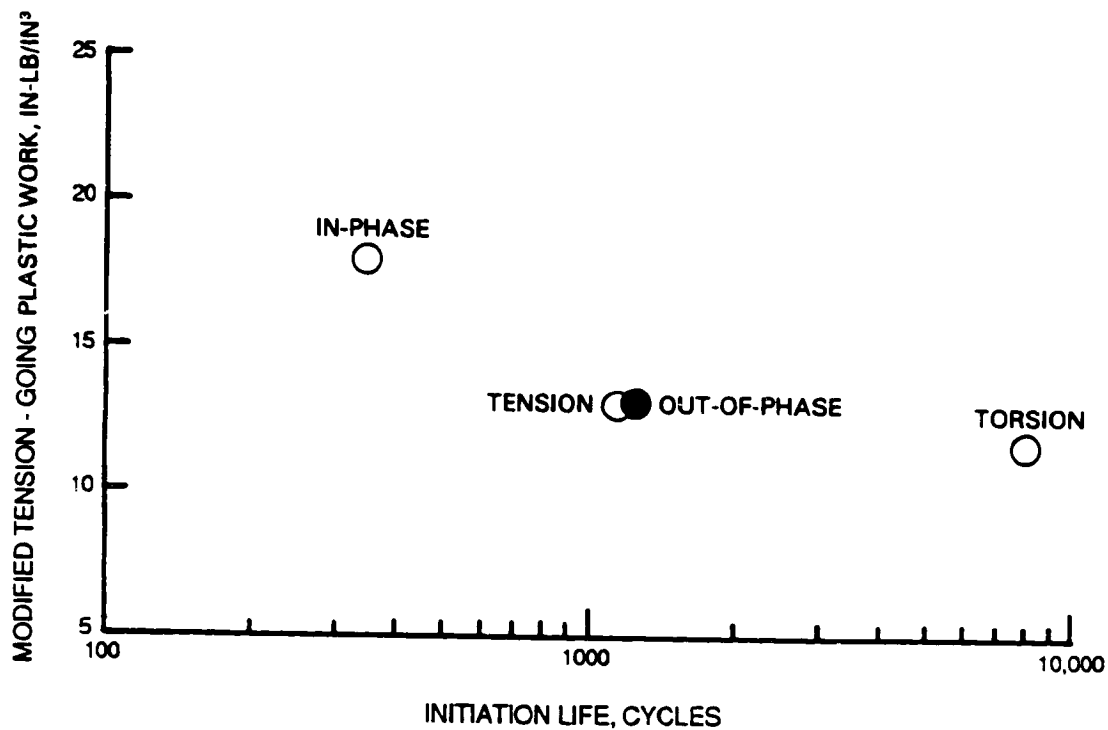


Figure 6-30 Modified Tension - Going Plastic Work Versus Crack Initiation Life

6.4 FUTURE WORK

The following work will be accomplished under Task VI:

- The multiaxial fatigue test program presented in Table 6.1 will be completed by testing twenty-two additional specimens of B1900+Hf material (PWA 1455).
- Concurrent with the tests, the physical damage processes will be determined through metallographic examinations and observations of the fatigue cracking mode.
- Additional single and multiple parameters will be investigated to characterize the multiaxial fatigue behavior.
- A multiaxial stress state creep fatigue life prediction model will be developed and verified using the specimen crack initiation data.

SECTION 7.0

TASK VII - CUMULATIVE LOADING MODEL

7.1 EXPERIMENTAL METHODS AND TEST TYPES

7.1.1 Overview of Cumulative Loading Testing

Actual gas turbine hot section components are subjected to operating conditions which include many reversals of strain within any given flight. It is therefore necessary that a practical life prediction method for such components be able to account properly for the cumulative effects of such loading. The intent of this task is to provide a body of test data for specimens subjected to various cumulative loadings and to develop a life model which can properly account for the observed effects.

A total of 50 cumulative loading tests have been completed under this task, including block, sequenced, and interrupted tests. Figure 7-1 presents a schematic diagram of each of these three test types. The block test consists of two blocks of loading (designated Block 1 and Block 2) in which all but one of the test parameters are identical. The number of Block 1 cycles is chosen to be a predetermined fraction of the continuous simple fatigue life under Block 1 conditions. The remainder of the test is then run under Block 2, in which one of the test parameters (such as strain ratio, temperature, or hold time) is changed. This type of test enables the determination of the influence of the Block 1 conditions on the fatigue life under the subsequent Block 2 cycling. It is then possible to determine if there are any interactions or ordering effects between loading blocks by comparing the test results with a linear damage accumulation rule. Thirty such block tests were completed as part of this task.

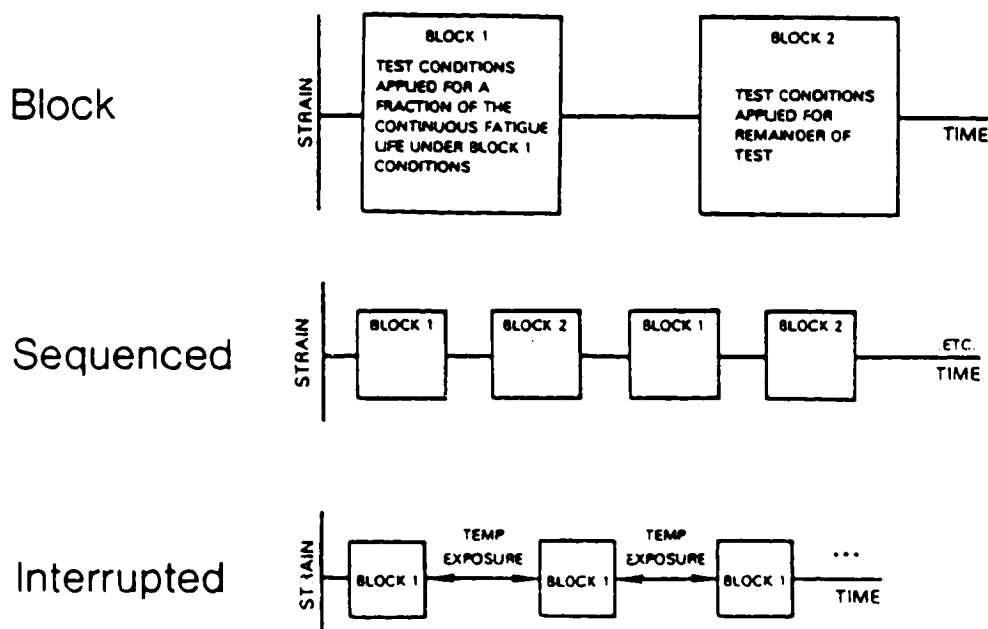


Figure 7-1 Types of Cumulative Loading Tests

The second type of test used for cumulative loading effects is the sequenced test. In this test two blocks of loading conditions are applied alternately until specimen failure. The number of cycles in each block is constant throughout the test and is chosen such that several blocks of cycles will be applied before crack initiation occurs. These tests are designed to investigate the classical pure fatigue cumulative damage problem as well as creep-fatigue ordering effects. A total of nine such tests were run under this task.

The last type of cumulative loading test used in this program is the interrupted test, which consists of blocks of cycling separated by periods of temperature exposure, either with or without static load. These tests enable investigation of the effects of periods of high temperature exposure and the material degradation that often results (e.g., overaging, changes in carbides). For some of these tests, the creep strain was permitted to accumulate during the test by re-zeroing the extensometer after the periods of temperature exposure. For other tests, however, the specimen was forced back to the original strain limits set at the beginning of the test, which meant that the creep strain did not accumulate. The third type of interrupted test is the prior creep test, in which a large fraction of the available specimen ductility is exhausted by creep testing prior to the fatigue cycling. Figure 7-2 shows a comparison of hysteresis loops which result from these three types of interrupted tests, and it is clear that understanding of the constitutive behavior of the specimen is especially important to interpretation of the results of interrupted tests. Eleven tests of this type were completed under this task. Detailed listings of the data for all 50 cumulative damage specimen tests are found in Appendix IV.

7.1.2 Experimental Procedure

All tests were conducted under strain control in the same MTS closed loop servohydraulic testing machine used for the base program tests. The gage section temperature was monitored continuously by an infrared pyrometer which provided feedback for closed loop control of an induction heating arrangement. Control signal generation was accomplished using a programmable waveform generator connected to the MTS interface system. Data acquisition was handled by a HP-9826 microcomputer interfaced to a multichannel digital voltmeter which continuously monitored the load and displacement signals. The testing utilized solid specimens of the same design used for the baseline fatigue testing. The specimens were prepared by grinding, followed by light electropolishing of the OD.

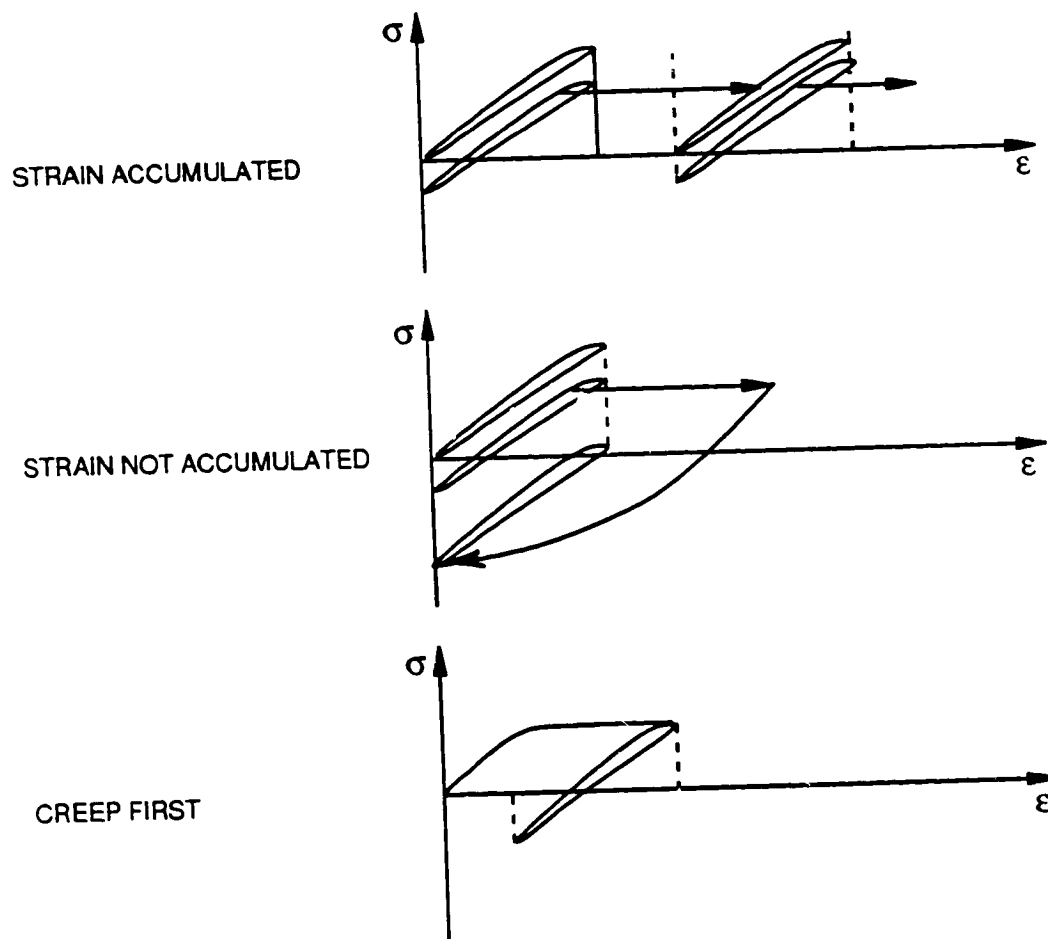


Figure 7-2 Hysteresis Loops of Interrupted Tests

7.2 BLOCK EXPERIMENTS

7.2.1 Strain Ratio Effects

The first section of Table 7-1 presents a matrix of all 15 R-ratio block tests completed under this task. This series of tests used either $R=0$ or $R=-1$ for the first block, followed by the other value for the remainder of the test. Figure 7-3 presents an interaction diagram based on the initiation lives from these tests, and some strong interactions can be clearly seen. Note that the specimens tested with 600 cycles of $R=0$ followed by $R=-1$ cycling showed much longer lives than the baseline specimens which were continuously cycled at $R=-1$. However, there was a much smaller effect with just one cycle of $R=0$, and there was a negative effect for 1200 cycles. Figure 7-4 shows a typical hysteresis response for the 600 cycle $R=0$ test, where the higher stresses during the initial block of cycles can be clearly seen. This history apparently generates a compliant dislocation network which persists throughout the remainder of test. Figures 7-5A and 7-5B show representative dislocation structures for continuous $R=0$ and $R=-1$ tests, respectively. Figure 7-5C shows the dislocation structure for a block test with 600 cycles of $R=0$, while Figure 7-5D shows the structure which results when the first 600 cycles are run with $R=-1$. Comparison of all four figures shows that, for both of the block tests, the $R=0$ dislocation structure is the dominant microstructural feature. When run first, $R=0$ cycling apparently work hardens the material for subsequent $R=-1$ cycling and consequently increases the overall life. However, $R=-1$ cycling in Block 1 does not have a hardening effect for the subsequent $R=0$ Block 2 cycling. This causes the $R=0$ type of dislocation structure to dominate the microstructure. Failure origins continued to be associated either with carbides, as in Figure 7-6, or with porosity, as in Figure 7-7.

TABLE 7-1
BLOCK LOADING TEST MATRIX

No. Tests	Strain Range (%)			R			Temp (C°)		Wave			Freq (CPM)		Median Lives (Cycles)	
	.3	.5	.8	1/2	-1	0	538	921	T-M	T-M	C-M	10	0.5	Initiation	50% Load Drop
2		X			50	BAL		X		X		X		1646	3990
3		X			600	BAL		X		X		X		1114	2700
4		X			BAL	1		X		X		X		1015	3830
4		X			BAL	600		X		X		X		3130	7196
2		X			BAL	1200		X		X		X		1079	4905
2		X				X	BAL	600		X		X		7290	11950
2		X				X	BAL	1200		X		X		6430	11690
3		X				X	3500	BAL		X		X		4908	7125
2*		X				X	7000	BAL		X		X		4419	8035
2		X				X		X	BAL	1200		X		1880	6250
1		X				X		X		1200	BAL	X		1561	2330
1		X				X		X		BAL	400	X		1092	4200
1		X				X		X		BAL	100	X		234	2919
1		X				X		X			BAL	X		446	1438

* One specimen failed during 538°C block. results shown are for specimen 1320

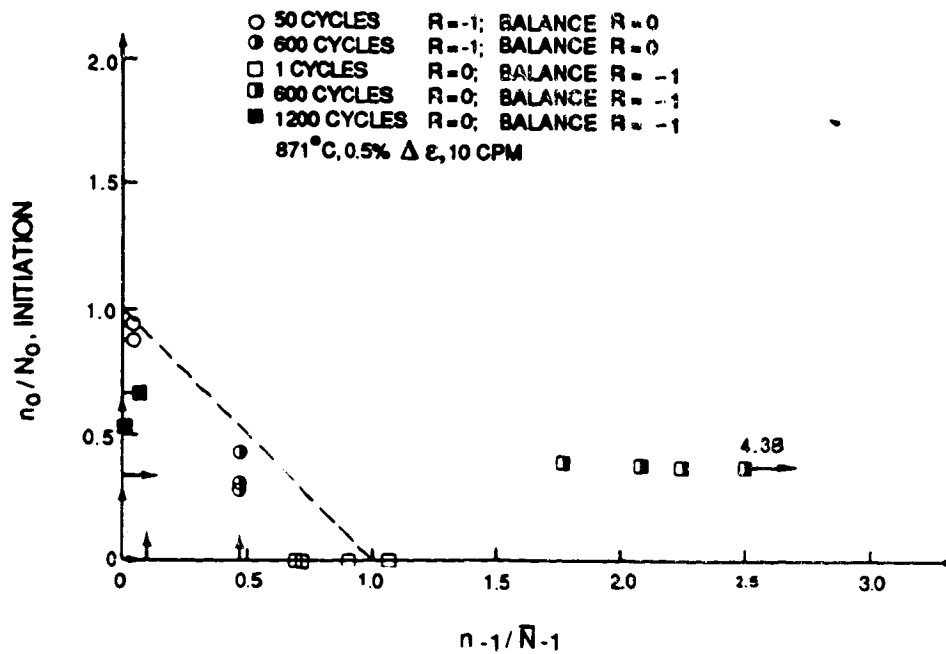


Figure 7-3 Interaction Diagram for Strain Ratio Block Tests

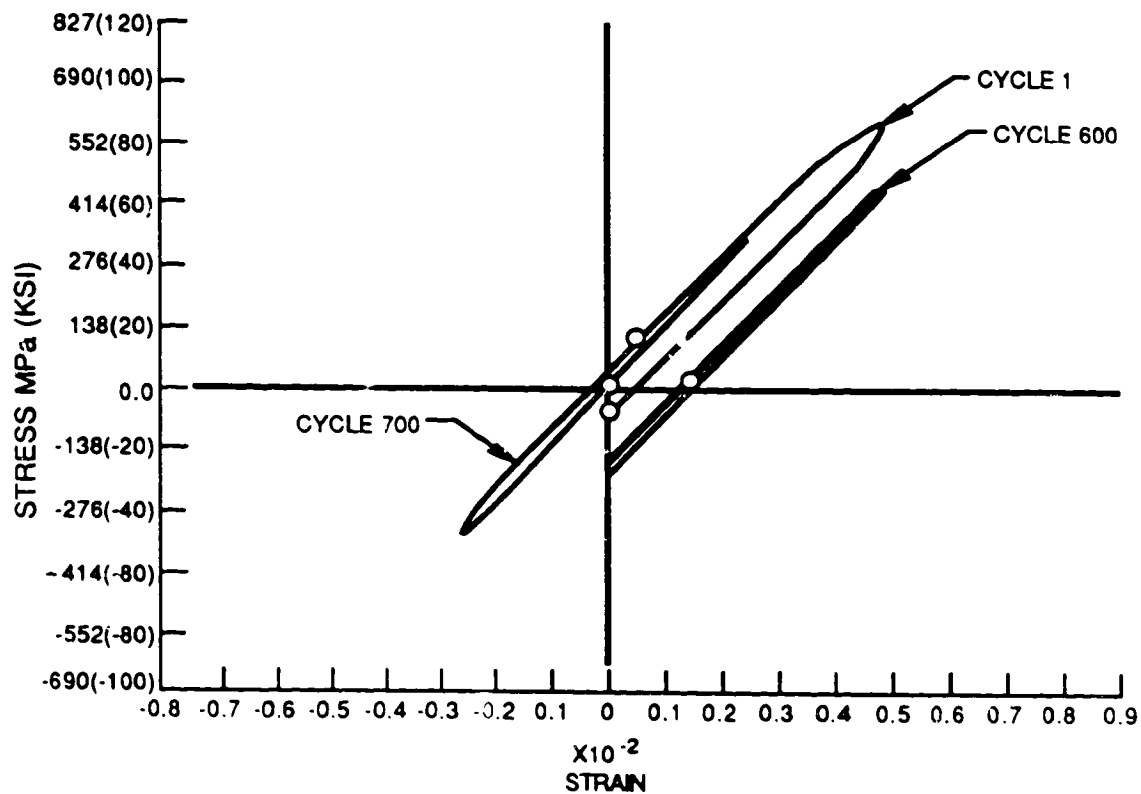


Figure 7-4 Hysteresis Response for Strain Ratio Block Test
(R = 0 followed R = -1)

ORIGINAL PAGE IS
OF POOR QUALITY.

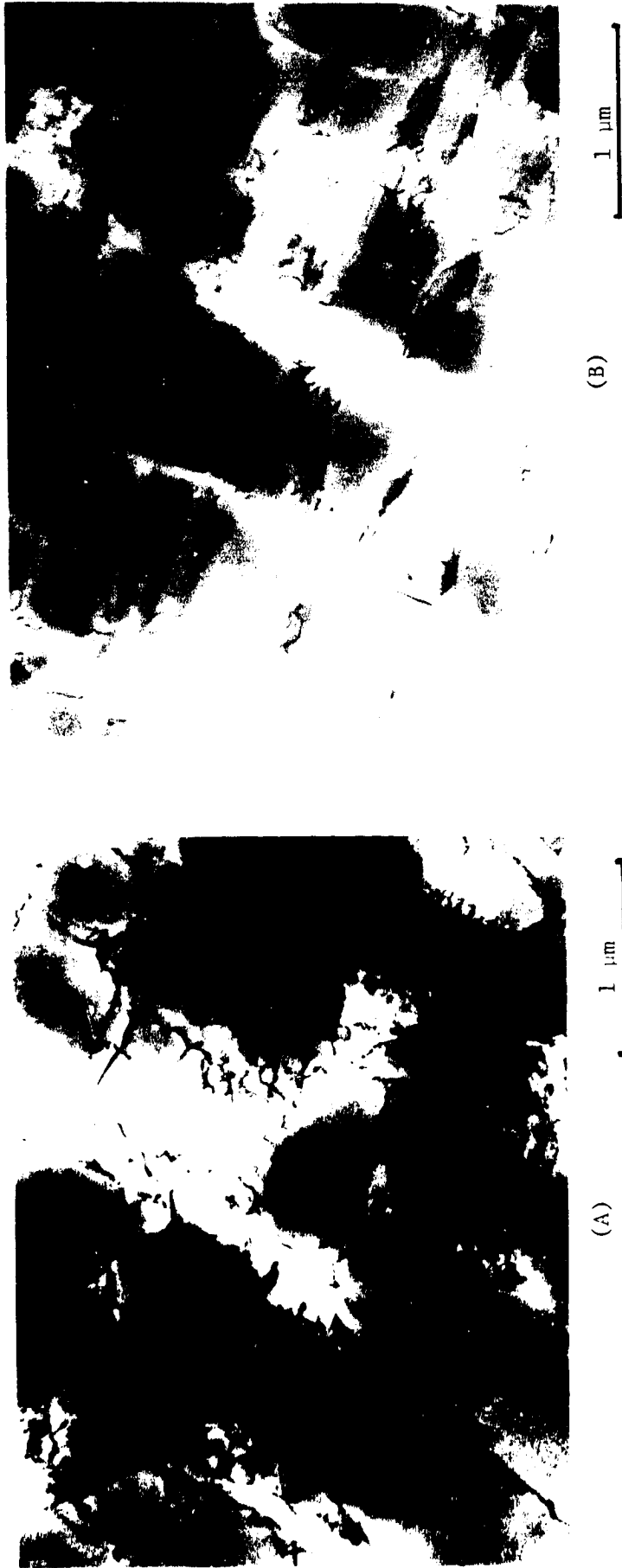


Figure 7-5 Dislocation structures after LCF testing 871°C (1600°F).

(A) Continuous $R = 0$, initiation life = 1558 cycles, 50% load drop life = 3500 cycles, Specimen 14A.

(B) Continuous $R = -1$, initiation life = 1127 cycles, 50% load drop life = 2,965 cycles.



(C)



(D)

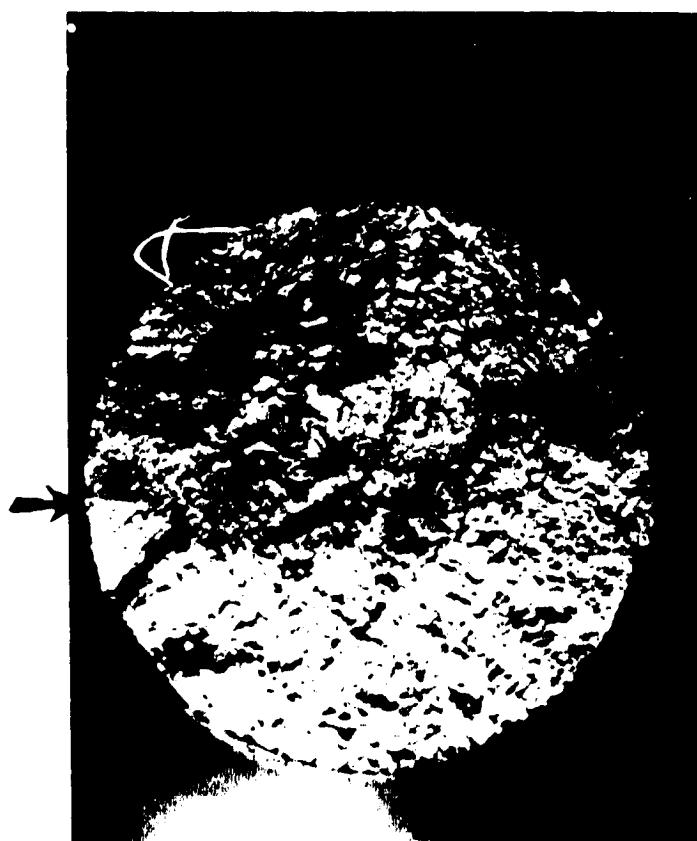
Figure 7-5 Dislocation structures after LCF testing 871°C (1600°F).
(Cont'd)

(C) Block loading, 600 cycles at $R = 0$ for block 1 and remainder of life at $R = -1$ for Block 2. Initiation life = 3393 cycles, 50% load drop life = 7800 cycles, Specimen 10D.

(D) Block loading, 600 cycles at $R = -1$ for Block 1 and remainder of life at $R = 0$ for Block 2. Initiation life = 1114 cycles, 50% load drop life = 2700 cycles, Specimen 8A.

ORIGINAL PAGE IS
OF POOR QUALITY

ORIGINAL PAGE IS
OF POOR QUALITY



(a)



(b)

Figure 7-6 Fracture Surface of Specimen 8A After Block Loading LCF Test.



(a)

2000 μm



(b)

200 μm

Figure 7-7 Fracture Surface of Specimen 10D After Block Loading LCF Test.

ORIGINAL PAGE IS
OF POOR QUALITY

7.2.2 Temperature Block Tests

The second type of block loading test used in this task was the temperature block test. Here, the first block was run for a predetermined number of cycles at either 538°C (1000°F) or 871°C (1600°F); the other temperature was then used for the remainder of the test. The middle section of Table 7-1 lists the actual conditions used for the 9 tests of this type completed under this task, and Figure 7-8 shows an interaction diagram based on the initiation lives. Note that one specimen, 132C, failed prematurely at 4950 cycles during the 538°C. Initial block of cycling; a mean stress of about +100 MPa developed during the test, lowering the life. The tendency of the data is to lie well above the linear interaction line, suggesting that there is little influence of initial cycling at one temperature on subsequent cycling at the other temperature. One explanation is that the damage is accumulating by different mechanisms at these two temperatures, hence the second block of cycling essentially starts at zero damage for its mechanism. This indicates the need to recognize explicitly the micromechanisms which are active at a given temperature in the formulation of advanced life prediction models.

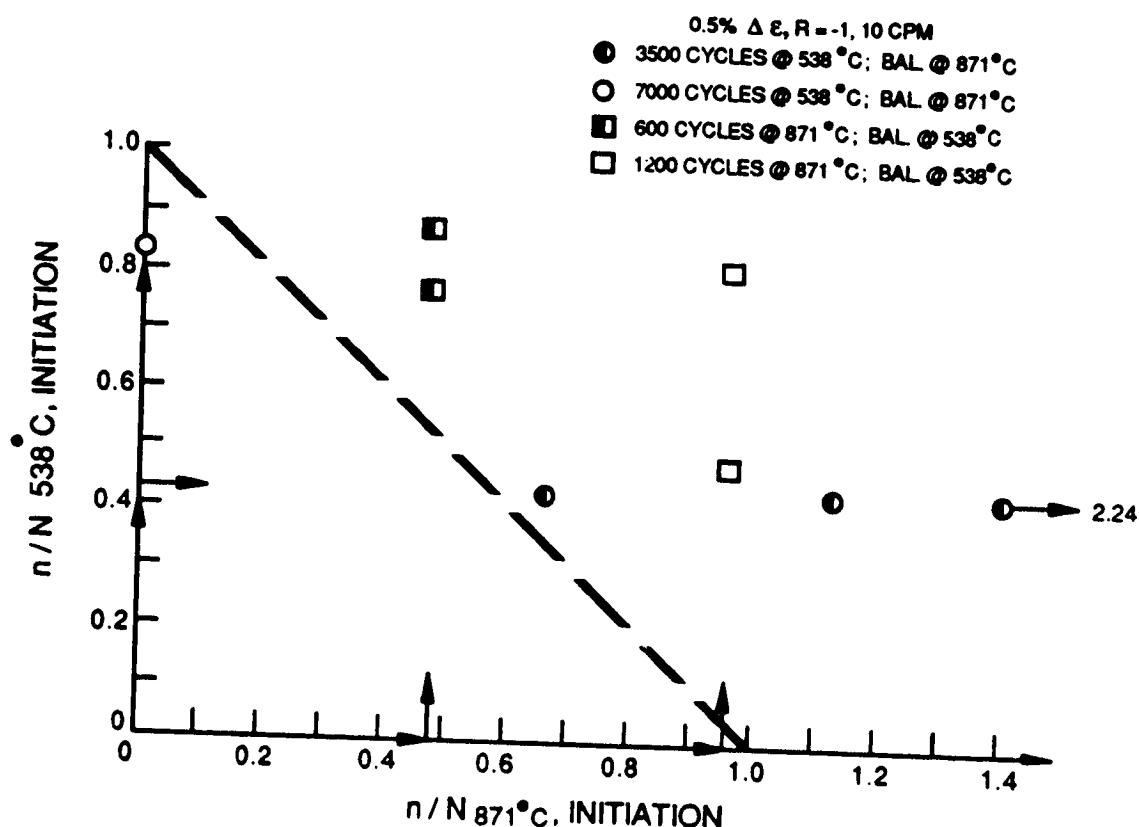


Figure 7-8 Interaction Diagram for Temperature Block Tests

In an effort to understand this behavior, several specimens were examined metallographically, including block temperature specimens as well as specimens which were continuously cycled at the two temperatures involved. Optical examinations of fracture surfaces have shown that 871°C (1600°F) fractures are much rougher than 538°C (1000°F) fractures, as can be seen in Figure 7-9. It was hoped that this fact could be used when examining the fracture surface morphology to determine exactly how much crack growth had occurred during each of the blocks of cycles. The optical micrographs of Figure 7-10 are from specimens 9D and 132D which both had 538°C (1000°F) for Block 1, followed by 871°C (1600°F) for Block 2. Both have smooth fracture surfaces near the initiation sites due to the low temperature cycling. Surrounding this is a rougher fracture surface representing the high temperature cycling, which is in turn followed by the overload failure area. The smooth area radiating from the initiation site of specimen 132D is larger than that of specimen 9D due to the greater number of 538°C (1000°F) Block 1 cycles used for specimen 132D (7000 vs. 3500). The transition from crack growth at 538°C (1000°F) to growth at 871°C (1600°F) is also quite evident in the SEM micrographs of Figure 7-11. However, the crack lengths measured using this method were consistently longer than the lengths determined using surface replication. For example, the optical technique indicated that the crack in specimen 132D had grown to a surface length of 2.79 mm. (0.110 in.) at the end of 7000 cycles at 538°C (1000°F), whereas the surface replica showed a length of only 2.03 mm. (0.080 in.). Estimates of initiation life for these tests were based on both types of measurements where possible, but the surface replica results were used in those cases where discrepancies existed.

7.2.3 Hold Time Block Tests

The third and final type of block test used in this task was the hold time block test. Here, one block was run with a one minute hold time, either in tension or compression, while the other block was continuously cycled. The last section of Table 7-1 contains the actual conditions run for the 6 specimens in this series of block tests. Figure 7-12 shows an interaction diagram of the initiation lives of these same specimens, and it is apparent that the hold time cycling had the greatest influence on the overall initiation lives. Also, the hold time lives were slightly lower than the median lives observed during the baseline testing (note the two data points along the abscissa; these cracked during the hold time Block 1 portion of the test).

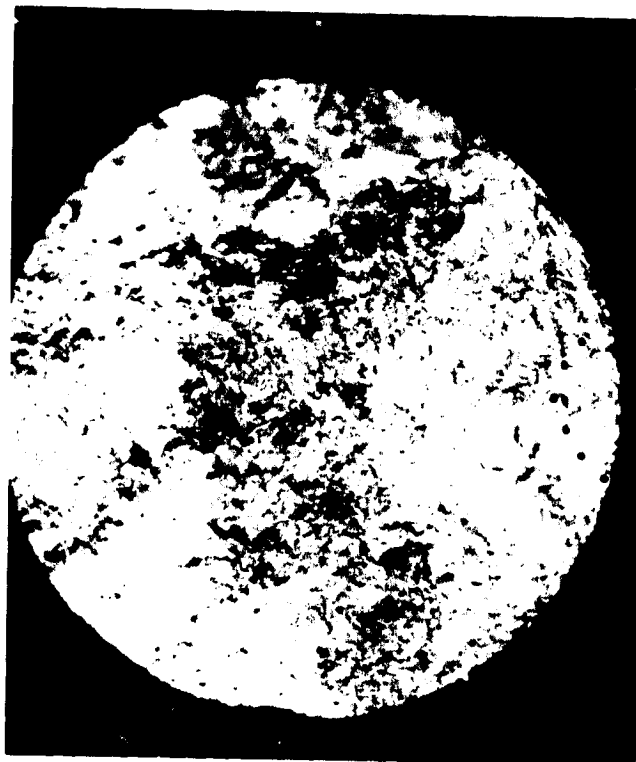
Typical dislocation structures for tension and compression hold time tests are shown in Figures 7-13A and 7-13C, respectively, and the dislocation structure of a continuously cycled $R=-1$ test is shown in Figure 7-13B for comparison. It is seen that a marked difference exists between the short segmented dislocation structure of the continuous test and the creep-like structures of the hold tests. This indicates that the apparent linearity of the hold time block test damage accumulation may be due to cancellation of the effects of two different damage mechanisms.

ORIGINAL PAGE IS
OF POOR QUALITY



(A)

11X



(B)

11X

Figure 7-9 Fracture surfaces after continuous LCF testing to 50% load drop.

(A) 538°C, $\Delta\epsilon_t = \pm 0.25\%$, $R = -1$, 10 cpm for 12,560 cycles,
Specimen 4D.

(B) 871°C, $\Delta\epsilon_t = \pm 0.25\%$, $R = -1$, 10 cpm for 2,965 cycles,
Specimen 6D

ORIGINAL PAGE IS
OF POOR QUALITY



(A)

11X



(B)

11X

Figure 7-10 Fracture surfaces after temperature block testing to 50% load drop. $\epsilon_{total} = 0.5\%$, $R = -1$, 10 cpm. Block 1 is 538°C (1000°F) and Block 2 is 871°C (1600°F).

(A) 3500 cycles for Block 1 and remaining 3625 for Block 2, Specimen 9D.

(B) 7000 cycles for Block 1 and remaining 1035 cycles for Block 2, Specimen 132D.



(A)

100 μm



(B)

20 μm

Figure 7-11

Specimen 132D, 7000 cycles for Block 1, 538°C (1000°F) and remaining 1035 cycles for Block 2, 871°C (1600°F).

(A) SEM micrograph showing the transition between crack propagation at 538°C (1000°F) Block 1, and 871°C (1600°F) Block 2.

(B) Detailed view of 538°C (1000°F) fracture surface.

(C) Detailed view of 871°C (1600°F) fracture surface.



(C)

20 μm

ORIGINAL PAGE IS
OF POOR QUALITY

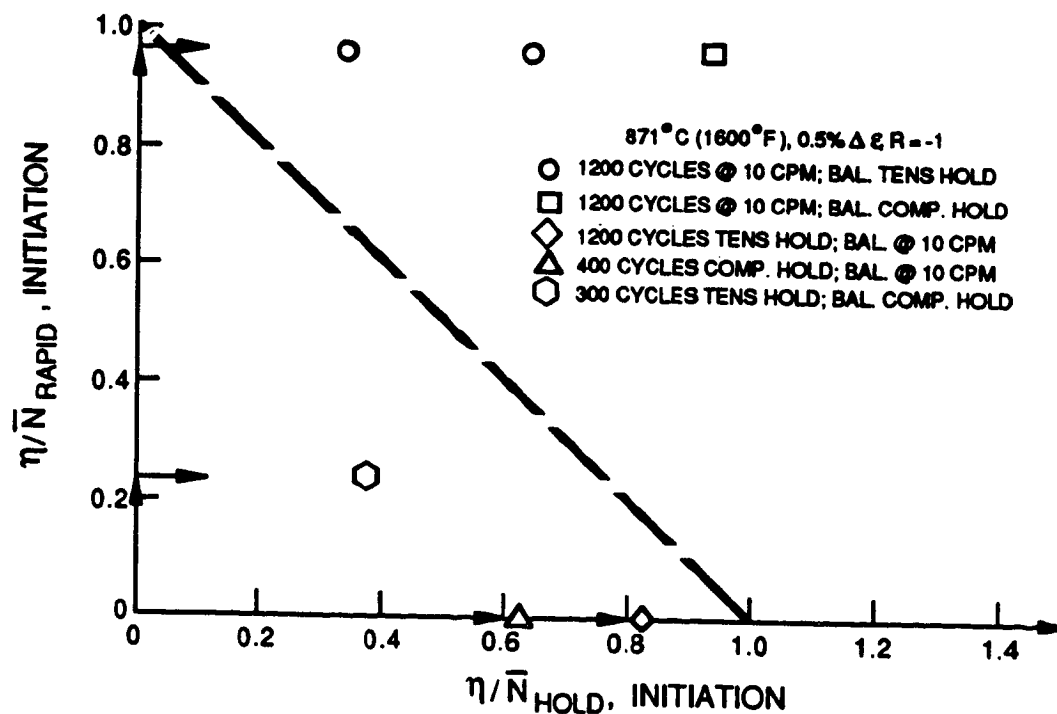


Figure 7-12 Interaction Diagram for Hold Time Block Tests



(A)

1 μm



(B)

2 μm



(C)

1 μm

Figure 7-13 Dislocation structures after being LCF tested at 871°C (1600°F), 10 cpm, $\epsilon_{\text{total}} = 0.5\%$, $R = -1$.
(A) Tension hold for 60 sec. at 0.25% ϵ .
(B) No hold.
(C) Compression hold for 60 sec. at -0.25% ϵ .

ORIGINAL PAGE IS
OF POOR QUALITY

7.3 SEQUENCED EXPERIMENTS

7.3.1 Strain Rate Sequenced Tests

Table 7-2 summarizes the results of the nine sequenced tests completed as part of this task, including five strain rate block tests and four strain range block tests. The strain rate tests all used a strain range of 0.5% and $R=0$, with a variable number of cycles at 10 CPM for Block 1 and a fixed number of cycles (5) at 0.5 CPM for Block 2. Note that 100 cycles at 10 CPM in Block 1 produces equal time for each block, while 5 cycles in Block 1 gives equal cycles in each block. The test with 15 cycles in Block 1 was designed to produce approximately equal damage in each block. Figure 7-14 presents an interaction diagram of the initiation life results of the rate sequenced tests. It can be seen that the data is clustered around the linear accumulation line, although the equal damage test (15 cycles in Block 1) is somewhat above the line. Figure 7-15 shows the dislocation structure for specimen 103C, which was tested with 5 cycles in Block 1. Note that the appearance of this structure is similar to that of previously examined specimens run continuously at $R=0$; no additional effects could be noted which could be attributed to the sequenced rates used for this test.

TABLE 7-2
SEQUENCED SPECIMEN TEST MATRIX

No. Tests	Fixed Conditions				Block 1 Conditions	Block 2 Conditions	Median Lives	
	Temp (C°)	Strain Range(%)	R	Strain Rate (sec ⁻¹)			Initiation (Cycles)	50% Load Drop (Cycles)
2	871	0.5	0	Variable	100 cyc @ .00167 sec ⁻¹	5 cyc @ .000083 sec ⁻¹	1240	4905
1					15 cyc @ .00167 sec ⁻¹	" "	1591	3060
2					5 cyc @ .00167 sec ⁻¹	" "	754	2129
1	871	Variable	-1	.00167	3 cyc @ .36%	1 cyc @ .45%	6792	20275
1					3 cyc @ .40%	1 cyc @ .50%	3040	7680
2					10 cyc @ .50%	1 cyc @ .80%	599	1617

7.3.2 Strain Range Sequenced Tests

Table 7-2 also lists the data for the four strain range sequenced tests completed as part of this task. For these tests, Block 1 consisted of a number of cycles at a lower strain range followed by a single cycle at a higher strain range. The number of cycles in the first block was chosen to give approximately equal amounts of damage in the two blocks. All tests utilized a strain ratio of -1 and a frequency of 10 CPM. Figure 7-16 presents an interaction diagram for these tests based on both initiation and separation lives, and the degree of non-linearity is seen to depend on the strain ranges used. The low strain ranges produce damage sums higher than 1, and as the strain ranges increase, the damage sum becomes smaller. Note also that, based on separation lives, the higher strain ranges produced damage sums less than one. This serves to highlight once again how the definition of "initiation" affects the interpretation of the test data.

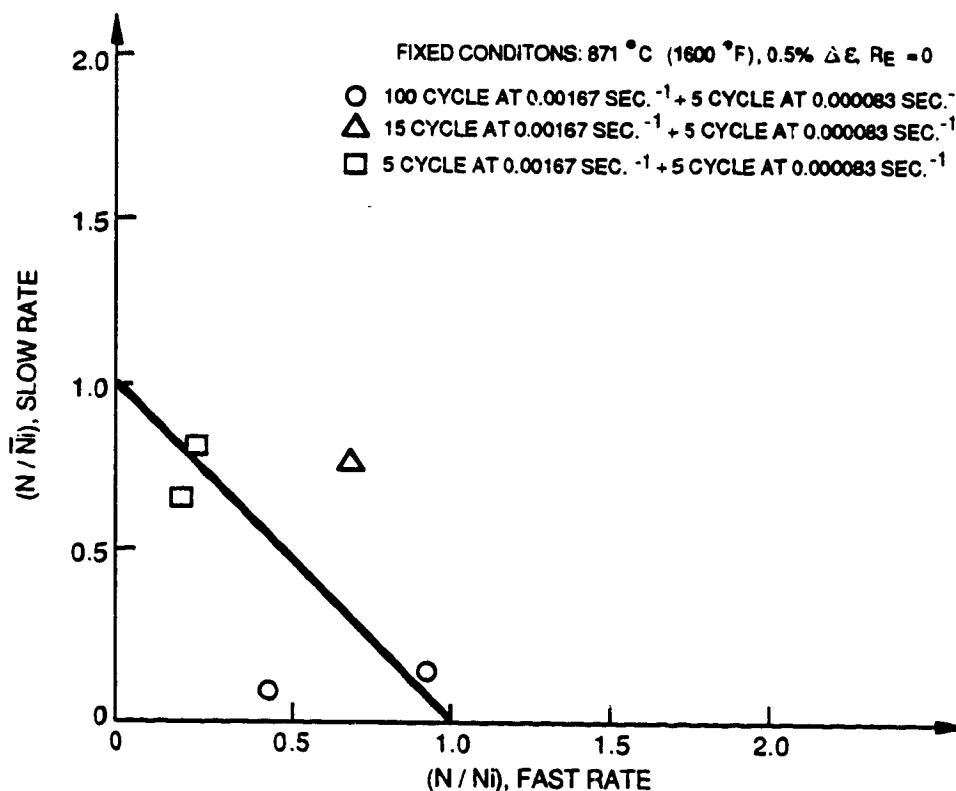


Figure 7-14 Interaction Diagram for Initiation Life Strain Rate Sequenced Tests

Figure 7-17 shows the dislocation structure of specimen 128D, which was tested with 3 cycles at 0.4% for Block 1, followed by one cycle at 0.5% for Block 2. This structure is markedly different from the bands of short segments previously observed in specimens tested continuously at a fixed strain range using $R=-1$. The structure of this sequenced test bears some resemblance to that resulting from creep rather than fatigue. No factors have yet been pinpointed that will explain this difference in dislocation structure.

7.4 INTERRUPTED EXPERIMENTS

7.4.1 Tests with Interspersed Exposure Time

The first section of Table 7-3 presents the series of six tests run using interspersed periods of temperature exposure. As in other cumulative loading tests, the periods of exposure and the associated load levels were chosen to produce approximately equal fractions of damage due to both fatigue and creep. Figure 7-18 shows the interaction diagram for these tests, using time as the correlating parameter for the amount of exposure time. All of the data points are well below the linear accumulation line, indicating that the time to failure is apparently reduced by this type of test. However, Figure 7-19 shows the interaction based on total creep strain instead of time as the correlating parameter. Here the damage sums are somewhat higher, although most of the data are still below the linear line. This leads to the conclusion that creep strain would be better than creep time as a correlating parameter for interrupted tests.



1 μm



1 μm

Figure 7-15 Typical dislocation structure after sequenced testing at 871°C (1600°F), 0.5% total strain, $R = 0$, using two different frequencies (cycles for Block 1 at 10 cpm and 5 cycles for Block 2 at 0.5 cpm). Specimen 103C, initiation life = 833 cycles, 50% load drop life = 2,688 cycles.

ORIGINAL PAGE IS
OF POOR QUALITY

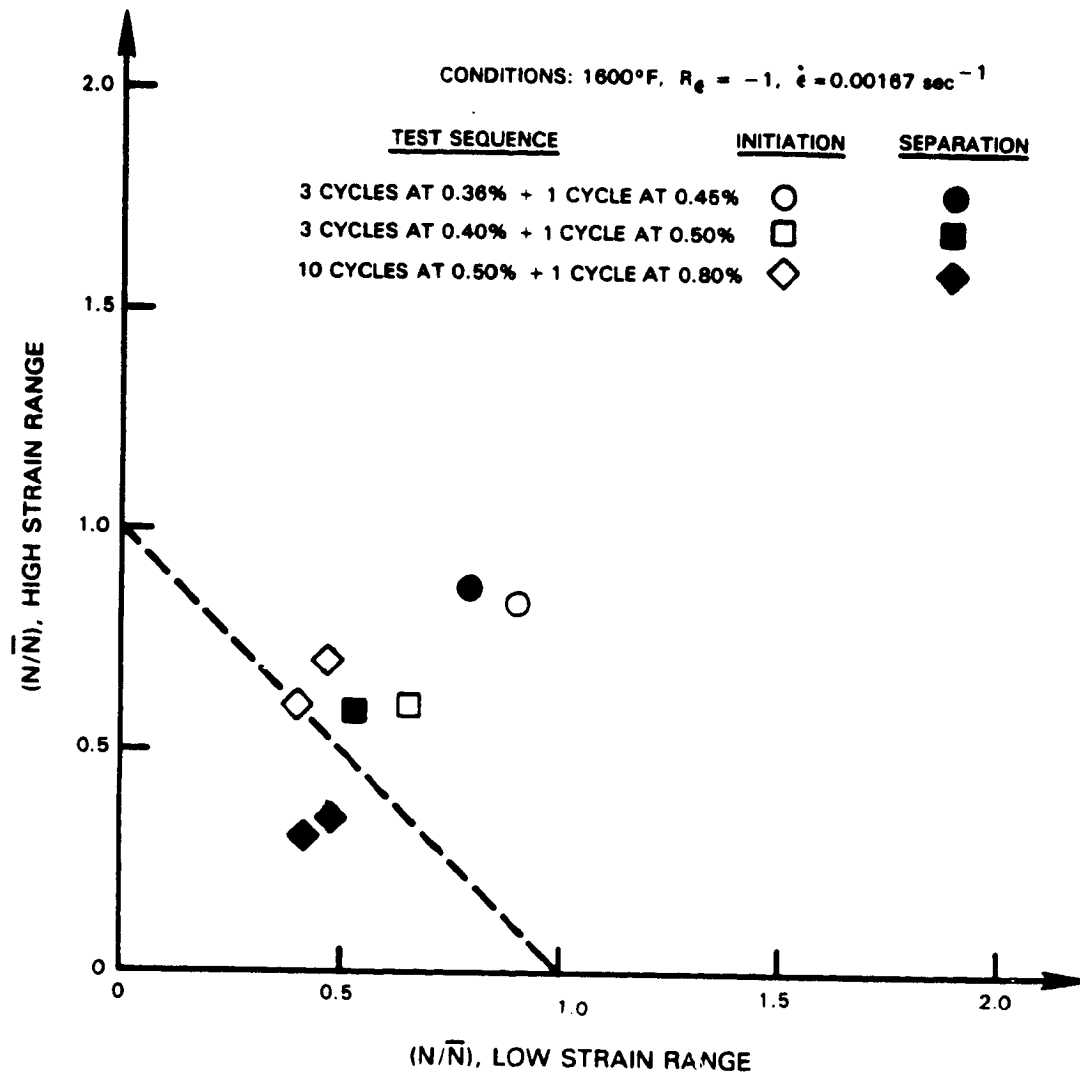


Figure 7-16 Interaction Diagram for Variable Strain Range

TABLE 7-3
INTERRUPTED SPECIMEN TEST MATRIX

No. Tests	Temp (°C)	Block 1 Conditions	Block 2 Conditions	Median Lives	
				Initiation (Cycles)	50% Load Drop (Cycles)
1	871	200 cycles at 0.5%, R=0, 10 CPM	1 hour at no load	1280	4000
2	871	200 cycles at 0.5%, R=0, 10 CPM	1 hour at 428 MPa (62 Ksi), Strain not accumulated	687	1300
2	871	200 cycles at 0.5%, R=0, 10 CPM	1 hour at 428 MPa (62 Ksi), Strain accumulated	539	1020
1	871	200 cycles at 0.5%, R=0, 10 CPM	0.5 hour at 428 MPa (62 Ksi), Strain accumulated	480	1000
2	871	Creep to 0.75% at 517 MPa (75 Ksi)	0.5%, R=1/3, 10 CPM	1587	3733
3*	871	Creep for 10 hours at 428 MPa (62 Ksi)	0.5, R=0, 10 CPM	327	135

* Two specimens failed during creep; results shown are for specimen 130°C

ORIGINAL PAGE IS
OF POOR QUALITY

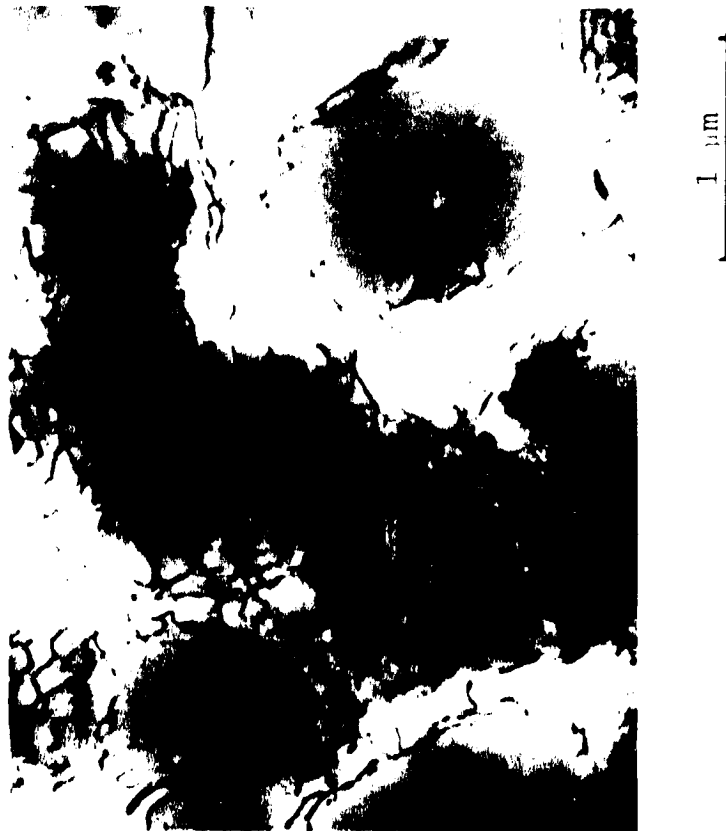


Figure 7-17 Typical dislocation structure after sequenced testing at 871°C (1600°F), 10 cpm, $R = -1$, using two different strain ranges (3 cycles for Block 1 at 0.4% and 1 cycle for Block 2 at 0.5%). Specimen 128D, initiation life = 3,040 cycles, 50% load drop life = 7,680 cycles.

INTERACTION DIAGRAM - INTERRUPTED TESTS

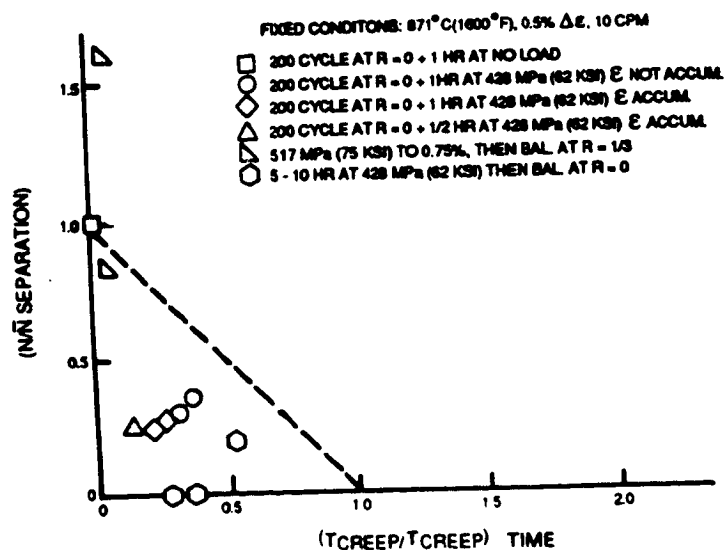


Figure 7-18 Interaction Diagram - Interrupted Tests

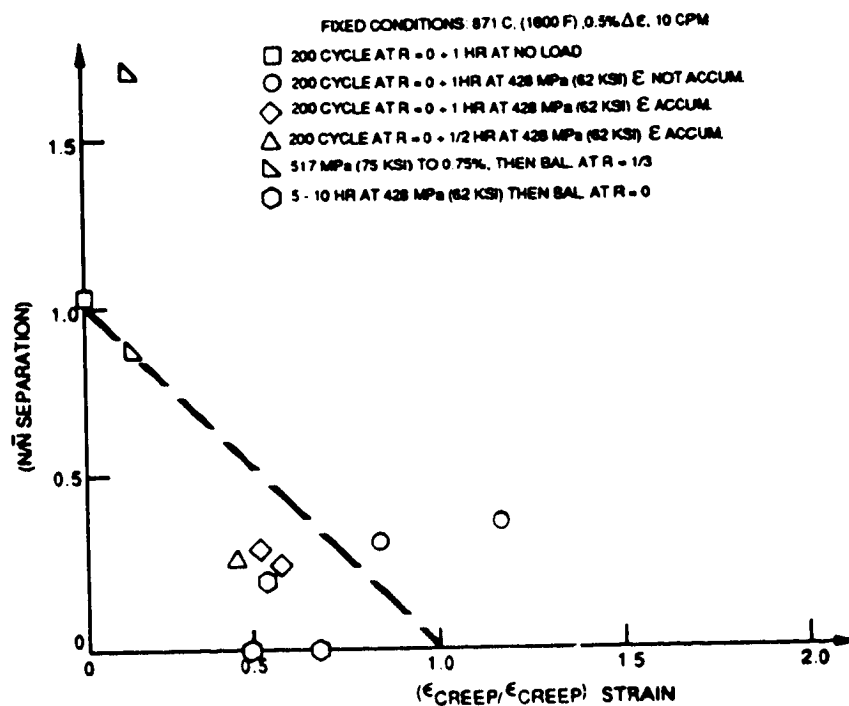


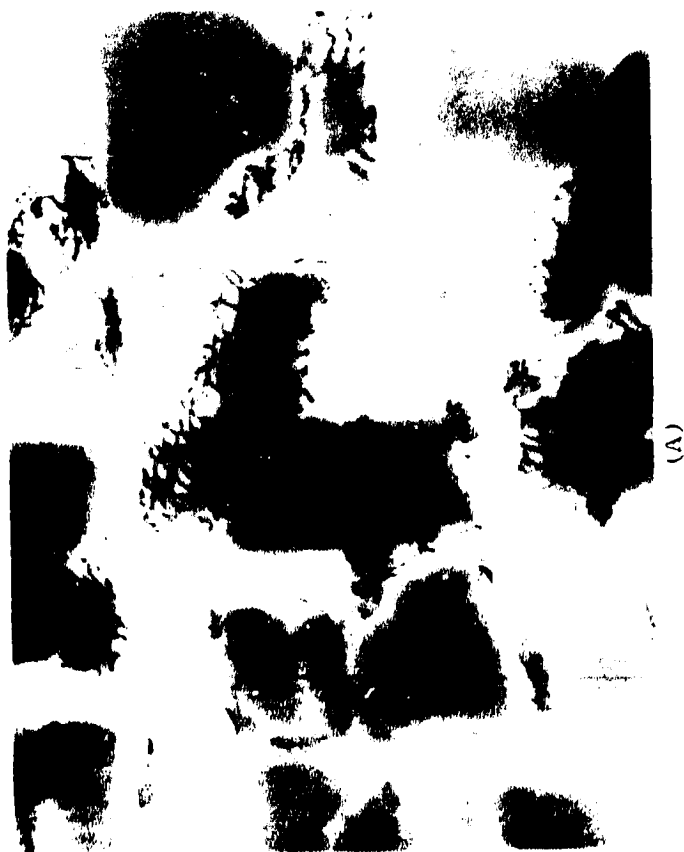
Figure 7-19 Interaction Diagram - Interrupted Tests

Various micrographic examinations were completed on these interrupted test specimens. Optical examination of the fracture surface morphologies revealed transgranular failure modes for the no-load holds, and intergranular failure modes for the 428 MPa (62 KSI) holds (for both accumulated strain and non-accumulated strain tests). The microstructure of the no-load hold sample, specimen 107B, is shown in Figure 7-20A, and the structures of the specimens with holds are shown in Figure 7-20B for non-accumulated strain tests and Figure 7-20C for accumulated strain tests. Note that the no-load hold test has a much lower dislocation density than the microstructures of the specimens which had 428 MPa (62 KSI) during the hold. The structures of the specimens with the loads during holds are indicative of creep, with high densities of dislocations surrounding the gamma prime particles. As would be expected, this creep damage exhausts the ductility available for fatigue and results in lower specimen lives.

7.4.2 Creep First Tests

The second section of Table 7-3 lists the data for the five specimens tests which were run using simple creep conditions for the first part of the test followed by fatigue cycling for the remainder of the test. The creep conditions were designed to exhaust all of the primary creep strain and some fraction of the secondary creep strain. The fatigue limits were set to maintain the same maximum stress levels used for the creep portion of the test. The data are shown in Figures 7-18 and 7-19 along with the interspersed exposure data, so the comments made regarding the use of creep strain as a correlating parameter also apply to the creep-first tests.

Specimen 138 was examined using both optical and SEM techniques. Figure 7-21 shows that the crack propagation mode was mixed transgranular/intergranular, and both carbide and porosity were present at the initiation site. Thin foil analysis revealed the dislocation structures shown in Figure 7-22, which closely resemble that produced by pure creep (networks surrounding gamma prime particles). However, the effect on the subsequent fatigue life was negligible despite this obvious change in microstructure.



(A)

1 μm



(B)

1 μm



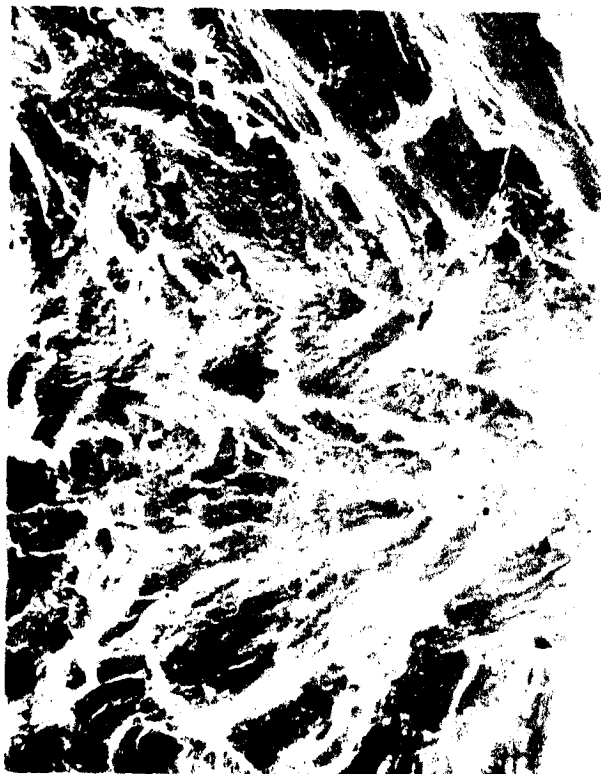
(C)

Figure 7-20 Dislocation structure after interrupted tests.

- (A) 200 cycles at $\epsilon_r = 0.5\%$, $R = 0$, then hold for 1 hr. at zero load, 50% load drop life = 4,000 cycles, Specimen 107B.
- (B) 200 cycles at $\epsilon_r = 0.5\%$, $R = 0$, then hold for 1 hr. at 428 MPa (62 Ksi), strain not accumulated, 50% load drop life = 1,400 cycles, Specimen 107B.
- (C) 200 cycles at $\epsilon_r = 0.5\%$, $R = 0$, then hold for 1 hr. at 428 MPa (62 Ksi), strain not accumulated, 50% load drop life = 1,100 cycles, Specimen 108B.

ORIGINAL PAGE IS
OF POOR QUALITY

ORIGINAL PAGE IS
OF POOR QUALITY



origin (b)

100X

Figure 7-21

Fracture surface of Specimen 13B after being LCF tested at 871°C (1600°F), crept to 0.75% strain first, $\Delta\epsilon_c = 0.5\%$, $R = 1/3$, 10 cpm for 2515 cycles (50% load drop).

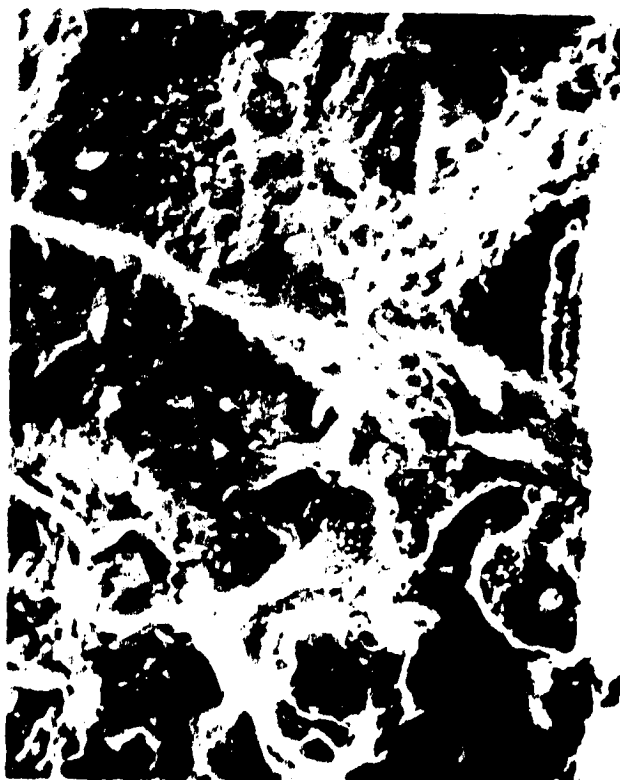
(a) Optical fractography (mixed).

(b) & (c) SEM showing porosity and carbide as crack initiation site.



(a)

11X



(c)

400X

ORIGINAL PAGE IS
OF POOR QUALITY

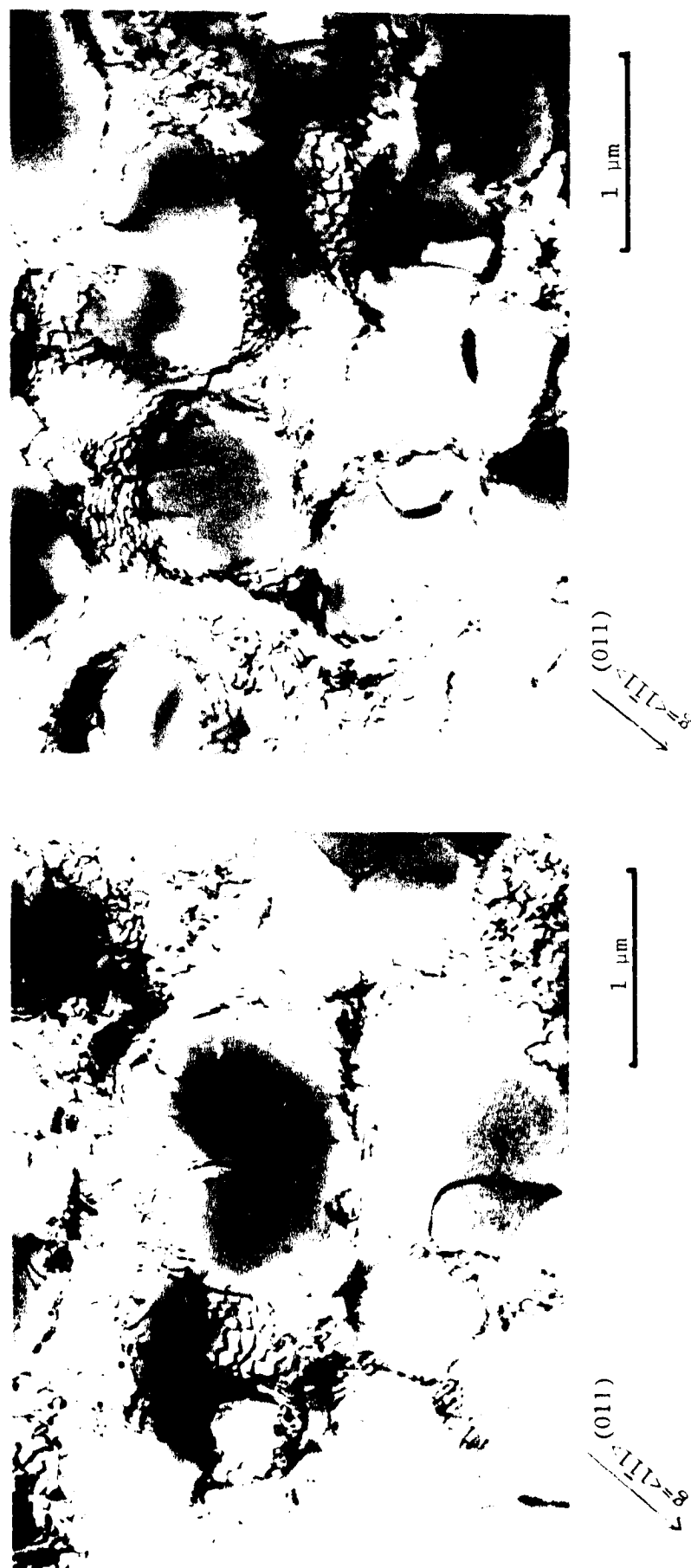


Figure 7-22 Dislocation structure of Specimen 13B, creep first to 0.75% 517 MPa at 871°C, (1600°F.75Ksi), ~1/8 hr, then LCF tested at 871°C (1600°F), $\Delta\epsilon_t = 0.25$ to 0.75%, 10 cpm for 2515 cycles (50% load drop).

7.5 MODIFICATIONS TO CDA LIFE PREDICTION MODEL

7.5.1 Overview of Current Cumulative Damage Life Prediction Methods

Because of the importance of cumulative damage life predictions in actual service components, many different methods have been advanced for this purpose. Although this section is by no means an exhaustive review of these, it does serve to show the complexity of the issue and some of the currently popular methods.

Perhaps the most widely used method is that of Palmgren-Miner, often referred to as "Miner's Rule" (Ref. 7.1, 7.2). This rule simply states that damage accumulates linearly, with failure occurring when the sum of the damage fractions exhausted in the various blocks of loading equals one. The simplicity of this rule allows it to be readily applied to design calculations, and it has been shown to be conservative for many situations. The universal nature of this rule is shown by the fact that the straight line representing this rule on an interaction diagram is usually the standard reference for other methods. However, there are many cases where data do not follow this "rule", and this has led to the development of methods which can account for such effects.

Some of the more popular rules in use today which can account for non-linear effects include the Double Linear Damage Rule (Ref. 7.3, 7.4) and the Continuous Damage Mechanics method (Ref. 7.5). Both of these can properly predict sequence effects (high-low and low-high) and mean stress effects for arbitrary groupings of cycles. Other methods have also been advanced to account for such effects, including modified versions of Miner's Rule to account for mean stress and fatigue strength reducing factors (Ref. 7.6) or probabilistic measures of material properties (Ref. 7.7). The accumulated hysteresis energy approach can produce non-linear cumulative loading predictions when used with cyclic deformation properties which vary during the test (Ref. 7.8).

Non-linear damage accumulation effects can also be predicted by assuming that the damage occurs as both surface layer damage and bulk damage (Ref. 7.9). This type of concept becomes even more useful when combined with some means of tracking the loading history of the area in question and including the effect of this on the fatigue capability of the material (Ref. 7.10).

Other researchers have focused on the need to define exactly what the concept of "damage" means. Many different material properties are affected as the test progresses, and these changes have been used to predict two-level block tests (Ref. 7.11). In the high temperature regime, particular attention must be paid to how creep damage is included (Ref. 7.12). Finally, the possibility of damage accumulation by several completely different damage mechanisms must be considered and properly accounted for in practical life prediction methods (Ref. 7.13).

7.5.2 Non-Linear CDA Life Prediction Model

During the course of the work under this task, it became clear that it would be necessary to modify the CDA life prediction model to allow damage to accumulate non-linearly in order to be able to predict all the various effects from the specimen tests. This involved the addition of two modifications to the original form of the CDA model: the concept of ductility fraction, and the non-linear rate modifier function, $G(N/N_i)$.

The ductility fraction concept permits the primary creep strain ductility to vary during the course of the test by bringing it under the integral. The ductility fraction, f_ϵ , is defined as the fraction of the available ductility which has been consumed:

$$\text{Ductility Fraction, } f_\epsilon = \frac{\text{Ductility Exhausted}}{\text{Available Ductility}}$$

The equation used to calculate this quantity may be written as follows, using CDA nomenclature:

$$f_\epsilon = \int_0^N \left(\frac{1}{\bar{\epsilon}_p} \right) \left(\frac{dD}{dN} \right)_{\text{Ref}} F(\sigma_T, \Delta\sigma) dN \quad (1)$$

where:

$$F(\sigma_T, \Delta\sigma) = \left(\frac{\sigma_T}{\sigma_{TR}} \right) \left(\frac{\Delta\sigma}{\Delta\sigma_R} \right) + \left[\left(\frac{\Delta\sigma_R}{\Delta\sigma} \right) \left(\frac{\sigma_T}{\sigma_{TR}} \right) \right]^{B'} \left[\left(\frac{t}{t_r} \right)^{C'} - 1 \right]$$

It can be seen that when f_ϵ reaches 1, N will equal the predicted initiation life, N_i . Note also that the current initial ductility is now inside the integral, which permits the algorithm to switch from one loading condition to another which has a different initial ductility.

We may also rewrite equation 1 to perform the integration over f_ϵ instead of N , and at the same time introduce a non-linear function $G(N/N_i)$ which has the property that its integral over the interval from 0 to 1 is always 1, no matter what values are chosen for its constants:

$$N_i = \int_0^1 \left[\frac{\bar{\epsilon}_p}{\left(\frac{dD}{dN} \right)_{\text{Ref}}} F(\sigma_T, \Delta\sigma) \right] G\left(\frac{N}{N_i}\right) df_\epsilon \quad (2)$$

The function $G(N/N_i)$ chosen for the initial trials of this method is a combination of a power law and a linear function:

$$G\left(\frac{N}{N_i}\right) = (1 - LF)(M + 1) \left[1 - \left(\frac{N}{N_i}\right)\right]^M + LF \quad (3)$$

Another possible function would be one derived from the fatigue portion of the continuous damage model by Chaboche:

$$G\left(\frac{N}{N_i}\right) = (1 - \alpha)(\beta + 1) \left[1 - \left(\frac{N}{N_i}\right)\right]^\beta \left[1 - \left(1 - \left(\frac{N}{N_i}\right)\right)^{\beta + 1}\right]^{-\alpha} \quad (4)$$

A comparison of these two functions is shown in Figure 7-23, where two sets of constants are used to show the variations possible with the combined power and linear law. This form (equation 7.3) was chosen for the final CDA life predictions for the specimen tests in this task, with the exponent $M=4.5$ and the linear fraction $LF=0.001$ (to prevent numeric problems during integration).

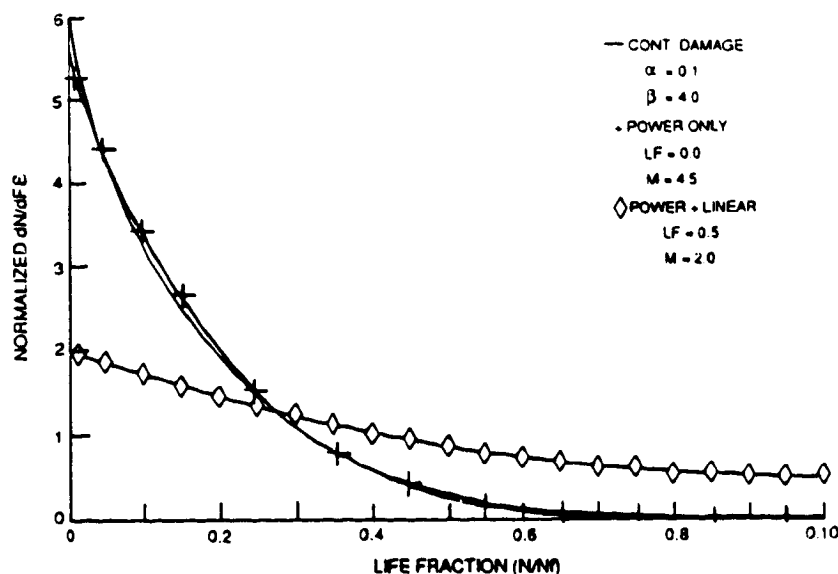


Figure 7-23 Non-Linear Damage Functions

The effect of the inclusion of the non-linear function $G(N/N_i)$ on the CDA life prediction for a strain ratio block test is shown by Figure 7-24. This plot shows how the ductility fraction increases as a function of cycles, both for linear and non-linear damage accumulation. In this case the non-linear prediction is lower than the linear prediction, because the basic damage rate (slope of the linear accumulation line) during the first block of the test is lower than the rate during the second block. This causes the ductility to be consumed earlier with the non-linear function than without it, and the net result is a lower prediction. The opposite effect is seen in Figure 7-25, where reversal of the order of the blocks causes the non-linear life prediction to be higher than the linear one. Note that this is the same effect which was observed during the specimen testing. Figure 7-26 shows the non-linear life predictions for all the strain ratio block tests completed during this task.

The effect of the non-linear damage accumulation is perhaps most dramatic when applied to the temperature block tests. Figure 7-27 shows how the life prediction can increase eightfold for a high-low temperature block sequence. In this case, the basic damage rate is much higher for Block 1 than for Block 2, so inclusion of the non-linear accumulation function results in very little damage during the first block. When the damage rate drops during the second block, the ductility is consumed very slowly, producing the large increase in predicted life. Figure 7-28 shows the non-linear CDA life predictions for all the temperature block tests completed during this task, and it is clear that the agreement is quite good.

It is, of course, possible that conditions in a block test could be chosen such that the basic total damage rate remains constant even though the individual components of the rate are changing. This was the case with the hold time block tests, as illustrated in Figure 7-29. This shows the history of the predicted time-dependent and time-independent damage factors (the sum of these is the total damage rate) for a specimen run with a one minute tensile hold time for the first block. It is clear that the sum of these factors is essentially unaffected by the transition from Block 1 to Block 2. It is not surprising, therefore, that the non-linear CDA life predictions for these tests are substantially the same as the linear predictions. Figure 7-30 shows the non-linear CDA predictions for all the hold time block tests.

The non-linear CDA predictions for the sequenced tests are shown in Figure 7-31, where good agreement can be noted. Here again, the non-linear method had a negligible effect, since the basic damage rate during the tests was essentially constant. These predictions were made by using an averaged value for the strain rate or range as applicable, and the agreement is quite good.

Figure 7-32 shows the non-linear CDA life predictions for the interrupted tests. Here one is faced with the question of how to handle the creep strain consumed during the testing (either prior to the cyclic portion of the test or interspersed during it). For this reason, two predictions are shown for each test, one in which the creep strains were ignored and one in which the full strains were subtracted from the available ductility as they accumulated. These two methods appear to bound the actual test lives, so it is reasonable to conclude that only a portion of the creep strains are effective in reducing the specimen life. The concept of an effective strain for CDA life calculation is therefore attractive and will be explored as part of the life prediction model development under other ongoing tasks.

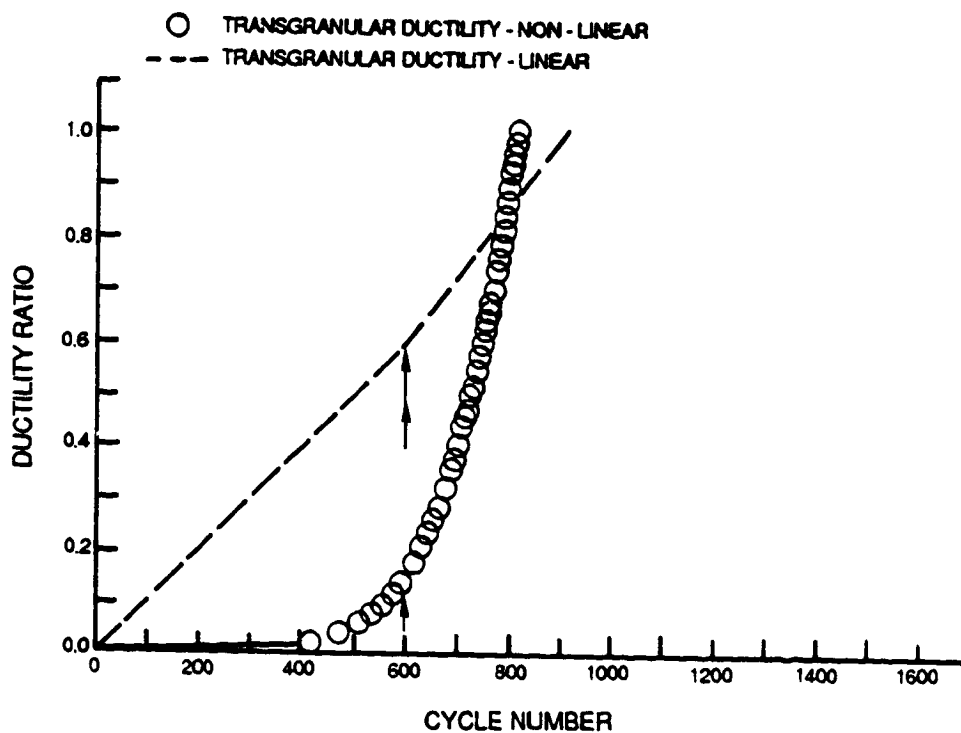


Figure 7-24 Example of Lower Life Prediction with Non-Linear Accumulation

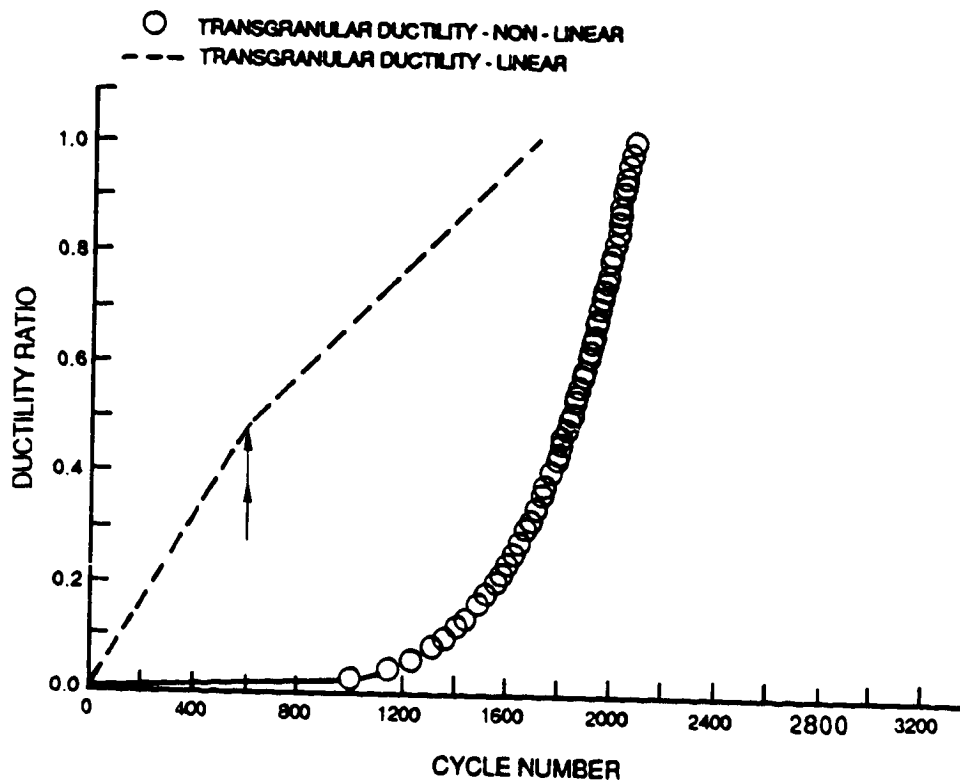


Figure 7-25 Example of Higher Life Prediction with Non-Linear Accumulation

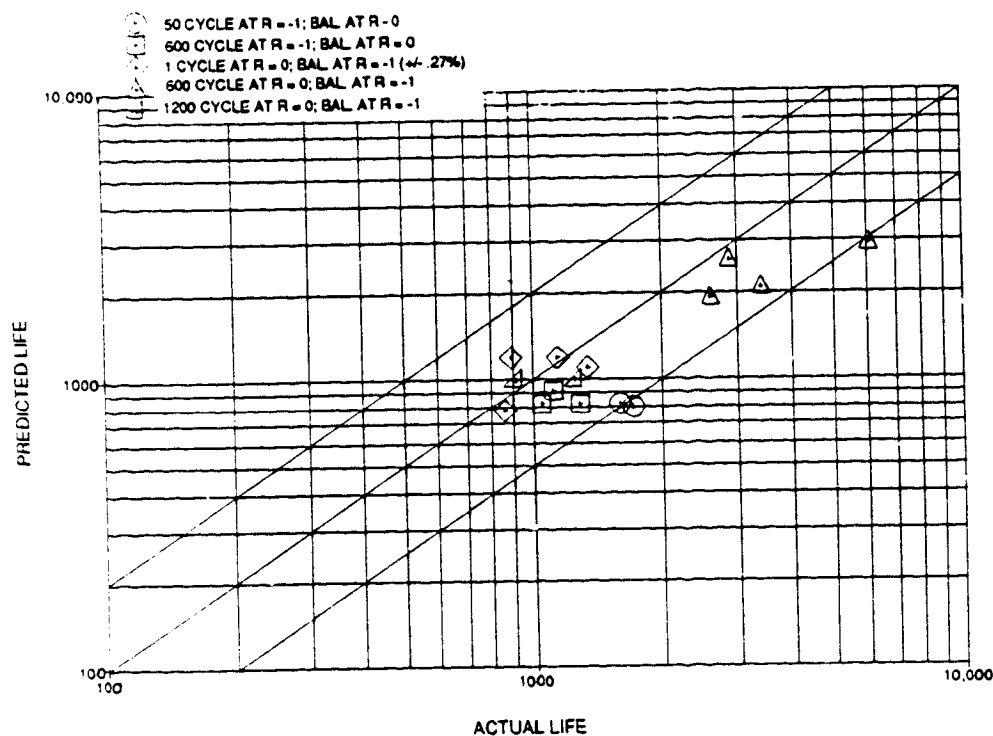


Figure 7-26 Non-Linear CDA predictions - Strain Ratio Block Tests

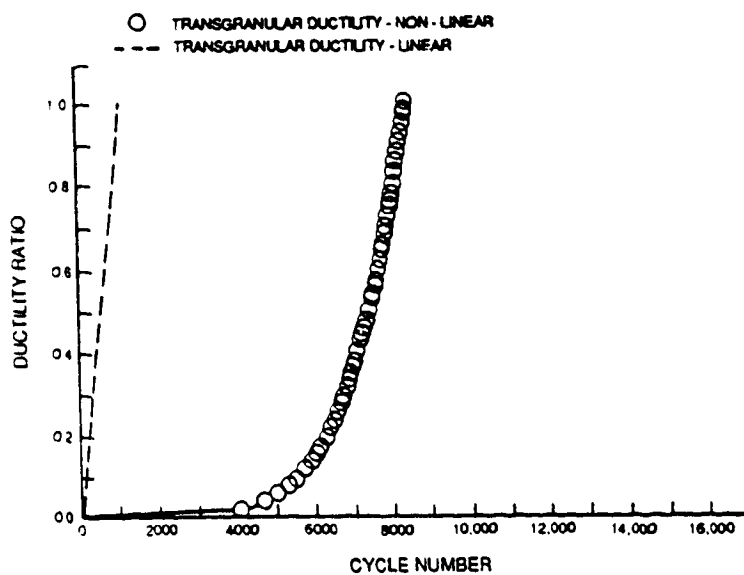


Figure 7-27 Variation of Ductility Ratio During Temperature Block Tests

ORIGINAL PAGE IS
OF POOR QUALITY

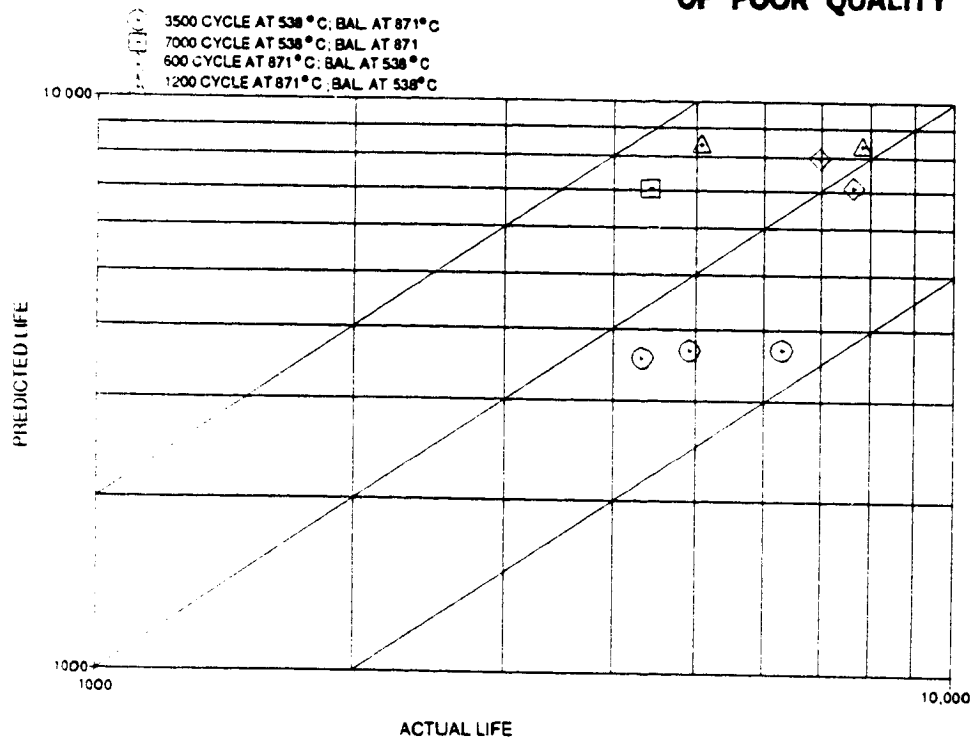


Figure 7-28 Non-Linear CDA Predictions - Temperature Block Tests

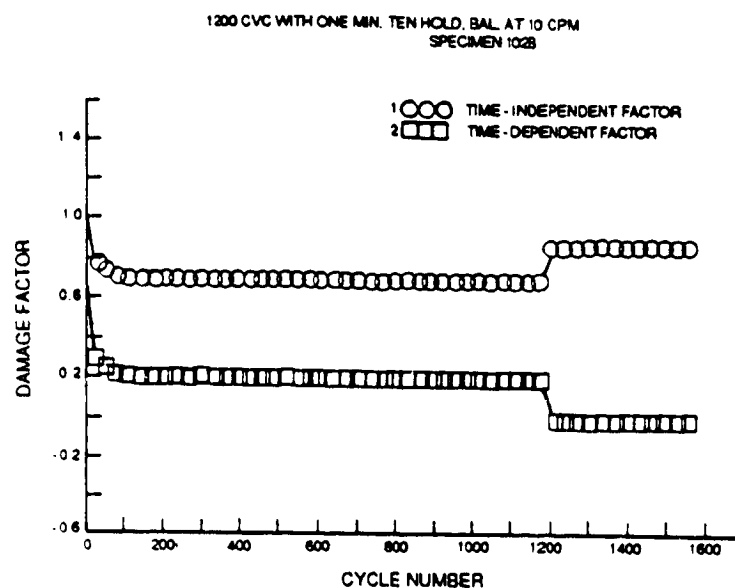


Figure 7-29 Damage Factor Variation During Hold Time Block Test

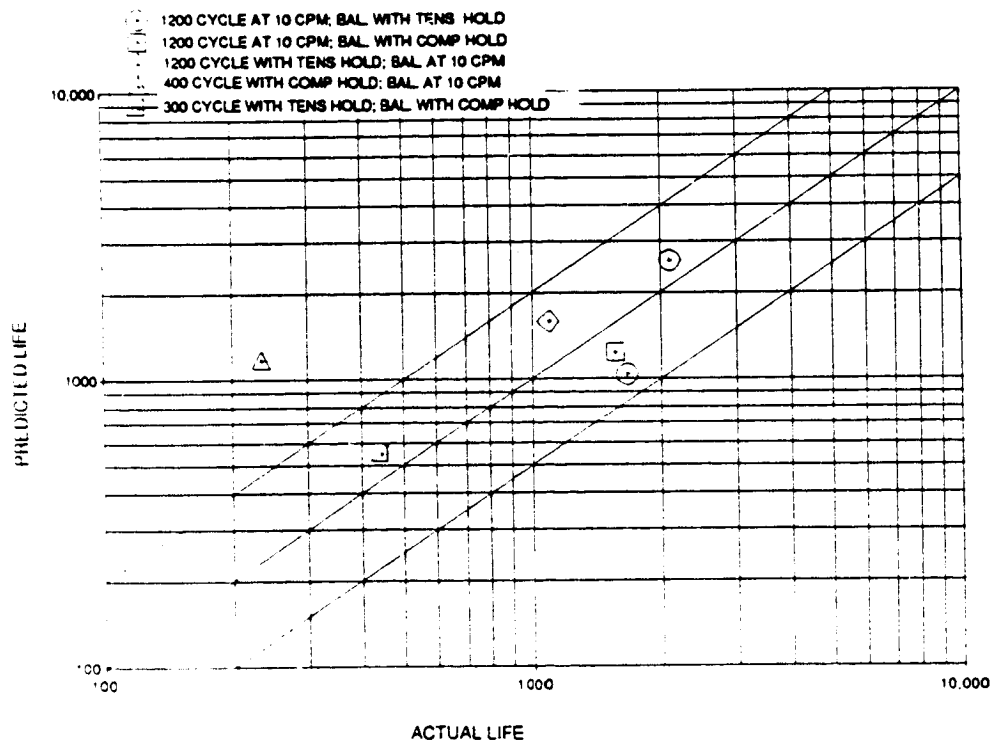


Figure 7-30 Non-Linear CDA Predictions - Hold Time Block Tests

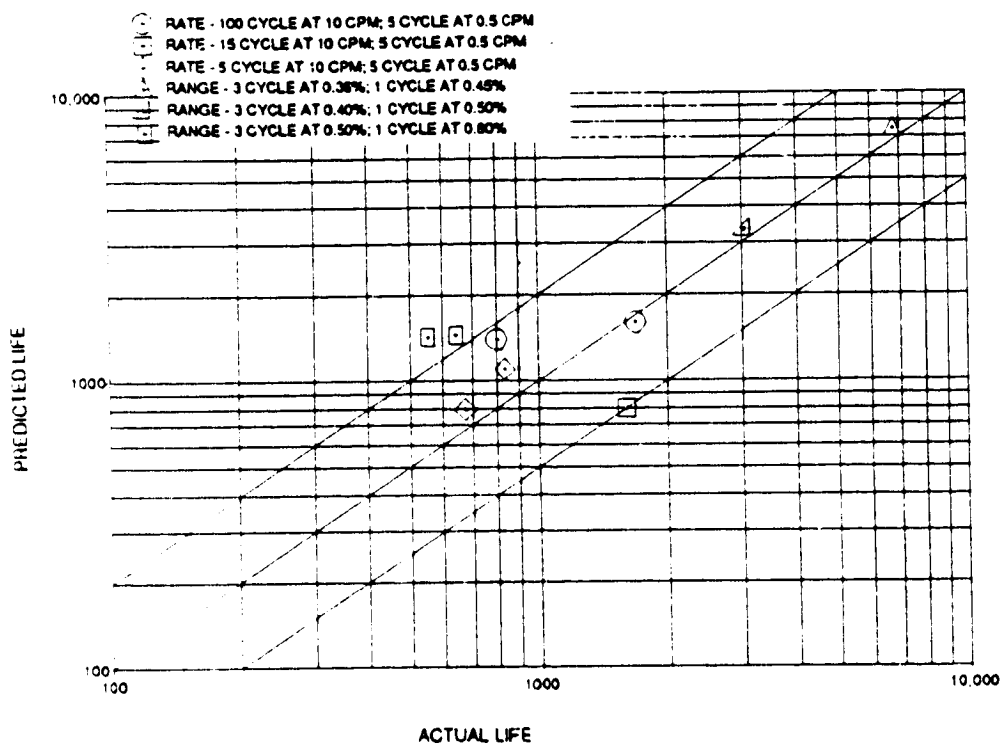


Figure 7-31 Non-Linear CDA Predictions - Sequenced Tests

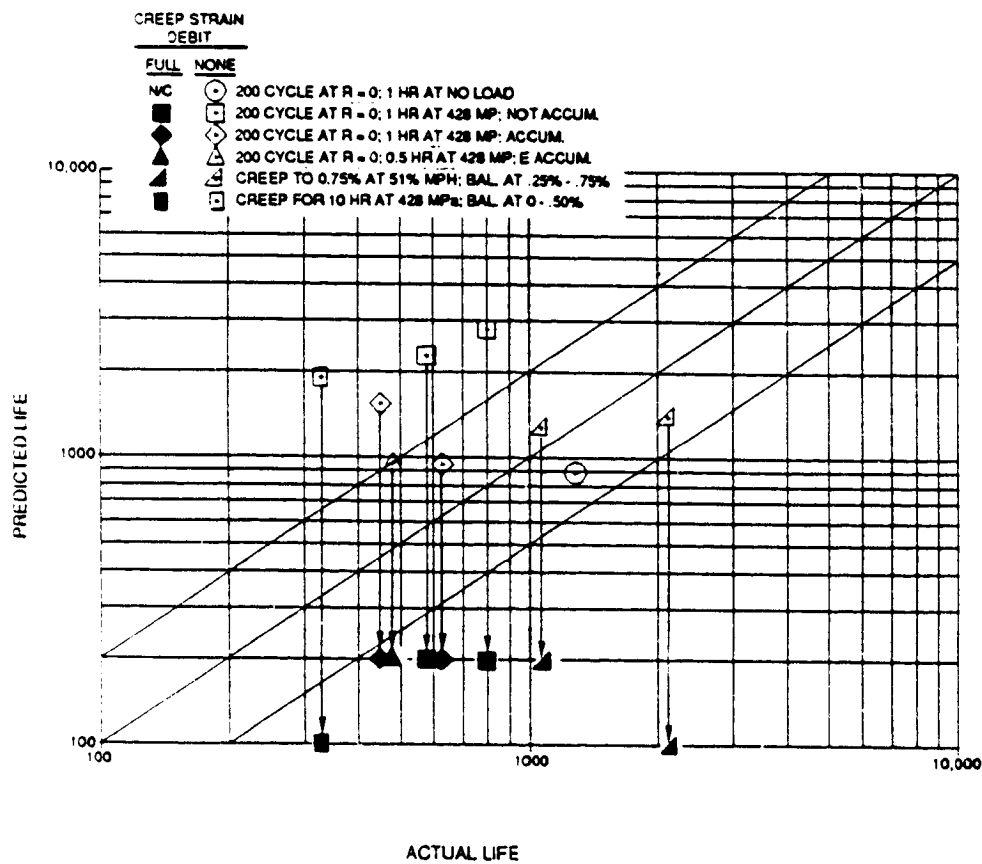


Figure 7-32 Non-Linear CDA Predictions - Interrupted Tests

A composite of all of the cumulative damage life predictions for the specimens tested under this task is shown in Figure 7-33. Note that both the linear and the non-linear predictions are shown for each of the tests, and in general the non-linear predictions are more accurate than the linear ones. It should also be mentioned that no further optimization of the fundamental life prediction constants was required for this task. Therefore, all the predicted lives in this figure were made using constants developed during the base program, further demonstrating the potential of the CDA life prediction method. Of course, final optimization of all model constants will be accomplished under Task XIID after the final form of the model has been developed, and it is expected that even more accurate predictions will be achieved at that time.

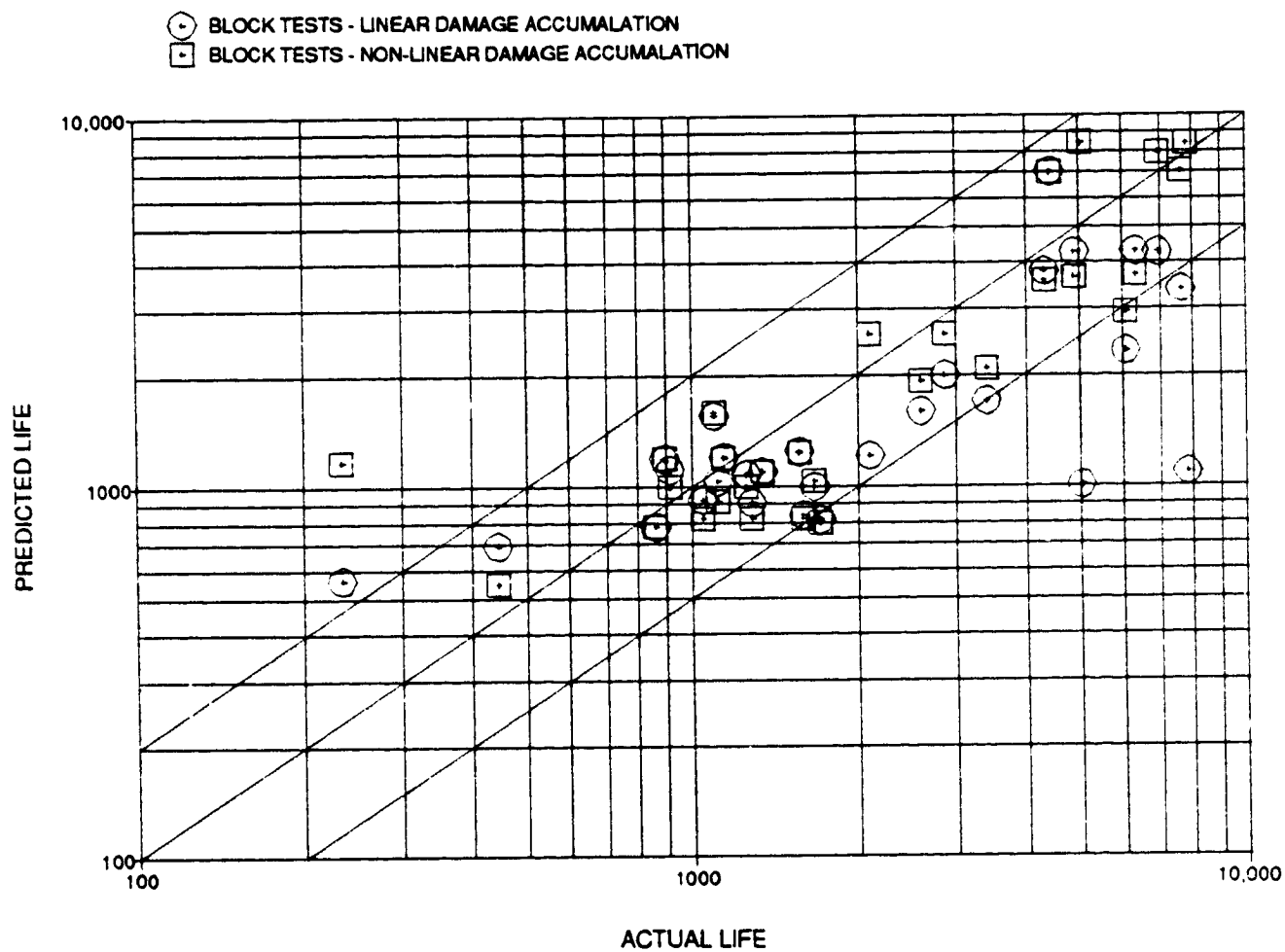


Figure 7-33 Effect of Non-Linear Damage Accumulation on CDA Life Predictions for Block Tests

SECTION 8.0

TASK VIII - SCREENING OF POTENTIAL ENVIRONMENTAL AND PROTECTIVE COATING MODELS

8.1 LITERATURE REVIEW OF ENVIRONMENTAL MODELS

A literature survey has been conducted to identify current models used for the prediction of environmental (oxidation) effects on the cyclic creep fatigue life of superalloys. These models were assessed for their suitability to predict these effects in hot section components of gas turbine engines.

Two recent literature surveys (Refs. 8.1, 8.2) cite many investigations regarding oxidation and the oxidation effect on fatigue life at elevated temperature. Metallographic and fractographic examinations have been conducted on many alloys to identify the micro-mechanisms involved. It is clear that oxidation may shorten the fatigue life considerably both in terms of fatigue crack initiation and fatigue crack propagation. However, a detailed quantitative relation between oxidation and fatigue life is still lacking (Ref. 8.1). This situation exists because the complexity of the oxidation process itself, especially in superalloys, as well as its synergistic interaction with the creep and fatigue processes make the development of a generic predictive method improbable.

There are models such as Coffin's equation for frequency modified life (Ref. 8.3) that implicitly include oxidation through general time dependent terms:

$$\Delta \epsilon_p = C \left(N_f \nu^{k-1} \right)^{-\beta}$$

where: $\Delta \epsilon_p$ = plastic strain range
 N_f = cycles to failure
 ν = frequency
 β = Manson-Coffin exponent
 C, k = constants

This equation can be interpreted to imply that at lower frequencies, there will be more time for oxidation which will then result in a reduced fatigue life.

Coffin (Ref. 8.4) has shown experimentally for several materials tested in high vacuum that the temperature sensitivity of the fatigue life is slight. Therefore life prediction models in which temperature is an explicit parameter might also be construed as implicitly including oxidation effects.

Udoguchi and Wada (Ref. 8.5) introduced thermally activated mechanisms to the Manson-Coffin law:

$$\frac{1}{N_f} = C \exp \left(- \frac{Q}{RT} \right) \Delta \epsilon_p^\beta$$

where: $\Delta \epsilon_p$, N_f , C and β have the same meaning as above.
 Q = activation energy
 R = gas constant
 T = temperature in degrees absolute

For the steels investigated, the Manson-Coffin exponent scarcely varied with temperature and was assumed to be constant in the activation energy evaluation.

Degallaix, et al (Ref. 8.6) developed a model that accounts for fatigue damage by two types of mechanisms, depending on the plastic strain range; those which are thermally activated and those which are not.

$$\frac{1}{N_f} = A_1 \Delta \epsilon_p^{b_1} \exp \left(- \frac{Q}{RT} \right) + A_2 \Delta \epsilon_p^{b_2}$$

where: $\Delta \epsilon_p$, N_f , Q , R and T have same meanings as above
 A_1 , b_1 , A_2 , and b_2 = material constants.

A considerable amount of experimental data at various temperatures was required to empirically determine the material constants for the steel investigated.

There have been very few attempts to construct a comprehensive model that explicitly considers the oxidation/fatigue interaction processes. The models that have been developed have assumed that the fatigue crack initiation life is related to the oxide depth and the fatigue crack growth rate is related to the oxidation rate. The models therefore require that the oxidation kinetics be defined. Oxidation has been assumed to be a diffusion process with a parabolic time relationship. Acceleration of the oxidation rate is caused by cyclic deformation and this has been quantified by experimental observation.

Antolovich, et al (Ref. 8.7) studied the low cycle fatigue behavior of cast Ni base superalloy Rene' 80 at elevated temperature and developed a fatigue life model that explicitly considers the influence of oxidation. He found that cracks initiated at oxide spikes in surface connected grain boundaries so that the expression for crack initiation life is based on a correlation between maximum stress and depth of oxidation.

$$\left[\bar{\sigma} + K \left(\frac{\Delta \epsilon_p}{2} \right)^{n'} \right]^8 D \alpha^2 \left[\left(\frac{1}{\nu} + t_h \right) \right] N_i = C$$

where: $\bar{\sigma}$ = mean stress
 K = cyclic stress-strain coefficient
 $\Delta \epsilon_p$ = cyclic plastic strain range
 n' = cyclic strain hardening exponent
 D = diffusion rate of oxygen = $D_0 \exp(-Q/RT)$
 α = geometric constant
 ν = cycle frequency
 t_h = hold time
 N_i = cycles to crack initiation
 C = constant

The term in the first bracket represents the maximum tensile stress in the cycle.

Wright (Ref. 8.8) has modified the Antolovich model for application to a single crystal superalloy, Rene' N₄, by recognizing differences in the oxidation time dependency and that life is not simply inversely proportional to exposure or cycle time.

$$\left[\sigma_{\max} \right]^m \left[k_1 (t_e)^{n_1} + k_2 (t_{cy})^{n_2} \right] N_i = C$$

where: σ_{\max} = maximum tensile stress in the cycle
 m = empirically determined constant
 k_1, n_1 = rate constants for uncycled oxidation
 t_e = prior exposure time
 k_2, n_2 = rate constants for cycled exposure
 t_{cy} = cycle time
 N_i = cycles to crack initiation
 C = constant

Challenger, et al (Ref. 8.9) developed an environmental fatigue interaction model to predict the cycles to crack initiation for a low alloy steel (2 1/4 Cr - 1 Mo) subjected to elevated temperature fatigue tests with hold times in air environments. The model is based on the time required for oxide cracking as a function of the tensile strain in the oxide and the temperature. In non-general terms, the model is:

$$N_i = \frac{8.5 \times 10^{-16} \exp \left(\frac{+12,297}{T} \right)}{t_c (\Delta \epsilon_T)^4 (1 - t_T/t_c)^4}$$

where: N_i = cycles to crack initiation
 T = temperature in degrees absolute
 $\Delta\epsilon_T$ = total strain range
 t_c = total time for one cycle
 t_T = time for the tensile half cycle

Reuchet and Remy (Ref. 8.10) studied the interaction between fatigue and oxidation for a cast cobalt base superalloy MAR-M 509. They developed a model for low cycle fatigue based on an integrated damage equation that sums the mechanical crack advance due to the fatigue process and an environmental crack advance due to the oxidation process at the crack tip. The generalized matrix oxidation and preferential oxidation along carbides were both considered contributory to the oxidation crack advance.

$$N_f = \frac{1}{B'} \ln \left[\frac{B' a_f}{(da/dN)_{ox}} + 1 \right]$$

where: B' = $0.51 \Delta\epsilon_p \left[1/\cos(\pi\sigma/2T) - 1 \right]$
 $\Delta\epsilon_p$ = plastic strain range
 σ = maximum cyclic tensile stress
 T = ultimate tensile stress
 a_f = final crack size
 $(da/dN)_{ox}$ = oxidation based crack growth rate

$$= \left(1 - f_c^* \right) \alpha_m^0 \left(1 + k_m \frac{\Delta\epsilon_p}{2} \right) t_1^{1/2} + f_c^* \alpha_c^0 \exp(b\sigma) t_1^{1/4}$$

f_c^* = effective fraction of carbides on the crack path
 α_m^0 = matrix oxidation constant when there is no stress
 α_c^0 = carbide oxidation constant when there is no stress
 k_m = constant related to the cyclic strain dependence of the matrix oxidation
 t_1 = fatigue cycle period
 b = constant

Wright (Ref. 8.8) applied this model to crack propagation in the single crystal superalloy Rene' N4 with unsuccessful results. He speculated that the crack tip oxidation/fatigue process for Rene' N4 is quite different from the surface process characterized in the Reuchet-Remy model.

As stated, simplifying assumptions have been made in the development of these models regarding oxidation kinetics and their interaction with cyclic plastic deformation. Many other aspects of the oxidation/fatigue interaction process have not even been addressed in the models, for instance, the effect of oxygen partial pressure. Although the application of the models may be quite limited in their present stage of development, specific parameters such as time and temperature appear consistently and must be considered as candidates for explicit inclusion in the Cyclic Damage Accumulation Model.

8.2 LITERATURE REVIEW OF COATING MODELS

In the concurrent NASA Anisotropic Materials Program (Ref. 8.11), the literature was searched extensively to identify current models used for the prediction of oxidation resistant coating effects on the creep-fatigue life of superalloys. No life prediction approaches were found that explicitly model the role of the coating on cracking of the coating-base alloy system although coated specimen data have been used by some investigators. With the development of methodology to account for the important effects of the coating, a number of existing life prediction models have the potential to characterize the coating-base alloy crack initiation behavior.

8.3 SPECIMEN EVALUATION

A methodology for metallurgical review of environmentally influenced and coated specimens is now being developed. Previously, in the baseline program, primary cracks in LCF samples were analyzed by examining the fracture surface of the specimen after separation, as shown in Figure 8-1. This procedure is adequate for determining the initiation site as well as the crack propagation mode but not for determining the role of oxidation in the crack initiation process, which is of vital importance in the study of environmental effects. In order to better quantify the effects of the environment on the initiation stage of the fatigue process, the following method is suggested:

1. Test the required samples in the desired environments using the same R-ratios, test temperature, frequency and waveshape, to the same number of cycles (e.g., 30% of life of basic specimen life tested in air).
2. Examine the surface of each specimen to confirm the existence of a primary crack and determine its origin.
3. Section the specimens longitudinally through the primary crack origin.
4. Mount and polish these sections to provide a view of the crack such as that shown in Figure 8-2.

As can be seen, the buildup of oxide along the crack is easily observed by this method. The crack length and depth of penetration of oxide produced by the different environments can be more accurately assessed than by examination of the fracture surface. Also, the crack growth mode can be easily determined. The primary crack should be examined as it is ultimately responsible for specimen failure. In previous tests, the number and length of secondary cracks have not been found to correlate with specimen life. Examination of these cracks would not provide information relevant to the primary crack growth process. By testing the specimens to the same number of cycles and maintaining the same test conditions except for environment, the relative influence of environment on the fatigue crack growth process can be more readily assessed.

A trial specimen was run to check the procedures that will be used to quantify the environmental effects on the initiation stage of the fatigue process. Specimen 131B was fatigue tested at 982°C (1800°F) with a total strain range 0.5% (R=-1), 1 CPM for 350 cycles. (Approximately 30% of separation life). A primary surface crack about 0.9 mm (35 mils) in length was observed as shown in Figure 8-3A. Longitudinal section through crack origin was made as indicated by the dashed line in Figure 8-3A. The crack was shown to penetrate about 0.25 mm (10 mils) in depth as shown in Figure 8-3B. The crack initiated and propagated transgranularly and then proceeded intergranularly. The crack followed a path of 'depleted zone'. The surface length and penetration depth of crack can be used to assess the environmental effects on the initiation stage of the fatigue crack.

A review of specimen test results from previously completed tasks revealed that the tests, most of which were conducted at temperatures ranging from 538 to 871°C (1000 to 1600°F), resulted in minimal oxidation effects. The observed crack initiation sites were near surface origins associated with either grain boundary carbides or microporosity. Transgranular cracking was observed at most of the initiation sites while oxidation enhanced fatigue tends to result mainly in intergranular cracking. For cast B1900 above 871°C (1600°F), Anton and Favrow (Ref. 8.12) found fatigue crack initiation was enhanced by local oxidation of surface connected carbides with fatigue crack propagation being predominantly intergranular. However, the 982°C (1800°F) baseline specimen tests show little frequency dependence (see Figure 8-4) whereas a stronger frequency dependence has been associated with oxidation enhanced crack initiation.

8.4 CANDIDATE MODEL SELECTION

Early test results from Task IX along with relevant test data from previously completed tasks will be used to screen the possible environmental models and select the most appropriate models for further development, evaluation and verification in subsequent tasks.

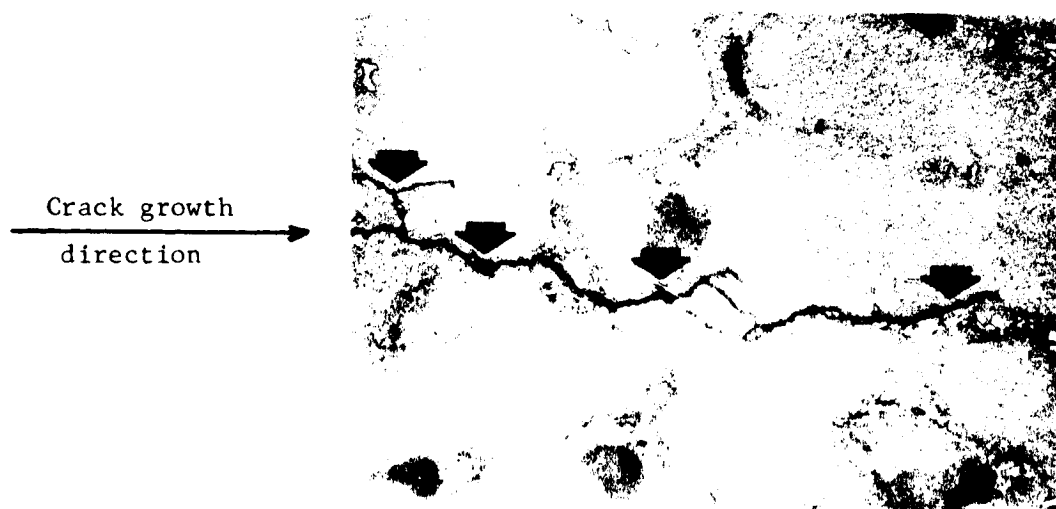
Screening of the possible models which will account for the effects of protective coatings is being accomplished in the Anisotropic Materials Program. Coated TMF tests conducted early in Task V will be used to select the most appropriate models for further development, evaluation and verification in subsequent tests.

ORIGINAL PAGE IS
OF POOR QUALITY



10X

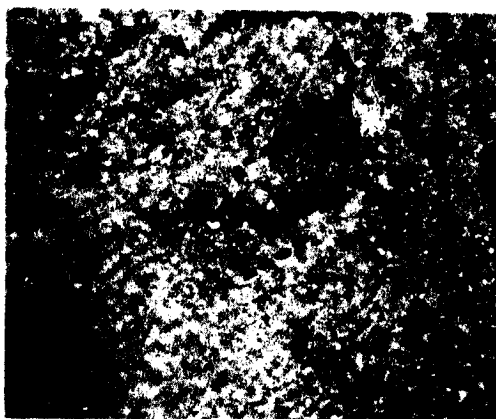
Figure 8-1 Fracture Surface of Separated LCF Sample



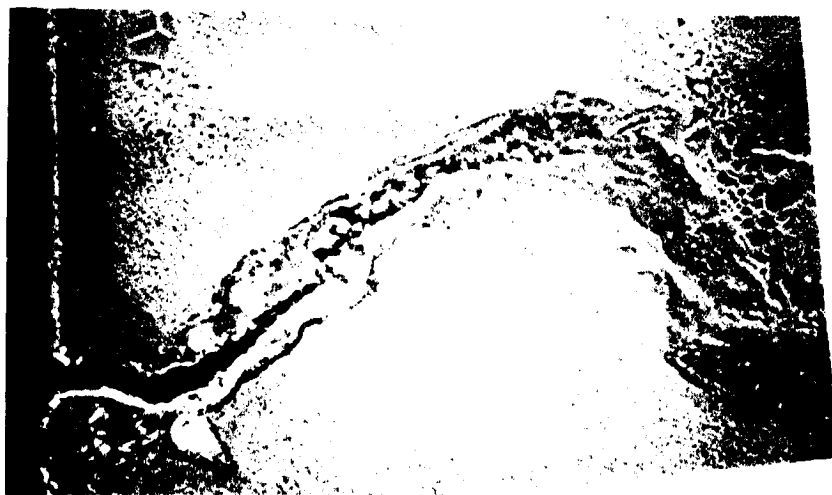
200X

Figure 8-2 View of crack after sectioning longitudinally through primary crack origin. Areas of oxide buildup are indicated by arrows.

ORIGINAL PAGE IS
OF POOR QUALITY



(A) 0.89mm 25X
CRACK LENGTH



(B) 0.25mm 560X
CRACK DEPTH

Figure 8-3 Specimen 131B after being LCF tested at 982°C (1800°F), $\Delta\epsilon = \pm 0.25\%$, 1 cpm for 350 cycles. (A) A surface crack about 0.89 mm (35 mils) long (replica measurement ≈ 0.97 mm (38 mils)). (B) Section longitudinally through crack origin showing crack which penetrated about 0.25 mm (10 mils) in depth. Crack initiated and propagated transgranularly and then proceeded intergranularly. Crack followed a path of γ' depleted zone.

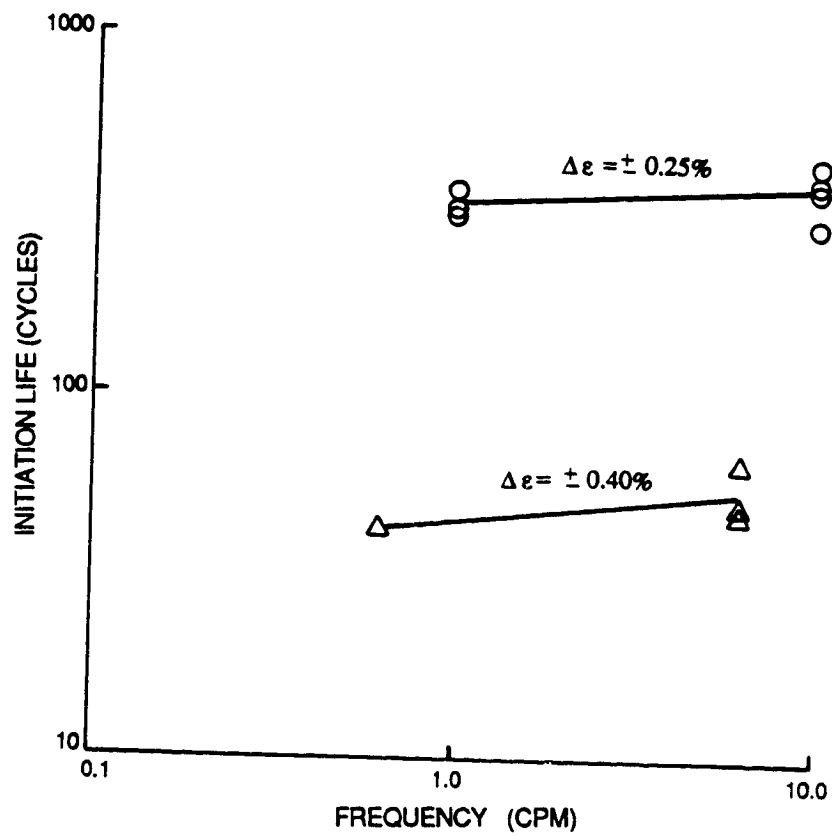


Figure 8-4 982°C (1800°F) Baseline Specimen Tests Test Frequency Versus Crack Initiation Life

SECTION 9.0

TASK IX - ENVIRONMENTAL ATTACK MODEL

9.1 TEST MATRIX FOR ENVIRONMENTAL EXPERIMENTS

The environmental creep-fatigue test program, which consists of 27 tests utilizing B1900+Hf solid smooth baseline fatigue specimens, is presented in Table 9-1. Isothermal, fully reversed, strain controlled tests will be conducted in inert argon, in oxygen at partial pressures typical of that encountered in the engine hot section and in laboratory air. The crack initiation results will be used to develop, evaluate and verify a model for prediction of environmental (oxidation) effects on the creep-fatigue life.

Tests results from previous tasks were reviewed to determine test conditions that would activate the various damage processes including oxidation. The program incorporates two temperature levels (982°C (1800°F); 871°C (1600°F)) and two strain rates ($1.67 \times 10^{-3} \text{ sec}^{-1}$; $1.67 \times 10^{-4} \text{ sec}^{-1}$). Testing will be done in two stages. Screening Tests will be run to determine the alternate environment (inert argon or pressurized oxygen) with the greatest effect. This alternate environment then will be used in conjunction with laboratory air by varying the length and order of exposure to demonstrate the effects of the environment at different stages in the development of a fatigue crack.

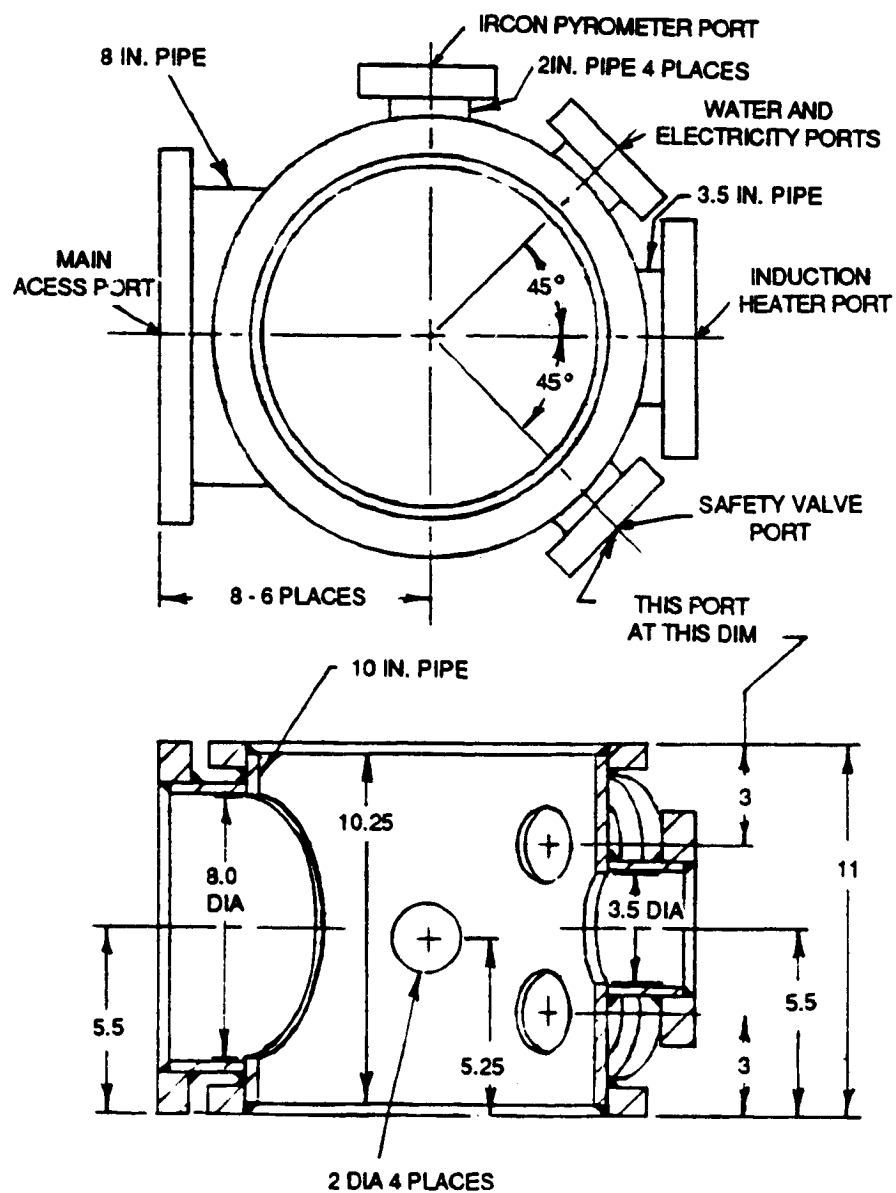
9.2 ENVIRONMENTAL TEST CHAMBER DESIGN

A stainless steel, low pressure test chamber shown in Figure 9-1 has been designed to accommodate the planned environmental tests described above. The chamber will be capable of withstanding a maximum pressure at least 2X greater than the working pressure of 5 atmospheres. The materials required for construction of the chamber are being assembled.

TABLE 9-1
ENVIRONMENTAL TEST PROGRAM MATRIX

Specimen	Type	Strain Range (%)			Strain Rate (sec ⁻¹)			Temperature (°C)		Environmental Exposure		
		±0.20	±0.25	±0.50	1.67 x 10 ⁻⁴	1.67 x 10 ⁻³	1.67 x 10 ⁻²	871 (1600°F)	982 (1800°F)	Inert Argon	Alternate Pressurized(1) Oxygen	Laboratory Air
1			X		X			X		X		
2			X		X			X			X	
3			X		X			X				X
4	Screening	X			X				X	X		
5		X			X				X		X	
6		X			X				X			X
7		X			X				X			
8		X			X				X	X		
9		X			X				X		X	X
10			X		X			X				
11			X		X			X				
12			X		X			X				
13					X				X			
14		X			X				X			
15	Mixed Environment	X			X				X			
16		X			X				X			
17		X			X				X			
18		X			X				X			
19			X		X				X			
20			X		X			X				
21			X		X			X				
22			X		X			X				
23		X			X				X			
24		X			X				X			
25		X			X				X			
26		X			X				X			
27		X			X				X			

(1) Five atmospheres of oxygen which approximates the partial pressure of oxygen in the engine hot section
(2) Length of exposure as a percentage of initiation life



NOTE: DIMENSIONS ARE SHOWN IN INCHES

Figure 9-1 Environmental Test Chamber

APPENDIX I

VERIFICATION TEST RESULTS (BASE PROGRAM)

Table I-1 - Hold Time Tests with R=0

Specimen Identification	8C	8D	10A	128A	29C
Type of Specimen	MERL 75	MERL 75	MERL 75	MERL 75	MERL 75
Test Conditions:					
Temperature (°F)	1600.	1600.	1600.	1600.	1000.
Strain Range	0.005079	0.005099	0.005064	0.005154	0.005081
Strain R-Ratio (min/max)	0.011	-0.005	0.002	-0.031	-0.000
Strain Rate (1/sec)	1.54E-04	1.55E-04	1.53E-04	1.56E-04	1.54E-04
Frequency (cyc/min)	0.909	0.909	0.909	0.909	0.909
Tension Hold (sec)	59.954	59.953	59.948	59.999	0.0
Compression Hold (sec)	0.0	0.0	0.0	0.0	60.000
Stress-Strain Response:					
Stress Range, Init (psi)	102944.0	108158.0	105538.0	109317.0	118978.0
Stress Range, Nf/2 (psi)	99358.0	104395.0	99800.0	101281.0	120193.0
Mean Stress, Init (psi)	18631.0	16736.0	17662.5	19648.5	34115.0
Mean Stress, Nf/2 (psi)	-9677.6	-11502.0	-12505.1	-11031.4	38358.4
Inel Stn Rng, Init	0.000646	0.000692	0.000739	0.000597	0.000098
Inel Stn Rng, Nf/2	0.000522	0.000583	0.000566	0.000780	0.000115
Hold Sts Rlx, Init (psi)	-3263.0	-5122.0	-3975.0	-6530.0	+43.0
Hold Sts Rlx, Nf/2 (psi)	-4684.0	-5833.0	-4867.0	-8331.0	+143.0
Life Results:					
Initiation (cycles)	210.	188.	280.	220.	4300.
5% Load Drop (cycles)	1278.	1300.	3300.	1179.	6025.
10% Load Drop (cycles)	1686.	1572.	3514.	1343.	6197.
50% Load Drop (cycles)	2100.	1880.	4050.	1570.	6400.

Table I-2 - High Strain Range Tests

Specimen Identification	108C	101A
Type of Specimen	MERL 75	MERL 75
Test Conditions:		
Temperature (°F)	1600.	1600.
Strain Range	0.008194	0.008109
Strain R-Ratio (min/max)	-0.974	-536.174
Strain Rate (1/sec)	2.70E-05	2.70E-03
Frequency (cyc/min)	0.099	9.999
Tension Hold (sec)	600.000	0.0
Compression Hold (sec)	0.0	0.0
Stress-Strain Response:		
Stress Range, Init (psi)	146081.0	146227.0
Stress Range, Nf/2 (psi)	158153.0	146001.0
Mean Stress, Init (psi)	-10445.7	-32032.0
Mean Stress, Nf/2 (psi)	-23074.7	-12021.0
Incl Stn Rng, Init	0.004306	0.001117
Incl Stn Rng, Nf/2	0.004758	0.001075
Hold Sts Rlx, Init (psi)	-7381.0	0.0
Hold Sts Rlx, Nf/2 (psi)	-8718.0	0.0
Life Results:		
Initiation (cycles)	24.	178.
5% Load Drop (cycles)	140.	776.
10% Load Drop (cycles)	155.	884.
50% Load Drop (cycles)	182.	960.

Table I-3 - R-Ratio Effects at Low Strain Rate and High Temperature

Specimen Identification	12B	47C	128C	131B
Type of Specimen	MERL 75	MERL 75	MERL 75	MERL 75
Test Conditions:				
Temperature (°F)	1800.	1800.	1800.	1800.
Strain Range	0.005106	0.005113	0.005142	0.005028
Strain R-Ratio (min/max)	-0.013	-0.001	-38.412	-1.040
Strain Rate (1/sec)	1.70E-04	1.70E-04	1.71E-04	1.68E-04
Frequency (cyc/min)	1.000	1.000	1.000	1.000
Tension Hold (sec)	0.0	0.0	0.0	0.0
Compression Hold (sec)	0.0	0.0	0.0	0.0
Stress-Strain Response:				
Stress Range, Init (psi)	70924.5	71016.7	70157.7	72151.0
Stress Range, Nf/2 (psi)	69633.9	67180.4	69230.6	71597.6
Mean Stress, Init (psi)	8307.3	9265.7	-6977.6	707.0
Mean Stress, Nf/2 (psi)	130.4	-85.4	1331.6	276.7
Incl Stn Rng, Init	0.001501	0.001428	0.001512	0.001394
Incl Stn Rng, Nf/2	0.001422	0.001505	0.001679	0.001394
Life Results:				
Initiation (cycles)	126.	104.	140.	290.
5% Load Drop (cycles)	843.	695.	472.	>350.
10% Load Drop (cycles)	868.	717.	551.	>350.
50% Load Drop (cycles)	900.	740.	635.	>350.

Table I-4 - Load Controlled Tests

Specimen Identification	11A	47A	131C	131D	121D
Type of Specimen	MERL 75	MERL 75	MERL 75	MERL 75	MERL 75
Test Conditions:					
Temperature (°F)	1600.	1600.	1600.	1600.	1600.
Strain Range	0.003630	0.003380	0.004742	0.004622	0.005197
Strain R-Ratio (min/max)	0.001	0.001	0.592	0.776	-999.000
Strain Rate (1/sec)	1.21E-03	1.13E-03	1.58E-03	1.54E-03	1.73E-03
Frequency (cyc/min)	10.002	9.994	10.003	10.002	10.000
Tension Hold (sec)	0.0	0.0	0.0	0.0	0.0
Compression Hold (sec)	0.0	0.0	0.0	0.0	0.0
Stress-Strain Response:					
Stress Range, Init (psi)	73613.0	74613.0	99485.1	100494.0	96621.6
Stress Range, Nf/2 (psi)	73613.0	74613.0	99485.1	100494.0	100274.0
Mean Stress, Init (psi)	36841.0	37342.0	49742.6	-50246.0	-49232.6
Mean Stress, Nf/2 (psi)	36841.0	37342.0	49742.6	-50246.0	-50276.0
Incl Stn Rng, Init	0.000227	0.000263	0.000673	0.000623	0.000309
Incl Stn Rng, Nf/2	0.000181	0.000167	0.000283	0.000453	0.000287
Life Results:					
Initiation (cycles)	5410.	5523.	423.	4000.	>400.
5% Load Drop (cycles)	6365.	7890.	950.	4000.	>400.
10% Load Drop (cycles)	6365.	7890.	950.	4000.	>400.
50% Load Drop (cycles)	6365.	7890.	950.	4000.	>400.

Table I-5 - Unpolished (As-Machined) Tests

Specimen Identification	9A	9C
Type of Specimen	MERL 75	MERL 75
Test Conditions:		
Temperature (°F)	1600.	1600.
Strain Range	0.005015	0.004012
Strain R-Ratio (min/max)	0.007	-0.959
Strain Rate (1/sec)	1.67E-03	1.34E-03
Frequency (cyc/min)	10.003	10.001
Tension Hold (sec)	0.0	0.0
Compression Hold (sec)	0.0	0.0
Stress-Strain Response:		
Stress Range, Init (psi)	98843.0	86104.5
Stress Range, Nf/2 (psi)	101959.0	87167.1
Mean Stress, Init (psi)	36139.2	1551.1
Mean Stress, Nf/2 (psi)	22532.5	11561.6
Incl Stn Rng, Init	0.000422	0.000204
Incl Stn Rng, Nf/2	0.000204	0.000153
Life Results:		
Initiation (cycles)	2278.	3374.
5% Load Drop (cycles)	5060.	10307.
10% Load Drop (cycles)	5086.	10424.
50% Load Drop (cycles)	5120.	10544.

APPENDIX II THERMOMECHANICAL TEST RESULTS

Table II-1 - Baseline In-Phase and Out-of-Phase Tests

Specimen Identification	1288	42B	102C	122A	45A	105D
Type of Specimen	MERL 73M	MERL 44C	MERL 44C	MERL 73M	MERL 44C	MERL 44C
Test Conditions:						
Strain-Temp Phase	IN	IN	IN	OUT	OUT	OUT
Temperature Range (°F)	1000-1600	1000-1600	1000-1600	1000-1600	1000-1600	1000-1600
Strain Range	0.003917	0.004888	0.004545	0.004060	0.004782	0.004800
Strain R-Ratio (min/max)	-1.027	-0.945	-0.995	-0.991	-0.947	-0.982
Strain Rate (1/sec)	1.31E-04	1.63E-04	1.51E-04	1.35E-04	1.59E-04	1.60E-04
Frequency (cyc/min)	1.000	1.000	1.000	1.000	1.000	1.000
Tension Hold (sec)	0.0	0.0	0.0	0.0	0.0	0.0
Compression Hold (sec)	0.0	0.0	0.0	0.0	0.0	0.0
Stress-Strain Response:						
Stress Range, Init (psi)	93093.2	124133.0	113304.0	99488.1	120647.0	116170.0
Stress Range, Nf/2 (psi)	98524.3	124970.0	117467.0	100640.0	116906.0	111859.0
Mean Stress, Init (psi)	-6926.0	-12228.0	-6507.0	8227.5	1601.0	8951.0
Mean Stress, Nf/2 (psi)	-12118.6	-18785.0	-4970.4	27923.7	4013.2	23838.0
Inel Stn Rng, Init	0.000035	0.000098	0.000064	0.000096	0.000107	0.000074
Inel Stn Rng, Nf/2	0.000109	0.000118	0.000082	0.000127	0.000104	0.000109
Life Results:						
Initiation (cycles)	5127.	370.	1472.	2116.	1000.	993.
5% Load Drop (cycles)	7980.	1706.	4709.	2990.	1548.	1918.
10% Load Drop (cycles)	8041.	1907.	4786.	3005.	1601.	1983.
50% Load Drop (cycles)	8138.	2041.	4905.	3023.	1817.	2256.

Table II-2 - Variable R-Ratio Tests

Specimen Identification	42D	104A	126A	42C	46C	107C	46D
Type of Specimen	MERL 44C	MERL 44C	MERL 73M	MERL 44C	MERL 44C	MERL 44C	MERL 44C
Test Conditions:							
Strain-Temp Phase	IN	IN	OUT	OUT	OUT	OUT	OUT
Temperature Range (°F)	1000-1600	1000-1600	1000-1600	1000-1600	1000-1600	1000-1600	1000-1600
Strain Range	0.004800	0.004688	0.003990	0.004864	0.004837	0.003859	0.004910
Strain R-Ratio (min/max)	0.0	0.0	-0.021	-0.000	-0.017	-81.173	-53.648
Strain Rate (1/sec)	1.60E-04	1.56E-04	1.33E-04	1.62E-04	1.61E-04	1.29E-04	1.64E-04
Frequency (cyc/min)	1.000	1.000	1.000	1.000	1.000	1.000	1.000
Tension Hold (sec)	0.0	0.0	0.0	0.0	0.0	0.0	0.0
Compression Hold (sec)	0.0	0.0	0.0	0.0	0.0	0.0	0.0
Stress-Strain Response:							
Stress Range, Init (psi)	112707.0	108316.0	99378.2	121536.0	123706.0	92283.6	114196.0
Stress Range, Nf/2 (psi)	114314.0	120607.0	96627.6	127105.0	119899.0	93537.4	110891.0
Mean Stress, Init (psi)	12790.1	18817.1	40896.4	36829.1	35547.4	-20381.1	-19960.4
Mean Stress, Nf/2 (psi)	-6278.1	5067.0	42903.6	33952.2	32280.8	1043.4	7402.7
Inel Stn Rng, Init	0.000250	0.000089	0.000058	0.000211	0.000063	0.000111	0.000193
Inel Stn Rng, Nf/2	0.000102	0.000145	0.000122	0.000114	0.000090	0.000063	0.000080
Life Results:							
Initiation (cycles)	1150.	719.	2017.	470.	730.	4162.	1720.
5% Load Drop (cycles)	2720.	1305.	2630.	808.	1250.	7287.	2087.
10% Load Drop (cycles)	2830.	1320.	2655.	841.	1312.	7529.	2239.
50% Load Drop (cycles)	2951.	1332.	2689.	932.	1456.	8004.	2769.

Table II-3 - Dogleg Cycle Tests

Specimen Identification	42A	101B	45D	108A	46A	105C
Type of Specimen	MERL 44C	MERL 44C	MERL 44C	MERL 44C	MERL 44C	MERL 44C
Test Conditions:						
Dogleg Cycle Type	LT	LT	LC	HT	HC	HC
Temperature Range (°F)	1000-1600	1000-1600	1000-1600	1000-1600	1000-1600	1000-1600
Strain Range	0.004698	0.004487	0.004738	0.004818	0.004738	0.004716
Strain R-Ratio (min/max)	-0.849	-0.860	-1.038	-1.003	-1.023	-1.027
Strain Rate (1/sec)	1.57E-04	1.50E-04	1.58E-04	1.61E-04	1.58E-04	1.57E-04
Frequency (cyc/min)	1.000	1.000	1.000	1.000	1.000	1.000
Tension Hold (sec)	54.000	54.000	0.0	54.000	0.0	0.0
Compression Hold (sec)	0.0	0.0	54.000	0.0	54.000	54.000
Stress-Strain Response:						
Stress Range, Init (psi)	123535.0	115887.0	126336.0	112619.0	110233.0	102716.0
Stress Range, Nf/2 (psi)	124255.0	122605.0	124321.0	105434.0	109305.0	106679.0
Mean Stress, Init (psi)	-10112.2	1680.6	-1015.2	1918.6	-4665.1	-3716.7
Mean Stress, Nf/2 (psi)	-23988.3	-11109.3	11074.4	8368.3	2315.0	-1386.9
Inel Stn Rng, Init	0.000065	0.000068	0.000063	0.000145	0.000209	0.000168
Inel Stn Rng, Nf/2	0.000085	0.000093	0.000046	0.000261	0.000324	0.000197
Life Results:						
Initiation (cycles)	300.	1110.	1300.	761.	800.	1832.
5% Load Drop (cycles)	1722.	2048.	1787.	2648.	1971.	2755.
10% Load Drop (cycles)	3128.	2263.	1910.	2879.	2225.	2816.
50% Load Drop (cycles)	3292.	2522.	2096.	3171.	2415.	3003.

Table II-4 - Elliptical Cycle Tests

Specimen Identification	1098	1228	127D	1298	124C	126D	108D	125D
Type of Specimen	MERL 73M	MERL 73M	MERL 73M	MERL 73M	MERL 73M	MERL 73M	MERL 44C	MERL 73M
Test Conditions:								
Elliptical Cycle Type	CW	CW	CW	CW	CCW	CCW	CCW	CCW
Temperature Range (°F)	1000-1600	1000-1600	1000-1600	1000-1600	1000-1600	1000-1600	1000-1600	1000-1600
Strain Range	0.003971	0.003977	0.004960	0.004955	0.003974	0.003975	0.004884	0.004939
Strain R-Ratio (min/max)	-1.029	-1.021	-1.033	-0.980	-1.008	-1.008	-0.968	-0.987
Strain Rate (1/sec)	1.32E-04	1.33E-04	1.65E-04	1.65E-04	1.32E-04	1.33E-04	1.63E-04	1.65E-04
Frequency (cyc/min)	1.000	1.000	1.000	1.000	1.000	1.10	1.000	1.000
Tension Hold (sec)	0.0	0.0	0.0	0.0	0.0	0.0	0.0	0.0
Compression Hold (sec)	0.0	0.0	0.0	0.0	0.0	0.0	0.0	0.0
Stress-Strain Response:								
Stress Range, Init (psi)	88601.7	98844.9	117869.0	116311.0	96975.9	92122.6	114925.0	126901.0
Stress Range, Nr/2 (psi)	90632.8	90780.6	115245.0	118401.0	101205.0	92561.0	116940.0	114027.0
Mean Stress, Init (psi)	-2168.2	-1861.3	8256.9	4076.0	565.4	-3047.5	4259.1	7704.2
Mean Stress, Nr/2 (psi)	7790.8	14532.7	13644.9	18726.7	6363.2	12161.8	7825.6	22943.3
Incl Stn Rng, Init	0.000049	0.000078	0.000063	0.000100	0.000083	0.000035	0.000085	0.000078
Incl Stn Rng, Nr/2	0.000151	0.000125	0.000044	0.000067	0.000069	0.000119	0.000163	0.000271
Life Results:								
Initiation (cycles)	5846.	3457.	668.	911.	8291.	7554.	3652.	1097.
5% Load Drop (cycles)	9947.	6262.	1793.	1520.	10862.	10300.	6684.	1919.
10% Load Drop (cycles)	10239.	6321.	1812.	1560.	10955.	10600.	6797.	2127.
50% Load Drop (cycles)	11242.	6523.	1855.	1599.	11681.1	10792.	7024.	2551.2

Notes: 1. Life estimated from gage section replicas; failed at 9497 cycles from crack outside extensometer.

2. Failure originated from large region of porosity.

Table II-5 - Variable Temperature Range Tests

Specimen Identification	1038	45C	106C
Type of Specimen	MERL 44C	MERL 44C	MERL 44C

Test Conditions:

Strain-Temp Phase	IN	OUT	OUT
Temperature Range (°F)	1000-1700	800-1700	1000-1800
Strain Range	0.003889	0.004831	0.004862 ¹
Strain R-Ratio (min/max)	-1.042	-1.016	-1.017
Strain Rate (1/sec)	1.30E-04	1.61E-04	1.62E-04
Frequency (cyc/min)	1.000	1.000	1.000
Tension Hold (sec)	0.0	0.0	0.0
Compression Hold (sec)	0.0	0.0	0.0

Stress-Strain Response:

Stress Range, Init (psi)	84359.4 ²	112360.0	107521.0
Stress Range, Nf/2 (psi)	90576.2	112160.0	108308.0
Mean Stress, Init (psi)	-18819.7	11182.5	18218.7
Mean Stress, Nf/2 (psi)	-16129.7	23868.8	25247.3
Inel Stn Rng, Init	0.000138	0.000134	0.000183
Inel Stn Rng, Nf/2	0.000075	0.000064	0.000231

Life Results:

Initiation (cycles)	3311.	780.	629.
5% Load Drop (cycles)	20030.	1269.	615.
10% Load Drop (cycles)	20780.	1333.	721.
50% Load Drop (cycles)	21131.	1412.	796.

- Notes: 1. Specimen was run first at about 0.0025 strain range for 2800 cycles.
 2. Extensometer interference caused low stress range for first 2682 cycles.

APPENDIX III CUMULATIVE DAMAGE TEST RESULTS

Table III-1 - Strain Ratio Block Tests: R=-1 Followed by R=0

Specimen Identification	7A	13D	8A	106D	1068
Type of Specimen	MERL 75	MERL 75	MERL 75	MERL 75	MERL 75
Block 1 Conditions:					
Length of Block (cycles)	50.	50.	600.	600.	600.
Temperature (°F)	1600.	1600.	1600.	1600.	1600.
Strain Range	0.005038	0.005037	0.005034	0.005184	0.005118
Strain R-Ratio (min/max)	-1.000	-1.000	-1.000	-1.000	-1.000
Strain Rate (1/sec)	1.68E-03	1.68E-03	1.68E-03	1.73E-03	1.71E-03
Frequency (cyc/min)	9.995	10.005	9.999	10.002	10.000
Tension Hold (sec)	0.0	0.0	0.0	0.0	0.0
Compression Hold (sec)	0.0	0.0	0.0	0.0	0.0
Block 2 Conditions:					
Length of Block (cycles)	3800.	4080.	2100.	2515.	1930.
Temperature (°F)	1600.	1600.	1600.	1600.	1600.
Strain Range	0.005038	0.005037	0.005034	0.005184	0.005118
Strain R-Ratio (min/max)	0.0	0.0	0.0	0.0	0.0
Strain Rate (1/sec)	1.68E-03	1.68E-03	1.68E-03	1.73E-03	1.71E-03
Frequency (cyc/min)	9.995	10.005	9.999	10.002	10.000
Tension Hold (sec)	0.0	0.0	0.0	0.0	0.0
Compression Hold (sec)	0.0	0.0	0.0	0.0	0.0
Stress-Strain Response:					
Stress Range, Init (psi)	99814.2	102746.0	105034.0	109426.0	104377.0
Stress Range, BL 1 (psi)	101000.0	103200.0	104500.0	107100.0	104300.0
Stress Range, BL 2 (psi)	97430.0	102540.0	99500.0	104044.0	101020.0
Mean Stress, Init (psi)	1350.5	2559.2	2927.4	3678.1	1726.0
Mean Stress, BL 1 (psi)	-200.0	1600.0	-250.0	950.0	850.0
Mean Stress, BL 2 (psi)	22700.0	21776.0	20750.0	18943.0	19350.0
Incl Stn Rng, Init	0.000153	0.000207	0.000201	0.000218	0.000277
Incl Stn Rng, BL 1	0.000128	0.000174	0.000170	0.000180	0.000233
Incl Stn Rng, BL 2	0.000191	0.000212	0.000226	0.000301	0.000286
Life Results:					
Initiation (cycles)	1588.	1704.	1114.	1285.	1044.
5% Load Drop (cycles)	3612.	3800.	2095.	3087.	2449.
10% Load Drop (cycles)	3692.	4000.	2527.	3095.	2475.
50% Load Drop (cycles)	3850.	4130.	2700.	3115.	2530.

Table III-2 - Strain Ratio Block Tests: One Cycle R=0 Followed by R=-1 ($\pm 0.27\%$)

Specimen Identification	88	10C	12C	47B
Type of Specimen	MERL 75	MERL 75	MERL 75	MERL 75
Block 1 Conditions:				
Length of Block (cycles)	1.	1.	1.	1.
Temperature (°F)	1600.	1600.	1600.	1600.
Strain Range	0.005126	0.005031	0.005047	0.005079
Strain R-Ratio (min/max)	0.0	0.0	0.0	0.0
Strain Rate (1/sec)	1.78E-03	1.82E-03	1.82E-03	1.94E-03
Frequency (cyc/min)	9.999	10.001	10.002	10.000
Tension Hold (sec)	0.0	0.0	0.0	0.0
Compression Hold (sec)	0.0	0.0	0.0	0.0
Block 2 Conditions:				
Length of Block (cycles)	4299.	5049.	3359.	3244.
Temperature (°F)	1600.	1600.	1600.	1600.
Strain Range	0.005341	0.005471	0.005473	0.005823
Strain R-Ratio (min/max)	-1.000	-1.000	-1.000	-1.000
Strain Rate (1/sec)	1.78E-03	1.82E-03	1.82E-03	1.94E-03
Frequency (cyc/min)	9.999	10.001	10.001	10.000
Tension Hold (sec)	0.0	0.0	0.0	0.0
Compression Hold (sec)	0.0	0.0	0.0	0.0
Stress-Strain Response:				
Stress Range, Init (psi)	89420.0	88400.0	91940.0	86280.0
Stress Range, BL 1 (psi)	107671.0	108853.0	108206.0	109531.0
Stress Range, BL 2 (psi)	107714.0	108521.0	107817.0	107685.0
Mean Stress, Init (psi)	44710.0	44200.0	45970.0	43140.0
Mean Stress, BL 1 (psi)	435.9	764.4	-608.6	-186.2
Mean Stress, BL 2 (psi)	3069.3	310.6	963.8	1595.0
Incl Stn Rng, Cyl	0.000710	0.000600	0.000530	0.000540
Incl Stn Rng, Init	0.000259	0.000242	0.000234	0.000280
Incl Stn Rng, Mf/2	0.000269	0.000271	0.000227	0.000279
Life Results:				
Initiation (cycles)	1140.	1338.	890.	860.
5% Load Drop (cycles)	4019.	4639.	2930.	3110.
10% Load Drop (cycles)	4098.	4821.	3043.	3159.
50% Load Drop (cycles)	4300.	5050.	3360.	3245.

Table III-3 - Strain Ratio Block Tests: R=0 Followed by R=-1

Specimen Identification	10D	11C	11D	13C	105B	107A
Type of Specimen	MERL 75	MERL 75	MERL 75	MERL 75	MERL 75	MERL 75
Block 1 Conditions:						
Length of Block (cycles)	600.	600.	600.	600.	1200.	1200.
Temperature (°F)	1600.	1600.	1600.	1600.	1600.	1600.
Strain Range	0.005086	0.004972	0.005045	0.005045	0.005138	0.005158
Strain R-Ratio (min/max)	0.0	0.0	0.0	0.0	0.0	0.0
Strain Rate (1/sec)	1.69E-03	1.68E-03	1.68E-03	1.68E-03	1.71E-03	1.72E-03
Frequency (cyc/min)	9.993	9.979	10.001	9.999	10.003	10.000
Tension Hold (sec)	0.0	0.0	0.0	0.0	0.0	0.0
Compression Hold (sec)	0.0	0.0	0.0	0.0	0.0	0.0
Block 2 Conditions:						
Length of Block (cycles)	7200.	13350.	5991.	5350.	2925.	4484.
Temperature (°F)	1600.	1600.	1600.	1600.	1600.	1600.
Strain Range	0.005086	0.004972	0.005045	0.005045	0.005138	0.005158
Strain R-Ratio (min/max)	-1.000	-1.000	-1.000	-1.000	-1.000	-1.000
Strain Rate (1/sec)	1.69E-03	1.65E-03	1.68E-03	1.68E-03	1.71E-03	1.72E-03
Frequency (cyc/min)	9.993	9.979	10.001	9.999	10.003	10.000
Tension Hold (sec)	0.0	0.0	0.0	0.0	0.0	0.0
Compression Hold (sec)	0.0	0.0	0.0	0.0	0.0	0.0
Stress-Strain Response:						
Stress Range, Init (psi)	99752.9	95686.8	96133.1	103643.0	107026.0	99948.4
Stress Range, BL 1 (psi)	100006.0	97568.4	97500.0	104094.0	111000.0	101000.0
Stress Range, BL 2 (psi)	102500.0	97000.0	99000.0	106000.0	111986.0	101496.0
Mean Stress, Init (psi)	35147.5	35058.7	37146.2	35109.3	35853.0	33320.9
Mean Stress, BL 1 (psi)	26000.0	26250.0	31100.0	25000.0	21500.0	25500.0
Mean Stress, BL 2 (psi)	750.0	-6500.0	-4500.0	-4000.0	-3779.0	-5859.0
Incl Strn Rng, Init	0.000435	0.000341	0.000404	0.000457	0.000571	0.000364
Incl Strn Rng, BL 1	0.000262	0.000192	0.000212	0.000210	0.000338	0.000277
Incl Strn Rng, BL 2	0.000266	0.000187	0.000202	0.000289	0.000337	0.000288
Life Results:						
Initiation (cycles)	3393.	6068.	2867.	2588.	908.	1250.
5% Load Drop (cycles)	6265.	12764.	4645.	5840.	3649.	5150.
10% Load Drop (cycles)	7039.	12839.	5100.	5887.	3833.	5344.
50% Load Drop (cycles)	7800.	13950.	6591.	5950.	4125.	5684.

Table III-4 - Temperature Block Tests

Specimen Identification		118	105A	12A	43A	9D	10B	43C	132C	132D
Type of Specimen		MERL 75	MERL 75	MERL 75	MERL 75	MERL 75	MERL 75	MERL 75	MERL 75	MERL 75
Block 1 Conditions:										
Length of Block (cycles)		600.	600.	1200.	1200.	3500.	3500.	3500.	4950.	7000.
Temperature (°F)		1600.	1600.	1600.	1600.	1000.	1000.	1000.	1000.	1000.
Strain Range		0.004987	0.005149	0.005029	0.005048	0.004996	0.005549	0.005048	0.005030	0.005078
Strain R-Ratio (min/max)		-0.966	-0.933	-0.952	-0.949	-0.970	-1.225	-0.952	-0.987	-0.973
Strain Rate (1/sec)		1.66E-03	1.72E-03	1.68E-03	1.68E-03	1.67E-03	1.85E-03	1.68E-03	1.68E-03	1.69E-03
Frequency (cyc/min)		10.006	9.995	10.001	10.007	10.001	10.007	9.994	9.996	9.999
Tension Hold (sec)		0.0	0.0	0.0	0.0	0.0	0.0	0.0	0.0	0.0
Compression Hold (sec)		0.0	0.0	0.0	0.0	0.0	0.0	0.0	0.0	0.0
Block 2 Conditions:										
Length of Block (cycles)		10800.	11900.	7980.	13000.	3625.	2650.	5700.	0.	1035.
Temperature (°F)		1000.	1000.	1000.	1000.	1600.	1600.	1600.	0.	1600.
Strain Range		0.004987	0.005149	0.005048	0.005029	0.004996	0.005549	0.005048	0.0	0.005078
Strain R-Ratio (min/max)		-0.966	-0.933	-0.949	-0.952	-0.970	-1.225	-0.952	0.0	-0.973
Strain Rate (1/sec)		1.66E-03	1.72E-03	1.68E-03	1.68E-03	1.67E-03	1.85E-03	1.68E-03	0.0	1.69E-03
Frequency (cyc/min)		10.006	9.995	10.007	10.001	10.001	10.007	9.994	0.0	9.999
Tension Hold (sec)		0.0	0.0	0.0	0.0	0.0	0.0	0.0	0.0	0.0
Compression Hold (sec)		0.0	0.0	0.0	0.0	0.0	0.0	0.0	0.0	0.0
Stress-Strain Response:										
Stress Range, Init (psi)		108398.0	104926.0	104641.0	101100.0	119447.0	123749.0	114495.0	122068.0	120869.0
Stress Range, BL 1 (psi)		108400.0	104400.0	104500.0	101100.0	120500.0	120580.0	116450.0	123063.0	119209.0
Stress Range, BL 2 (psi)		129000.0	126322.0	121000.0	122002.0	105897.0	102000.0	98000.0	0.0	107000.0
Mean Stress, Init (psi)		2126.8	1535.7	1918.6	1450.0	1662.4	1966.1	-179.5	0.0	1022.4
Mean Stress, BL 1 (psi)		1800.0	1100.0	4750.0	2250.0	5250.0	3710.0	3975.0	1298.6	11011.3
Mean Stress, BL 2 (psi)		1500.0	3993.0	3000.0	3312.0	2159.5	-4000.0	1000.0	12113.3	0.0
Incl Stn Rng, Init		0.000183	0.000183	0.000165	0.000206	0.000099	0.000080	0.000081	0.000093	-3500.0
Incl Stn Rng, BL 1		0.000195	0.000189	0.000163	0.000192	0.000087	0.000076	0.000078	0.000075	0.000099
Incl Stn Rng, BL 2		0.000080	0.000086	0.000090	0.000082	0.000230	0.000265	0.000211	0.000075	0.000077
									0.0	0.000293
Life Results:										
Initiation (cycles)		6954.	7625.	5049.	7810.	4908.	4318.	6298.	2425.	4419.
5% Load Drop (cycles)		11094.	10480.	8138.	13738.	6206.	5769.	7730.	4485.	6532.
10% Load Drop (cycles)		11229.	11528.	8729.	13944.	6893.	6116.	9171.	4507.	7455.
50% Load Drop (cycles)		11400.	12500.	9180.	14200.	7125.	6150.	9200.	4950.	8035.

Table III-5 - Hold Time Block Tests

Specimen Identification	13A	102B	103A	104C	103D	132A
Type of Specimen	MERL 75	MERL 75	MERL 75	MERL 75	MERL 75	MERL 75
Block 1 Conditions:						
Length of Block (cycles)	300.	1200.	400.	1232.	1300.	1200.
Temperature (°F)	1500.	1600.	1600.	1600.	1600.	1600.
Strain Range	0.005022	0.004790	0.004980	0.004900	0.004950	0.005078
Strain R-Ratio (min/max)	-0.979	-1.000	-1.000	-1.000	-1.000	-1.001
Strain Rate (1/sec)	1.52E-04	1.67E-02	1.67E-02	3.88E-03	1.53E-03	1.54E-04
Frequency (cyc/min)	0.909	10.000	10.000	10.009	10.007	0.909
Tension Hold (sec)	60.000	60.000	0.0	0.0	0.0	0.0
Compression Hold (sec)	0.0	0.0	60.000	0.0	0.0	0.0
Block 2 Conditions:						
Length of Block (cycles)	1138.	3000.	2519.	1098.	7800.	2200.
Temperature (°F)	1600.	1600.	1600.	1600.	1600.	1600.
Strain Range	0.005022	0.004790	0.004980	0.004870	0.004900	0.005078
Strain R-Ratio (min/max)	-0.979	-1.000	-1.000	-1.000	-1.000	-1.001
Strain Rate (1/sec)	1.52E-04	1.60E-03	1.66E-03	1.48E-04	1.48E-04	1.54E-04
Frequency (cyc/min)	0.909	10.000	10.000	0.909	0.909	0.909
Tension Hold (sec)	0.0	0.0	0.0	0.0	60.000	60.000
Compression Hold (sec)	60.000	0.0	0.0	60.000	0.0	0.0
Stress-Strain Response:						
Stress Range, Init (psi)	105319.0	106953.0	103133.0	99854.5	99926.4	105509.0
Stress Range, BL 1 (psi)	103200.0	100445.0	99738.0	98400.0	99900.0	104800.0
Stress Range, BL 2 (psi)	99000.0	100728.0	100445.0	97000.0	91000.0	102852.0
Mean Stress, Init (psi)	-975.1	5376.0	637.0	1386.4	2908.5	2529.2
Mean Stress, BL 1 (psi)	-8400.0	-6932.0	12096.0	3100.0	2650.0	5400.0
Mean Stress, BL 2 (psi)	12500.0	3871.0	4668.5	13000.0	-15500.0	-7954.0
Inel Stn Rng, Init	0.000378	0.000420	0.000390	0.000161	0.000221	0.000240
Inel Stn Rng, BL 1	0.000426	0.000410	0.000400	0.000160	0.000194	0.000152
Inel Stn Rng, BL 2	0.000719	0.000222	0.000205	0.000295	0.000630	0.000515
Hold Sts Rlx, Init (psi)	-3780.0	-3112.0	+3098.0	0.0	0.0	0.0
Hold Sts Rlx, BL 1 (psi)	-3570.0	-2829.0	+3310.0	0.0	0.0	0.0
Hold Sts Rlx, BL 2 (psi)	+6510.0	0.0	0.0	+1960.0	-6126.0	-6932.0
Life Results:						
Initiation (cycles)	446.	1092.	234.	1561.	2093.	1666.
5% Load Drop (cycles)	948.	3950.	2650.	2298.	4357.	2819.
10% Load Drop (cycles)	1241.	4100.	2800.	2318.	6795.	3210.
50% Load Drop (cycles)	1438.	4200.	2919.	2330.	9100.	3400.

Table III-6 - Sequenced Tests

Specimen Identification	101D	121C	121B	103C	121A	104B	128D	130A	130B
Type of Specimen	MERL 75	MERL 75	MERL 75	MERL 75	MERL 75	MERL 75	MERL 75	MERL 75	MERL 75
Block 1 Conditions:									
Length of Block (cycles)	100.	100.	15.	5.	5.	3.	3.	10.	10.
Temperature (°F)	1600.	1600.	1600.	1600.	1600.	1600.	1600.	1600.	1600.
Strain Range	0.004950	0.005040	0.005000	0.005050	0.005030	0.003371	0.003978	0.004982	0.004988
Strain R-Ratio (min/max)	0.0	0.0	0.0	0.0	0.0	-0.983	-1.000	-1.000	-1.000
Strain Rate (1/sec)	1.65E-03	1.68E-03	1.67E-03	1.68E-03	1.68E-03	1.40E-03	1.66E-03	1.66E-03	1.66E-03
Frequency (cyc/min)	10.000	10.000	10.000	10.000	10.000	12.500	12.500	10.000	10.000
Tension Hold (sec)	0.0	0.0	0.0	0.0	0.0	0.0	0.0	0.0	0.0
Compression Hold (sec)	0.0	0.0	0.0	0.0	0.0	0.0	0.0	0.0	0.0
Block 2 Conditions:									
Length of Block (cycles)	5.	5.	5.	5.	5.	1.	1.	1.	1.
Temperature (°F)	1600.	1600.	1600.	1600.	1600.	1600.	1600.	1600.	1600.
Strain Range	0.004950	0.005040	0.005000	0.005050	0.005030	0.004202	0.005064	0.008060	0.008070
Strain R-Ratio (min/max)	0.0	0.0	0.0	0.0	0.0	-0.983	-1.000	-1.000	-1.000
Strain Rate (1/sec)	8.25E-05	8.40E-05	8.33E-05	8.42E-05	8.38E-05	1.40E-03	1.69E-03	1.68E-03	1.68E-03
Frequency (cyc/min)	0.500	0.500	0.500	0.500	0.500	10.000	10.000	6.250	6.250
Tension Hold (sec)	0.0	0.0	0.0	0.0	0.0	0.0	0.0	0.0	0.0
Compression Hold (sec)	0.0	0.0	0.0	0.0	0.0	0.0	0.0	0.0	0.0
Stress-Strain Response:									
Stress Range, Init (psi)	97517.0	103397.0	104315.0	99597.0	102315.0	80601.0	90259.0	101011.0	104124.0
Stress Range, BL 1 (psi)	95636.0	104347.0	102411.0	95141.0	102172.0	70382.0	88939.0	100634.0	101463.0
Stress Range, BL 2 (psi)	91484.0	101071.0	100029.0	91768.0	98814.0	86676.0	112329.0	152908.0	152413.0
Mean Stress, Init (psi)	37119.0	40874.7	36439.0	38481.0	37725.1	964.0	283.0	707.0	-566.0
Mean Stress, BL 1 (psi)	6725.0	16189.0	17862.0	10293.0	16790.2	1096.0	330.0	-47.0	-2641.0
Mean Stress, BL 2 (psi)	6778.0	17826.0	16052.0	10328.0	17470.0	142.0	142.0	47.0	-3112.0
Incl Stn Rng, Init	0.000370	0.000354	0.000389	0.000375	0.000414	0.000073	0.000057	0.000172	0.000180
Incl Stn Rng, BL 1	0.000190	0.000230	0.000194	0.000223	0.000170	0.000077	0.000067	0.000189	0.000177
Incl Stn Rng, BL 2	0.000375	0.000359	0.000256	0.000391	0.000260	0.000101	0.000139	0.000751	0.000773
Life Results:									
Initiation (cycles)	1680.	800.	1591.	833.	675.	6792.	3040.	554.	643.
5% Load Drop (cycles)	6720.	2175.	2175.	1650.	1510.	11097.	6924.	1133.	1675.
10% Load Drop (cycles)	6930.	2400.	2560.	2350.	1550.	20042.	7128.	1452.	1735.
50% Load Drop (cycles)	7000.	2810.	3060.	2688.	1570.	20275.	7680.	1496.	1738.

Table III-7 - Interrupted Tests: Interspersed Exposure Time

Specimen Identification	107B	107D	129A	108B	129C	132B
Type of Specimen	MERL 75	MERL 75	MERL 75	MERL 75	MERL 75	MERL 75
Block 1 Conditions:						
Length of Block (cycles)	200.	200.	200.	200.	200.	200.
Temperature (°F)	1600.	1600.	1600.	1600.	1600.	1600.
Strain Range	0.005462	0.005175	0.005056	0.005220	0.005082	0.005070
Strain R-Ratio (min/max)	-0.059	0.002	0.0	0.004	0.0	0.0
Strain Rate (1/sec)	1.82E-03	1.72E-03	1.69E-03	1.74E-03	1.69E-03	1.69E-03
Frequency (cyc/min)	10.002	9.997	10.000	10.000	9.996	9.996
Tension Hold (sec)	0.0	0.0	0.0	0.0	0.0	0.0
Compression Hold (sec)	0.0	0.0	0.0	0.0	0.0	0.0
Block 2 Conditions:						
Length of Hold (sec)	3600.	3600.	3600.	3600.	3600.	1800.
Temperature (°F)	1600.	1600.	1600.	1600.	1600.	1600.
Hold Stress (psi)	0.0	62000.0	62000.0	62000.0	62000.0	62000.0
Strain Accumulated ?	No	No	No	Yes	Yes	Yes
Stress-Strain Response:						
Stress Range, Init (psi)	99262.0	101023.0	100728.0	101750.0	101294.0	106531.0
Stress Range, BL 1 (psi)	101048.0	98531.3	100162.0	100529.0	99596.6	104679.0
Stress Range, BL 2 (psi)	0.0	62000.0	62000.0	62000.0	62000.0	62000.0
Mean Stress, Init (psi)	33937.7	33028.1	34256.3	28125.0	25041.0	22218.0
Mean Stress, BL 1 (psi)	21842.6	-19097.0	-6507.0	39167.1	12944.7	35249.0
Mean Stress, BL 2 (psi)	0.0	31000.0	31000.0	31000.0	31000.0	31000.0
Incl Stn Rng, Init	0.000500	0.000515	0.000400	0.000469	0.000400	0.000420
Incl Stn Rng, BL 1	0.000336	0.000349	0.000200	0.000354	0.000230	0.000210
Total Creep Strain	0.0	0.032570	0.023050	0.013720	0.015210	0.011780
Life Results:						
Initiation (cycles)	1280.	798.	576.	627.	451.	480.
5% Load Drop (cycles)	1376.	1100.	1200.	1026.	783.	850.
10% Load Drop (cycles)	1433.	1400.	1200.	1057.	855.	882.
50% Load Drop (cycles)	4000.	1400.	1200.	1100.	940.	1000.

Table III-8 - Interrupted Tests: Creep First Before Fatigue

Specimen Identification	138	102D	130C	130D	131A
Type of Specimen	MERL 75	MERL 75	MERL 75	MERL 75	MERL 75
Creep Conditions:					
Creep Time (sec)	450.	450.	36000.	18420.	25200.
Temperature (°F)	1600.	1600.	1600.	1600.	1600.
Hold Stress (psi)	75000.0	75000.0	62000.0	62000.0	62000.0
Fatigue Conditions:					
Length of Block (cycles)	2515.	4950.	735.	0.	9.
Temperature (-F)	1600.	1600.	1600.	0.	1600.
Strain Range	0.005101	0.004871	0.005045	0.0	0.005050
Strain R-Ratio (min/max)	0.328	0.335	0.0	0.0	0.0
Strain Rate (1/sec)	1.70E-03	1.62E-03	1.68E-03	0.0	1.68E-03
Frequency (cyc/min)	10.004	9.999	10.000	0.0	10.000
Tension Hold (sec)	0.0	0.0	0.0	0.0	0.0
Compression Hold (sec)	0.0	0.0	0.0	0.0	0.0
Stress-Strain Response:					
Stress Range, Init (psi)	102226.0	101524.0	93655.0	0.0	95564.7
Stress Range, Nf/2 (psi)	104867.0	102916.0	99738.0	0.0	89269.2
Mean Stress, Init (psi)	38142.0	34292.3	39754.0	0.0	34342.0
Mean Stress, Nf/2 (psi)	22237.5	24753.6	26385.0	0.0	21998.5
Inel Stn Rng, Init	0.000376	0.000333	0.000300	0.0	0.000500
Inel Stn Rng, Nf/2	0.000236	0.000207	0.000275	0.0	0.000550
Total Creep Strain	0.002910	0.003230	0.014700	0.012700	0.017900
Life Results:					
Initiation (cycles)	1069.	2104.	327.	0.	0.
5% Load Drop (cycles)	2466.	4489.	210.	0.	1.
10% Load Drop (cycles)	2488.	4558.	390.	0.	1.
50% Load Drop (cycles)	2515.	4950.	735.	0.	9.

REFERENCES

- 3.1. Moreno, V., Nissley, D. M., and Lin, L. S., "Creep Fatigue Life Prediction for Engine Hot Section Materials (Isotropic) - Second Annual Report," NASA CR-174844, March 1985.
- 4.1 Saltsman, J.F., and Halford, G.R., "An Update of the Total-Strain Version of SRP", NASA TP-2499, October, 1985.
- 4.2 Moreno, V., Nissley, D.M., Halford, G.R., and Saltsman, J.F., "Application of Two Creep Fatigue Life Models for the Prediction of Elevated Temperature Crack Initiation of a Nickel Base Alloy", AIAA-85-1420, AIAA/SAE/ASME/ASME 21st Joint Propulsion Conference, Monterey, California, July, 1985.
- 4.3 Cailletaud, G., Nouailhas, D., Escaravage, C., Heliot, J., Kang, S., Grattier, J., Levillant, C., Mottot, M., Tortel, J., "A Review of Creep Fatigue Life Prediction Methods", 7th International Conference on "Structural Mechanics in Reactor Technology", Chicago, Illinois, August, 1983.
- 4.4 Lemaitre, J., "Phenomenological Relations for the Prediction of Low-Cycle Fatigue", ESA TT-402, July, 1977.
- 4.5 Savalle, S., and Cailletaud, G., "Microinitiation, Micropropagation, and Damage", La Recherche Aerospatiale, No. 1982-6, pp. 17-32.
- 4.6 Polhemus, J.F., Spaeth, C.E., and Vogel, W.H., "Ductility Exhaustion Model for Prediction of Thermal Fatigue and Creep Interaction", Fatigue at Elevated Temperatures, ASTM STP 520, American Society for Testing and Materials, 1973, pp. 625-636.
- 4.7 Levillant, C., and Pineau, A., "Assessment of High-Temperature Low-Cycle Fatigue of Austenitic Stainless Steels by Using Intergranular Damage as a Correlating Parameter", Low-Cycle Fatigue and Life Prediction, ASTM STP 770, American Society of Testing and Materials, 1982, pp. 169-193.
- 4.8 Winstone, M.R., Nikbin, K.M., and Webster, G.A., "Modes of Failure under Creep/Fatigue Loading of a Nickel-Based Superalloy", Journal of Materials Science, Vol. 20 (1985), pp. 2471-2476.
- 4.9 Bernstein, H.L., "An Evaluation of Four Creep-Fatigue Models for a Nickel-Base Superalloy", Low-Cycle Fatigue and Life Prediction, ASTM STP 770, American Society of Testing and Materials, 1982, pp. 105-134.
- 4.10 Milligan, W.W., and Bill, R.C., "Low Cycle Fatigue Behavior of Conventionally Cast MAR-M 200 at 1000 deg C.", NASA TM-83769, September, 1984.

- 4.11 Morishita, M., Asada, Y., and Ishikawa, A., "An Evaluation of Creep-Fatigue Behavior of 304 Stainless Steel in a Very High Vacuum Environment", Bulletin of JSMÉ, Vol 28, No. 235, January, 1985, pp. 7-12.
- 4.12 Morris, W.L., and James, M.R., "Statistical Aspects of Fatigue Failure Due to Alloy Microstructure", Fatigue Mechanisms: Advances in Quantitative Measurement of Physical Damage, ASTM STP 811, American Society for Testing and Materials, 1983, pp. 179-206.
- 4.13 James, M.R., and Morris, W.L., "The Role of Microplastic Deformation in Fatigue Crack Initiation", *ibid.*, pp. 46-70.
- 5.1 Hopkins, S. W., "Low-Cycle Thermal Mechanical Fatigue Testing," in Thermal Fatigue of Materials and Components, STP 612, D. A. Spera and D. F. Mowbray, Eds., American Society of Testing and Materials, Philadelphia, 1976, pp.157-169.
- 5.2 Gemma, A. E., Ashland, F. X., and Masci, R. M., "The Effects of Stress Dwells and Varying Mean Strain on Crack Growth During Thermal Mechanical Fatigue," Journal of Testing and Evaluation, JTEVA, Vol. 9, No. 4, July 1981, pp.209-215.
- 5.3 Bill, R. C., Verrilli, M. J., McGaw, M. A., and Halford, G. R., "Preliminary Study of Thermomechanical Fatigue of Polycrystalline MAR-M 200," NASA TP-2280, AVSCOM TR 83-C-6, February 1984.
- 5.4 Lesne, P. M., and Chaboche, J. L., "Prediction of Crack Initiation Under Thermal Fatigue and Creep," Second International Conference on "Fatigue Thresholds - Fatigue 84", Birmingham, G.B., September 3-7, 1984.
- 6.1 Garud, Y.S., "Multiaxial Fatigue: A Survey of the State of the Art", Journal of Testing and Evaluation, JTEVA, Vol. 9, No. 3, May 1981, pp. 165-178.
- 6.2 Jordan, E.P., "Fatigue - Multiaxial Aspects", a chapter in Pressure Vessels and Piping Design Technology - 1982 - A Decade of Progress, eds. S.Y. Zamrik and D. Dietrich, PVP of ASME, 1982, pp. 507-518.
- 6.3 Manson, S.S. and Halford, G.R., "Multiaxial Rules for Treatment of Creep - Fatigue Problems by Strainrange Partitioning", 1976 ASME - MPC Symposium on Creep - Fatigue Interaction, ASME, 1976, pp. 299-322.
- 6.4 Manson, S.S. and Halford, G.R., Discussion to paper: "Multiaxial Low-Cycle Fatigue of Type 304 Stainless Steel" by J.J. Blass and S.Y. Zamrik, 1976 ASME - MPC Symposium on Creep - Fatigue Interaction, ASME, 1976, pp 129-159.
- 6.5 Garud, Y.S., "A New Approach to the Evaluation of Fatigue Under Multiaxial Loadings", ASME Journal of Engineering Materials and Technology, Vol. 103, April 1981, pp. 118-125.

- 6.6 Kanazawa, K., Miller, K.J., and Brown, M.W., "Low-Cycle Fatigue Under Out-of-Phase Loading Conditions", ASME Journal of Engineering Materials and Technology, Vol. 99, No. 3, July 1977, pp. 222-228.
- 6.7 Jordan, E.H., "Elevated Temperature Biaxial Fatigue", Final Report, Grant No. NAG-3-160, February 1981 to October 1984, NASA.
- 6.8 Socie, D.F. and Shield, T.W., "Mean Stress Effects in Biaxial Fatigue of Inconel 718", ASME Journal of Engineering Materials and Technology, Vol. 106, July 1984, pp. 227-232.
- 6.9 Moreno, V., Nissley, D.M., and Lin, L.S. "Creep Fatigue Life Prediction For Engine Hot Section Materials (Isotropic), Second Annual Report," NASA CR-174844, March 1985.
- 7.1 Miner, M.A., "Cumulative Damage in Fatigue," ASME Journal of Applied Mechanics, Vol. 67, 1945, pp. A159-A164.
- 7.2 Palmgren, A., "Die Lebensdauer von Kugellagern," Zetschrift des Vereines, Deutsches Ingenieure, Duesseldorf, West Germany, Vol. 68, No. 14, 1924.
- 7.3 Manson, S.S.; Freche, J.C.; and Ensign, C.R., Fatigue Crack Propagation, ASTM STP 415, American Society for Testing and Materials, Philadelphia, 1967, pp. 384-412.
- 7.4 Manson, S.S.; and Halford, G.R., "Practical implementation of the double linear damage rule and damage curve approach for treating cumulative fatigue damage," International Journal of Fracture, Vol. 17, No. 2, April 1981, pp. 169-192.
- 7.5 Chaboche, J.L., "Lifetime Predictions and Cumulative Damage under High-Temperature Conditions," Low-Cycle Fatigue and Life Prediction, ASTM STP 770, C. Amzallag, B.N. Leis, and P. Rabbe, Eds., American Society for Testing and Materials, 1982, pp.81-104.
- 7.6 Bagci, C., "Fatigue Design of Machine Elements Under Cumulative Damage Effect, Using Bagci's Fatigue Failure Surface Line," ASME Journal of Vibration, Acoustics, Stress, and Reliability in Design, Vol. 106, October 1984, pp. 466-475.
- 7.7 Kutt, T.V.; and Bieniek, M.P., "Cumulative Damage and Fatigue Life Prediction," AIAA 85-0614, 1985, pp. 53-61.
- 7.8 Kliman, V., "Fatigue Life Prediction for a Material under programmable loading using the cyclic stress-strain properties," Materials Science and Engineering, Vol. 68, 1984, pp. 1-10.
- 7.9 Aslam, M.; Jeelani, S., "Prediction of cumulative fatigue damage," Journal of Materials Science, Vol. 20, 1985, pp. 3239-3244.

- 7.10 Leis, B.N., "A History Dependent Damage Model for Low Cycle Fatigue," ASME 84-PVP-112, 1984.
- 7.11 Pluvinage, G.C.; and Raguet, M.N., "Physical and Mechanical Measurements of Damage in Low-Cycle Fatigue: Applications for Two-Level Tests," Fatigue Mechanisms: Advances in Quantitative Measurement of Physical Damage, ASTM STP 811, J. Lankford, D.L. Davidson, W.L. Morris, and R.P. Wei, Eds., American Society for Testing and Materials, 1983, pp. 139-150.
- 7.12 Endo, T.; and Sakon, T., "Creep-fatigue life prediction using simple high-temperature low-cycle fatigue testing machines," Metal Technology, Vol. 11, November, 1984, pp. 489-496.
- 7.13 Reuchet, J.; Reger, M.; Rezai-Aria, F.; and Remy, L., "Cumulation of High-Temperature Fatigue Damage in Two-Temperature Tests," Low-Cycle Fatigue and Life Prediction, ASTM STP 770, C. Amzallag, B.N. Leis, and P. Rabbe, Eds., American Society for Testing and Materials, 1982, pp. 194-211.
- 8.1 Liu, H.W. and Oshida, Y., "Literature Survey on Oxidation and Fatigue Lives at Elevated Temperatures", NASA Contractor Report 174639, March 1984.
- 8.2 Ericsson, T., "Review of Oxidation Effects on Cyclic Life at Elevated Temperature", Canadian Metallurgical Quarterly, Vol. 18, pp. 177-195, 1979.
- 8.3 Coffin, L.F., "Fatigue at Elevated Temperatures", p. 5, ASTM STP 520, 1973.
- 8.4 Coffin, L.F., Metallurgical Transactions A, 3 (1972) p. 1777.
- 8.5 Udoguchi, T., and Wada, T., in D.J. Littler (ed.), "Thermal Stresses and Thermal Fatigue", Butterworth, London, 1971, p. 109.
- 8.6 Degallaix, G., Degallaix, S. and Foct, J., "A Damage Law for Predicting the Elevated Temperature Low Cycle Fatigue Life of a Martensitic Stainless Steel", Materials Science and Engineering, 58 (1983) pp. 55-62.
- 8.7 Antolovich, S.D., Liu, S., and Baur, R., "Low Cycle Behavior of Rene' 80 at Elevated Temperature", Metallurgical Transactions A, Vol. 12A, March 1981, pp. 473-481.
- 8.8 Wright, P.K., "Environmental Effects on the Low Cycle Fatigue of a Single-Crystal Superalloy", Final Report, Contract No. N00019-82-C-0269 (Part II), Dept. of Navy, October 1984.

- 8.9 Challenger, K.D., Miller, A.K. and Langdon, R.L., "Elevated Temperature Fatigue with Hold Time in a Low Alloy Steel: A Predictive Correlation", Journal of Materials for Energy Systems, Vol. 3, June 1981 pp. 51-61.
- 8.10 Reuchet, J., and Remy, L., "Fatigue Oxidation Interaction in a Superalloy-Application to Life Prediction in High Temperature Low Cycle Fatigue", Metallurgical Transactions A, Vol. 14A, January 1983, pp. 141-149.
- 8.11 Swanson, G.A., et al, "Life Prediction and Constitutive Models for Engine Hot Section Anisotropic Materials Program", Annual Status Report, NASA CR-174952, February 1986.
- 8.12 Anton, D.L. and Favrow, L.H., "The Effect of HIP on the Elevated Temperature LCF Properties of an Equiaxed Cast Superalloy", to be published in the Proceedings of the ASTM Symposium on Low Cycle Fatigue: Directions for the Future, Lake George, NY, October 1985..